Quantitative PET data extraction for precise clinical decisions

Maria Teresa Gandia-Ferrero

Directors:
Irene Torres-Espallardo
Luis Martí-Bonmatí

Tutor:
José David Martín-Guerrero

Doctoral Programme In Electronic Engineering - 3131

May, 2025

Dr. Irene Torres-Espallardo, Specialist in Hospital Radiophysics in the Nuclear Medicine Service of the Clinical Imaging Area at the Hospital Universitari i Politècnic La Fe.

Dr. Luis Martí-Bonmatí, Director of the Biomedical Imaging Research Group and the Clinical Imaging Area at the Hospital Universitari i Politècnic La Fe.

Dr. Jose David Martín-Guerrero, Professor in the Department of Electronic Engineering at the Universitat de València.

CERTIFY: That the present thesis, titled: *Quantitative PET data extraction for precise clinical decisions*, corresponds to the work carried out under their supervision and guidance by Ms. Maria Teresa Gandia-Ferrero, for submission as a Doctoral Thesis in the Ph.D. Program in Electronic Engineering at the Universitat de València.

For the record, they sign this certificate:

IRENE| TORRES| ESPALLARDO
Firmado digitalmente por IRENE|TORRES|ESPALLARDO
Fecha: 2025.05.27 11:01:56 +02'00'

Director: Irene Torres-Espallardo

LUIS| MARTI| BONMATI
Firmado digitalmente por LUIS|MARTI|BONMATI
Fecha: 2025.05.28 07:45:34 +02'00'

Director: Luis Martí-Bonmatí

Digitally signed by JOSE DAVID| MARTIN| GUERRERO
Date: 2025.05.28 08:31:45 +02'00'

Tutor: Jose David Martín-Guerrero

Acknowledgements

This work would not have been possible without the support of the Health Research Institute La Fe. I would like to express my deepest gratitude to the Institute, and in particular to the Biomedical Imaging Research Group ($GIBI2^{30}$) and the Clinical Area of Medical Imaging, for providing me with the resources and the environment to grow academically.

My deepest thanks go to all the people who have accompanied me along this journey.

To my thesis supervisors, Irene Torres-Espallardo and Luis Martí-Bonmatí, for their guidance, patience, and commitment. Their knowledge and dedication were essential to the completion of this work. I also thank my thesis tutor, José David Martín-Guerrero, for his valuable advice and for always being available whenever I needed help.

I want to especially highlight the dedication of my supervisor Luis in promoting scientific research in the field of medical imaging, as well as his efforts in creating and consolidating a research group that has grown exponentially in both people and projects. Thank you for your professionalism, your ideas, and your sound advice.

To my supervisor Irene, I owe not only the undertaking of this PhD but also having truly enjoyed the journey. She has been, and continues to be, a role model for me both professionally and personally. Thank you for welcoming me into your office, for teaching me so much, for your brilliant ideas, your patience, your clear explanations, and your constant professionalism. Thank you also for helping me integrate with the hospital staff, for sharing your enthusiasm for research, and for being there through both laughter and encouraging words when I needed them most. Words cannot express how grateful I am to you. Working by your side has been a true joy.

I would also like to thank Manel Perucho-Pla, who has been a role model for me both academically and personally. As my professor and thesis supervisor during my undergraduate Physics degree at the University of Valencia, his support was key to restoring my motivation for research at a crucial moment. Thanks to him, I began the path that led me to complete this thesis.

To my colleagues at the Nuclear Medicine Department of Hospital Universitari i Politècnic La Fe —nuclear medicine and radiophysics residents, nuclear physicians, technicians, nurses, radiopharmacists, and orderlies— thank you for your collaboration and your constant willingness to help. Special thanks to Merche, for her warmth and for spreading her joy from the early morning. To Matthew, for reviewing the English in my thesis, your attention to detail have been greatly appreciated. To Begoña, Pablo, and

Stefan, for their involvement in the projects I have worked on and for always resolving my medical questions with such clarity.

Last but not least, to my family. To my parents, Pepe and Tere, for teaching me the value of hard work and dedication. To my sister Laura, for always being a role model, and to my brother-in-law Lluís, who, together with her, have been the best math teachers I could have asked for. To my partner Jordi, for sharing this journey with me, for bringing joy to it, and for being there even on the toughest days. Thank you to my whole family for your unconditional love, unwavering support, and belief in me.

Agraïments

Aquest treball no hauria sigut possible sense el suport de l'Institut d'Investigació Sanitària La Fe. Vull expressar el meu més sincer agraïment tant a l'Institut com, en particular, al Grup d'Investigació Biomèdica en Imatge ($GIBI2^{30}$) i a l'Àrea Clínica d'Imatge Mèdica, per oferir-me els recursos i l'entorn necessaris per a desenvolupar-me acadèmicament.

El meu agraïment més profund és per a totes les persones que m'han acompanyat al llarg d'aquest camí.

Als meus directors de tesi, Irene Torres-Espallardo i Luis Martí-Bonmatí, per la seua guia, paciència i compromís. El seu coneixement i dedicació han sigut fonamentals per a la realització d'aquest treball. També vull agrair al meu tutor de tesi, José David Martín-Guerrero, pels seus valuosos consells i per estar sempre disponible quan l'he necessitat.

Vull destacar especialment el compromís del meu director Luis per impulsar la investigació científica en l'àmbit de la imatge mèdica, així com per la creació i consolidació d'un grup d'investigació que ha crescut exponencialment tant en persones com en projectes. Gràcies per la teua professionalitat, per les teues idees i pels bons consells.

A la meua directora Irene, li dec no sols haver iniciat aquest doctorat, sinó també haver-lo gaudit de veritat. Ha sigut, i continua sent, un referent per a mi, tant en l'àmbit professional com personal. Gràcies per acollir-me al teu despatx, per ensenyar-me tant, per les teues idees brillants, la paciència, les explicacions clares i per la teua professionalitat constant. També gràcies per ajudar-me a integrar-me amb tot el personal de l'hospital, per contagiar-me les teues ganes d'investigar i per compartir amb mi tant somriures com paraules d'ànim quan més ho necessitava. No hi ha paraules per a expressar com n'estic d'agraïda. Treballar al teu costat ha sigut una autèntica alegria.

També vull agrair a Manel Perucho-Pla, que ha sigut un referent per a mi tant a nivell acadèmic com personal. Va ser el meu professor d'Àlgebra i Geometria en el primer curs del grau de Física a la Universitat de València, i director del meu treball de fi de grau. El seu suport va ser clau per a recuperar la motivació per la investigació en un moment decisiu. Gràcies a ell vaig iniciar el camí que m'ha portat fins ací.

Als meus companys del Servei de Medicina Nuclear de l'Hospital Universitari i Politècnic La Fe —residents de medicina nuclear i radiofísica, metges nuclears, tècnics, infermeres, radiofarmacèutiques i zeladors— gràcies per la vostra col · laboració i per la vostra disposició constant per ajudar. Un agraïment especial a Merche, pel seu afecte i per contagiar-me la seua alegria des de primera hora del matí. A Matthew, moltes

gràcies per la teua atenció als detalls en revisar l'anglés de la meua tesi. A Begoña, Pablo i Stefan, per la seua col · laboració en els projectes en què he treballat i per resoldre sempre els meus dubtes mèdics amb tanta claredat.

I finalment, però no menys important, a la meua família. Als meus pares, Pepe i Tere, per haver-me ensenyat des de sempre el valor de l'esforç i la dedicació. A la meua germana Laura, per ser sempre un referent, i al meu cunyat Lluís, que juntament amb ella han sigut els millors professors de matemàtiques que podria haver tingut. A la meua parella, Jordi, per compartir aquest camí amb mi, omplir-lo d'alegria i estar al meu costat, fins i tot en els dies més difícils. Gràcies a tota la meua família pel vostre amor incondicional, el suport constant i la confiança en mi.

Abstract

The present thesis aims to enhance clinical decision-making in the management of dementia and neuroendocrine tumors using advanced PET imaging analysis. The research focuses on the extraction and analysis of quantitative data from PET images to make diagnoses more precise and treatment decisions more reliable, while also exploring ways to optimize imaging technology for better clinical outcomes.

In the context of dementia, the study explores how [^{18}F]FDG PET scans, combined with a test of social cognition (the Reading the Mind in the Eyes Test, RMET), can assist in early diagnosis. A deep learning-based classification algorithm was also externally validated, which could enhance the accuracy of detecting neurodegenerative diseases. Another part of the study focused on evaluating a new dedicated brain PET scanner, comparing its image quality and diagnostic power with standard PET/CT scans. These devices could help reduce the burden on general PET/CT scanners while still providing reliable neurological diagnoses.

For patients with neuroendocrine tumors, the study examines two different hybrid PET imaging scanners, PET/CT and PET/MR, to determine how well they align in classifying lesions and guiding treatment decisions. By harmonizing the data from both devices, the aim is to ensure that regardless of the imaging method used, the recommended treatment remains consistent. This would help standardize diagnostic practices and improve the reliability of PET imaging for these rare tumors.

The findings supported the hypothesis that PET image analysis provides meaningful information that impacts clinical decisions in both dementia and neuroendocrine tumor cases. In the context of dementia, results demonstrated that social cognition impairment correlates with specific neuroanatomical changes observed in PET imaging. In particular, the study confirmed that emotion recognition deficits are present in mild cognitive impairment (MCI) patients, but these deficits are not exclusive to Alzheimer's disease. This suggests that including RMET in the neuropsychological test battery will not improve the accuracy of Alzheimer's disease diagnosis.

The external validation of a deep learning model designed to classify MCI patients further confirmed the feasibility of AI-based approaches in nuclear medicine. The model achieved 80% balanced accuracy in distinguishing MCI patients with neurodegenerative disease from those without. The study reinforced that AI tools could support nuclear medicine physicians in the early and more precise identification of neurodegenerative diseases, although additional refinements are necessary to improve classification accuracy, especially in cases involving dementia with Lewy bodies and frontotemporal dementia.

Additionally, the comparison between brain-dedicated PET scanners and conventional PET/CT systems highlighted the potential for reducing the neurological burden without compromising image quality or diagnostic reliability. The evaluation showed that brain-dedicated PET scanners provide comparable image contrast and spatial resolution. However, variations in attenuation correction techniques were noted, emphasizing the need for ongoing improvements in image harmonization methods to ensure consistency between different imaging systems.

For neuroendocrine tumors, the study underscored the critical need for consistent quantitative PET imaging to guide theragnostic applications. Given that Peptide Receptor Radionuclide Therapy (PRRT) eligibility relies on uptake intensity measurements, variations in PET scanner parameters could significantly impact treatment decisions. The analysis revealed that different PET systems produce varying standardized uptake value (SUV) measurements, potentially leading to discrepancies in treatment recommendations.

To address this issue, the study employed ComBat harmonization to align SUV values between PET/CT and PET/MR scanners. Prior to harmonization, 23% of lesions were classified differently depending on the imaging system used, reflecting moderate agreement (kappa coefficient of 0.54). After harmonization, agreement significantly improved (kappa coefficient of 0.60 for PET/MR, 0.74 for PET/CT and 0.65 for the arbitrary system as references), demonstrating the effectiveness of harmonization methods in ensuring consistent treatment recommendations across different imaging platforms.

The study's findings confirm that PET imaging can be enhanced through advanced computational methods, leading to improved diagnostic accuracy and more reliable treatment planning. However, several challenges remain, including the need for larger datasets to refine statistical analysis and further validation of harmonization techniques in multicenter studies.

This study provides strong evidence that quantitative PET imaging plays a crucial role in clinical decision-making for dementia and neuroendocrine tumors. By extracting useful information from the quantification of PET images, PET imaging can be optimized for better diagnostic accuracy and consistency. The findings support the continued advancement of quantitative PET in nuclear medicine and emphasize the need for standardization to ensure that clinical decisions remain robust across different imaging platforms. Future research should build upon these insights to further enhance the role of PET imaging in precision medicine.

Resum

Aquesta tesi té com a objectiu millorar la presa de decisions clíniques en la gestió de la demència i els tumors neuroendocrins mitjançant l'anàlisi avançat d'imatges PET. La investigació se centra en l'extracció i anàlisi de dades quantitatives d'imatges PET per tal de proporcionar diagnòstics més precisos i decisions en quant a tractaments més fiables, alhora que explora formes d'optimitzar la tecnologia d'imatge per a millorar els resultats clínics.

En el context de la demència, l'estudi estudia com les exploracions PET amb [^{18}F]FDG, combinades amb una prova de cognició social ("Reading the Mind in the Eyes Test", RMET), poden ajudar en el diagnòstic precoç. També s'ha validat externament un algorisme de classificació basat en aprenentatge profund, per tal d'augmentar la precisió en la detecció de malalties neurodegeneratives. Una altra part de l'estudi s'ha centrat en avaluar un nou escàner PET dedicat al cervell, comparant la seua qualitat d'imatge i capacitat diagnòstica amb els escàners PET/CT convencionals. Aquests dispositius podrien reduir la càrrega sobre els escàners PET/CT generals i, al mateix temps, proporcionar diagnòstics neurològics fiables.

Per als pacients amb tumors neuroendocrins, l'estudi examina dos escàners híbrids d'imatge PET: PET/CT i PET/MR, per a determinar el grau de coincidència d'aquests dos equips en la classificació de lesions i, per tant, en l'orientació de les decisions terapèutiques. En harmonitzar les dades de tots dos dispositius, es busca garantir que, independentment del mètode d'imatge utilitzat, el tractament recomanat siga coherent. Això ajudaria a estandarditzar les pràctiques de diagnòstic i a millorar la fiabilitat de la imatge PET per a aquests tumors poc freqüents.

Els resultats de la tesi han confirmat la hipòtesi que l'anàlisi quantitatiu d'imatges PET proporciona informació significativa que impacta les decisions clíniques en quant a demència i tumors neuroendocrins. En el context de la demència, els resultats van demostrar que el deteriorament de la cognició social es correlaciona amb canvis neuroanatòmics específics observats en les imatges PET. En particular, l'estudi va confirmar que els dèficits en el reconeixement emocional estan presents en pacients amb deteriorament cognitiu lleu (DCL), però que aquests dèficits no són exclusius de la malaltia d'Alzheimer. Això suggereix que la inclusió de la prova RMET en la bateria de proves neuropsicològiques no millorarà la precisió del diagnòstic de la malaltia d'Alzheimer.

La validació externa d'un model d'aprenentatge profund dissenyat per a classificar pacients amb DCL va confirmar encara més la viabilitat dels enfocaments basats en intel · ligència artificial en medicina nuclear. El model va aconseguir un 80% de precisió balancejada en la diferenciació de pacients amb DCL amb malaltia neurodegenerativa

d'aquells que no la presentaven. L'estudi va reforçar que les eines d'intel · ligència artificial podrien ajudar els metges nuclears en la identificació primerenca i més precisa de malalties neurodegeneratives, encara que són necessaris refinaments addicionals per a millorar la precisió de classificació, especialment en casos de demència amb cossos de Lewy i demència frontotemporal.

A més, la comparació entre els escàners PET dedicats al cervell i els sistemes PET/CT convencionals ha destacat el potencial per a reduir la càrrega neurològica sense comprometre la qualitat d'imatge ni la fiabilitat del diagnòstic. L'avaluació ha mostrat que els escàners PET dedicats al cervell ofereixen un contrast d'imatge i una resolució espacial comparables. No obstant això, s'han observar variacions en les tècniques de correcció d'atenuació, cosa que subratlla la necessitat de continuar millorant els mètodes d'harmonització d'imatges per a garantir la coherència entre diferents sistemes d'imatge.

Per als tumors neuroendocrins, l'estudi destaca la necessitat crítica de la imatge PET quantitativa estandarditzada per a guiar les aplicacions teragnòstiques. Atés que l'elegibilitat per a la teràpia amb radionúclids dirigits a receptors de pèptids (PRRT) depén de les mesures d'intensitat de captació, les variacions en els paràmetres dels escàners PET podrien afectar significativament les decisions de tractament. L'anàlisi ha subratllat que diferents sistemes PET produeixen valors de captació estandarditzats (SUV) variables, la qual cosa podria generar discrepàncies en les recomanacions terapèutiques.

Per a abordar aquest problema, l'estudi ha emprat l'harmonització amb el mètode ComBat per a alinear els valors SUV entre els escàners PET/CT i PET/MR. Abans de l'harmonització, el 23% de les lesions es classificaven de manera diferent segons el sistema d'imatge utilitzat, la qual cosa reflectia un acord moderat (coeficient kappa de 0,54). Després de l'harmonització, l'acord va millorar significativament (coeficient kappa de 0,60 per a PET/MR, 0.74 per a PET/CT i 0,65 per al sistema arbitrari com a referències), demostrant l'efectivitat dels mètodes d'harmonització per a garantir recomanacions terapèutiques consistents en diferents plataformes d'imatge.

Els resultats de l'estudi confirmen que la imatge PET pot millorar-se mitjançant mètodes computacionals avançats, cosa que condueix a una major precisió diagnòstica i una planificació del tractament més fiable. No obstant això, persisteixen diversos desafiaments, inclosa la necessitat de conjunts d'un nombre més elevat de dades per a refinar l'anàlisi estadística i la validació addicional de les tècniques d'harmonització en estudis multicèntrics.

Aquest estudi proporciona una evidència sòlida que la imatge PET quantitativa té un paper crucial en la presa de decisions clíniques per a la demència i els tumors neuroendocrins. En extraure informació útil de la quantificació de les imatges PET, es pot optimitzar la imatge per a millorar la precisió i la consistència del diagnòstic. Els resultats d'aquesta tesi donen suport a l'avanç continu de la imatge PET quantitativa en medicina nuclear i subratllen la necessitat d'estandardització per a garantir que les decisions clíniques siguen sòlides per a diferents plataformes d'imatge. La investigació futura hauria de basar-se en aquests coneixements per a continuar millorant el paper de la imatge PET en la medicina de precisió.

Resumen

La presente tesis tiene como objetivo mejorar la toma de decisiones clínicas en el manejo de la demencia y los tumores neuroendocrinos mediante el análisis avanzado de imágenes PET. La investigación se centra en la extracción y análisis de datos cuantitativos de imágenes PET para hacer los diagnósticos más precisos y las decisiones de tratamiento más confiables, al tiempo que explora formas de optimizar la tecnología de imágenes para mejores resultados clínicos.

En el contexto de la demencia, el estudio examina cómo las exploraciones PET con [^{18}F]FDG, combinadas con una prueba de cognición social (la prueba "Reading the Mind in the Eyes Test", RMET), pueden ayudar en el diagnóstico temprano. También se ha validado externamente un algoritmo de clasificación basado en aprendizaje profundo, lo que podría mejorar la precisión en la detección de enfermedades neurodegenerativas. Otra parte del estudio se ha centrado en evaluar un nuevo escáner PET dedicado al cerebro, comparando su calidad de imagen y capacidad diagnóstica con los escáneres PET/CT convencionales. Estos dispositivos podrían reducir la carga sobre los escáneres PET/CT generales y, al mismo tiempo, proporcionar diagnósticos neurológicos confiables.

Para los pacientes con tumores neuroendocrinos, el estudio examina dos escáneres híbridos de imágenes PET, PET/CT y PET/MR, para determinar qué tan bien coinciden en la clasificación de lesiones y la orientación de las decisiones terapéuticas. Al armonizar los datos de ambos dispositivos, se busca garantizar que, independientemente del método de imagen utilizado, el tratamiento recomendado sea coherente. Esto ayudaría a estandarizar y mejorar la fiabilidad de la imagen PET para estos tumores poco frecuentes.

Los hallazgos de esta tesis respaldaron la hipótesis de que el análisis de imágenes PET proporciona información significativa que impacta las decisiones clínicas en los casos de demencia y tumores neuroendocrinos. En el contexto de la demencia, los resultados demostraron que el deterioro de la cognición social se correlaciona con cambios neuroanatómicos específicos observados en las imágenes PET. En particular, el estudio confirmó que los déficits en el reconocimiento emocional están presentes en pacientes con deterioro cognitivo leve (DCL), pero que estos déficits no son exclusivos de la enfermedad de Alzheimer. Esto sugiere que la inclusión del RMET en la batería de pruebas neuropsicológicas no mejorará la precisión del diagnóstico de la enfermedad de Alzheimer.

La validación externa de un modelo de aprendizaje profundo diseñado para clasificar a pacientes con DCL ha confirmado aún más la viabilidad de los enfoques basados en inteligencia artificial en medicina nuclear. El modelo logró una precisión balanceada

del 80% en la diferenciación de pacientes con DCL con enfermedad neurodegenerativa de aquellos sin ella. El estudio ha reforzado que las herramientas de inteligencia artificial podrían ayudar a los médicos nucleares en la identificación temprana y más precisa de enfermedades neurodegenerativas, aunque se requieren refinamientos adicionales para mejorar la precisión de clasificación, especialmente en casos que involucren demencia con cuerpos de Lewy y demencia frontotemporal.

Además, la comparación entre los escáneres PET dedicados al cerebro y los sistemas PET/CT convencionales ha destacado el potencial de reducir la carga neurológica sin comprometer la calidad de imagen ni la fiabilidad del diagnóstico. La evaluación ha mostrado que los escáneres PET dedicados al cerebro ofrecen un contraste de imagen y una resolución espacial comparables. Sin embargo, se observaron variaciones en las técnicas de corrección de atenuación, lo que subraya la necesidad de continuar mejorando los métodos de armonización de imágenes para garantizar la coherencia entre diferentes sistemas de imagen.

Para los tumores neuroendocrinos, el estudio ha destacado la necesidad de una imagen PET cuantitativa consistente para guiar las aplicaciones teragnósticas. Dado que la elegibilidad para la terapia con radionúclidos dirigida a receptores de péptidos depende de la cuantificación de la intensidad de captación, las variaciones en los parámetros de los escáneres PET podrían afectar significativamente las decisiones de tratamiento. El análisis ha subrallado que diferentes sistemas PET producen valores de captación estandarizados (SUV) variables, lo que podría generar discrepancias en las recomendaciones terapéuticas.

Para abordar este problema, el estudio ha empleado la armonización con ComBat para alinear los valores SUV entre los escáneres PET/CT y PET/MR. Antes de la armonización, el 23% de las lesiones se clasificaban de manera diferente según el sistema de imagen utilizado, reflejando un acuerdo moderado (coeficiente kappa de 0,54). Después de la armonización, el acuerdo mejoró significativamente (coeficiente kappa de 0,60 para PET/MR, de 0.74 para PET/CT y de 0,65 para el sistema arbitrario como referencias), demostrando la efectividad de los métodos de armonización para garantizar recomendaciones terapéuticas consistentes en diferentes plataformas de imagen.

Los hallazgos del estudio confirman que la imagen PET puede mejorarse mediante métodos computacionales avanzados, lo que conduce a una mayor precisión diagnóstica y una planificación del tratamiento más fiable. Sin embargo, persisten varios desafíos, incluida la necesidad de conjuntos de datos más grandes para refinar el análisis estadístico y la validación adicional de las técnicas de armonización en estudios multicéntricos.

Este estudio proporciona evidencia sólida de que la imagen PET cuantitativa juega un papel crucial en la toma de decisiones clínicas para la demencia y los tumores neuroendocrinos. Extrayendo información útil de la cuantificación de imágenes PET, se puede optimizar y mejorar la precisión y consistencia del diagnóstico. Los hallazgos respaldan el avance continuo de la imagen PET cuantitativa en medicina nuclear y enfatizan la necesidad de estandarización para garantizar que las decisiones clínicas sean sólidas en diferentes plataformas de imagen. La investigación futura debería basarse en estos conocimientos para seguir mejorando el papel de la imagen PET en la medicina de precisión.

Contents

Chapter 1

INTRODUCTION

1.1 Medical imaging

According to the U.S. Food and Drug Administration (FDA), "medical imaging refers to several different technologies that are used to view the human body in order to diagnose, monitor, or treat medical conditions. Each type of technology gives different information about the area of the body being studied or treated, related to possible disease, injury, or the effectiveness of medical treatment" [1]. This definition highlights the main purpose of medical imaging: to non-invasively reveal the inner structures hidden behind the skin and bones in order to identify abnormalities and guide the treatment of diseases.

All imaging systems and techniques are based on the fundamental principle of mapping, which states that every object property that can be detected and localized in space and time may be mapped into image space. These properties may then be examined using visible light [2].

The spatial map of light, which is a visual image, has no inherent intellectual importance. The intellectual worth of such an image is mostly determined by the mental comparison of the image to the library of images stored inside the brain, followed by an assessment of the image's meaning. The overwhelming majority of medical imaging is a pattern recognition procedure that consists of comparing visual patterns to other ones or surrogating them to known biological or pathological features. Evaluating similarities and contrasts with established patterns leads to a "best fit" or "most likely" diagnosis [3].

Understanding the image relies on the physical interpretation of its intensity. Consequently, this means that the information stored in the image differs significantly between imaging modalities and sometimes even within the same modality (as in mag-

netic resonance (MR)). The image is assessed by a qualified specialist, often a radiologist or a nuclear medicine physician. The professional combines the information captured in the images along with their knowledge of the patient's symptoms, history, anatomy, and pathology to develop a diagnosis. Moreover, computerized image processing can improve the image by reducing noise, highlighting edges, boosting contrast, or obtaining measurements, among other functions [4].

Medical images can be considered representational because the pixel character does not seek to replicate the tissue's visible light characteristic, but rather another physical parameter that has been measured and can be translated into the image. The character of a pixel may be used to represent almost any measurable quantity that can be spatially defined [3].

Some form of energy is required for medical imaging of the human body (Figure 1). The energy used to generate the image in the nuclear medicine and radiology areas needs to be able to penetrate tissues. Visible light images have applications in pathology (light microscopy), dermatology (skin photography), and gastroenterology and obstetrics (endoscopy). However, visible light is mostly employed outside the radiology and nuclear medicine department for medical imaging due to its limited capacity to penetrate tissues at a deep level.

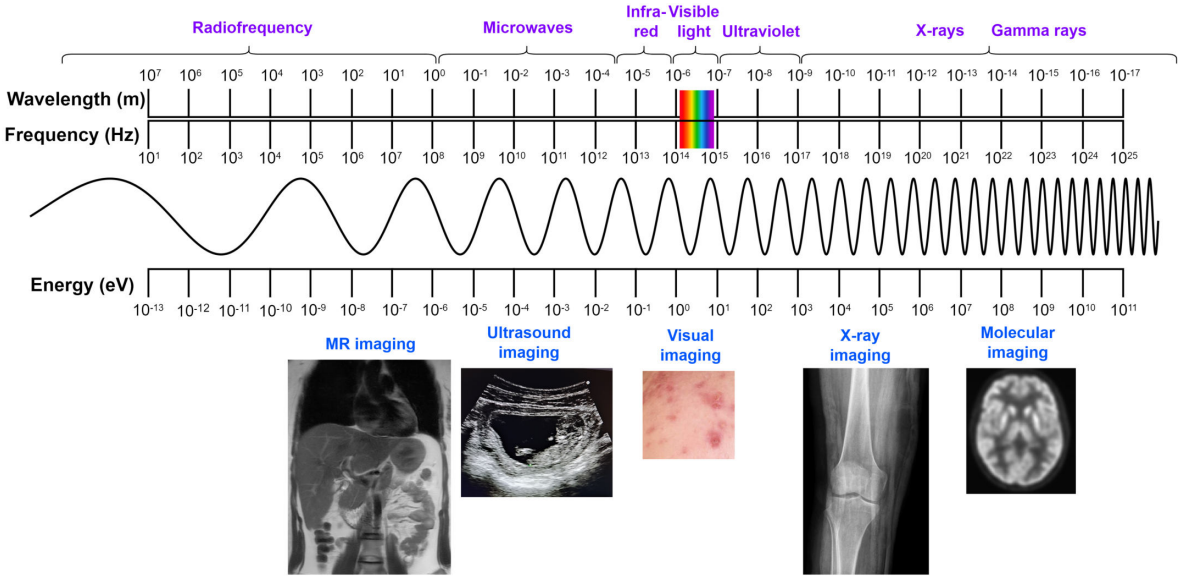

Figure 1: The electromagnetic spectrum displaying ranges of energy, frequency, and wavelength for medical imaging.

The electromagnetic spectrum outside of the visible light range is utilized in diagnostic radiology and nuclear medicine for medical imaging. This includes the use of radiofrequency (RF) in magnetic resonance imaging, gamma rays in nuclear medicine, X-rays in mammography and computed tomography (CT) and positrons in positron emission tomography (PET). Mechanical energy, in the form of high-frequency sound waves, is used in ultrasound imaging [5]. These medical imaging techniques are being

used to diagnose a wide range of critical medical diseases, including congenital heart disease, neurological disorders, complicated bone fractures, cardiac diseases, and cancers of different tissues [6].

Ionizing radiation has enough energy to take knock electrons free from atoms, resulting in positive ions. This applies to high-energy electromagnetic radiation (X and γ radiation). Non-ionizing electromagnetic radiation includes light, radio waves, and microwaves [7].

The ability of medical images to be used for diagnosis depends on both the image's technical quality and the specific conditions surrounding its acquisition. As a result, technical evaluation is essential to assess image quality in medical imaging. Usually, obtaining better images from medical imaging devices requires making acquisition protocol adjustments. For instance, higher radiation doses to patients might result in better X-ray images; longer image acquisition times can produce better magnetic resonance images; and higher ultrasound power levels can produce better images. It goes without saying that patient comfort and safety must be considered while obtaining medical images; as such, overdosing on patients in an attempt to obtain the ideal image is unacceptable. Instead, patient safety and image quality must be balanced to obtain medical images [5].

There is a wide range of characteristics that can be used to describe the quality of an image. Some of the most common are spatial resolution, contrast and noise. All three of these characteristics can be used to characterize distinct aspects of the image's quality, but they cannot be treated as fully independent parameters since gains in one sometimes come at the cost of or deterioration of one or more of the others [8].

Spatial resolution represents the capacity to perceive very small details. When an imaging system can clearly show the existence of small parts in the image, it has a high spatial resolution. The minimal object size that an imaging system is able to resolve is known as the limiting spatial resolution [5]. Sometimes, the spatial resolution has been used to describe the smallest image element of a digital image. That being said, is only an upper constraint on the resolution. The resolution decreases with increasing blurring. An image's lack of sharpness can be caused by three factors: the imaging system's features (such as the focal spot and detector blur amount); the scene's geometry and characteristics (such as the subject's shape, position, and motion); and the viewing conditions. A tiny, but intense spot on a dark background will typically not look as sharp in the image as it does in real life. After smoothing it, the resulting distribution is known as the point spread function (PSF). The full width at half maximum (FWHM) of the PSF is a useful indicator of resolution. Two such distributions will become indistinguishable from one another as two different objects when positioned at this distance or less from one another [9].

The contrast in an image refers to the variation in intensity between neighbouring areas. Image contrast manifests the variations in the greyscale values within an

image. An image with sharp and large transitions between light and dark grey illustrates significant contrast, while an image with uniform grey indicates little contrast at all [5]. Contrast is, more precisely, the amplitude of the image's Fourier transformation as a function of spatial frequency. The image is divided into sinusoidal patterns with corresponding amplitudes using the Fourier transform; these amplitudes reflect the contrast at different spatial frequencies. The imaging process, (which includes the source intensity and the capturing device's absorption efficiency or sensitivity), as well as the scene characteristics, (which include the object's size, shape, and physical attributes) and the viewing conditions (which involve the amount of illumination in the room and the display equipment) all contribute to the definition of contrast. The spatial resolution will also affect the contrast of very tiny objects [9].

The third measure of quality is image noise. There is always noise in imaging due to its statistical nature. It is the image's random element. When the amount of noise exceeds the intensity of an object's image, significant information becomes masked by the noise. A crucial metric derived from signal theory is the signal-to-noise ratio, known as SNR [9]. Another important metric related to the noise is contrast-to-noise ratio (CNR). For a lesion or other object to be identified in an image, the observer must be capable of differentiating it from noise-generated contrast patterns in background areas of the same size [8].

Finally, artefacts are visual elements that can reduce the quality of medical images. Metal streak artefacts in computed tomography (CT) and geometric distortions in MR images are two examples of medical image artefacts. Digital image processing can potentially produce artefacts, including edge enhancement. It is crucial to prevent artefacts and to understand where they came from, as they can impair diagnosis or provide inaccurate readings [9].

All things considered, proper diagnosis and treatment planning rely heavily on the quality of medical imaging. However, it is likewise essential to prioritize patient safety and comfort throughout the imaging procedure. By ensuring high image quality standards while also considering the well-being of the patient, healthcare professionals can provide optimal care.

1.1.1 Types of tomographic medical imaging

With developments in computer power and algorithms, the impact of technology on medicine has increased and will keep growing in the future. Tomographic three-dimesional 3D medical images, including CT, MR, and PET, are the backbone of modern medical practices and research. [10]

The relevance of anomalous voxel brightness in terms of tissue features is directly proportional to the imaging acquisition method, which in MR images, for example, is

the use of different RF pulses and gradient magnetic fields. Therefore, for each imaging modality, the interpreter must know which pathophysiologic changes modify the pixel brightness, leading to increased or decreased pixel values [3].

In this subsection, we will discuss the modalities of CT and MR, including their applications, advantages, and limitations. Particular attention will be given to PET, as it is the focus of this thesis on quantitative PET data extraction for precise clinical decisions. We will dive deeper into its principles, corrections, and the hybrid and dedicated PET scanners for medical imaging. By exploring these imaging techniques, we aim to highlight PET's vital role in enhancing diagnostic accuracy and optimizing treatment planning through quantitative data analysis.

1.1.1.1 Computed Tomography

Computed tomography is a volumetric imaging method that became clinically available in the early 1970s, and was the first medical imaging modality enabled by computers. Tomography refers to a picture (graph) of a slice (tomo). CT scans are created by sending X-rays through the body at a variety of angles while rotating the x-ray tube around it. Unlike projection X-ray imaging, CT can reconstruct a two- or three-dimensional attenuation map. The projection data from different orientations is combined and 3D images of an object are reconstructed (see Figure 2) [4].

The aim of CT is to obtain a spatial map of attenuation coefficients $\mu(x, y)$. Studies have demonstrated that there is a linear relationship between the grey levels in CT images and the linear attenuation coefficients of the materials being imaged. This relationship allows for the derivation of Hounsfield units from the measured grey levels in CT images [11, 12]. Hounsfield advocated expressing attenuation in terms of water, and the normalized attenuation values are named after him as Hounsfield units (HU). Water is the reference point with 0 HU, while air has -1000 HU [4]. Table 1 depicts the typical values in HU for diverse tissues [13].

The equation below can be employed to translate reconstructed values $\mu(x, y)$ into Hounsfield units:

$$HU(x, y) = 1000 \frac{\mu(x, y) - \mu_{water}}{\mu_{water}} \tag{1.1.1}$$

CT produces a greyscale image where tissue density is represented by varying shades of grey. Since bones are significantly denser than surrounding soft tissues, they appear distinctly in CT scans, as illustrated in Figure 2. This makes CT a valuable tool for examining structural anatomy. Likewise, the substantial density contrast between soft tissues and air enables clear visualization of features such as the nasal airways.

However, soft tissues and organs have similar Hounsfield value ranges, making it challenging to distinguish adjacent structures like fat and muscle in CT images. To enhance visibility artificial contrast agents can be introduced into the body, highlighting specific structures more effectively [14].

Table 1: Typical values in Hounsfield Units for diverse tissues.

Tissue	Hounsfield Units (HU)
Fat	-500 to -55
Liver	40 to 60
Brain tissue	37 to 45 (grey matter) to 20 to 30 (white matter)
Blood	30 to 45
Kidney	30
Contrast agents	100 to 300

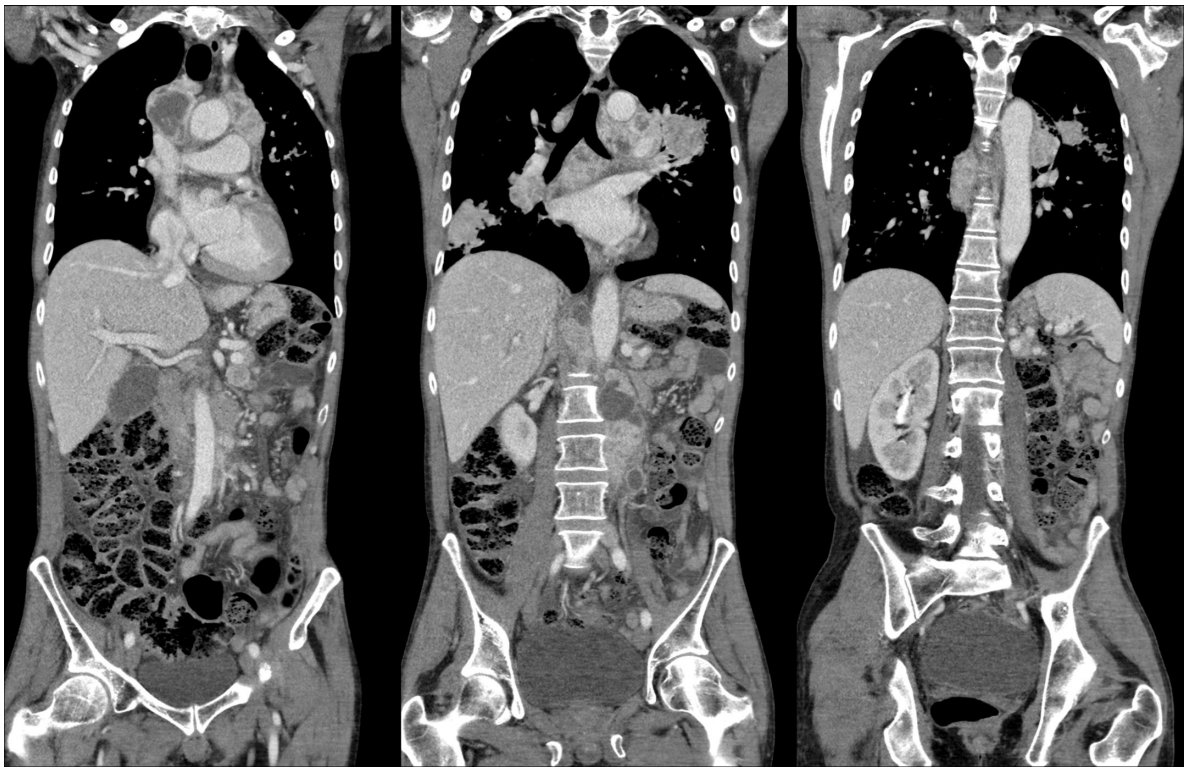

Figure 2: Example of a coronal reconstruction of CT images acquired at Hospital La Fe.

1.1.1.1.1 Sectional images

Conventional chest X-rays reveal anatomical features based on the varying attenuation of X-ray beams by different tissues, with bones appearing more intense and air-filled lungs less intense. However, soft tissues like blood vessels and heart structures are not easily distinguishable without contrast media, such as iodine-based solutions

that enhance visibility. Additionally, X-ray images lose depth information by collapsing 3D structures onto a 2D plane, making it difficult to resolve spatial relationships. These limitations necessitate alternative imaging techniques, such as tomosynthesis or tomography, to improve contrast and depth resolution [15].

With CT, a planar reconstruction slice of the body is defined from a helical acquisition, and X-rays are transmitted in directions that are parallel to and contained inside the slice's plane. The X-ray beam doesn't explore any area of the body outside the slice. With a density (linear attenuation coefficient) discrimination of better than 1% and a spatial resolution of roughly 1 mm, the generated images display the human anatomy in a section. A CT scanner appears as a machine with a central opening where the head or body is positioned for imaging. However, behind the covers of the machine lies a complex system that has undergone multiple advancements since its development. Figure 3 shows a representation of four different source–detector geometries [15].

The evolution of CT scanners has progressed through several generations to improve speed and image quality. The first-generation scanner used a single X-ray beam and detector, capturing one projection at a time by stepping linearly across the patient, which provided high scatter rejection but was slow, taking about 4 minutes per section. The second generation, introduced in 1974, used a fan-shaped X-ray beam and multiple detectors, significantly reducing scan time to around 20 seconds. By 1975, third-generation scanners expanded the fan beam to cover the entire field of view, allowing continuous rotation and reducing scan time to under 5 seconds. Fourth-generation scanners followed, featuring a stationary detector ring with only the X-ray source rotating, achieving similar speeds. Ultimately, third-generation geometry became the standard due to its efficiency and widespread adoption [15].

Line integrals and projection sets

In CT, image reconstruction relies on transmission measurements of X-rays passing through the patient. These measurements follow an integral relationship where the X-ray intensity decreases according to the tissue's attenuation properties. The fundamental equation describing this process extends Beer's Law to account for spatial variations in attenuation:

$$I_\phi(x') = I_\phi^0(x') \exp\left(-\int_{AB} \mu[x,y]\, dy'\right) \tag{1.1.2}$$

where $\mu[x,y]$ represents the 2D distribution of the linear attenuation coefficient, ϕ and x' define the position of the measurement, and $I_\phi^0(x')$ is the unattenuated intensity. This integral equation forms the mathematical foundation for reconstructing cross-sectional images from projection data (see Figure 4) [15].

A complete set of projections is necessary to reconstruct an accurate image (see

Figure 3). In CT, multiple X-ray beams capture projections at different angles. These projections must be collected over a full 180° range to ensure sufficient data coverage. Each projection provides information about the internal structure of the scanned region, and overlapping projections improve the accuracy of the final image [15].

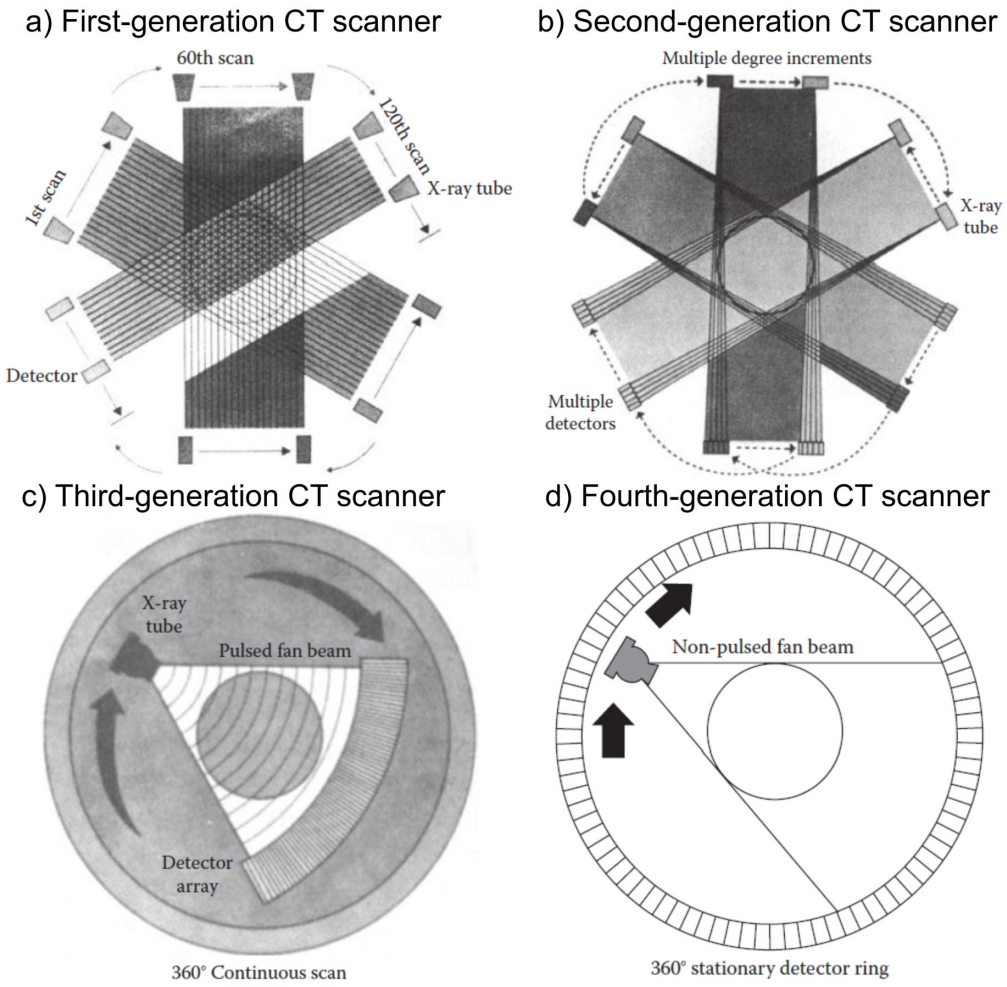

Figure 3: Schematic representation of four different Source–Detector Geometries. From *"Webb's Physics of Medical Imaging"* by M. A. Flower. 2016. Pages 102-104. Copyright 2016 by The Taylor & Francis Group.

The Central-Section Theorem (also called the Fourier Slice Theorem) states that the one-dimensional Fourier transform of a projection corresponds to a single slice of the two-dimensional Fourier transform of the object being imaged. This theorem is critical because it links projection data to Fourier space, allowing for an efficient mathematical framework for CT image reconstruction. It implies that if projections are acquired from multiple angles, they provide a full representation of the object in the frequency domain [15].

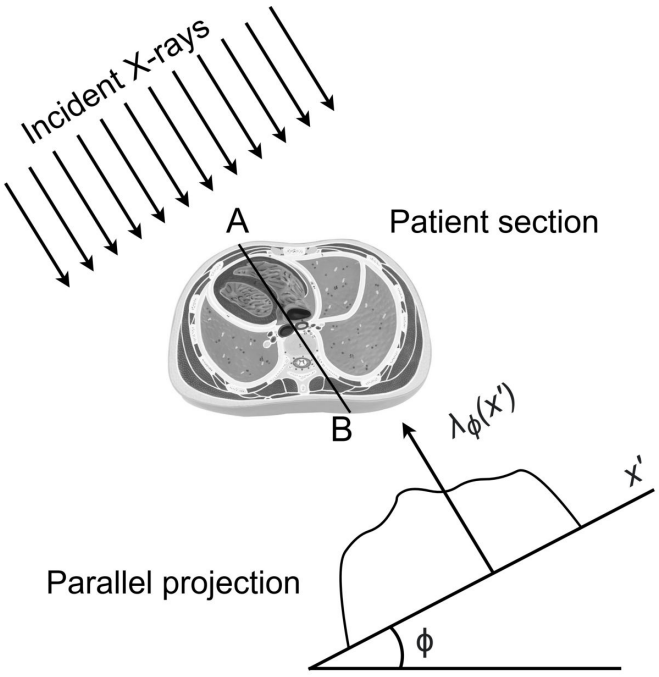

Figure 4: Schematic representation of projection data from a sectional image.

CT Image Reconstruction

The problem of reconstructing images from projections was first analyzed by Radon in 1917 and later rediscovered in various fields, including radioastronomy and electron microscopy. CT reconstruction techniques fall into two main categories: convolution and backprojection methods and iterative methods. For a long time, there was debate about the superiority of one method over the other. However, it is now recognized that different techniques suit different imaging modalities. Iterative methods, for instance, have found applications in emission CT due to their ability to handle poor photon statistics [15].

Filtered backprojection is the standard algorithm used in most CT scanners. It involves two steps: filtering (the projection data is filtered using specific mathematical functions) and backprojecting (the filtered projections are summed to reconstruct the final image). The method is efficient and widely used because it provides rapid image reconstruction, making it clinically practical [15].

Regarding the iterative reconstruction methods, initially, they were commonly used in CT but were later abandoned in favor of faster analytical methods like filtered backprojection. However, iterative techniques have recently regained attention due to advancements in computing power. Iterative reconstruction refines the estimated image by repeatedly comparing calculated projections with measured projections and adjusting the estimate accordingly. The key equation in iterative reconstruction involves

a large, sparse matrix that represents projection paths through the object. Because direct matrix inversion is impractical, iterative adjustments are used instead [15].

Several iterative techniques exist, including Algebraic Reconstruction Technique (ART), Simultaneous Iterative Reconstruction Technique (SIRT), and Iterative Least Squares Technique (ILST). These methods were originally abandoned for X-ray CT due to their high computational demands but are still used in applications where data are noisy or incomplete, such as emission CT. Modern iterative reconstruction techniques can use an initial estimate from filtered backprojection to reduce computation time. While these methods significantly improve image quality and noise reduction, they are computationally intensive and not always practical for routine clinical use. However, all major CT manufacturers have now incorporated iterative reconstruction techniques into their systems [15].

1.1.1.2 Magnetic Resonance

A clinical MR image is essentially a map of the magnetic properties of hydrogen nuclei within atoms in the body [3]. It is based on the interaction of the ^{1}H nuclei within a powerful external magnetic field, the magnet, and radiofrequency pulses [16]. MR is an imaging method that allows to investigate the anatomy and function of organs and tissues throughout the human body *in vivo*. Its superior contrast resolution in observing and characterizing soft tissues distinguishes it from other tomographic methods such as computed tomography. Furthermore, it employs non-ionizing radiation (in the radio frequency spectrum), making it a safe and harmless approach under typical conditions of use. In the current clinical context, almost all medium-sized hospital centers are equipped with MR equipment [17]. The key advantages of magnetic resonance imaging might be highlighted as follows:

- Non-ionizing radiation.
- High contrast between soft tissues.
- Multi-planar acquisition.
- Extensive information for each anatomical level, allowing for improved differential diagnosis.
- Excellent balance of spatial and temporal resolution for dynamic and functional studies.

The primary drawbacks are:

- Longer acquisition time compared to other procedures.
- Claustrophobia.
- Absolute value scales are not feasible since image intensity levels are relative.
- Sequences are challenging to optimize.
- Higher cost than other imaging techniques.
- Acoustic noise.

MR places the patient in an intense magnetic field that aligns the hydrogen protons in the body, and generates a pulse of radio waves using antennas ("coils") positioned around the subject. The protons of the ^{1}H nuclei in the patient absorb the radio waves and then reemit the energy after a time period determined by the tissue's spatially dependent magnetic characteristics. The protons in the patient generate radio waves, which are detected by the coils around the patient. Since frequency is related to magnetic field intensity, applying magnetic field gradients to gradually change the intensity of the magnetic field as a function of position in the patient causes the proton resonance frequency to vary. The MR system determines the position of each patient signal by analyzing the frequency and phase of the returned radio waves [5].

MR generates a series of tomographic pictures displaying slices through the body, with each point in the image dependent on the micromagnetic characteristics of the tissue at that location. Since many types of tissue, such as fat, white and grey matter in the brain, cerebral spinal fluid, and cancer, have differing local magnetic properties, MR images are very sensitive to anatomical differences and hence high contrast. MR has showed remarkable value in neurological imaging (Figure 5) and musculoskeletal applications, such as imaging the knee after a sports injury (Figure 6) [5].

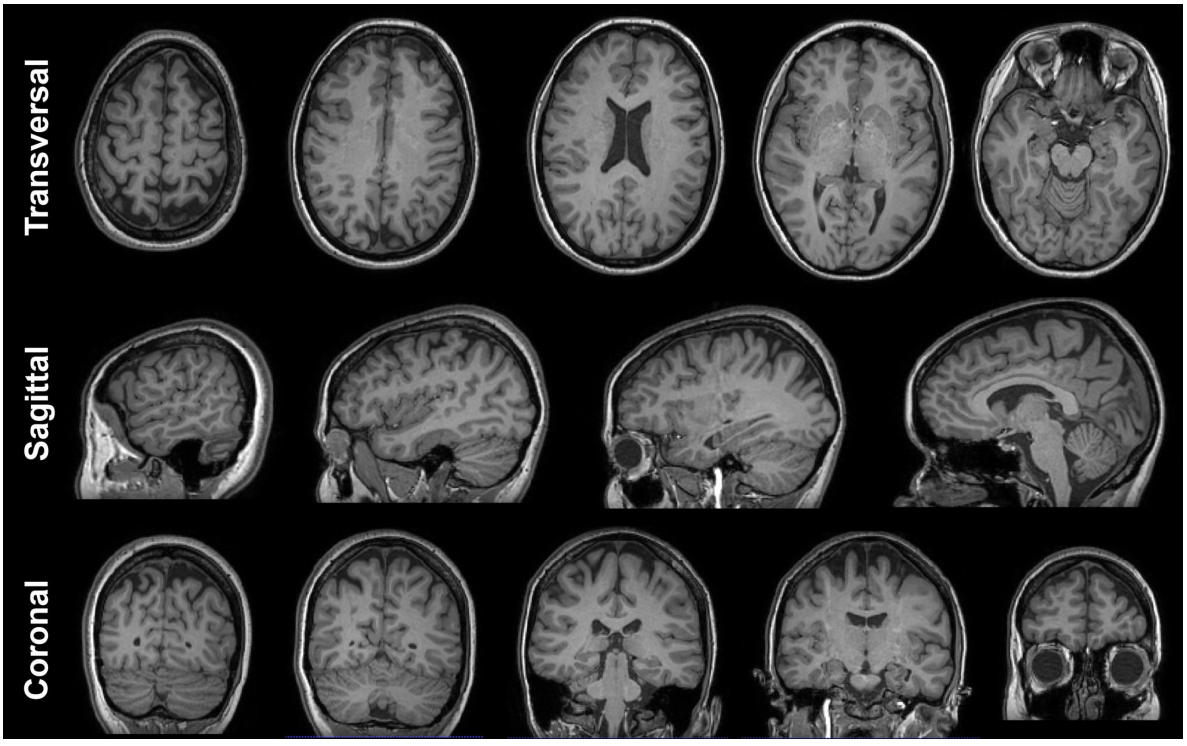

Figure 5: Example of a T1 MR brain image of a healthy subject acquired in Plataforma de Radiología Experimental y Biomarcadores de Imagen (PREBI).

The physical properties of the voxels in an MR image are diverse, and images can reflect a combination of several tissue characteristics. The numerical value of an MR voxel is primarily controlled by the following MR parameters: proton density (PD),

spin lattice relaxation time (T1), and spin-spin relaxation time (T2). Chemical shift, magnetic susceptibility, and motion flow are secondary factors influencing MR voxel values. The weighting assigned to each of these factors varies substantially depending on the timing of the RF pulses and the applied gradient magnetic fields [3].

Figure 6: Example of an MR knee image of a person after a sports injury acquired at Hospital La Fe.

Relaxation is the process by which protons return to their original state before the administration of a radiofrequency excitation pulse. T1 relaxation occurs when protons return energy to the molecular environment, which varies by tissue and therefore affects the relaxation process. Because free water molecules move at greater natural frequency than precession frequencies, the energy exchange is less effective; as a result, the T1 is long, and the tissue seems hypointense in the images. On the contrary, bound water has a frequency near the frequencies of precession; hence, the relaxation occurs quicker, with a short T1 and hyperintense tissue. Pathological tissues often have a larger fraction of free water [16].

T2 relaxation occurs when protons dephase based on two causes: interaction with the oscillatory magnetic fields of the protons in their surroundings and heterogeneities in the magnetic field. When both factors contribute to relaxation, the result is known as T2*. If the heterogeneities of the magnetic field are adjusted, as with the re-phase pulses in the spin echo sequence, and the relaxation is solely due to protons' interactions, we refer to relaxation T2, which is slower than T2*. T2 is also known as spin-spin relaxation and it additionally depends on the distance between molecules. The interaction between the magnetic fields generated by protons decreases as their distance from one other increases. As a result, free water exhibits a slower T2 relaxation (long T2). In bound water, dephasing is favored, leading to a short T2 [16].

Although magnetic resonance imaging generates tomographic images, meaning in slices, there are two main ways to acquire them: 2D and 3D. Two-dimensional MR acquires images slice by slice, with each slice representing a thin section of the anatomy. This method is traditionally used due to its simplicity and robustness, but it

has limitations such as longer acquisition times for multiple planes, potential issues with slice misregistration, and partial volume effects. Three-dimensional MR, on the other hand, acquires volumetric data in a single acquisition, allowing for isotropic resolution. This means that the voxel dimensions are equal in all three spatial directions, enabling high-quality multiplanar reformation and reducing the need for multiple acquisitions in different planes. 3D MR offers several advantages over 2D MR, including improved spatial resolution, higher signal-to-noise ratio, and shorter overall scan times due to the ability to cover larger volumes more efficiently [18–20].

1.1.1.2.1 Sequences in MR imaging

Sequences are a succession of RF pulses and gradients controlled by a computer to produce an image. In principle, each sequence adds a particular level of contrast to the image. The sequences have two essential characteristics that determine the image's contrast: repetition time (TR) and echo time (TE). The TR is the time between two consecutive pulses of excitation. The TE is the period between the excitation pulse and echo generation. Both are measured in milliseconds. The TR parameter controls the amount of longitudinal magnetization that recovers between pulses, thereby influencing T1 weighting [16].

The TE parameter determines the extent of transverse magnetization decay, thus affecting T2 weighting. When a sequence is described as T1-weighted, it means that the resulting contrast between tissues primarily reflects differences in their T1 relaxation times. Similarly, T2-weighted sequences emphasize differences in T2 relaxation. A proton density (PD)–weighted sequence is designed to highlight variations in the number of protons within different tissues. However, image contrast is rarely purely dependent on a single parameter; while one factor may dominate, others also contribute to the final image appearance. [16].

Pulse sequences are essentially split into two types: spin echo and gradient echo sequences. In general, both families can benefit from inversion recovery and echo planar imaging. In practice, however, spin-echo sequences are linked with inversion recovery pulses, whereas echo planar imaging trajectories are used with gradient echo sequences [21]. For practical reasons, we can consider the three groups of sequences listed below:

- Spin-echo sequence (SE)
- Gradient Echo Sequence (GRE)
- Inversion Recovery Sequences (IR)

Spin echo sequence

A conventional spin-echo sequence produces one or more spin-echoes by using a 90° RF excitation pulse followed by one or more 180° RF rephasing pulses. Each 180° RF

rephasing pulse produces a distinct spin-echo, which is received by a coil and utilized to form an image. Although any number of echoes may be generated, spin-echo sequences generally produce one or two echoes. The spin-echo is primarily responsible for contrast, but negative polarity applications of the slice select and frequency-encoding gradients also contribute to it. Furthermore, spoiler gradients are applied at the conclusion of each TR period to ensure that there is no coherent transverse magnetization at the start of the next repetition [22].

Spin-echo pulse sequences are regarded as the gold standard since the contrast they generate is understandable and predictable. They yield high-quality T1-, T2-, and PD-weighted images across the body. However, one downside is that the scan times are rather long [22].

Gradient Echo Sequence

There are three main distinctions between SE and GRE sequences [21].

- There is no 180-degree pulse in GRE. Gradients are used to rephase transverse magnetization (TM) in GRE, specifically the reversal of the frequency encoding gradient. Gradient echo sequence is named for the fact that gradient rephasing produces a signal.
- The flip angle in GRE is frequently less than 90 degrees. Because the flip angle is narrower, longitudinal magnetization will recover more quickly, allowing TR and hence scanning time to be minimized.
- Transverse relaxation can be generated by two mechanisms: irreversible dephasing of the TM due to nuclear, molecule, and macromolecular magnetic interactions with the proton. Alternatively, magnetic field inhomogeneity causes dephasing.

In the SE sequence, the 180-degree pulse eliminates dephasing produced by magnetic field inhomogeneity. Hence, there is "true" transverse relaxation in SE sequence. There is no 180-degree pulse in the GRE sequence to compensate for the dephasing effects of magnetic field inhomogeneity. T2 relaxation in GRE is referred to as T2* relaxation [21].

Gradient-echo sequences are categorized based on which of these signals they employ. They are often referred to as follows:

- Coherent or rewound gradient-echo: Coherent or rewound gradient-echo pulse sequences are commonly employed to provide T2*-weighted images in a short scan duration. Because water is hyperintense, it is frequently described as having a myelographic, lymphographic or arthrographic effect. They can be used to assess if a vessel is patent or if fluid is present in a particular location. They can be obtained slice by slice or as a 3D volume acquisition. Because the TR is short, slices may be obtained in a single breath-hold.

- Incoherent or spoiled gradient-echo: Because the stimulated echo comprises primarily T2* and T2 information, which is spoiled, these pulse sequences provide T1- or PD-weighted images. Flowing water (blood and cerebrospinal fluid (CSF)) may have a relatively large signal due to gradient rephasing. These sequences are employed for 2D and volume acquisitions, with 2D acquisitions providing T1-weighted breath-hold images because to their short TR. Incoherent or spoiled gradient-echo sequences show acceptable T1 anatomy and pathology after gadolinium contrast enhancement.

- Reverse-echo gradient-echo: These sequences were employed to acquire images with proper T2 weighting. They were particularly effective in the brain and joints, using both 2D and 3D volumetric scans. Turbo Spin Echo (TSE) has essentially annulled this sequence, resulting in superior T2 weighting in shorter scan durations. Shifting the stimulated echo is employed in sequences that require rapid data collection and extended time to echo. An example of this is in perfusion imaging.

- Balanced gradient-echo: Balanced GRE was originally created to image the heart and major vessels, but it is now employed in spinal imaging, particularly the cervical spine and internal auditory meatus, where CSF flow is restricted. It is also employed to image the abdomen.

- Fast gradient-echo: The echo planar imaging pulse sequence reduces physiological motion in MR images, making it useful for studying the heart and coronary veins, as well as performing interventional methods. Rapid imaging also allows for the visualization of physiological processes including perfusion and blood oxygenation. Nerve stimulation may occur as a result of this pulse sequence's fast flipping of gradient polarity, particularly in the frequency encoding axis [22].

Inversion Recovery Sequences

The IR sequence begins with an inverted 180-degree pulse followed by the standard spin-echo or gradient echo sequence. In practice, it is frequently used with SE sequences. The inverting 180-degree pulse switches longitudinal magnetization (LM) from the positive to negative side of the Z-axis. This saturates all of the tissues. LM then progressively recovers and rebuilds along the positive side of the Z-axis. The LM recovery varies per tissue, depending on its T1 value. After a while, the standard series of 90-180 degree pulses is applied. Tissues will exhibit varying degrees of LM recovery based on their T1 values. This can be noticed in the enhanced T1 contrast in the images. The period between inversion 180 degree and excitatory 90 degree pulses is known as "time to invert" and it is the main determinant of contrast in IR sequences [21].

IR is commonly used to generate substantially T1-weighted images that depict anatomy. Because the fat and water vectors are fully saturated at the start of each TR, the 180° RF inverting pulse causes a significant contrast difference between them.

Tissues begin to recover from complete inversion rather than from the transverse plane, as in traditional spin-echo. This gives more time for variations in T1 recovery periods between tissues to become apparent, hence IR pulse sequences provide higher T1 weighting than traditional spin-echo. Furthermore, because gadolinium preferentially shortens the T1 recovery periods of certain tissues, IR pulse sequences boost signal from contrast-enhanced structures [22].

The two main sequences in this category are Short Tau Inversion Recovery (STIR) and Fluid Attenuated Inversion Recovery (FLAIR). STIR is an extremely significant sequence in musculoskeletal imaging because it suppresses normal bone, which includes fatty marrow, allowing lesions inside bone, such as bone bruises and tumours, to be seen more clearly. It is also a very helpful sequence for lowering fat in general MR imaging [22].

FLAIR images are employed in brain and spine imaging to better reveal periventricular and cord lesions since it cancels out the strong signal from nearby CSF. It is highly effective for detecting multiple sclerosis plaques, acute subarachnoid hemorrhage, and meningitis. Another variation on this pattern in brain imaging is choosing an inversion time (TI) that corresponds to the null point of white matter. This TI value suppresses signal from normal white matter, making lesions inside it look significantly brighter in contrast. This sequence (with a TI of around 300 ms) is effective for detecting white matter lesions such as periventricular leukomalacia and congenital grey/white matter abnormalities [22].

1.1.1.3 Positron Emission Tomography

PET is a noninvasive imaging modality that provides physiological information by administering radioactive compounds (radiopharmaceuticals) containing a positron-emitting radioisotope. As the radioisotope decays, emitted positrons annihilate with electrons, generating gamma photon pairs. PET scanners detect these photons and reconstruct the radiotracer's 3D distribution, enabling functional imaging of metabolic and biochemical processes [23] (see Figure 7).

Figure 8 illustrates the sequential steps involved in a PET examination. The first stage in a PET exam is the production of a radiopharmaceutical suitable for imaging the condition in question. Then, the radiopharmaceutical is then administered into the body, normally by an injection but occasionally through inhalation. The period between radiopharmaceutical injection and data acquisition is determined by the specific pharmacokinetics of the drug and is based on the goal of the imaging investigation and the specific type of tracer used. In some studies, the acquisition begins immediately, whereas in others it may take hours or days after the radiopharmaceutical is administered [2].

When the radioisotope undergoes positron (β^+) disintegration, a positron is emitted that travels a distance of up to a few millimeters before annihilating itself with an electron of the tissue-forming materials. The annihilation generates a pair of photons that move in almost opposite directions. The pairs of photons of annihilation that leave the human body and are detected in coincidence by the PET scanner are the basis of the image of this mode. These emissions travel in all directions from within the patient's body at a rate in proportion to the local concentration of radiopharmaceutical [24].

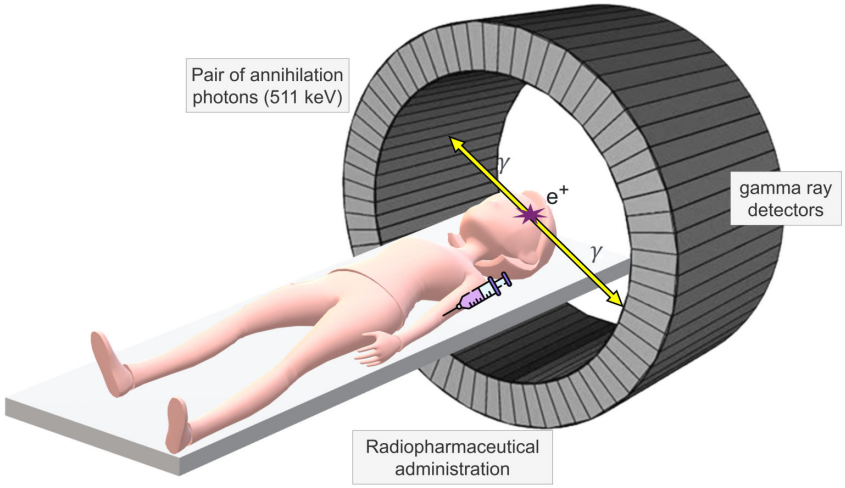

Figure 7: Graphical representation of Positron Emission Tomography. Source: Created by the author.

Imaging equipment detects photons, and coincident events form a line of response to identify the isotope of origin within the patient. Each position, energy and direction of each photon pair are measured and stored for subsequent 3D reconstruction [2].

In the past, image analysis in medicine primarily relied on clinicians visually inspecting and evaluating images, although some quantitative assessments (such as ratios and other simple metrics) were also extracted. However, with the advent of advanced instrumentation and the ability of PET imaging to accurately reproduce activity concentration, image quantification has significantly evolved. Nowadays, computerized analysis of medical images plays a crucial role in modern medicine, offering physicians additional information to guide decision-making processes.

As previously stated, PET imaging provides insights into the physiological and metabolic processes that occur within the body. At this point we'll look at the underlying concepts that motivate PET imaging, providing an overview of the complex processes that enable this technique. Radiopharmaceuticals are an important component of PET imaging because they help to visualize and measure biological activities. We will look at PET's numerous medical uses, ranging from cancer to neurology, and demonstrate its versatility in clinical practice. Furthermore, integrating PET with complementary and structural imaging modalities like CT or MR has considerably

improved diagnostic accuracy, while dedicated PET scanners have optimized imaging performance. This detailed review is intended to offer an understanding of the complexities and improvements in PET imaging technology.

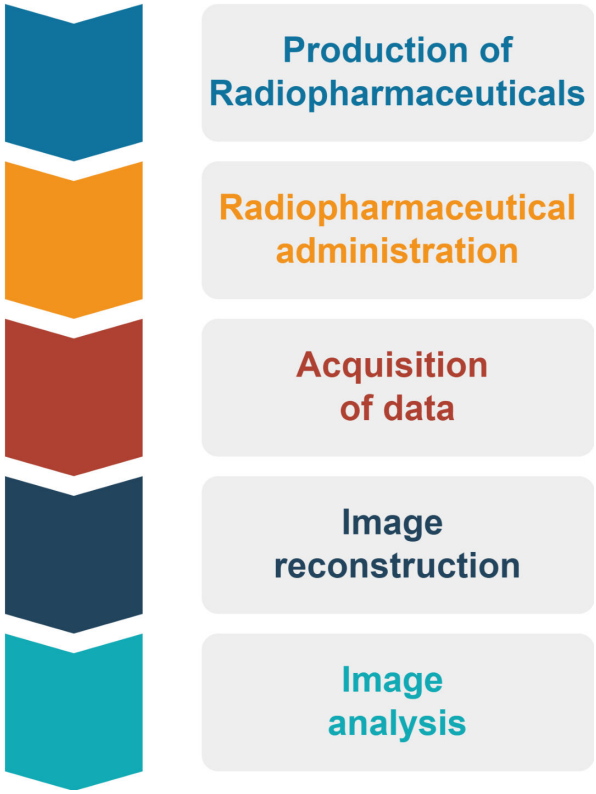

Figure 8: Steps involved in a typical Positron Emission Tomography examination.

1.1.1.3.1 PET Imaging Basics

To begin with, we will cover the general concepts of PET, followed by an exploration of the data acquisition process, the degradation phenomena and its corrections and techniques used for image reconstruction. This will provide a concise understanding of how PET works and how it generates detailed images for medical diagnosis.

1.1.1.3.1.1 General concepts

The following paragraphs go into the fundamental principles necessary for understanding PET imaging. We will begin looking into the nuclear structure and nuclide excited states. The radioactive processes will also be described. Furthermore, relevant photon interaction with matter will be explored, including the photoelectric effect, Compton scattering, and pair production. These interactions are critical in the detection, which is the first step for imaging.

Nuclear structure, excited states and stability of nuclides

At present, matter is considered to be composed of compounds, which in turn are made up of elements. Elements are defined by the atoms that compose them. Atoms consist of a nucleus containing protons and neutrons, with electrons orbiting in the outer shell. The different types of atomic nuclei are referred to as nuclides. An element is defined by its atomic number (Z), while a nuclide is identified by both its atomic number (Z) and its mass number (A). The mass number (A) represents the total sum of protons (Z) and neutrons (N) in the nucleus, expressed as $A = Z + N$. A general notation for a nuclide is ${}^{A}_{Z}\mathrm{X}$, where X is the element to which this nuclide belongs. Nuclides are classified based on their mass number, neutron number, and atomic (proton) number. Nuclides with the same mass number are referred to as isobars, those with the same number of protons are known as isotopes, and those with the same number of neutrons, isotones [25].

Regarding the structure of a nucleus, it is postulated that nucleons are arranged in energetic levels within the nucleus, similar to electrons in an atom. Nucleons can be excited to higher unoccupied energetic levels through the absorption of energy from outside the nucleus. The ground state of a nuclide refers to the lowest energy arrangement of its nucleons. When nucleons move to higher energy levels, these are called excited states or energy levels. However, nucleons are strongly bound within the nucleus, with binding energies ranging from 5 to 8 MeV, which is about 1,000 times greater than the energy required to remove electrons from an atom. Therefore, removing a proton or neutron from the nucleus requires a considerable amount of energy, which can only be achieved in nuclear reactors, particle accelerators, or cyclotrons [25].

Excited states of a nucleus are highly unstable and typically last for less than 10^{-11} seconds before they decay to the ground state or a lower energy state by emitting high-energy radiation. Since excited nuclei have the same mass number, atomic number, and number of neutrons as their ground state, they are referred to as isomers. However, many nuclides remain unstable even in their lowest energy state. These unstable nuclides are called radionuclides. To become more stable, they release energy by emitting either electromagnetic radiation (such as gamma rays) or charged particles (such as alpha or beta particles). This process is known as radioactive decay. The stability of a nuclide depends on the interaction of two fundamental forces: the strong nuclear force and the electromagnetic force. The balance between these attractive (strong force) and repulsive (electromagnetic force) interactions determines whether a nuclide remains stable or undergoes radioactive decay [25].

Radioactive Processes

The three three most common radioactive decay processes by which a radionuclide achieves stability are called alpha, beta, and gamma decay.

A radionuclide emits a heavy, charged particle known as the α particle during

alpha decay. An α particle carries twice the electric charge of a proton and is four times heavier than a proton or neutron. With atomic mass number $A = 4$ and atomic number $Z = 2$, the α particle is indeed a stable nuclide. This happens to be the nucleus of a helium atom. According to the principles of conservation of mass number and electric charge, when a nucleus undergoes alpha decay, it loses four units from its mass number (A) and two units from its atomic number (Z). This means the new nucleus formed, called the daughter nucleus, is lighter and has a lower atomic number. Alpha decay mainly occurs in heavy radioactive elements with a mass number greater than 150. The kinetic energy of the emitted alpha particle is always specific and fixed for each type of decay [25]. The process can be represented using the following equation:

$$ {}^{A}_{Z}\mathrm{X} = {}^{A-4}_{Z-2}\mathrm{Y} + {}^{4}_{2}\mathrm{He}\,(\,\alpha\ particle) \tag{1.1.3} $$

During **beta decay**, a neutron or a proton inside the nucleus of a radionuclide is converted to a proton or a neutron, respectively. Weak forces govern the transformation of a neutron into a proton or a proton into a neutron. One of three processes (electron emission (β^-), positron emission (β^+), or electron capture (EC)) occurs in this phenomena. Following any of these three processes, the mass number A stays constant, and is hence known as an isobaric transition, whereas the Z number changes in $\pm$ 1 [25].

Electron emission: In beta decay by electron emission, a neutron inside the radionuclide is converted into a proton, and the excess energy is released as a pair of particles, an electron (e^-) and an antineutrino ($\bar{\nu}$). When radioactive decay occurs, extra energy is converted into these. The antineutrino has no biological significance given that it rarely interacts with matter [25]. The process of β^- can be represented using the following equation:

$$ {}^{A}_{Z}\mathrm{X} = {}^{A}_{Z+1}\mathrm{Y} + e^- + \bar{\nu} \tag{1.1.4} $$

Positron emission: In beta decay by positron emission, a proton in the nucleus is transformed into a neutron and emits extra energy as a pair of particles: a positron (e^-) and a neutrino (ν) [26]. The process can be represented using the following equation:

$$ {}^{A}_{Z}\mathrm{X} = {}^{A}_{Z-1}\mathrm{Y} + e^+ + \nu \tag{1.1.5} $$

Image formation of PET is based on radioactive decay via positron emission. The positron is the antiparticle of the electron. Following its ejection from the nucleus, it collides with atoms in the surrounding matter, losing kinetic energy and coming to rest typically a few millimeters from where it originated in the body's tissues. To be

more precise, the positron and an electron combine to create the positronium, a transient "atom" with a lifetime of around 10^{-10} seconds with the positron operating as its "nucleus". Then, in an annihilation reaction, the positron and the negative electron unite, converting their masses into energy. Each particle has a mass-energy equivalence of 511 keV. Two 511 keV annihilation photons are produced, which depart the annihilation event site in almost opposite directions (180 degrees apart) [26]. Figure 9 shows a schematic representation of the process.

For a stationary electron-positron pair, momentum conservation requires the "back-to-back" emission of annihilation photons. The annihilation photons, however, may be emitted in directions that deviate from the ideal by only a few tenths of a degree since both particles are in fact moving. A positron is ejected from the nucleus during β^+ decay, and since the atomic number decreased by one, the daughter atom also releases an extra electron to return to its ground state. To conserve total energy, the mass of nuclide X must exceed that of nuclide Y by at least 1.02 MeV, which corresponds to twice the mass of an electron. This requirement arises because a nuclide's mass includes the mass of the nucleus and the electrons associated with it. Nuclide X contains the mass of Z electrons, while nuclide Y has only (Z - 1) electrons. Additionally, a positron is produced using the nuclear energy of nuclide X. Therefore, nuclide X must have a mass greater than that of nuclide Y plus the mass equivalent of two electrons. The extra transition energy over 1.022 MeV in β^+ decay is shared by the neutrino and the positron (kinetic energy).

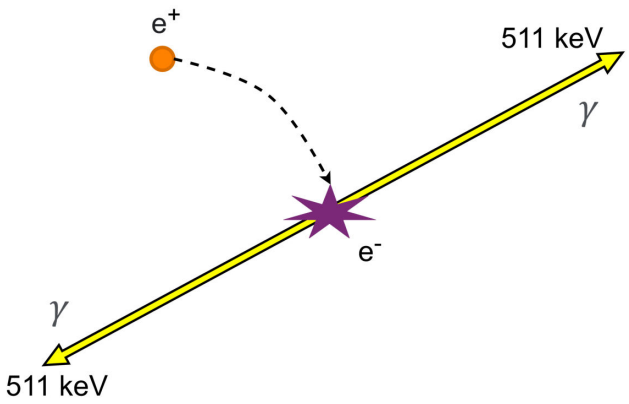

Figure 9: Annihilation process between a positron (β^+) and an electron (e^-). A pair of 511 keV annihilation photons are emitted at 180 degrees from one another.

Given that each nuclear decay event produces two photons, positron emitters are useful in nuclear medicine because they produce two simultaneous photons traveling in opposite directions, allowing for their detection in coincidence. Furthermore, innovative "coincidence-counting" techniques may be applied owing the accurate directional connection between the annihilation photons [26].

Electron Capture: In beta decay by electron capture, a proton within the nucleus converts into a neutron by capturing an electron from one of the atom's shells. The only

particle released is a neutrino, with no emission of an electron or positron. Electron capture is one of the rare cases where a nucleus directly interacts with an atom's orbital electrons. The process can be represented using the following equation:

$$ {}^{A}_{Z}\mathrm{X} + e^{-}(orbital) = {}_{Z-1}{}^{A}\mathrm{Y} + \nu \tag{1.1.6} $$

Finally, **gamma decay** is a type of radioactive decay where an excited atomic nucleus releases excess energy in the form of gamma rays (high-energy photons). Unlike alpha or beta decay, gamma decay does not change the number of protons or neutrons in the nucleus, instead, it allows the nucleus to transition to a lower energy state. This process often follows alpha or beta decay when the nucleus remains in an excited state [27, 28].

Radioactivity

Radioactivity, also referred to as the activity of a radionuclide, is the number of disintegrations of a sample of nuclei (atoms) per unit of time (decay rate) [25]. The parameter known as the radionuclide's half-life describes the rate at which nuclei spontaneously undergo radioactive decay. The half-life is the time required for half of the unstable nuclei to decay. The number of atoms decaying at a given time is governed by the number of unstable nuclei present and the nuclide's decay constant (λ), which is expressed as an exponential function. The activity of a radionuclide refers to the rate at which unstable nuclei decay at any given time [7]. The activity of the nuclide after a time t is given by the next equation:

$$ A_t = A_0 e^{-\lambda t} \tag{1.1.7} $$

where A_0 corresponds to the amount of activity at the initial time. The decay constant can be expressed as:

$$ \lambda = \frac{\ln(2)}{T_{\frac{1}{2}}} \tag{1.1.8} $$

The units for (λ) are $time^{-1}$. The SI unit for radioactivity is the becquerel (Bq), and one Becquerel equals to one disintegration per second.

Interaction of Photons with Matter

Energy may be transferred to a material through interactions between ionizing radiation and the matter. One frequent result is the ionization or excitation of the atoms in the absorbing material, however other processes could also occur. Generally

speaking, a particle's likelihood of being absorbed by a material increases with its mass. While beta particles are more penetrating, large particles like alpha particles have a comparatively short range in matter. The neutrino interacts poorly with matter due to its relatively small mass and lack of charge, making it difficult to stop or detect. Since photons have no mass, they are highly penetrating. In the energetic range for the medical applications that we are interested, the photons interact with matter by three main mechanisms: the photoelectric effect, the Compton effect, and pair production [7].

These interactions allow us to detect the gamma photons, which contributes valuable information for image formation. However, as a consequence of this interactions, gamma rays may be scattered outside the field of view and lost during imaging, or they may be absorbed inside the object. The impact is depth-dependent because gamma rays emitted from deep within the object have a higher possibility of being absorbed. Attenuation makes the reconstructed image look dark inside the object if it is not taken into consideration [2]. This aspect will be discussed later in the image reconstruction subsection.

Photoelectric effect: The interaction of photons with an atom's orbital electrons where the electron receives all of the energy from the photon is known as the photoelectric effect. It receives the remaining energy as kinetic energy after part of it has been used to overcome the electron's binding energy. An inner shell electron is often involved in the photoelectric effect. A more loosely bound electron from the outer orbital descends to fill the vacancy left by the electron's ejection from the atom, ionizing the atom. When this occurs, the changes in the binding energies of the various electron levels will lead to radiation emission. This is a characteristic X-ray. A photoelectron is the name given to the released electron. Figure 10 represents this effect. Alternately, an Auger electron is the name for the second electron that the atom may release in place of an X-ray in order to remove the energy. The atom is now doubly charged as a result. Based on the characteristics of the released particles, spectroscopic techniques are employed to identify materials using characteristic X-rays and Auger electrons [7].

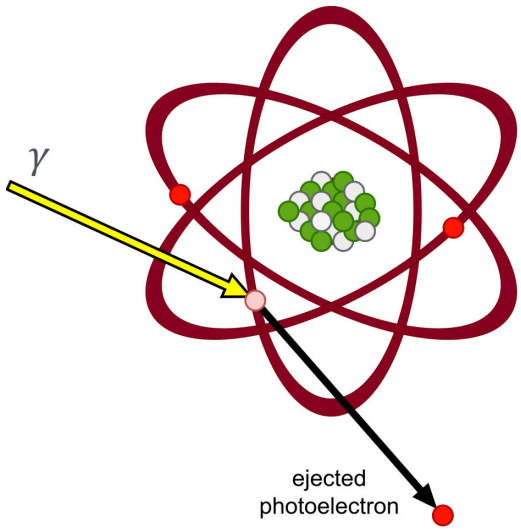

Figure 10: Schematic representation of the photoelectric effect.

In human tissue, for elements with low Z, the photoelectric effect predominates at energies lower than around 100 keV. It is especially important for low-energy radionuclide imaging and X-ray imaging. At the energy of annihilation radiation (511 keV), it has little effect; however, with the development of combined PET/CT systems, in which the CT system is used for attenuation correction of the PET data, understanding the physics of interaction through the photoelectric effect is crucial for determining the appropriate values of the attenuation factors from the X-ray CT [7]. Moreover,the photoelectric effect becomes relevant in the instrumental detection of these photons. Detectors are typically made of materials with high Z to enhance photoelectric interactions and improve the efficiency of photon detection at this energy.

Compton scattering: The interaction of a photon with a loosely bound orbital electron, and there is a change in the direction, is known as Compton scattering. Since the electron and atom are so loosely connected, the electron is basically free. In human tissue, this impact is most prominent at energies greater than 100 keV and lower than 2 MeV. When weighed against the photon's energy, the electron's binding potential to the atom is so minimal that it might be insignificant in the calculation. Following the interaction, the electron is ejected from the atom and the photon changes direction. The photon's energy loss is split between the electron's kinetic energy imparted to the Compton recoil and the energy level's small binding energy. Figure 11 represents Compton scattering. The material's characteristics or electron density have no effect on the energy transmitted [7].

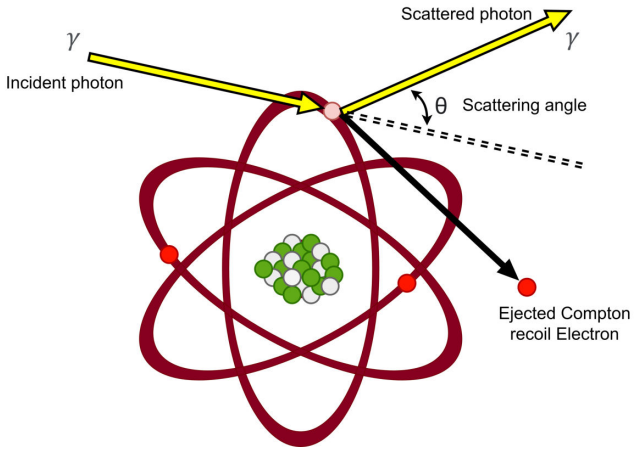

Figure 11: Schematic representation of Compton scattering.

The Compton equation may be used to determine the photon's energy following Compton scattering:

$$E'_\gamma = \frac{E_\gamma}{1 + \frac{E_\gamma}{m_0 c^2}(1 - \cos(\theta_c))} \tag{1.1.9}$$

Most ($> 80\%$) of detected scattered events have only experienced one scattering

interaction, according to several Monte Carlo computer simulation studies of annihilation radiation interaction with tissue-equivalent material in PET [7].

Pair production: In order to preserve charge, photons with energies larger than 1.022 MeV (twice the energy of an electron at rest) may spontaneously be converted into a positron-electron pair when they pass close to a nucleus. This process is represented in Figure 12. At high energies, direct pair production in the Coulomb field of a nucleus dominates the interaction process. The probability of pair production increases with energy over the threshold of 1.022 MeV. The probability of this happening is around 60% at 10 MeV [7].

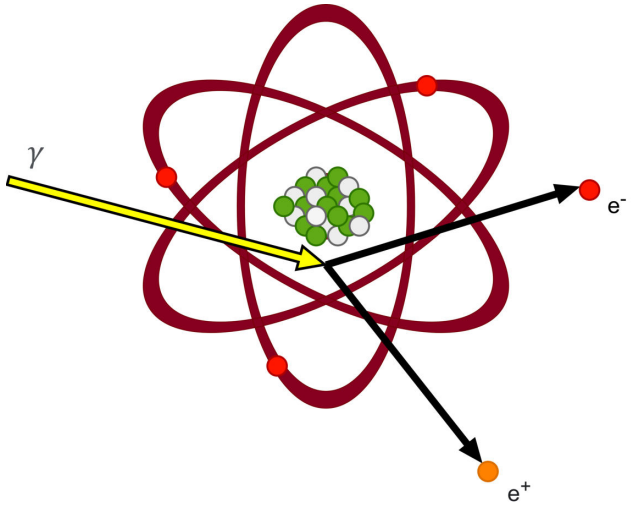

Figure 12: Schematic representation of pair production.

1.1.1.3.1.2 Data acquisition

The data acquisition process in PET imaging is critical for acquiring high spatial-resolution images. The next paragraphs explore the PET system architecture for accurate gamma ray detection, with a focus on scintillation crystals and photosensors. It will also go over the basics of list mode data acquisition, which allows for the recording of events as they take place, as well as the coincidence detection, which assures that only true simultaneous gamma ray events are analyzed. Finally, we'll read about the advantages of having time-of-flight (TOF) information, which improves image quality by increasing photon localization accuracy, resulting in clearer and more detailed images.

PET system architecture for the detection of gamma rays

As previously pointed out, PET imaging involves the detection of 511 keV photons, which are produced when an electron and a positron annihilate. The scintillation detector is the key component of most PET detector systems. The detector is comprised of a scintillation crystal and a photodetector, such as a photomultiplier tube (PMT)

and recently a SiPM. When the annihilation photon interacts with the scintillator material, the released energy is converted in optical photons. A portion of these photons is converted in an electric signal proportional to the number of light photons produced within the scintillation crystal and the energy of the incident annihilation photon. The photon's original energy of 511 keV may decrease because of Compton scattering as it travels through the patient's body to the scintillation crystal surface. Additionally, the annihilation photon may not completely lose its energy in the initial crystal and instead scattered to a nearby crystal, where it is absorbed. As a result, the two crystals receive only a portion of the original 511 keV energy [29]. Figure 13 shows the general design of a PET system.

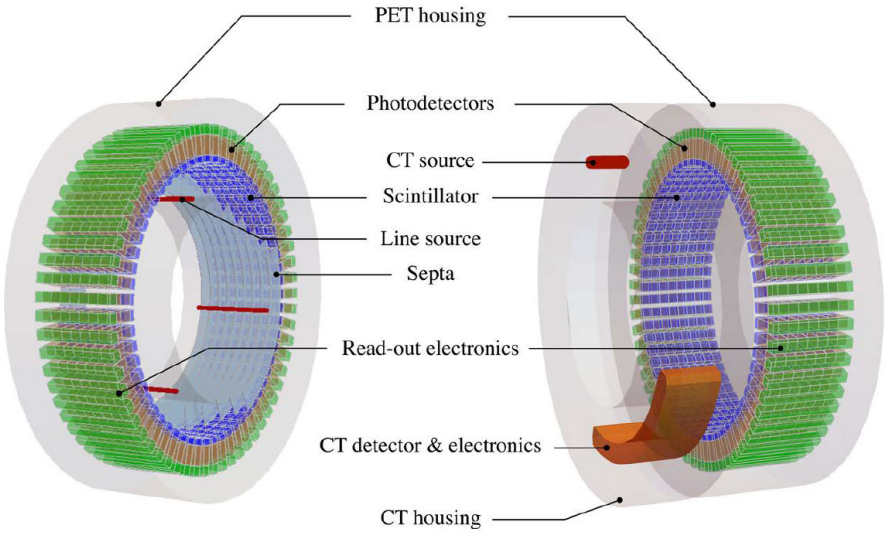

Figure 13: PET system design. Left scheme represents PET scanner. On the right, a combined PET/CT scanner is represented. From *"Hybrid MR-PET Imaging: Systems, Methods and Applications"* by C.W. Lerche, U. Pietrzyk, and M. Lenz. 2019. Page 158. Copyright 2019 by The Royal Society of Chemistry.

Scintillation crystals: Scintillation is the process by which light is emitted from crystals when they are irradiated with ionizing radiation. In the past, bismuth germanate (BGO) and thallium-doped sodium iodide (NaI(Tl)) were frequently employed because of their appropriate scintillation qualities. But thanks to developments in scintillator materials, cerium-doped lutetium oxyorthosilicate (LSO) and lutetium-yttrium oxyorthosilicate (LYSO), which have better performance characteristics, have been developed and adopted. The state-of-the-art scintillator for PET is LYSO, which is preferred for its high light yield, fast decay time, and high stopping power [30, 31].

The conversion of gamma rays to light is a complicated process that may be summarized as the crystal absorbing gamma ray energy and leaving its electrons in an excited state. The gamma photon's energy is transferred to the crystal via one or more Compton or photoelectric interactions. Each of the energetic electrons produced by these gamma ray interactions distributes its energy to electrons in the crystal, leaving them in an excited state. As they return to their previous states, part of their energy

is released as optical photons [32]. Thicker crystals have better sensitivity because they attenuate more of the original and dispersed gamma rays, but thinner crystals have lower sensitivity because they let more photons out. However, thinner crystals have better spatial resolution. After absorbing energy, excited electrons return to their original state. As a result, light photons are emitted [32].

Photosensors: In order to detect the gamma photons generated by positron annihilation, PET uses advanced photosensor technologies. Photomultiplier tubes have historically been used largely because of their fast temporal response, low noise, and high gain. However, they are less appropriate for current multimodal imaging systems due to their size, fragility, high voltage requirements, and magnetic field susceptibility. Although they are smaller and have less magnetic field resistance than PMTs, avalanche photodiodes (APDs) were a solid-state substituted that lacks PMTs in terms of gain and timing accuracy.

Around the mid-2010s, silicon photomultipliers (SiPMs) began gaining significant traction in PET imaging. They have been positioned as the leading technology for PET imaging. SiPMs combine the compactness and magnetic insensitivity of APDs with the high gain and timing performance of PMTs, making them ideal for applications such as time-of-flight PET and hybrid PET/MRI systems. Cadmium zinc telluride (CZT) detectors, which convert gamma photons directly into electrical signals, offer excellent energy resolution but are still undergoing research for widespread PET adoption. To satisfy the requirements of high-performance, multi-modal medical imaging, the field is gradually moving away from conventional PMTs and towards more sophisticated solid-state detectors like SiPMs and CZTs.

In Figure 13, an implementation of a PET scanner is displayed on the left. An integrated PET/CT scanner is illustrated on the right. The emission data and transmission data will be obtained sequentially in both scenarios. The PET and CT rings are positioned in a close, in-line arrangement in the PET/CT scanner. To reduce the number of detection events scattered between both modalities, additional γ ray shields, may be positioned between the CT and PET components [29].

List mode data acquisition

The main design and crucial performance parameter of PET scanners are determined by the need to stop and detect both annihilation photons. Both photons are emitted in opposite directions during the positron annihilation process, and their flight directions create a straight line between the two scintillation pixels where the γ rays were detected. This line, known as the line-of-response (LOR), establishes the γ rays' flight direction (see Figure 14). Since the pair of photons are emitted simultaneously, coincidence detection is used in this technology [29].

The total amount of tracer in the LOR will determine the number of coincidence events observed, assuming that physical factors like attenuation, random and scattered

coincidences, and detector efficiency changes are not present. Image reconstruction is the process of estimating, from the measured data, the distribution of radiopharmaceutical activity inside the body.

Currently, list mode is commonly employed in PET imaging due to its ability to record each detected event with precise timing and spatial information. This detailed data allows for list mode reconstruction, where images are generated directly from individual events. List mode reconstruction enables greater flexibility and accuracy, particularly in advanced applications like dynamic imaging, motion correction, and time-of-flight PET, leading to improved image quality and temporal resolution [2].

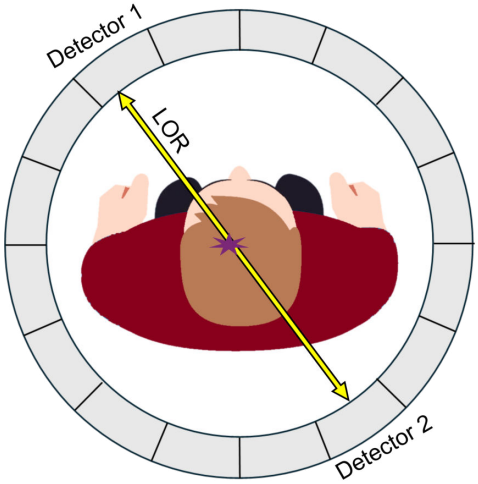

Figure 14: Line of response of pair photon detection in coincidence. (LOR = Line of Response). Source: Created by the author.

In this mode, a time stamp indicating the moment when the coincidence event happened is sequentially stored. The outcome of the scan is a single file with a list of coincidence events arranged chronologically. After a scan is finished, the events in this list can be integrated across any time interval, enabling the number and duration of frames to be selected and changed as needed. This may, for instance, make it possible to remove data points if a patient relocated. Following the organization of the projection data into frames, each representing a distinct time interval, the frames are separately reconstructed into tomographic images [26].

Coincidence Detection

As previously mentioned, PET imaging is based on pairs of annihilation photons that leave the human body and are detected by the PET scanner simultaneously. The patient is surrounded by ring-shaped detectors that detect the annihilation photons. These photons may be detected individually and are referred to as single events. The single event rate is the total number of events that each detector processes. We are able to distinguish true coincidence from scattered coincidence and random or multiple coincidence [24]. These different forms of matching that occur in a traditional PET

scanner are shown in Figure 15.

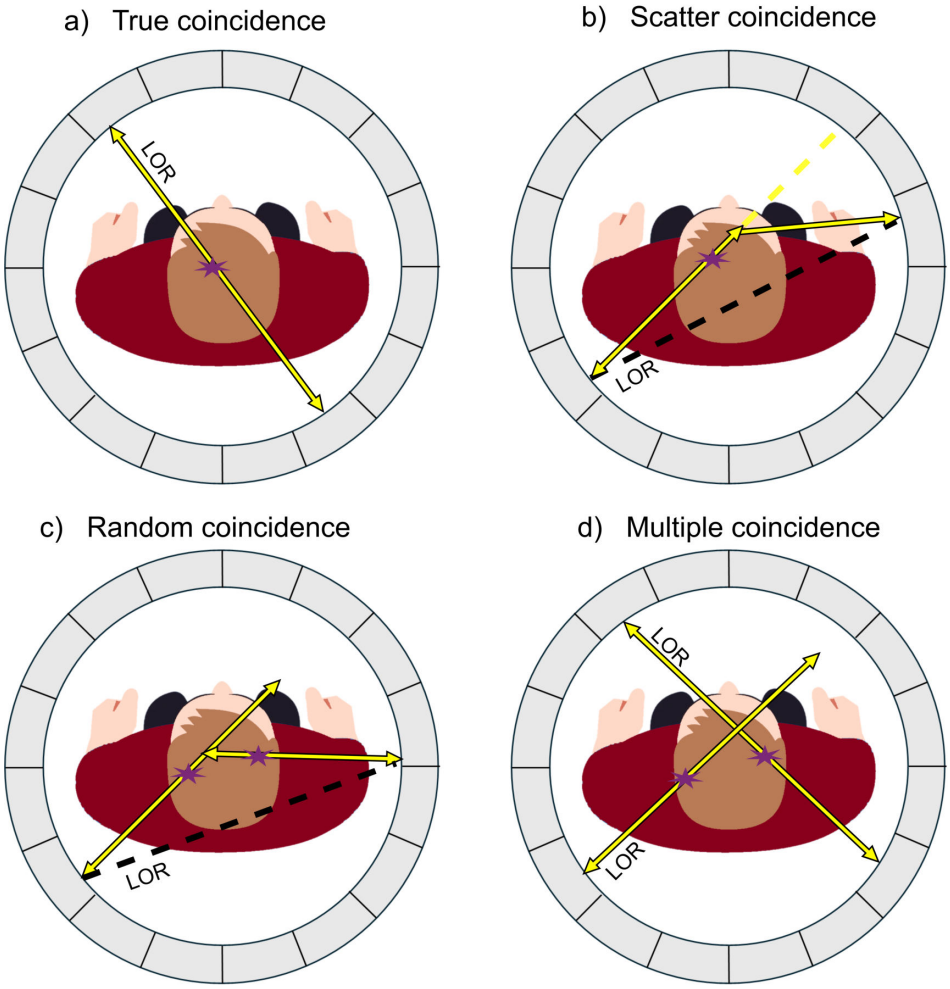

Figure 15: Different event types of photon detection of annihilation coincidence. (LOR = Line of Response). Source: Created by the author.

The first are the ones that are desired (a), as it suggests that the coincidence detection is the result of a single annihilation in which the photons have maintained their original direction. When one of the annihilation photons is scattered and fails to travel in the original direction, scattered coincidences (b) happen. Two photons that were originally detected in coincidence from two different annihilations are the subject of random or multiple coincidences (c, d). Reconstructing the original distribution of the radioactive substance throughout the body from the detections is the primary goal of the PET image, which corresponds with the true coincidences. Consequently, they must be minimized, estimated and corrected by scattered and random coincidences. It should be known that although the patient's activity increases true and scattered coincidences linearly, the rise in random coincidences is squarely related to the patient's activity, and the latter occur more frequently when the patient's activity level is high [24].

Time-of-Flight PET

The disparity in arrival timings can only be used to approximate the annihilation position along this LOR. We refer to this method as TOF PET [29].

TOF information on a PET scanner involves knowing exactly when each annihilation photon was detected. Because the annihilation photons are released at the same moment, the difference in detection timings of the photons during the coincidence provides an understanding of the difference in photon pathways. This enables for greater annihilation localization throughout the LOR, as well as improved image quality [24]. Figure 16 shows a schematic representation of TOF.

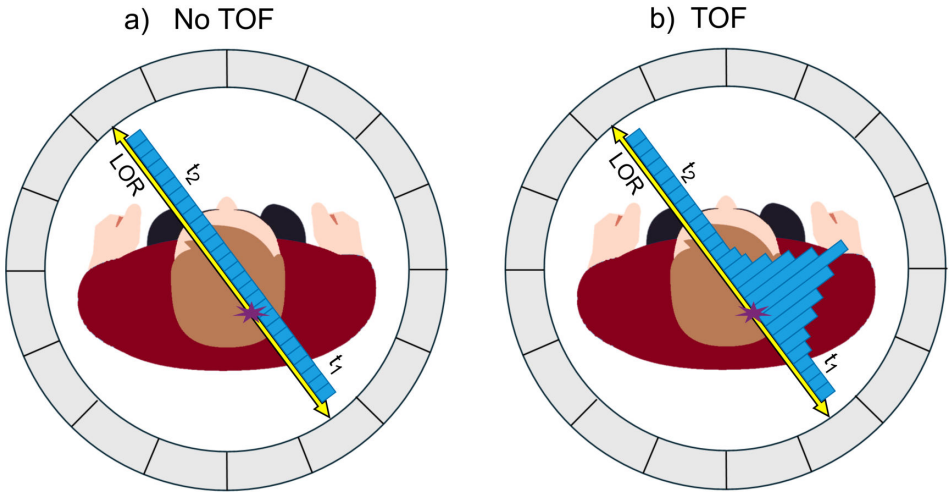

Figure 16: Time of Flight (TOF) reconstruction. a) The No TOF reconstruction increments all pixels along the LOR by the same amount. b) TOF reconstruction increments each pixel on the LOR based on the probability of the source's location. Source: Created by the author.

Prior to the development of PET, it was discovered that monitoring the difference in arrival times of annihilation photons could correctly establish the three-dimensional position of each positron. By constraining the positron's location to a point instead of a line, three-dimensional images may be generated without using a reconstruction algorithm. The measured location along the line has an accuracy of

$$\Delta x = \frac{c}{2}\Delta t \tag{1.1.10}$$

where Δx is the position error, c is the speed of light, and Δt is the timing measurement error. Obtaining subcentimeter position resolution requires timing resolution of less than 50 ps, which is currently difficult to achieve [33].

The first generation of TOF PET scanners, developed in the 1980s, employed CsF or BaF_2 scintillators connected to photomultiplier tubes to achieve TOF resolutions of 400-600 ps. However, these scintillators showed low system sensitivity and

poor spatial and energy resolution. The introduction of increased light output and dense lutetium-based scintillators in the 1990s prompted the introduction of a second generation of TOF PET scanners in the mid-2000s, with significantly higher system sensitivity and spatial resolution [34].

The last few years have seen a lot of activity in TOF PET hardware technology, particularly in photosensor development, which has led to the widespread commercial introduction of silicon photomultiplier (SiPM)-based (digital) whole-body TOF PET systems (third-generation TOF PET systems) by all major manufacturers. These new scanners offer significantly higher TOF resolution, sensitivity, and spatial resolution than the second generation of TOF PET devices. The majority of these advancements were made possible by the development of smaller SiPM photodetectors, which give better intrinsic timing and detector performance due to decreased or no signal multiplexing. The most recent digital TOF PET system provides another generational advancement in PET image quality, potentially leading to reduced imaging times and increased diagnostic performance [34].

Reconstruction approaches that use TOF data minimize statistical noise in PET. No TOF reconstruction uses coincident events measured in a single chord to contribute to all image pixels along that chord, rather than simply the pixel from where the source originated. The reconstruction filter reduces the mean contribution to other pixels, but statistical fluctuations in the measurement data cannot be eliminated, resulting in noise across all pixels. TOF reconstruction limits the statistical fluctuations of the measurement data to a smaller number of image pixels. This may be used to generate the variance reduction formula, which can help to decrease noise amplification in PET [33].

The noise reduction is easily predicted for simple, uniform distributions, but the improvement is determined by the radioisotope distribution, which is not often homogenous. The variance reduction applies not just to “true” events, but also to those that experience Compton scatter in the patient and random coincidences. When TOF reconstruction is employed, the noise due to randoms decreases as the timing precision increases, despite the fact that the hardware coincidence window is restricted by the TOF measurement resolution [33].

1.1.1.3.1.3 Image reconstruction

Reconstruction of PET scans is a key step in transforming raw data into clinically relevant images. The following paragraphs discuss important data corrections such as normalization, random coincidence correction, scattered radiation correction, attenuation correction, partial volume correction and dead time correction. Each of these corrections tackles a distinct distortion or inefficiency in the data, ensuring that the images generated are precise and reliable. This part will also cover a short overview of the reconstruction methods used to integrate corrected data into coherent images.

Data corrections

PET imaging aims to match the intensity of the reconstructed image to the amount of activity at the exact location of the object. This allows for precise comparisons of activity levels in different voxels. To make this possible, some corrections are needed.

Normalization: For a variety of factors, such as differences in detector efficiency, solid angle subtended, and summing of neighbouring data elements, lines of response in a PET dataset exhibit varying sensitivity. Reconstructing quantitative and artifact-free images requires knowledge of these variances, in fact, the majority of algorithms demand that these fluctuations be removed before reconstruction can begin. The independent correction factors for each LOR are referred to as normalization coefficients. The technique of taking into consideration these effects is called normalization [7].

Conceptually, the simplest way to normalize would be measuring the counts that each coincidence detector pair detects while exposing all pairs to the same radiation source. However, doing so would take several hours of scanning. To decrease the number of counts needed without raising statistical noise, this strategy must be modified. Instead of estimating the efficiency of every conceivable detector pair, the majority of the updated approaches rely on calculating the efficiencies of each individual detector element and then combining them to estimate the efficiency of the detector pairs [26].

Correction for Random Coincidences: Random coincidences, often known as "accidental" or "chance" coincidences, occur due to the limited electronic time window used to identify true coincidences. Due to the finite width, two uncorrelated single detection events that occur near together in time may be mistaken for a coincidence event caused by a single annihilation [7].

Random coincidences provide a homogenous background in reconstructed images, reducing contrast and confusing the relationship between image intensity and actual amount of activity [26].

To adjust for random coincidences, the most popular approach is to remove a delayed coincidence channel in real-time. This method does not introduce bias but does increase noise. An alternative approach is the postacquisition subtraction of a low-noise random coincidence estimate, derived by a smoothed delayed coincidence sinogram, calibration scan, or direct estimation, can be subtracted after acquisition. Each technique takes distinct decisions regarding noise amplification, bias, and data processing needs. The choices depend on the activity injected, the imaging environment, and the reconstruction algorithm [35].

Correction for Scattered Radiation: The impact of scatter detection on reconstructed PET images was initially perceived as a loss of contrast, but later scientists recognized the complexity of artefacts caused by Compton scatter detection, which af-

fect visual interpretation and the accuracy of quantitative analysis of PET data. In PET, scattered LORs can occur outside the body and/or outside of the imaging field of view [36].

Scattered radiation can lead to errors in the relationship between image intensity and object activity as well as a loss in contrast. Particularly in 3D imaging of the abdomen, the percentage of scattered events in PET can be considerable, ranging from 60% to 70%. This is mostly due to three factors: the energy resolution of dense scintillators, the need that only one of the two annihilation photons be scattered, and Compton scattering, which is the major mechanism of interaction in scintillators at 511 keV [26].

Scatter correction in PET includes two main approaches. The first method includes calculating the correction using information from both the original scatter-contaminated image and the transmitted image. The emission image reflects the distribution of activity in the patient, whereas the transmission image represents the tissue's attenuation coefficient. Computer simulations of photon interaction physics may estimate the underlying distribution of scattered events and their contribution to individual profiles. Hybrid PET/CT scanners can compute scatter distribution from registered CT images, but it is computationally expensive. The second technique studies projection profiles outside the object, accounting for random coincidences and assessing events that are misplaced owing to scattering. This approach is quick and compensates for dispersion from radioactivity outside the FOV, but it may produce considerable inaccuracies in complicated circumstances [26].

Partial Volume Correction: PET imaging resolution is limited by factors such as positron range, photon noncollinearity, crystal size, acquisition method, and reconstruction process. To minimise excessive noise or sampling artefacts, functional imaging uses relatively large voxels. The tissue-fraction effect, which integrates contributions from many tissues inside a single voxel, is a challenge in higher-resolution structural imaging modalities like CT and MR imaging. This phenomenon is called partial volume effects (PVE), and it is also known as scanner blurring or point spread. It occurs when activity within one zone "spills over" into other regions. PVE result from PET imaging's limited resolution capabilities [37].

The PVE causes intensity values in images to deviate from their ideal values. It is produced by two phenomena: the imaging system's limited spatial resolution and the image sampling. The PET scanner's detector design and reconstruction process limit spatial resolution, resulting in 3D blurring and spillover between areas. This causes a tiny source to look bigger but dimmer, as seen in Figure 17. This effect is technically defined as a 3D convolution process that combines the real source with the imaging system's 3D point spread function [38]. Another phenomenon is image sampling, which occurs when the sampled radiotracer distribution does not match the tracer distribution's real contours (see Figure 18).

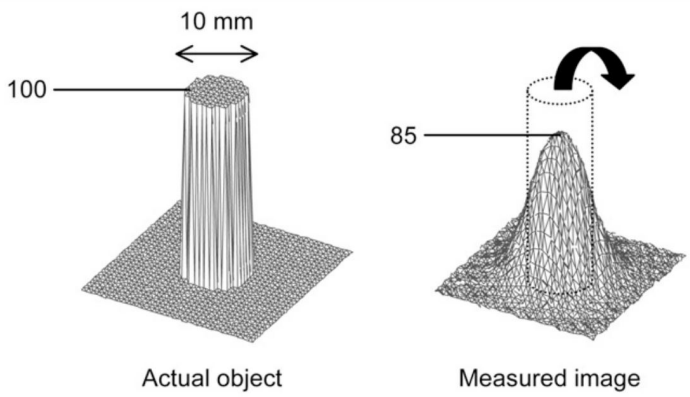

Figure 17: A circular source (10 mm in diameter) with uniform activity (100 arbitrary units) in a nonradioactive background generates a measured image with a portion of the signal visible outside the source. Maximum activity in the measured picture is lowered to 85. From *"Partial-volume effect in pet tumour imaging"* by Marine Soret, Stephen L. Bacharach, and Irene Buvat. 2019. Page 933. Copyright 2007 by The Journal of Nuclear Medicine.

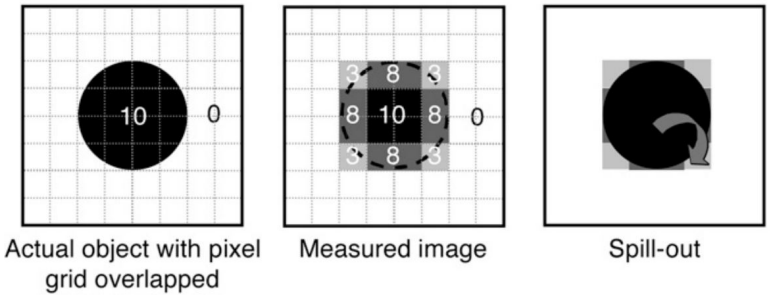

Figure 18: Impact of image sampling on PVE. Pixels near the periphery of the source include both the source and background tissues. The signal intensity in these pixels is the mean of the signal intensities in underlying tissues. Signal spilling occurs when a portion of the source's signal is visible outside of the object. From *"Partial-volume effect in pet tumour imaging"* by Marine Soret, Stephen L. Bacharach, and Irene Buvat. 2019. Page 933. Copyright 2007 by The Journal of Nuclear Medicine

This effect is seen not just in emission tomography, which has lower spatial resolution than other imaging modalities, but also in high-resolution imaging, such as MR or CT. Compensation for PVE should consider both the limited resolution impact and the tissue fraction effect [38].

The partial volume effect can be minimized or corrected using a variety of techniques. These include techniques which use additional information from anatomical imaging modalities like CT and MR, as well as techniques that try to recover resolution losses before or during image reconstruction [7].

Dead Time Correction: PET scanners require a minimum period of time between successive events in order to register them as distinct. Radioactive decay is a random process, and at high count rates, the percentage of events falling into this group can be

substantial. This decreases the total number of coincidence occurrences detected by the scanner, and as photon flux increases, the system's linear response becomes degraded. The metric that defines counting behaviour at high event rates is known as "dead time," which is the ratio of the measured count rate to the expected count rate if the system behaved linearly [7].

Dead time corrections in PET scanners are critical for avoiding underestimating radioactivity concentrations at high counting rates. Most scanners employ empirical dead time models to calculate the observed counting rate for different object sizes and energy thresholds. These data are then analyzed using paralyzable or nonparalyzable dead time models. Some systems use a global dead time correction factor, whilst others use corrections for particular detector modules [26].

Attenuation Correction:

The natural interaction between photons emitted by radiopharmaceuticals and tissue during their path through the body is the basis for the attenuation phenomenon. Photoelectric interactions are possible for photon intensities comparable to those used in nuclear medicine, in which the incident photon is totally absorbed. In other situations, the primary radionuclide photon scatters as a result of interactions with loosely bound electrons in the surrounding material. The scattered photon's energy might be less than or equal to the incident photon's [39].

Given that a coincident event occurs when both photons produced by positron annihilation are detected at the same time, this cannot occur if a photon is absorbed by the body or scattered outside the field of view. The probability of detection is based on the combined path of both photons. Because all sources on a line connecting two detectors have the same total route length, the probability of attenuation remains constant regardless of source position [7].

Attenuation correction is the most crucial correction in PET. Image noise, artifacts, and distortion are increased when counts are lost as a result of attenuation. Important artifacts on whole-body PET scans without attenuation correction include: significant activity at body surface edges due to relative lack of attenuation at the surfaces compared to deeper structures; distorted appearance of areas of intense activity due to varying degrees of attenuation in different directions of activity originating from these areas; and diffuse, relatively increased activity in tissues of relatively low attenuation [40]. Figure 19 shows an example of an image with and without attenuation correction.

Fortunately, the correction is simple to determine. Consider a source at depth x within an object with thickness T (as shown in Figure 20). A true annihilation event requires detection of both photons from the source. The probability of both photons reaching the detector is equal to the product of their individual probabilities, provided they are emitted in the correct directions [26]. The probability follows the equation:

$$P_{det} = e^{-\mu x} \times e^{-\mu(T-x)} = e^{-\mu T} \tag{1.1.11}$$

where μ is the linear attenuation coefficient of tissue at 511 keV. It should be noted that regardless of the source position along the line connecting the two detectors, the probability that both photons will reach the detector remains constant [26].

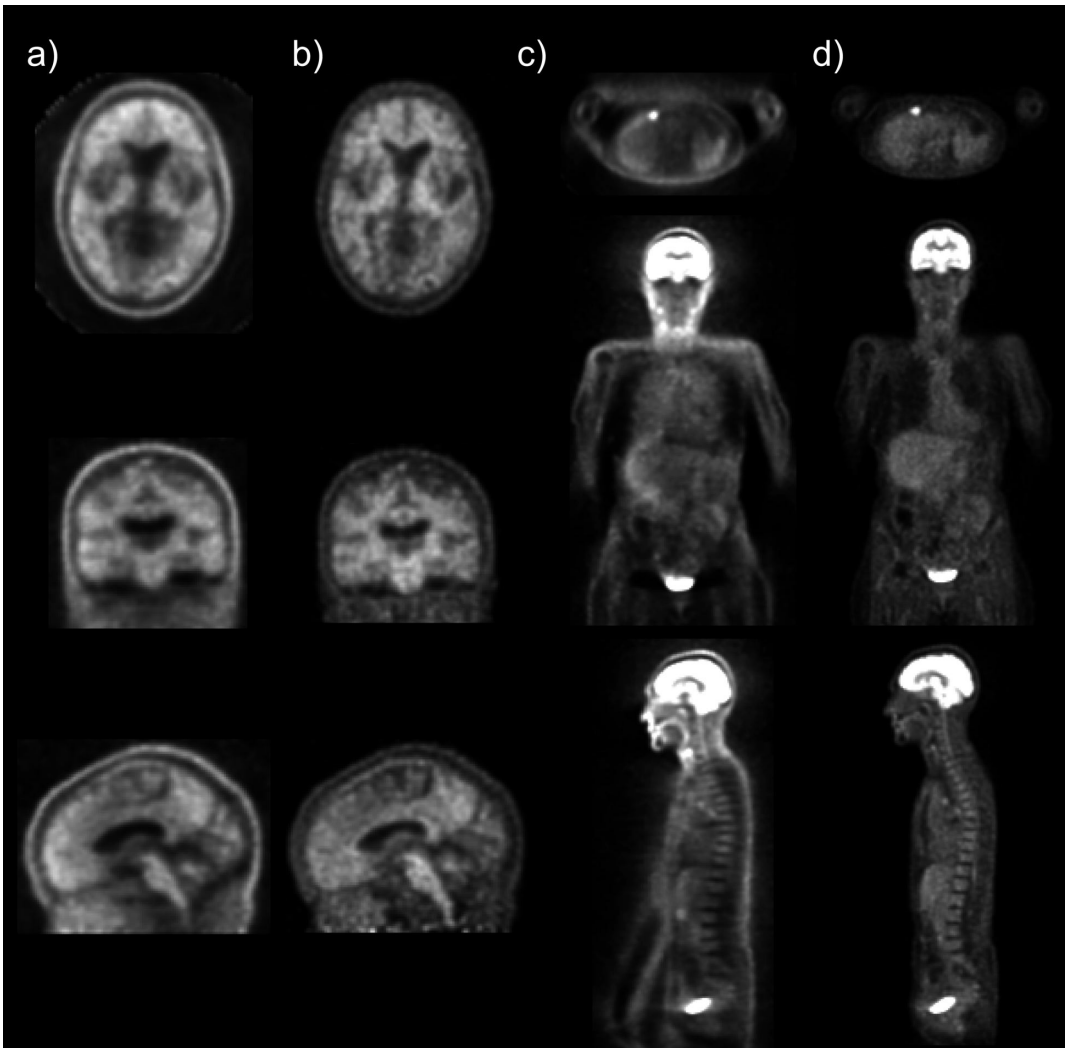

Figure 19: Example of brain (a, b) and whole-body (c, d) images without (a, c) and with (b, d) attenuation correction. Images acquired at Hospital La Fe.

Transmission measurements can help for attenuation correction in PET. It involves taking two measurements using a source positioned on a line connecting each pair of coincidence detectors. The initial measurement, known as the blank scan, is taken without the person in the scanner. Then, the individual is positioned in the scanner, and measurements are repeated. This is known as a transmission scan [26]. The attenuation correction factor (A) for a detector pair (i,j) is:

$$A_{i,j} = \frac{Blank_{i,j}}{Trans_{i,j}} \tag{1.1.12}$$

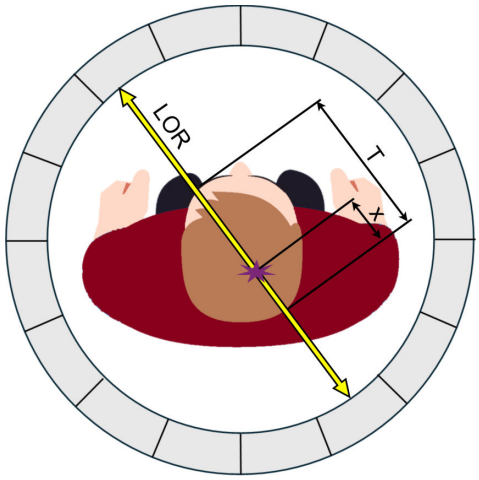

Figure 20: Parameters involved in PET attenuation correction. (LOR = Line of Response). Source: Created by the author.

Conceptually, the simplest approach involves obtaining the scan before injecting the radiotracer in order to avoid interference between the scans. A second approach, known as postinjection transmission scanning, takes place immediately after the emission scan but while the patient is still active. This saves time and decreases patient motion and misalignment between scans. However, this approach requires the capacity to discriminate between transmission and emission events generated by leftover radiotracer in the body. At any one moment, the transmission source irradiates a small fraction of detector pairs, and the counting rate in those pairs is significantly larger than the counting rate in the same detectors generated by emission radiations [26].

Despite the effectiveness of these methods, the use of transmission scans with external radionuclide sources for attenuation correction has been greatly decreased due to the widespread adoption of hybrid PET scanners. Attenuation correction is instead carried out using data from the anatomical imaging scan. This will be discussed later in the subsection "1.1.1.3.4 Hybrid equipment".

Reconstruction Algorithms

Reconstruction techniques may be divided into two basic groups: iterative and analytical methods. The analytical methods use a linear detection model and are fast. Filtered backprojection (FBP) is the most widely used analytical reconstruction technique. On the other hand, iterative techniques are nonlinear and slower. Despite this, its usage has become routine in the majority of clinical scanners, since it can include more extensive models of the physics of the detection process and the distribution of radiopharmaceuticals, as well as simulate the statistical distribution of raw data.

Furthermore, the ability to rebuild the image at a time suitable for clinical realities is made possible by the advancements in processing capabilities of modern systems [24].

An approach that provides a less noisy and more accurate substitute for FBP is iterative reconstruction. It involves estimating an initial guess of the 3D object that could have led to the set of acquired projections, and assuming a model of the imaging process that may include assumptions about photon attenuation, Compton scatter, and device spatial resolution. Using this model and the object's current estimate, a new set of projections is simulated and compared to the real acquired set. To generate a new estimate of the object, variations between the two sets are backprojected and added to the current estimate based on pixel value ratios or differences. These stages are iterated until an acceptable version of the object is obtained. Statistical criteria, such as maximum likelihood, are commonly used to assess the quality of a current estimate. The procedure determines which object is most likely to have resulted in the collected projection data [41].

Iterative reconstruction consists of an approach that outperforms filtered backprojection. However, reconstruction time may be 50 times longer than for a single filtered backprojection. To decrease iterations, projection data can be divided into ordered groups of equally spaced projections and updated between each subset. This method can lead to faster reconstructions and comparable image quality results [41].

Maximum Likelihood Estimation (MLE) is the most used iterative technique. When used for image reconstruction, this conventional statistical technique maximizes the verosimilitude function and generates an image that with high probability would produce the measured raw data. The image's noise ratio is improved by iterative reconstruction techniques based in statistical principles. The expectation maximization (EM) algorithm, which finds the estimator of maximum probability with great efficiency, is one of the most helpful iterative techniques [24].

Maximum-likelihood expectation maximization (MLEM) is the technique that finds the optimal solution by combining the algorithm for maximising the expected value with maximum probability as an optimization criterion. However, in clinical settings, an accelerated version of this technique called ordered subset expectation maximization (OSEM), which arranges the measured data into ordered subsets, is more frequently employed. It is now possible to employ iterative approaches in clinical routines due to the 20–30% reduction in reconstruction time achieved by this technique, as well as the enhanced processing capabilities and numerical projection algorithms [24].

1.1.1.3.2 Radiopharmaceuticals for PET imaging

PET radiopharmaceuticals are made up of two components: a molecular structure (vector, vehicle, ligand) and a positron emitting radionuclide. The vehicle specifies biological properties and regulates chemical and biochemical interactions *in vivo*. The

positron emitting radionuclide generates a measurable signal, allowing for coincident measurements of annihilation radiation within a specific PET device, such as a PET/CT scanner [42].

The vehicular molecules must be highly specific and selective towards the target site, which can be selected according to receptor systems, antigens, enzymes, transporters, metabolic alterations, up-regulated conditions, tissue hypo-oxygenation, differing cellular energy demands, changes in gene and protein expression, and differences in vascularization and perfusion. A molecule is labelled with a radionuclide to form a radiotracer. All extensively utilized PET nuclides have short half-lives and limited availability. However, the radionuclide's widespread and feasible availability is required for successful everyday use [42].

Radiopharmaceuticals are chemically indistinguishable from non-radioactive equivalents, therefore the organism uses them as surrogates in all metabolic processes. Radiopharmaceuticals provide direct visualization of functional processes *in vivo*. Pathological changes that cause aberrant function at the molecular level can be detected before morphological symptoms appear [42]. Figure 21 illustrates the enormous potential of PET scans, demonstrating that using the same radioisotope along with different molecules can provide an incredible variety of images on the same equipment.

The most commonly used PET radiopharmaceutical in the world is [^{18}F]Fluorodeoxyglucose ([^{18}F]FDG), a radiolabeled analogue of glucose. When it comes to identifying malignant tumours with elevated glucose metabolism, [^{18}F]FDG is helpful. [^{18}F]FDG is still a non-specific tracer, though, and absorption of the substance has also been shown in a number of benign diseases, including inflammatory and infectious processes. As a result, during the past decade, there has been an an increasing interest in novel radiopharmaceuticals that can target particular biomarkers to investigate molecular pathways in tumour biology, such as oxygen delivery, protein synthesis, metabolism, proliferation, receptor and gene expression, and choline and radiolabelled amino acids [43].

All of the radionuclides employed in modern nuclear medicine are synthetic or "artificial" in nature. They are created by bombarding the stable atoms' nuclei with subnuclear particles like protons and neutrons, which activate nuclear processes that change the stable atoms' nuclei into unstable (radioactive) ones. The methods used to produce radionuclides for nuclear medicine are: reactors, accelerators and generators [26]. For PET imaging, the radionuclides most used are produced on generators and on accelerators (cyclotrons).

A radionuclide generator requires a parent-daughter radionuclide pair in an apparatus enabling separation and extraction. The daughter product activity is continually replenished by the decay of the parent and can be extracted several times [26]. Table 2 highlights a few radionuclide generators with significance in nuclear medicine. They are an essential source of metastable radionuclides.

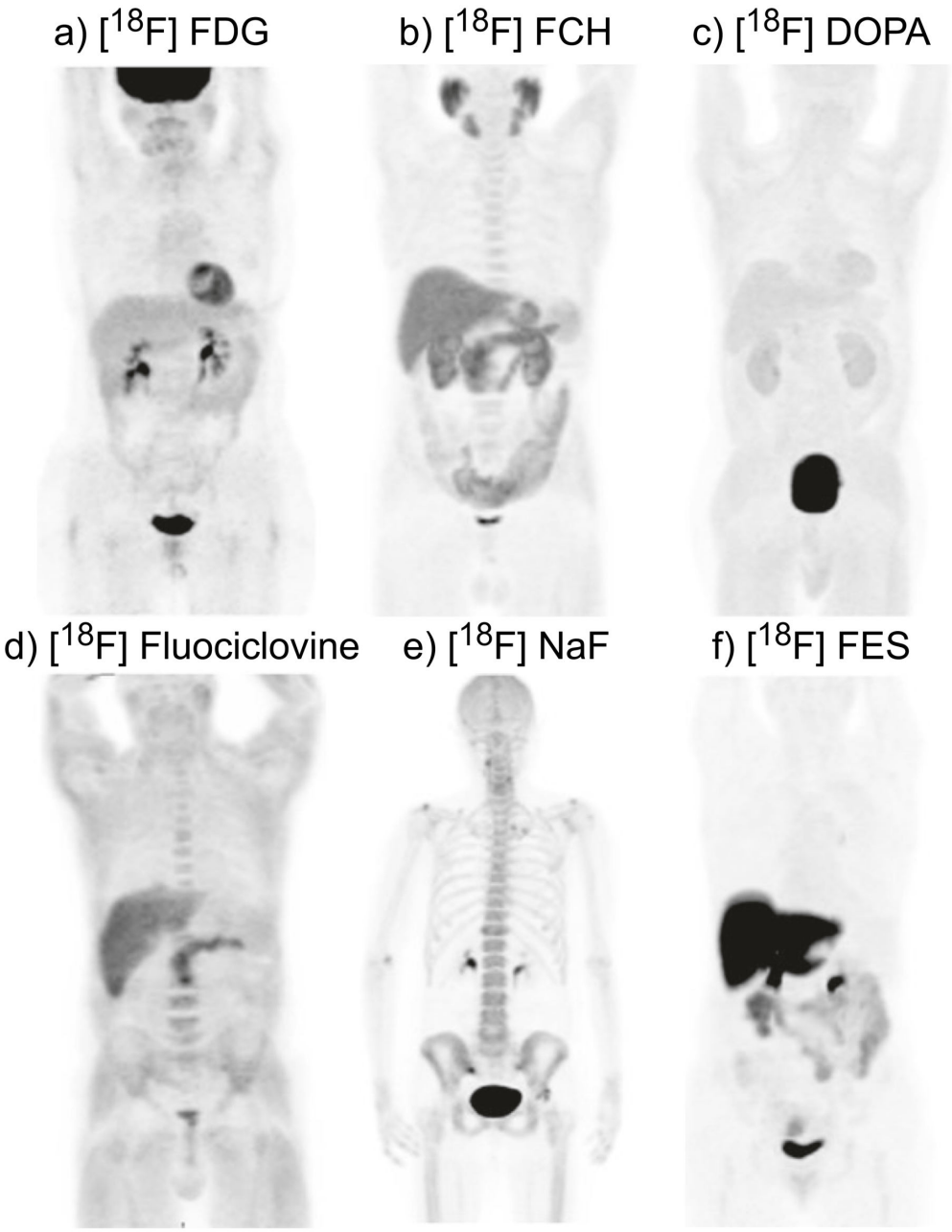

Figure 21: Biodistribution of [^{18}F] PET radiopharmaceuticals. From *"Evidence-based Positron Emission Tomography Summary of Recent Meta-analyses on PET: Summary of Recent Meta-analyses on PET"* by Giorgio Treglia and Luca Giovanella. 2020. Page 14. Copyright by Springer.

The most popular form of particle accelerator for producing radionuclides of medicinal significance is the cyclotron. Larger institutions produce the shorter-lived, positron-emitting radionuclides on-site using compact biomedical cyclotrons. Figure 22 shows an schematic representation of a cyclotron. Because cyclotron products have high photon/particle emission ratios in β^+ and EC decay, they have great potential for applications in nuclear medicine imaging studies. Table 3 depicts some cyclotron-

produced radionuclides with significance in PET imaging [26].

A cyclotron is made up of two hollow electrodes, known as 'Dees', connected by an AC current to create a potential difference between them. The whole structure is set up inside a magnetic field. An ion source in the gap emits charged particles that are attracted to the oppositely charged dee. The charged particle has a curved trajectory due to its acceleration in the magnetic field. The alternating current supply switches when charged particles arrive at the gap between the dees, accelerating them with an increasing radius of trajectory. As the current switches, the charged particle will always arrive in the gap due to the increasing radius and corresponding change in speed. When a charged particle is fully accelerated, it may be fired at a target material, causing nuclear reactions and producing desired radioisotopes [44].

Table 2: Example of radionuclide generators with significance in PET imaging. From *Physics in Nuclear Medicine.* Simon R. Cherry, James A. Sorenson, and Michael E. Phelps. Elsevier, 2012.

Parent	$T_{1/2}$	**Daughter**	$T_{1/2}$
^{62}Zn	9.3 h	^{62}Cu	9.7 min
^{68}Ge	271 d	^{68}Ga	68 min
^{82}Sr	25 d	^{82}Rb	1.3 min

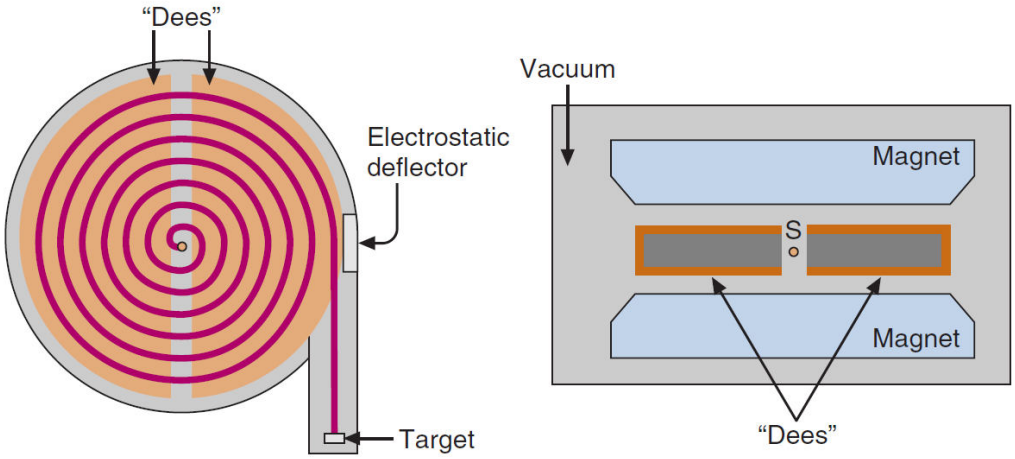

Figure 22: Schematic representation of a cyclotron. The left drawing corresponds to the top view, and the right, to the side view. From *"Physics in Nuclear Medicine"* by Simon R. Cherry, James A. Sorenson, and Michael E. Phelps. 2012. Page 48. Copyright by Elsevier

PET radionuclide selection is determined by availability, physical properties, radiochemical concerns, and radiopharmacological properties. Because radionuclides with short half-lives, such as ^{15}O (2 min) and ^{13}N (10 min), have limited clinical application, only a few PET centres worldwide employ them on a regular basis. Overall, the radionuclide's half-life should be sufficient for effective radiolabelling within the time frame of the imaging process [42].

Table 3: Example of cyclotron-produced radionuclides with significance in PET imaging. From *Physics in Nuclear Medicine.* Simon R. Cherry, James A. Sorenson, and Michael E. Phelps. Elsevier, 2012.

Product	Common production reaction	Natural abundance of targeted isotope	Energy threshold	$T_{1/2}$
^{11}C	^{14}N(p, α)^{11}C	99.6	3.1	20 min
	^{10}B(d, n)^{11}C	19.9	0	
^{13}N	^{16}O(p, α)^{13}N	99.8	5.5	10 min
	^{12}C(d, n)^{13}N	98.9	0.35	
^{15}O	^{14}N(d,n)^{15}O	99.6	0	2 min
	^{14}N(p, n)^{15}O	0.37	-	
^{18}F	^{18}O(p, n)^{18}F	0.20	2.57	110 min
	^{20}Ne(d, α)^{18}F	90.5	0	

The introduction of new radiopharmaceuticals has enhanced PET molecular imaging in recent decades. Some tracers are well-established, while others show promising early findings. Amino acid tracers, radiolabelled choline, amyloid tracers, and other radiopharmaceuticals are becoming a viable alternative to [^{18}F]FDG in some therapeutic contexts [45]. PET tracers are essential for molecular imaging as they give life to PET/CT scans. PET radiopharmaceuticals are still in their early stages, but the future of the field is promising [42].

An example of the great relevance of research in this field is the following. According to a research communication presented at the Society of Nuclear Medicine and Molecular Imaging (SNMMI) 2019 Annual Meeting, a single radiotracer, [^{68}Ga]FAPI revealed significant uptake and image contrast for several highly prevalent cancers on PET/CT images. Figure 23, which shows the great potential of this radiopharmaceutical for many applications, has been named the 2019 SNMMI Image of the Year [46].

1.1.1.3.3 Clinical applications of PET imaging

The emergence of molecular medicine is the consequence of close cooperation among scientists, physicists, and clinicians. Numerous new molecules offer promise for personalized care, newer drugs, and disease response evaluation, as well as the potential for individualized therapies for specific patients based on disease behavior. With radiomics and theranostics preparing for the future of oncology, this would be particularly relevant to the field of oncological imaging [47].

PET was created in the early 1970s, shortly after CT and about the same time as MR. PET was first used to diagnose brain and heart disorders by quantitatively imaging biologically important molecules labelled with short-lived positron emitting radionuclides. The radiopharmaceutical [^{18}F]FDG, initially developed in the late 1970s, has had the most significant influence on clinical PET imaging [48].

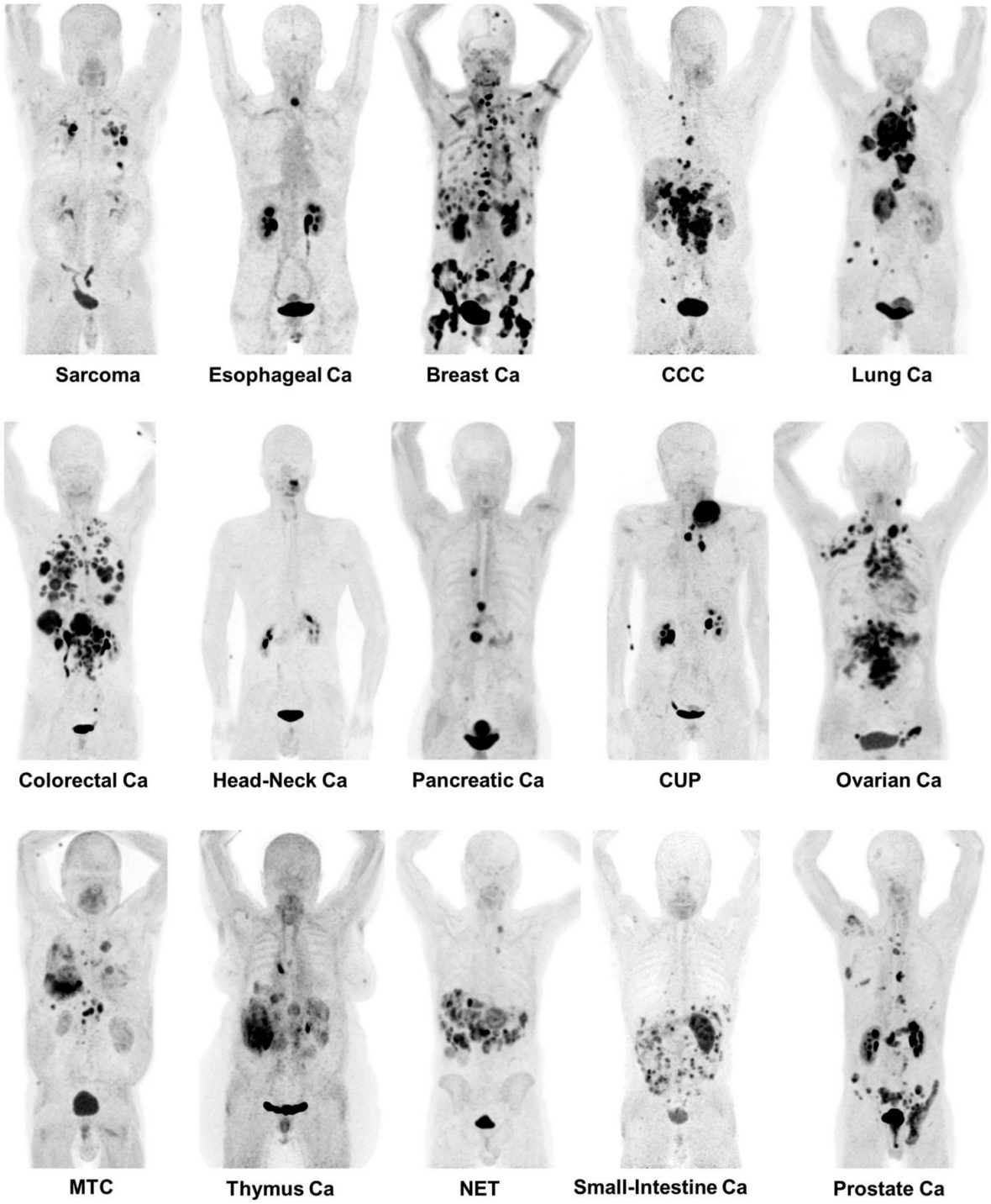

Figure 23: Maximum-intensity projections of [^{68}Ga]FAPI PET/CT in 15 patients with distinct confirmed tumor entities. From *"[^{68}Ga]FAPI PET/CT: Tracer uptake in 28 different kinds of cancer"* by Clemens Kratochwil, Paul Flechsig, et al. 2019. Page 803. Copyright by Journal of Nuclear Medicine. Note: Medullary thyroid cancer (MTC), cholangiocellular carcinoma (CCC), neuroendocrine tumour (NET), carcinoma of unknown source (CUP), and cancer (Ca).

PET is a powerful metabolic imaging technique that provides images of outstanding quality, which even non-nuclear medicine specialists recognise as important, and has a significant clinical impact. Any oncologist very quickly appreciates its value. Clinical PET is an imaging method in Nuclear Medicine that has become an integral aspect of patient treatment, particularly in Oncology, Cardiology, and Neurology [23].

PET's applications in oncology have advanced since the 1980s. In 1998, the Health Care Financing Administration (now the Centres for Medicare and Medicaid Services) authorized PET for coverage. The first two indications were evaluating the indeterminate solitary pulmonary nodule and initial staging of lung cancer. Coverage has increased to encompass diagnosis, staging, and restaging for cancers including lung, colon, esophageal, head and neck, lymphoma, and melanoma. Additionally, breast cancer is addressed for staging, restaging, and treatment monitoring. Future coverage will include other malignancies [48].

In oncology, [^{18}F]FDG is a very effective tracer for assessing metabolic activity. This molecule follows the metabolism of glucose. In contrast to glucose, [^{18}F]FDG remains trapped within the cell and is only partially metabolized. As a result, [^{18}F]FDG accumulates proportionally to glucose uptake. In a PET image, a tumor is shown as an active region or "hot spot" since the majority of tumors have glucose metabolisms that are significantly greater than those of the surrounding tissue. Whole-body [^{18}F]FDG has established itself as a routine procedure for both the therapeutic assessment of chemotherapy and radiotherapy and the staging of cancer patients [9].

Within the field of oncology, in this work we will focus on applications of PET in rare neuroendocrine tumors. It will also cover applications in the field of neurology.

In the case of rare neuroendocrine tumors, in the context of theragnosis it is crucial to precisely measure the uptake intensity of the lesions in addition to detecting them. Specific uptake is required if Peptide Receptor Radionuclide Therapy is to be considered. A PET scan is essential for this condition because determining the level of somatostatin receptor expression may have therapeutic consequences [49].

Regarding the field of neurology, PET-based neuroimaging using suitable radiotracers plays a leading role in the detection of neurodegeneration, abnormal protein deposition in the brain, neuroinflammatory responses, and other biochemical and molecular alterations *in vivo*. PET methods help distinguish between neuropathology, brain dysfunction, and clinical characteristics. Combining brain metabolism, Aβ, and tau imaging investigations is likely to provide significant results. Pathophysiological processes have been linked to neurodegeneration (measured by [^{18}F]FDG PET) and cognitive impairment. Future therapies for neuropathological processes may require a combined brain neuroimaging assessment due to their complexity [50].

1.1.1.3.4 Hybrid equipment

Combining PET imaging with anatomical imaging provided by CT or MR results in a synergistic combination of information regarding what (from PET) and where (from CT or MR). Furthermore, anatomical information from CT and MR is frequently employed to predict the quantitative corrections required for accurate PET imaging. These synergies, together with advancements in PET technology, have created an ideal environment for the development of novel imaging methods and applications [23].

1.1.1.3.4.1 PET/CT

The development of integrated PET/CT device represents a substantial advancement in imaging technology. Tomographic imaging has made substantial improvements to disease diagnosis and staging since the early 1970s, when the first prototype computed tomography scanner was introduced. The first CT scanner became commercially available in 1972, and within three years, over a dozen companies were offering or planning to commercialize CT scanners. After the development of magnetic resonance imaging in the early 1980s, CT was expected to survive another 5 years before being supplanted by MR for anatomical imaging. However, CT continues to advance and serve an important role in clinical imaging, particularly for anatomic areas beyond the brain [51].

Since the early 1950s, nuclear medicine has focused on functional imaging as a complement to anatomic imaging. Initially, planar imaging using a scintillation camera was the primary method of nuclear medicine. Functional imaging using positron-emitting isotopes was initially proposed in the early 1950s as an imaging technology with more sensitivity than traditional nuclear medicine procedures. The first commercial PET scanners were introduced in 1980, at the same time as MR became commercially accessible. The first combined PET/CT prototype scanner was developed in 1998, with clinical evaluations beginning in June [51].

A PET/CT scanner includes three elements: a PET scanner, a CT scanner, and a patient bed. Most commercial systems include a PET, which contains detectors, electronics, and a procurement system separate from the CT's own modules. PET/CT design has been influenced by its use in oncology, which requires large-open devices with great sensitivity and spatial resolution. The bed had to be adapted for the combined system since it needed to minimize the vertical deflection caused by the patient's weight traverse the bore. Because the two fields of view are separated, if not rectified, the PET and CT images will be poorly aligned vertically, resulting in poor recording [24]. Figure 24 depicts a schematic representation of a PET/CT device.

Accuracy in PET and CT image recording is critical for properly visualizing combined images and performing attenuation correction. The discrepancy in PET and CT fields of view requires resampling to represent both integrated images as a single

square. Alpha mixing, a method that averages pixels to pixels and has a variable transparency factor ranging from 0 to 1, is widely used to depict recorded images on display monitors. However, this approach is ineffective when merging PET and CT greyscale images. The design of beds might cause misalignment; thus calibration is required for proper positioning and volume adjustment [24].

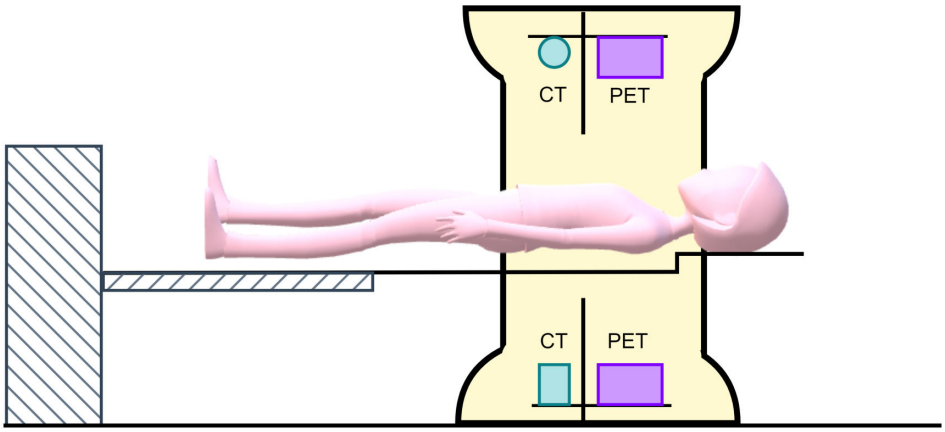

Figure 24: Representation of a PET/CT scanner. Source: Created by the author.

PET/CT devices provide multiple benefits over PET scanners alone, including improved image quality due to CT attenuation correction, automated registration of anatomic and metabolic information, and faster imaging times. In these devices, attenuation correction technology combines data from a CT system and PET scanning. CT X-rays have different attenuation properties than 511 keV radiation, however adjustments may be made to the attenuation map to calculate attenuation factors for each line of response. CT images offer greater anatomical information than radionuclide attenuation maps, making them useful for interpreting PET images. Moreover, CT offers faster acquisition time for attenuation correction compared to rotating positron emitting sources [48].

The combined PET/CT scanner used for attenuation correction of PET emission data avoids the requirement for a separate PET transmission scan. This approach reduces whole-body scan durations by at least 40% compared to traditional PET transmission measures. The attenuation values are energy dependent, thus the correction factors must be scaled to the PET energy of 511 keV. Scaling algorithms generally employ a bilinear function to transform attenuation values above and below a threshold using various factors. Because of its calcium and phosphorus concentration, bone tissue requires a distinct scale factor that reflects a water-cortical bone combination. The breakpoint between these two mixture types is 300 HU and 0 HU. The scale factor for air-water mixes below 100 HU is unaffected by the tube's kVp, but not for water-bone mixing. Scaled CT images are resampled from CT to PET voxel size, scaled pixel by pixel, and attenuation correction factors are generated by reprojection [51].

Finally, several factors, including dental plasters, metal implants, and contrast agents used in CT to emphasize anatomical features, can produce artefacts in PET

imaging. Discordance between CT and PET resulting from intentional and involuntary movements of the patient, such as breathing and movements of the myocardium and intestine wings, can also produce artefacts. It is advised to use certain breathing protocols with external signals to reduce these artefacts. Due to the absence of values for attenuation correction at the boundaries of PET's axial field of view, truncation artefacts are also produced by the disparity in axial fields of view between PET and CT. The PET scan shows these artefacts as an underestimate of the activity concentration in the afflicted region [24].

1.1.1.3.4.2 PET/MR

In the year 1990, PET/MR was introduced along with the proposal of PET/CT. PET/CT was more successful than PET/MR due to technological problems associated with merging the two technologies [52]. The technology of PET and CT imaging remains largely unchanged, with only the PET component modified to no longer offer a transmission scan. PET and MR scanners, however, cannot be combined in a single device. The primary challenge comes from the fact that conventional PET detectors are delicate to magnetic fields. Scintillation light is converted into electrical signals using photomultipliers; however, because of the intense magnetic field present in magnetic resonance imaging, these electronics need to be properly protected. Large forces would affect the homogeneity of the magnetic field, rendering MR imaging unfeasible even in the case of ferromagnetic shielding. The electronics used in PET signal processing are another problem that could negatively impact MR images. It is necessary to take additional measures to protect the PET electronics [29].

PET and MR data integration has been a source of debate for more than three decades, with the earliest practical implementations being independent systems linked by a shared rail system. These methods put the MR far enough away from the traditional PET to prevent interference. The truly integrated technique was first tested with avalanche photodiodes (APDs), which were unaffected by magnetic fields even at high field strengths. Siemens was the first to deploy APDs with lutetium oxyorthosilicate (LSO) crystals, initially as a "slide-in" PET insert for a standalone 3 T MR system, and then as a fully integrated device. General Electric followed with the SIGNA PET/MR system, which employs SiPM-based PET detectors to enable time-of-flight PET imaging with a time resolution of less than 400 picoseconds [53]. Figure 25 depicts a schematic representation of an integrated PET/MR device.

However, both vendors used a conventional 70-cm bore MR to surround a PET ring, decreasing the inner bore diameter to 60 cm and lengthening the scanner's length. This caused discomfort for patients and reduced the number of elegible patients for PET/MR scans. The greater part of PET/MR research has concentrated on PET inserts, such as the BrainPET insert for a 3T MAGNETOM Trio MR system and the brain PET/MR insert, which uses monolithic cerium-doped lutetium-based (LYSO) scintillation crystals and a retroreflector [53].

PET/MR has better soft tissue contrast than PET/CT, requires less radiation, and may be used on any area of the body. Low dose is potentially useful in small animal imaging for serial and longitudinal studies. PET/CT is limited by its sequential imaging design. The process includes acquiring CT data from two systems and correcting for attenuation using software modules. However, mistakes may occur owing to patient mobility between acquisitions. In contrast, PET/MR uses MR data to account for motion. As a result, the PET/MR proves to be effective in a variety of clinical and preclinical applications with strong benefits. Clinical applications in the fields of neurology, cardiology, cancer, and musculoskeletal disorders have advanced significantly [54].

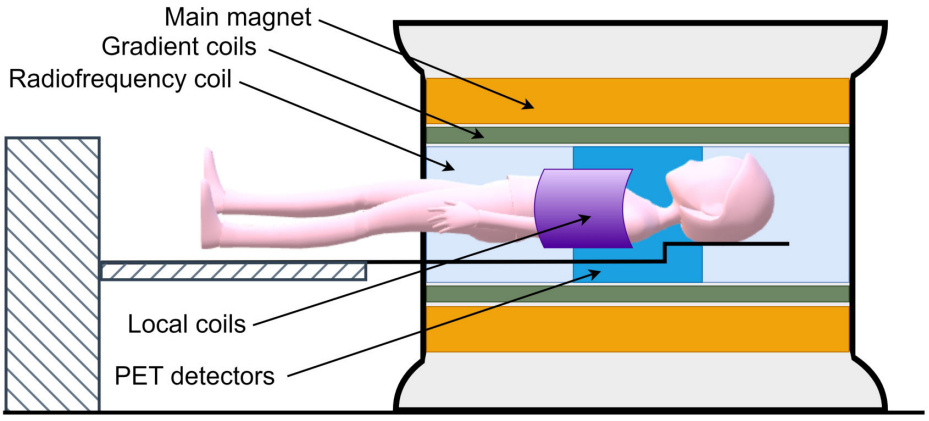

Figure 25: Representation of an integrated PET/MR scanner. Source: Created by the author.

Compared to PET/CT, PET/MR is a newer system that has several benefits. Because it lacks ionizing radiation, it may be used for pediatric imaging, which makes it suitable for ongoing therapy progress monitoring. With its superior soft-tissue contrast and ability to control tissue contrast using different imaging sequences, MR provides a superior method of imaging complex heterogeneous tissue environments, such as the liver and brain, without the need for a contrast substance. With its superior functional and molecular imaging capabilities, both MR and PET can provide more thorough physiological and pathological data at the cellular and molecular levels. Furthermore, simultaneous data acquisition by PET/MR enables the observation of anatomical, metabolic, and molecular information at the same time [55].

Attenuation correction is critical for producing reliable PET data. However, concerns regarding PET/MR's clinical effectiveness emerged with the introduction of PET/CT. To generate an estimated attenuation map, an MR-image-based technique was designed involving the use of the Dixon sequence and segmentation. The Dixon sequence differentiates between fat and water signals, which are then used to create attenuation maps of four compartments: fat, soft tissue, background air, and lungs. Bone is excluded from this notion because of its difficult segmentation from MR data. Dixon-based AC established the basis for PET/MR AC methods. Dixon AC, on the other hand, has enabled faster data collection, increased spatial resolution, and respiratory gating. Hardware modifications were necessary for the new PET/MR systems.

Examples include the patient bed and stationary coils, which have been adjusted to reduce their attenuating properties. Unfortunately, the added hardware contributes negatively to the PET image quality [53].

Another drawback of PET/MR regarding attenuation correction is that it faces limitations for clinical acceptance and inclusion in trials. They cannot be validated in the same way as PET/CT scanners, which are typically performed by scanning standardized phantoms filled with a radioactive mixture with water. This method works well for PET/CT scanners because the linear attenuation coefficient of water is close to that of soft tissue. However, PET/MR scanners cannot accurately acquire these phantoms due to the difficulty of converting MR images of physical structures into electron density maps. The transverse relaxation time of protons in phantom materials is too short to capture conventionally, leading to little measurable signal in almost all types of MR pulse sequences. Despite progress in manufacturing phantoms capable of mimicking electron density and contrast characteristics of human tissue, there are currently no phantoms available to evaluate the performance of multiple MRAC techniques. Additionally, water-filled phantoms, a key pillar in the accreditation of PET scanners, produce resonance artifacts in MR images, meaning that while standard phantoms accurately replicate PET and CT imaging physics for patients, the same is not true for MR [56].

Recent improvements and the clinical application of PET/MR indicate that it will most likely find a role in hybrid imaging. Current MR technology has matured, but more research is needed to examine the possibility of multiparametric imaging, such as combining DCE, DWI, and MRS with PET to determine therapeutic response in malignant diseases. Hyperpolarized MR and specific MR contrast agents, such as ultrasmall iron oxide particles, provide additional possibilities. PET/MR might potentially improve imaging of moving tissues like the liver and heart, with more options for MR-based motion correction of PET data. However, developing PET/MR techniques based on radiotracers is critical for novel applications, particularly in oncologic and neurologic imaging. Translational research should be a significant focus of development in laboratories across the world to prove beneficial for daily patient care [57].

1.1.1.3.5 Dedicated PET scanners

Over the last 70 years, there has been a substantial evolution in PET technology, with advances in sensitivity and spatial resolution resulting in a wider clinical application. On the other hand, fabrication costs determine accessibility and worldwide availability. Only 109 nations have access to PET technology, according to the International Atomic Energy Agency, and at least 96 nations must install more PET/CT scanners in order to treat prevalent cancer types. Dedicated or organ-specific PET scanners are suitable for small clinics in high-income countries as well as low- and middle-income nations due to their satisfactory performance and low production costs [58, 59].

The demand for detecting and measuring changes in metabolic pathways is growing, especially for evaluating neurological conditions. There is also a need to improve whole-body PET systems, particularly in spatial resolution and sensitivity to image small structures. As a result, dedicated PET devices have been developed. These systems are much smaller and less expensive than traditional whole-body PET scanners. These systems are also significantly smaller and less expensive than traditional whole-body PET devices. Thus, dedicated systems appear to be a good fit for PET clinical practice [60].

Conventional or multipurpose PET scanners are designed for nearly all clinical uses, including as brain, heart, prostate, breast, and static wholebody scans, as well as absorbed dose verification for heavy-ion radiation treatment [61, 62].

A brief history of the development of dedicated and irregular PET scanners is shown in Figure 26. The history of dedicated PET systems began in 1953, when Dr. Brownell and Dr. Aronow designed and developed the first dual-head PET scanner. In 1969, Dr. Brownell developed the first PET scanner featuring two planar arrays of crystals. In this innovative design, the patient was positioned between the two detectors, marking a significant improvement in imaging technology. By 1974, Dr. Ter-Pogossian had built the first positron emission tomography (PETT) scanner. This scanner employed a hexagonal array of NaI scintillation detectors arranged around a single transaxial plane, further advancing the field of medical imaging. The year 1979 saw the development of the first commercial emission computerized axial tomograph (ECAT), which also utilized a hexagonal array of detectors. In 1990, the University of Geneva in Switzerland developed the PRT-1, a rotating PET scanner. This low-cost design used two opposing BGO block detectors that rotated around the patient to acquire a full 3D image, reducing the number of detectors by 40% compared to a full ring scanner [59].

By 2006, a dedicated prostate PET scanner had been introduced, featuring a pair of external curved detector modules. These modules could adjust their distance to position the detectors as closely as possible to the patient, enhancing sensitivity for patients of various sizes. In 2007, the HOTPET scanner was developed. This versatile PET system could change its axial field of view (AFOV) and transverse field of view (TFOV), allowing it to transform from whole-body mode to brain or breast mode. The PEMi, a dedicated breast PET scanner with a polygonal structure and LYSO crystal arrays mounted on a position-sensitive photomultiplier, was developed in 2009. In 2011, the PET-HAT was introduced as a low-cost, wearable brain PET scanner. Its mechanical supports allowed the detector ring to scan subjects with freedom of motion. 2016 saw the development of the helmet-chin PET geometry, which consisted of a hemispheric-shaped detector and a chin detector. This design increased sensitivity, improving the quality of brain imaging [59].

By 2018, a dedicated brain PET system with a dodecahedral geometry and 11 regular pentagon detectors was introduced. This system increased overall sensitivity

by a factor of 4.91 compared to cylindrical brain PET systems. Additionally, Dr. Cherry and Dr. Badawi created the first clinical total body PET scanner, marking a significant milestone in PET technology. In 2019, the CareMiBrain, a dedicated cylindrical brain PET based on monolithic crystals, was developed. This design aimed to enhance imaging for neurological applications. The ProsPET scanner, introduced in 2020, was dedicated to prostate imaging. It featured monolithic LYSO and two movable parts that could open and close. Finally, in 2022, the Active-PET scanner was developed. This multifunctional PET scanner included two different types of detector modules and a mechanical jack for repositioning the detectors. This flexibility allowed the implementation of various geometries and configurations [59].

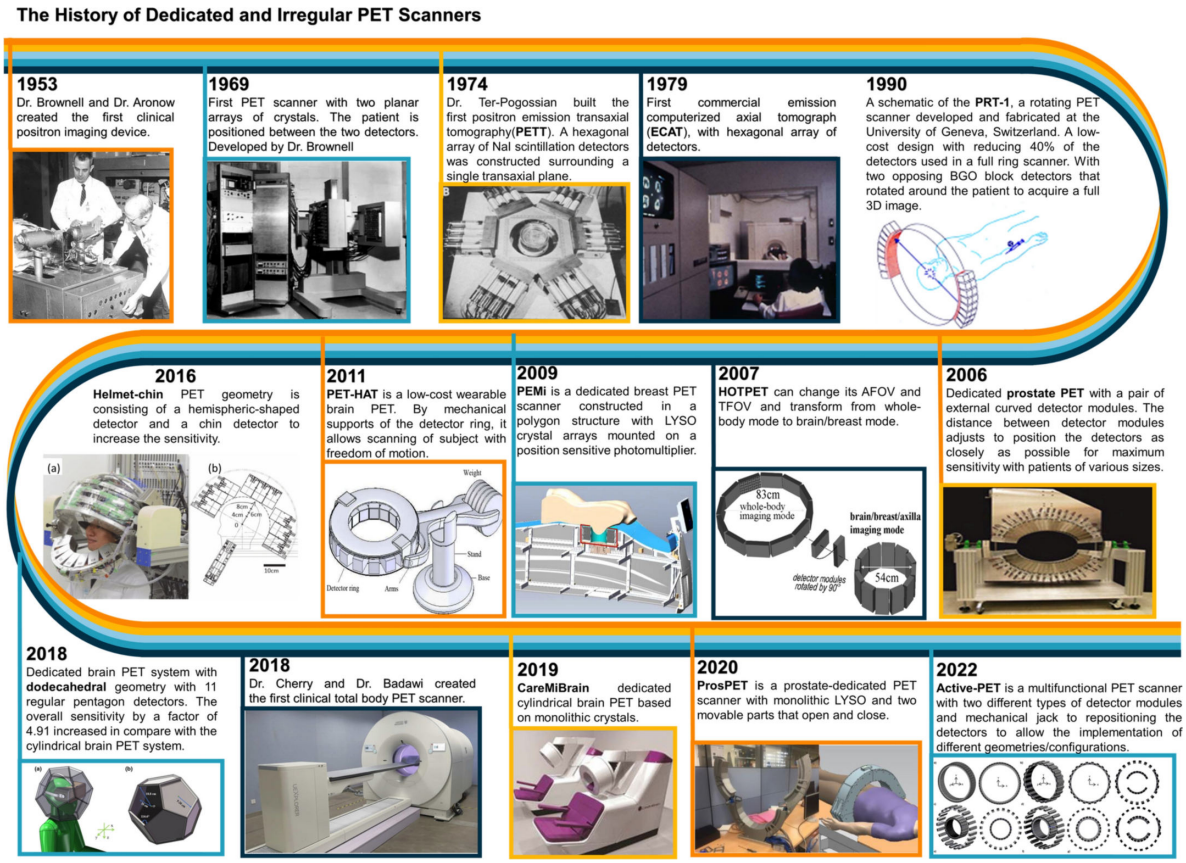

Figure 26: The history of dedicated and irregular PET scanners. From *"The quest for multifunctional and dedicated PET instrumentation with irregular geometries"* by Amirhossein Sanaat, Mehdi Amini, Hossein Arabi, and Habib Zaidi. 2023. Page 22. Copyright by Springer.

Regarding attenuation correction in these devices, a major issue is that dedicated PET systems do not often incorporate a CT scanner that can generate attenuation maps. The non-use of the CT, along with a considerable improvement in sensitivity, can result in a reduction in the radiation dose received by patients. Nonetheless, the effect of attenuation not being corrected is visible in the final images as a systematic distortion that leads to an overestimation of peripheral structures in comparison to internal ones if attenuation is present. It also causes considerable problems in areas of

varying density, where the existence of lesions might be ignored [60].

Consequently, AC is crucial for both quantitative accuracy and image quality in PET. Thus, developing a viable and stable approach for accurate AC is a special issue for brain-dedicated PET that lacks CT or an emission source system. As a result, several research projects have presented methods for estimating attenuation maps [63–65]. In the next subsection (1.2.2), more information about brain-dedicated PET scanners is provided.

1.1.2 Medical Data Communication

Hospitals are becoming more digitalized, with the goal of achieving a paperless environment to streamline processes and workflows. A hospital's fundamental components include the hospital information system (HIS), radiology information system (RIS), picture archiving communication system (PACS), clinical information system (CIS), cardiovascular information systems (CVIS), and electronic health record (EHR). These systems are supposedly integrated within the hospital to guarantee that the patient's health records are accurate, correct, and up to date [66].

However, the imaging procedures in the radiology and nuclear medicine departments require a comprehensive system since medical images cannot be handled in the same way that other hospital data can. Furthermore, medical images require routing, storage, and access, demanding the development of a specialized system such as a PACS to locate, archive, and process images from one or more sources. The primary goal of the system is to improve image routing, retrieval, and display capabilities inside a healthcare facility [66].

PACS and DICOM

PACS stands for picture archiving communication system are image repositories designed to allocate digital medical imaging [67]. It consists of:

- Connections to modalities: integrates several imaging modalities, including X-ray, MR, CT, ultrasound, PET, SPECT, and other comparable technologies.
- Digital image archives: where the acquired images are stored.
- Workstations: where radiologists and nuclear medicine physicians view ("read") images.

Almost every professional who works with images in the healthcare industry is currently employing or will soon make use of Digital Imaging and Communications in Medicine (DICOM), which is an international standard for all medical imaging modalities. This imaging standard easily addresses the integration of data connected by multiple speciality applications into the patient's EHR, which stores patient's medical history, treatment data, and health status. It replaces traditional paper-based medical

records, allowing for more effective coordination of healthcare service providers, better patient care, and fewer medical mistakes and expenses [68].

The DICOM Standards Committee is in charge of maintaining worldwide standards for communicating biological diagnostic and therapeutic information in fields that rely on digital images and related data [69]. It emerged quickly in answer to a specific demand. Historically, medical physicists and computer scientists in radiology focused on complex image processing techniques. The scientific community had expressed a strong interest in automated analysis of medical images to improve diagnosis [70].

In response to the development of computer-aided imaging in the 1970s, the American College of Radiology (ACR) and the National Electrical Manufacturers Association (NEMA) formed a joint committee to establish the standard. They originally released an ACR-NEMA standard in 1985, which was modified in 1988. Version 3 was launched in 1993, with the name changed to DICOM. The standard currently incorporates all types of medical images as well as other data such as patient name, reference number, study number, dates, and reports. Most manufacturers follow the standard, and data transmission issues are far less common than in the past. The DICOM standard (ISO 12052) allows medical images to be transferred to and from software and scanners by different manufacturers, and it has facilitated the development of image archiving and communication systems that can be integrated with larger medical information or records systems [71].

Contrary to common misconception, DICOM is not only an image or file format. It is an all-encompassing data transfer, storage, and display protocol meant to cover all functional elements of modern medicine [67]. The goal of DICOM is to facilitate compatibility and increase workflow efficiency between imaging equipment and other information systems in healthcare settings worldwide. Currently, nearly all diagnostic medical imaging manufacturers have implemented the standard into their product design, and the majority are actively working to improve the standard. Every member has the ability to suggest modifications to the standard, which are then considered for inclusion in future versions [69].

Without a doubt, DICOM controls actual digital medicine. Taking everything into consideration, DICOM revolutionized modern medicine by defining a universal standard for digital medicine, ensuring high image quality, supporting multiple image acquisition parameters and data types, encoding medical data, and clearly describing digital imaging devices and their functionality which is the backbone of any medical imaging project [67].

Clinical data comes in a wide range of formats. The standard provides 27 fundamental data types, known as value representations (VRs), which are intended to cover all potential clinical data types. Anything written (encoded) in DICOM must be one of these 27 types. Each VR has an abbreviated two-letter name, a definition of what it represents, a description of the characters that can be used in its data, and a specified

data length [67]. Tables 4 and 5 list the 27 DICOM VRs.

The DICOM Data Dictionary uses these data types to encode all standard DICOM attributes. The DICOM Data Dictionary is a registry of standard data items (attributes) employed in digital medicine, formatted into the 27 VR types. In addition to the standard dictionary, DICOM vendors can create their own dictionaries for proprietary data attributes. In any instance, the dictionary construction will follow the same standards [67]. Table 6 depicts some of the most used DICOM Data Dictionary items in PET imaging.

Every item in the DICOM Data Dictionary is identified by its own (Group, Element) number, commonly known as an element tag. These tagged items are also known as attributes or DICOM data elements. The column "Attribute name" describes the real-world data that should be stored in the element. All DICOM applications relate to data elements using (Group, Element) tags rather than descriptive attribute names. The "Keyword" column contains descriptive element tags, which are textual equivalents to the (Group, Element) pairs used in XML, HTTP, and other text-based standards. Finally, the Value Multiplicity (VM) of a data element specifies whether it may contain only one or many values of its type. DICOM concatenates many values into one single multi-value value, which can be binary (with binary VRs) or text (without set sizes). The backslash (\) in DICOM represents "or" in multi-value attributes [67].

Standardization is an important concept in the digital image field. The lack of a standard limits the use and sharing of images. It demands users to deal with a wide range of data types and transform them from one to another. In addition to pixel data, every image file contains metadata, which describes an image and has a non-secondary purpose in digital imaging. Metadata, in scientific formats can describe the subject, the instrumentation setup, the image acquisition parameters, and any other aspect of the imaging workflow that is relevant. Beyond revolutionizing clinical practice, the DICOM standard has fostered and enabled data exchange among researchers, adding value to research [72].

Table 4: Value Representations (VR) of DICOM (part I). From *Digital Imaging and Communications in Medicine (DICOM)*. Oleg S. Pianykh. Springer, 2012.

Short VRs	Full VRs	Description
CS	Code String	A string of characters with leading or trailing spaces being non significant. Example: "CD123_4"
SH	Short String	A short character string 16 maximum. Example: telephone numbers, IDs
LO	Long String	A character string that may be padded with leading and/or trailing spaces 64 maximum. Example: "Introduction to DICOM"
ST	Short Text	A character string that may contain one or more paragraphs.
LT	Long Text	A character string that may contain one or more paragraphs – same as LO, but can be much longer.
UT	Unlimited Text	A character string that may contain one or more paragraphs, similar to LT.
AE	Application Entity	A string of characters that identifies a device name with leading and trailing spaces being non-significant 16 maximum. Example: "MyPC01"
PN	Person Name	Person's name, with a caret character (^) used as name delimiter 64 maximum. Example: "SMITH^JOHN"
UI	Unique Identifier (UID)	A character string containing a UID that is used to uniquely identify a wide variety of items. Example: "1.2.840.10008.1.1"
DA	Date	A string of characters of the format YYYYMMDD; where YYYY shall contain year, MM shall contain the month, and DD shall contain the day. Example: "20050822"
TM	Time	A string of characters of the format HHMMSS.FFFFFF; where HH contains hours (range "00"–"23"), MM minutes (range "00"–"59"), SS seconds (range "00"–"59"), and FFFFFF contains a fractional part of a second as small as 1 millionth of a second. Example: "183200.00" stands for 6:32 PM

Table 5: Value Representations (VR) of DICOM (part II). From *Digital Imaging and Communications in Medicine (DICOM)*. Oleg S. Pianykh. Springer, 2012.

Short VRs	Full VRs	Description
DT	Date Time	Concatenated date-time string in the format: YYYYMMDDHHMMSS. FFFFFF&ZZXX. The components of this string, from left to right, are YYYY = Year, MM = Month, DD = Day, HH = Hour, MM = Minute, SS = Second, FFFFFF = Fractional Second; &ZZXX is an optional suffix for offset from Coordinated Universal Time (UTC), where & is either "+" or "−", and ZZ = Hours and XX = Minutes of offset. Example: "20050812183000.00" stands for 6:30 PM, August 12, 2005
AS	Age String	A string of characters with one of the following formats: nnnD, nnnW, nnnM, nnnY; where nnn contains the number of days for D, weeks for W, months for M, or years for Y. Example: "018 M" would represent an age of 18 months.
IS	Integer String	A string of characters representing an integer.
DS	Decimal String	A string of characters representing either a fixed point number or a floating point number.
SS	Signed Short	Signed binary integer 16 bits long
US	Unsigned Short	Unsigned binary integer 16 bits long
SL	Signed Long	Signed binary integer
UL	Unsigned Long	Unsigned binary integer 32 bits long
AT	Attribute Tag	Ordered pair of 16-bit (2-byte) unsigned integers that is the value of a Data Element Tag
FL	Floating Point Single	Single precision binary floating point number
FD	Floating Point Double	Double precision binary floating point number
OB	Other Byte String	A string of bytes ("other" means not defi ned in any other VR)
OW	Other Word String	A string of 16-bit (2-byte) words
OF	Other Float String	A string of 32-bit (4-byte) floating point words.
SQ	Sequence of Items	Sequence of items.
UN	Unknown	A string of bytes where the encoding of the contents is unknown.

Table 6: Example of some DICOM Data Dictionary items.

Tag	Attribute name	Keyword	VR	VM
(0008,0020)	Study Date	StudyDate	DA	1
(0008,0021)	Series Date	SeriesDate	DA	1
(0008,0022)	Acquisition Date	AcquisitionDate	DA	1
(0008,0030)	Study Time	StudyTime	TM	1
(0008,0031)	Series Time	SeriesTime	TM	1
(0008,0032)	Acquisition Time	AcquisitionTime	TM	1
(0008,0033)	Content Time	ContentTime	TM	1
(0008,0050)	Accession Number	AccessionNumber	SH	1
(0008,0060)	Modality	Modality	CS	1
(0008,103E)	Series Description	SeriesDescription	LO	1
(0010,0010)	Patient's Name	PatientName	PN	1
(0010,0020)	Patient ID	PatientID	LO	1
(0010,0030)	Patient's Birth Date	PatientBirthDate	DA	1
(0010,0040)	Patient's Sex	PatientSex	CS	1
(0010,1030)	Patient's Weight	PatientWeight	DS	1
(0018,0050)	Slice Thickness	SliceThickness	DS	1
(0018,1071)	Radiopharmaceutical Volume	RadiopharmaceuticalVolume	DS	1
(0018,1072)	Radiopharmaceutical Start Time	RadiopharmaceuticalStartTime	DS	1
(0018,1074)	Radionuclide Total Dose	RadionuclideTotalDose	DS	1
(0018,1075)	Radionuclide Half Life	RadionuclideHalfLife	DS	1
(0018,9758)	Decay Corrected	DecayCorrected	CS	1
(0018,9759)	Attenuation Corrected	AttenuationCorrected	CS	1
(0018,9760)	Scatter Corrected	ScatterCorrected	CS	1
(0018,9761)	Dead Time Corrected	DeadTimeCorrected	CS	1
(0018,9765)	Randoms Corrected	RandomsCorrected	CS	1
(0028,0030)	Pixel Spacing	PixelSpacing	DS	1
(0028,1052)	Rescale Intercept	RescaleIntercept	DS	1
(0028,1053)	Rescale Slope	RescaleSlope	DS	1
(7FE0,0010)	Pixel Data	PixelData	OB or OW	1

1.2 Dementia

Dementia presents as a global epidemic caused by a growing elderly population. It has been defined by persistent deterioration of brain functions, including memory, orientation, calculation, language, and spatial perception. This degeneration results in a loss of autonomy for the patient as well as a negative impact on their social, work, and leisure activities. Dementia is an important cause of dependency and incapacity among the elderly, resulting in enormous economic, social, and health costs for family members. Globally, over 50 million people suffer with dementia. According to a 2016 Alzheimer's Disease International report, this figure continues to grow and without appropriate treatment, the number is expected to rise to 131 million by 2050 [73].

Dementia is widely recognized as a major public health issue that requires early detection, effective treatment, and prognosis assessment [74]. Given this urgent necessity, brain-dedicated devices are crucial for addressing neurodegenerative diseases. Dedicated brain PET scanners aim to outperform whole-body scanners by improving spatial resolution and sensitivity, enabling imaging of smaller brain regions. Dedicated PET scanners improve device portability, mobility, and cost efficiency [75].

Most common neurodegenerative diseases

Approximately 70% of dementia cases are linked to Alzheimer's disease. The most common causes of dementia after Alzheimer's disease are Dementia with Lewy Bodies (DLB) and Frontotemporal Degeneration (FTD) [76].

Alzheimer's disease is a progressive neurodegenerative disease most typically characterized by initial memory impairment and cognitive decline that can progressively impact behavior, speech, visuospatial orientation, and the motor system. It is the most prevalent form of dementia [77].

The preclinical and prodromal phases of Alzheimer's disease can last up to 20 years, with an average clinical course of 8-10 years. There are currently no treatments available to reverse the disease's course. The risk of developing Alzheimer's disease is varied. Preventable risk factors include type 2 diabetes, hypertension, smoking, sedentary lifestyle, obesity, and head injuries. Nonpreventable risk factors include age and genetics. The e4 allele for apolipoprotein E (ApoE), detected in 60% of individuals with Alzheimer's disease, is the leading genetic cause. One e4 allele triples the risk of Alzheimer's disease compared to non-carriers, whereas homozygous for the e4 allele raises the risk sevenfold [78].

AD is mainly characterized by the pathological accumulation of amyloid-β (Aβ) plaques and tau neurofibrillary tangles [77]. Plaques begin to accumulate 10-20 years before clinical impairment [79]. These changes cause neuronal dysfunction and death, followed by atrophy of selectively sensitive brain networks and the emergence of clin-

ical symptoms such as cognitive impairment. Depending on which brain regions and networks are compromised, AD can manifest as a variety of clinical syndromes, including the typical amnestic syndrome, posterior cortical atrophy, a frontal/dysexecutive syndrome, and the logopenic variation of primary progressive aphasia [80].

Frontotemporal Dementia is a group of neurodegenerative illnesses characterized by altered conduct and language, as well as a progressive decline in executive function. FTD is the second most prevalent form of younger-onset dementia after Alzheimer's disease, with most cases occurring before the age of 65 [81, 82].

FTD can be defined by focal cerebral atrophy, primarily affecting the frontal, front parietal, and temporal regions. To varying degrees, all of the clinical and pathological phenotypes share a non-Alzheimer-type histological profile. Approximately 25-50% of FTD is familial, indicating a significant hereditary contribution to these diseases. Three important genetic loci have been identified: two on chromosome 17, one associated to the tau gene and the other to progranulin, and one on chromosome 9, linked to RNA regulation [83].

FTD is clinically classified into three subtypes: behavioral-variant frontotemporal dementia and two language variants, semantic dementia (also known as semantic variant primary progressive aphasia) and progressive non-fluent aphasia. FTD overlaps with two additional categories of movement disorders: progressive supranuclear palsy and corticobasal degeneration. Behavioral-variant frontotemporal dementia is the most frequent form of FTD, characterized by a variety of symptoms such as disinhibited behavior, apathy, increased consumption of sweet foods and alcohol, loss of empathy and emotional processing, and impairment of executive function. Semantic dementia is defined by a loss of semantic knowledge, which usually manifests as progressive anomia in the setting of fluent expressive speech. Progressive nonfluent aphasia, on the other hand, is distinguished by effortful and distorted speech, with or without agrammatism, yet preserving comprehension [84].

Individuals with **Dementia with Lewy bodies** exhibit Lewy bodies in both the cortical and subcortical areas. Lewy bodies are intracellular structures made up mostly of α-synuclein and ubiquitin. Patients with DLB also have different levels of amyloid plaque pathology and, to a lesser extent, tau pathology. DLB, like Alzheimer's disease, is identified by widespread neurone degeneration. However, unlike Alzheimer's disease, DLB also causes neuronal death in the substantia nigra [83].

Parkinson's disease dementia and dementia with Lewy bodies overlap similar symptoms, and many people consider they are on the same spectrum, however some claim that they involve different anatomical circuits.DLB and Parkinson's disease are caused by α-synuclein Lewy body inclusions in neurons in the cortex, brainstem, and substantia nigra. The fundamental distinction between Parkinson's disease and DLB is the the period of symptom emergence: development of cognitive symptoms before or within the same year as the onset of motor symptoms. Requires a diagnosis of

DLB, and motor symptoms that occur at least a year before cognitive decline suggest a Parkinson's disease diagnosis. DLB is characterized by increasing decline in executive and visuospatial abilities, as well as memory, which typically occurs later in the disease. Other fundamental and associated characteristics include cognitive fluctuations, visual hallucinations, neuroleptic sensitivity, and REM sleep behavior disorder [80].

Mild Cognitive Impairment

Mild cognitive impairment (MCI) can be described as cognitive impairment that exceeds that seen with normal age-related cognitive decline but is not severe enough to seriously limit daily function. Clinically, age-related cognitive decline refers to memory and cognition changes associated with normal ageing. While learning and memory, social functioning, language, visuospatial function, complex attention, and executive functioning are the six primary cognitive domains that may be affected, MCI typically refers to a decline in the capacity to learn new information or retrieve previously learnt information [85].

Mild cognitive impairment is considered a transitory state between ageing and dementia. Since memory loss is a common complaint in MCI and an essential feature of AD, MCI research aims to identify individuals who are likely to develop Alzheimer's disease and those who will not. The potential for pharmacologic intervention to slow or prevent development to Alzheimer's disease has generated interest in MCI. Patients with MCI may remain stable or progress to dementia. MCI is diagnosed based on memory impairment, general cognitive and functional abilities, and absence of dementia [86, 87].

1.2.1 Diagnosis of neurodegenerative diseases

It is frequently clinically difficult to identify dementia patients who present with MCI on an early stage. An accurate diagnosis might not be determined until after the individual's health has clear signs of deterioration. Due to the huge amount of patients with MCI, being able to identify and categorise dementia in its early stages would help lower the cost of long-term care by enabling more knowledgeable decisions regarding clinical interventions and treatment planning [88].

Recent advancements in diagnostic testing have improved the detection of dementia patients in the MCI stage. Currently, MCI is diagnosed with a complete neuropsychological evaluation (cognition and function) and imaging (FDG-PET, MR). If objective cognitive impairment is identified, the amyloid status shall be determined. To find out whether MCI patients are at risk for Alzheimer's disease, biomarkers in cerebrospinal fluid (CSF) or fibrillary amyloid retention using amyloid PET can be measured. AD is the leading cause of dementia and patients with impaired CSF biomarkers have an increased risk of developing AD. CSF sample has some drawbacks, including being invasive, causing discomfort for patients, and having probable side effects. There-

fore, combining imaging diagnosis with neuropsychological examination may offer a minimally invasive method for detecting MCI caused by AD or other neurodegenerative diseases, such as frontotemporal dementia or dementia with Lewy Bodies [89–92].

Neuropsychological evaluation

The neuropsychological evaluation usually includes a global dementia rating (CDR), a general mental state (MMSE), and a battery of different cognitive domains (RBANS), functionality and emotion recognition.

The Clinical Dementia Rating is a global rating test that accurately distinguishes between older individuals with different degrees of cognitive function, from healthy to severely impaired [93]. CDR evaluates the severity of dementia. Experienced neuropsychologists use a semi-structured interview protocol with patients and proper informants. The CDR assesses cognitive and functional performance in six categories (memory, orientation, judgement and problem-solving, community affairs, home and hobbies, and personal care). The global score categorises dementia symptoms into five levels: normal cognition (CDR=0), very mild (CDR=0.5), mild (CDR=1), moderate (CDR=2), and severe (CDR=3) [94, 95].

The Repeatable Battery for Assessment of Neuropsychological Status (RBANS) assesses five cognitive domains. The RBANS is a structured battery of 12 subtests that examine five domains: immediate memory (RBANS.IM), visuospatial/constructional (RBANS.V/C), language (RBANS.L), attention (RBANS.A), and delayed memory (RBANS.DM). The domain scores are based on typical scores ($\leq$85 indicates a deficiency). The total score is calculated by adding the five index scores (RBANS.SI) [95, 96].

The Mini-Mental State Examination (MMSE) evaluates cognitive impairment and severity. The MMSE has a total score range of 0 to 30, with higher scores indicating greater cognitive function. A total score of 21-26 on the MMSE indicates MCI, while a score of 27 or higher indicates normal cognition [95, 97].

Cerebrospinal fluid biomarkers

CSF biomarkers include Aβ and Tau levels. Findings can be detected 15-20 years before symptoms appear. The AD CSF profile (low Aβ-42 and high T-tau and P-tau) is 85% to 90% sensitive and specific for AD. Aβ-42 is an amyloid-β marker, while T-tau is a neuronal damage marker. Low Aβ-42 levels can signal future cognitive deterioration. High T-tau levels indicate severe neuronal damage. High P-tau levels are linked to rapid clinical deterioration and hippocampus shrinkage [98].

However, for individuals with MCI who have a low risk of developing neurodegenerative dementia, CSF, which is acquired via lumbar puncture, is an invasive procedure that should not be used [78, 99].

Use of PET

Functional neuroimaging is a valuable method for diagnosing Alzheimer's disease and other non-Alzheimer's dementias. It aids in differential diagnosis and personalized treatment [100]. Brain metabolism can be measured noninvasively using Positron Emission Tomography. Even in the early stages, when the patient only exhibits MCI, it has been used in the identification and diagnosis of neurodegenerative diseases [101].

Substantial research initiatives aimed at studying AD biomarkers, such as the large-scale Alzheimer's Disease Neuroimaging Initiative (ADNI) and the Imaging Dementia Evidence for Amyloid Scanning (IDEAS) research, have revealed that neuroimaging biomarkers improve clinical diagnosis in AD. In fact, current AD diagnostic criteria use neuroimaging as a biomarker, which improves the degree of diagnostic certainty that the clinical manifestation stands for underlying AD pathology [80].

Molecular imaging can identify biomarkers *in vivo*: amyloid PET can identify Aβ plaques and tau PET, NFT aggregates. MR and FDG-PET can detect neurodegeneration through volume loss and hypometabolism, respectively [102]. Amyloid PET and FDG-PET give complementing information in Alzheimer's disease, as the former measures the amount of amyloid plaques and the latter identifies metabolic disruption [100]. In this work FDG and Amyloid PET images were employed.

Amyloid PET imaging can quantify the abnormal accumulation of amyloid. Numerous multisite cohort studies have evaluated the clinical benefit of amyloid PET [103–105]. In the past, postmortem analysis of a person's brain tissue for Aβ plaques and neurofibrillary tangles, which consist primarily of hyperphosphorylated tau protein, was the only reliable method of diagnosing AD. Since the development of Aβ PET tracers, an important biomarker of AD can now be measured *in vivo* and quantified, potentially enabling a diagnosis to be made significantly earlier [106].

Amyloid PET has been extensively used in clinical research over the last decade to screen for treatment eligibility and assess target engagement for drugs that are intended for reducing amyloid plaques. This diagnostic imaging approach reliably reveals cerebral Aβ deposition and is highly specific for AD neuropathology. In clinical settings, it can aid in early differential diagnosis and patient selection for disease-specific treatment [107].

Pittsburgh compound B (PiB) labelled with C-11 was the first Aβ-specific PET tracer to be introduced to offer precise imaging data of Aβ pathology. Although [^{11}C]PiB can be useful in research settings, its broad applicability is constrained by C-11's brief half-life, which calls for radiochemistry and a local cyclotron [108, 109]. To facilitate clinical use, an F-18 (110-min half-life)-based Aβ tracer was developed, which can be given via an off-site cyclotron. Currently, the FDA and EMA have approved three F-18-labelled Aβ PET tracers for clinical use. These include [^{18}F]flutemetamol, [^{18}F]florbetapir, and [^{18}F]florbetaben [110, 111].

The recent FDA's approval of two drugs for Alzheimer's disease (aducanumab and lecanemab), which may be approved by EMA soon, has increased the need for amyloid brain PET-CT. The number of amyloid brain PET/CT studies is expected to increase by 20-fold [112]. PET/CT studies will be used not only to select patients for treatments, but also to guide therapy (e.g., determining treatment duration and dose, identifying participants who do not respond). Despite being acknowledged as the preferred tracer, amyloid PET's cost and accessibility may be an issue [113].

[^{18}F]FDG is the most widely used and accessible PET radiopharmaceutical. The potential of [^{18}F]FDG PET to identify neurodegenerative processes and provide information on the location and degree of neuronal dysfunction at an early stage supported its clinical use in the diagnosis of prodromal and dementia stages of the majority of neurodegenerative diseases [114]. Even while magnetic resonance imaging can be used to diagnose dementia, it is often limited because brain alterations may be too small to detect, particularly in the early stages of the disease [115].

The brain uses glucose as its primary energy source. It circulates in the blood and can pass the blood-brain barrier. Glucose is phosphorylated to release energy when needed. FDG, an artificial analogue of glucose, replicates its activity until phosphorylation. Phosphorylated FDG remains in tissue and is not metabolized further. The rate of FDG trapping is associated with glucose metabolism. Regional glucose consumption correlates with synaptic activity, while reduced FDG trapping (hypometabolism) indicates neuronal damage [106, 116].

The EANM-EAN (European Association of Nuclear Medicine and European Academy of Neurology) recommends using brain [^{18}F]FDG PET to identify the underlying neurodegenerative disorder in MCI conditions. This includes AD, FTD, and DLB [114].

In Alzheimer's disease, hypometabolism can occur prior to apparent atrophy. The temporoparietal, posterior cingulate, and medial temporal cortices are typically symmetrically hypometabolic. Frontotemporal dementia affects hypometabolic regions such as the frontal and front temporal lobes, cingulate gyrus, uncus, insula, basal ganglia, and medial thalamus. Hypometabolism is commonly asymmetric. Dopamine transporter imaging can distinguish between occipital hypometabolism in AD and dementia with Lewy bodies, as dopamine transport is reduced in Dementia with Lewi Bodies [106].

[^{18}F]FDG PET stands out because it is widely accessible, less costly, and useful for identifying different patterns of cortical hypometabolism in the early stages of neurological disorders. It has demonstrated diagnostic and prognostic utility in evaluating patients with cognitive impairment, and distinguishing between primary neurodegenerative diseases and other forms of cognitive impairment [117–119].

1.2.2 Brain-dedicated PET scanners

In the field of neurological science, the requirement for increased performance in comparison to whole-body devices, notably greater spatial resolution and higher sensitivity for imaging small brain regions, motivated the development of dedicated brain PET hardware. Physics limitations, detection systems, and image reconstruction methods can all be reduced in a dedicated brain scanner. The scanner's sensitivity is determined by solid-angle coverage and photon detection efficiency; decreasing the scanner's diameter and increasing the detector area can enhance sensitivity. Additional goals include increased portability, mobility, and wearability, as well as a lower cost of the scanner when compared to whole-body systems. The most obvious trade-off is between sensitivity and spatial resolution, as employing longer crystals might reduce the latter owing to parallax error unless detectors support depth-of-interaction (DOI) encoding [75].

Brain-dedicated scanners are needed, given the pressing for reducing the huge burden caused by neurological psychiatric diseases [112]. Several scanners designed specifically for studying the brain have been recently developed. The High-Resolution Research Tomograph (HRRT) [120], the jPET-D4 prototype scanner [121], the NeuroPET/CT scanner [122], the Hamamatsu [123], the BBX, PET-Hat [124], Helmet-PET [125], Mind-Tracker [126], NeuroLF [127], and CareMiBrain [128] are some of the brain-dedicated PET devices that have been developed in recent years. Figure 27 shows the progress in image quality for the 3D brain phantom from 1975 to 2022.

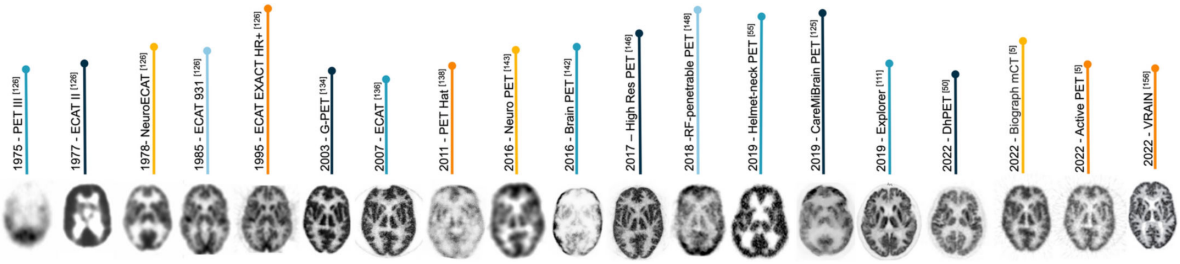

Figure 27: PET images of people or 3D Hoffman brain phantoms were obtained using various simulated or actual PET scanners, including conventional and irregular systems. From *"The quest for multifunctional and dedicated PET instrumentation with irregular geometries"* by Amirhossein Sanaat, Mehdi Amini, et al. 2023. Page 22. Copyright by Springer.

The figure illustrates how varied data acquisition and reconstruction techniques affected the images produced by these systems. Scanners with limited geometrical coverage, such as helmets and PET-hats, result in worse quality and fewer anatomical information. Insert PET scanners, such as RF-penetrable, can provide images that are blurred because to incorrect attenuation correction [59].

Brain PET scanners have shown improved performance compared to whole-body systems and provide more flexible designs for neuroimaging investigations. However, the

majority of these scanners were created in academic settings and are not commercially available. PET has been used to image neurodegeneration and has the potential to extend into other areas, such as imaging neurotransmitter function with high temporal resolution or metabolic processes. The development of machine learning approaches for artificially raising PET performance may move the attention away from improving dedicated brain PET hardware and towards overcoming some of PET's weaknesses [75].

1.3 Neuroendocrine tumors

Neuroendocrine tumors (NETs) represent a diverse group of neoplasms that primarily originate from endocrine cells found in the gastrointestinal tract, pancreas, and bronchial tree [129]. NETs are classified according to their level of differentiation and tumor grade. Well-differentiated NETs are further categorized into three groups: low-grade (G1), intermediate-grade (G2), and high-grade (G3), based on their mitotic rate and Ki-67 proliferation index. In contrast, poorly differentiated neuroendocrine carcinomas are always classified as high-grade (G3). The World Health Organization classification system is widely used for grading these tumors [130].

Paragangliomas (PGLs) and pheochromocytomas (PHEOs), collectively abbreviated as PGGLs, are rare neuroendocrine tumors originating from chromaffin cells of the adrenal medulla as well as from extra-adrenal sympathetic or parasympathetic ganglia, spanning from the skull base to the sacral region. Within this classification, the term PHEO specifically refers to a PGL arising from the adrenal medulla. Among PGGLs, approximately 80%–85% are PHEOs, while about 15%–20% are PGLs [131]. The majority (85%) of PGGLs associated with the sympathetic nervous system produce catecholamines, whereas parasympathetic PGGLs are largely non-secretory [132].

The annual incidence of PGGLs ranges between 1 and 2 cases per million, with 5%–20% of PHEOs and 15%–35% of PGLs presenting at an advanced stage. Around 5%–10% of cases are isolated, while the occurrence of metachronous or synchronous extra-adrenal PGLs is linked to either germline or somatic mutations. PGGLs exhibit a significant hereditary component, with 30%–40% of cases being associated with autosomal dominant germline mutations. The mutation type influences the phenotypic characteristics observed in imaging studies [132]. To date, 32 genes have been identified in relation to PGGLs. Among metastatic PGGLs, SDHx mutations are the most prevalent, appearing in 43%–71% of adults and 70%–82% of children, followed by VHL mutations (1%–13%). The combined occurrence of RET, NF1, TMEM127, and MAX mutations is reported to range between 1% and 11% [133].

The treatment of NETs typically involves a multidisciplinary approach. Surgery remains the preferred option for localized disease, offering the highest potential for a cure. However, for metastatic or inoperable cases, therapeutic options include somato-

statin analogs, peptide receptor radionuclide therapy (PRRT), targeted agents such as everolimus and sunitinib, as well as chemotherapy [134, 135]. The National Comprehensive Cancer Network (NCCN) guidelines provide a framework for NET management, emphasizing the necessity of an individualized treatment plan based on tumor characteristics, grade, and stage [130].

For patients with advanced disease, treatment aims to reduce tumor burden and manage symptoms. In this context, theranostic radiopharmaceuticals in nuclear medicine play a crucial role in personalized healthcare, enabling tailored diagnostic and therapeutic approaches. This advancement introduces a clinical challenge in selecting the most appropriate radionuclide therapy [136, 137]. To address this issue, nuclear medicine imaging techniques can provide phenotypic insights into tumor characteristics at the molecular and genetic levels, revealing the expression of specific receptors or transporters [138].

1.3.1 Theranostics

The term theranostics is a blend of the words *therapeutics* and *diagnostics*, denoting agents or techniques that integrate diagnostic imaging with targeted therapy [139]. This systematic fusion of targeted diagnostics and therapeutics aligns with the principles of personalized precision medicine, aiming to enhance patient outcomes [140, 141]. The diagnostic component of a theranostic compound serves to determine the presence and extent of a specific biological target within a given disease, including cancer, thereby identifying patients who are most likely to benefit from the associated therapeutic agent. This concept is particularly crucial due to the significant molecular heterogeneity observed within individual tumors, among cancers of the same type, and between primary tumors and their metastatic counterparts [142].

Nuclear medicine plays a crucial role in theranostics, particularly in oncology, where it is a key component in both clinical and research applications. Theranostics in nuclear medicine refers to the use of radioactive compounds for imaging biological processes based on the expression of specific disease-associated targets, such as cell surface receptors or membrane transporters. Subsequently, targeted agents are employed to deliver ionizing radiation precisely to tissues expressing these markers [143].

The foundation of nuclear medicine theranostics lies in combining radioisotopes with molecules that selectively bind to critical cellular pathways. This approach allows for both diagnostic imaging and therapeutic intervention using radiopharmaceuticals that interact with the same cellular structures and biological processes. Such paired diagnostic and therapeutic agents are termed theranostic pairs. Figure 28 shows a diagram of the theranostic strategy in nuclear medicine, highlighting both diagnostic and therapeutic components along with their corresponding radioisotopes and benefits. A well-established example of theranostic pairing in nuclear medicine is the management

of neuroendocrine tumors. In this context, ^{68}Ga-DOTA–based agents serve as the diagnostic component, while ^{177}Lu-octreotate functions as the therapeutic agent, both targeting somatostatin receptors (SSTR) [143].

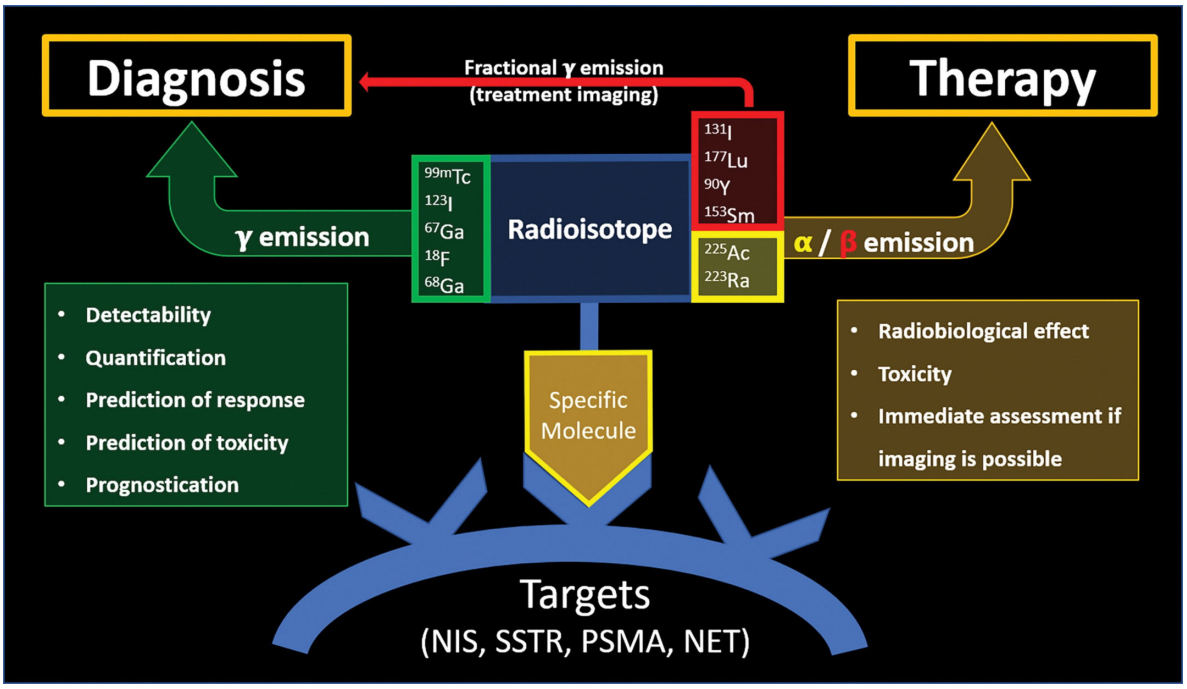

Figure 28: Diagram of the diagnostic and therapeutic components along with their corresponding radioisotopes and benefits. The radioisotopes include ^{225}Ac (actinium-225), ^{18}F (fluorine-18), ^{67}Ga (gallium-67), ^{68}Ga (gallium-68), ^{123}I (iodine-123), ^{131}I (iodine-131), ^{223}Ra (radium-223), ^{153}Sm (samarium-153), ^{99m}Tc (technetium-99m), and ^{90}Y (yttrium-90). Frequently targeted biological structures include NET (norepinephrine transporter), NIS (sodium iodide co-transporter), PSMA (prostate-specific membrane antigen), and SSTR (somatostatin receptor). From *"Theranostics in nuclear medicine: Emerging and re-emerging integrated imaging and therapies in the era of precision oncology"* by Marin, J. F. G., Nunes, R. F. et al. 2020. Copyright by RadioGraphics.

Theranostics has played a fundamental role in the field of nuclear medicine for many years, and the growing interest in theranostic pairings continues to expand as our understanding of relevant biological markers deepens and as advancements are made in the synthesis of targeted agents [144]. Since its inception with the use of radioiodine in thyroid disease, theranostics research and clinical applications have seen a remarkable increase. This progress is largely attributed to significant advancements in our comprehension of cancer biology and the refinement of strategies for designing and synthesizing targeted theranostic agents.

Radiotheranostics specifically refers to the application of radioactive substances within the theranostic paradigm [145]. Beyond radiotheranostics, which involves the use of radioactive materials, several alternative theranostic platforms exist, including nanotheranostics, optotheranostics, and magnetotheranostics [146, 147].

Somatostatin analog radioligands

In the past, the diagnosis and treatment options for neuroendocrine tumors were extremely limited. This was largely due to the rarity of these malignancies, which resulted in minimal market demand for targeted therapies and diagnostic tools. However, towards the end of the 20th century, significant advancements were made in understanding the biological and molecular properties of somatostatins. Over the last few decades, there has been a noticeable rise in the incidence of NETs, particularly gastroenteropancreatic neuroendocrine neoplasms, with cases increasing from 10.9 to 52.4 per million in the United States [148].

Somatostatin is an oligopeptide hormone naturally present in the hypothalamus, nervous system, pancreas, and gastrointestinal tract [149]. Somatostatin receptors, particularly the somatostatin subtype 2a receptor, belong to the G-protein coupled receptor family and are significantly overexpressed in neuroendocrine tumors, whereas their expression remains relatively low in most other tissues and organs [129]. SSTRs are found on various neuroendocrine-derived cells, including tumors, where somatostatin plays a crucial role in inhibiting cellular growth. The discovery that certain tumors overexpress SSTRs led to the development of radiolabeled somatostatin analogs for theranostic applications [145].

For SSTR imaging, ^{68}Ga, a positron-emitting radiometal, has been widely adopted due to its superior resolution and quantitative capabilities compared to ^{111}In [150, 151]. The early 2000s saw the introduction of ^{68}Ga-labelled SSTR analogs such as ^{68}Ga-DOTATOC, ^{68}Ga-DOTATATE, and ^{68}Ga-DOTANOC for PET imaging [151]. This innovation revolutionized the diagnosis, staging, and monitoring of neuroendocrine tumors. Compared to conventional imaging and scintigraphy, ^{68}Ga-labelled SSTR analogs provide superior image resolution, greater sensitivity, and improved specificity. These advantages have significantly enhanced clinical practice by increasing diagnostic confidence, reducing costs, shortening imaging times, expediting results, and minimizing radiation exposure for patients. As a result, the body of evidence supporting the superiority of SSTR PET imaging has grown exponentially [152], driving increased physician adoption and patient interest in this modality [153].

SSTR PET imaging is now recommended by multiple clinical guidelines and appropriate-use criteria established by multidisciplinary panels [154–156]. Clinical scenarios where SSTR PET is considered appropriate include:

- Initial staging of neuroendocrine tumors.
- Identification of unknown primary tumors.
- Evaluation of lesions suspected to be neuroendocrine but not suitable for biopsy.
- Assessment of patients with biochemical markers and symptoms suggestive of neuroendocrine tumors.

- Investigation of patients with biochemical evidence of neuroendocrine tumors but no detectable lesions on conventional imaging and no prior histologic confirmation.

The development of somatostatin analog radioligands has dramatically improved the diagnosis and treatment of neuroendocrine tumors. The introduction of ^{68}Ga-labelled PET tracers has particularly transformed imaging methodologies, improving accuracy and clinical efficiency. Among functional imaging techniques, PET scans utilizing somatostatin receptor (SSR)-targeting radiopharmaceuticals, such as [^{68}Ga]Ga-DOTA-TATE, DOTA-NOC, and DOTA-TOC, exhibit superior diagnostic accuracy compared to conventional imaging methods. This advantage arises from their strong affinity for SSRs and the high spatial resolution of PET imaging, which also enables the quantification of SSR expression [157, 158]. As research continues to refine these approaches, theranostic applications in nuclear medicine are expected to further enhance personalized oncology treatments [145].

Peptide receptor radionuclide therapy

Peptide receptor radionuclide therapy (PRRT) is an established theranostic approach, particularly for neuroendocrine tumors, which often express high levels of somatostatin receptors (SSTR) [159]. Initially, imaging of these receptors began in the late 1980s using radioiodine and later with ^{111}In [160]. PRRT with beta emitters was introduced in the 1990s, with subsequent studies confirming its efficacy [161].

A major breakthrough occurred in 1994 when the U.S. Food and Drug Administration (FDA) approved OctreoScan for imaging. It demonstrated significantly higher sensitivity and specificity for evaluating gastroenteropancreatic neuroendocrine tumors compared to conventional imaging techniques. In 1997, peptide receptor radionuclide therapy (PRRT) was first investigated using ^{90}Y-labelled DOTA, specifically ^{90}Y-DOTATOC. This study demonstrated the eradication of pancreatic neuroendocrine tumors in experimental rats [162].

Peptides offer several advantages as diagnostic and therapeutic agents, including ease of production, rapid clearance, efficient tissue penetration, and minimal antigenicity. These benefits supported the development of radiolabeled peptides, particularly somatostatin analogs, for oncologic applications [163, 164]. This progress facilitated the emergence of new imaging radiotracers and targeted PRRT strategies.

Today, PRRT has evolved into a well-accepted treatment paradigm for NETs affecting various organs, including the small bowel, pancreas, and lungs. The most commonly used therapeutic radionuclides for PRRT are ^{90}Y (half-life: 62.4 hours) and ^{177}Lu (half-life: 6.73 days). Both are beta emitters, with ^{90}Y offering a longer range for treating larger metastases and ^{177}Lu providing a shorter range to minimize off-target radiation. These agents allow direct dosimetry assessment by pairing diagnostic ^{68}Ga imaging with therapeutic beta emitters [145, 165].

The first-line pharmacological treatment for well-differentiated metastatic or inoperable neuroendocrine tumors that express somatostatin receptors consists of somatostatin analogs. These reduce the symptoms derived from hormonal hypersecretion and also have an antiproliferative effect. When the disease progresses under somatostatin analogs treatment, other systemic therapies are available, such as everolimus, sunitinib, cytotoxic chemotherapy, and peptide receptor radionuclide therapy. Among these, PRRT with [^{177}Lu]Lu-DOTA-TATE allows the selective administration of high doses of radiation to tissues that overexpress SSTR with minimal systemic toxicity [166].

In Spain, PRRT has been authorized since January 2018 by the Spanish Agency of Medicines and Medical Devices (AEMPS) under the name [^{177}Lu]Lu-DOTA-TATE (Lutathera®). It is indicated for patients with metastatic or inoperable gastroenteropancreatic neuroendocrine tumors that overexpress SSTR and are well-differentiated (G1 and G2) [166].

In the context of theragnosis, it is essential not only to detect lesions but also to accurately quantify their uptake intensity. The necessary condition for administering PRRT is the confirmation of a high expression of SSTR in functional imaging studies. To characterize uptake intensity in both SPECT/CT and PET/CT scans, the qualitative Krenning scale, with numerical values ranging from 0 to 4, is commonly used. This scale was initially described for planar SSTR scintigraphy but has later been validated for SSTR PET/CT. In the latter, uptake levels on the Krenning scale have been observed to be significantly higher than in planar imaging and SPECT/CT, especially for lesions smaller than 2 cm. The uptake intensity in functional SSTR imaging should be integrated with tumor size and extent to optimize candidate selection for PRRT [167].

Therefore, as with other tumors, a structured reporting system called the SSTR Reporting and Data System (SSTR-RADS) has been proposed for the theragnosis of NETs. This report correlates uptake intensity in functional SSTR imaging with lesion location (typical or atypical), findings from conventional imaging, and the presence or absence of prior biopsy. Patients with a Krenning scale score ≥ 3 and an SSTR-RADS score ≥ 4 are considered candidates for PRRT (see Table 7) [168].

Table 7: Krenning Scale for Uptake Intensity and Integrated SSTR-RADS Evaluation. Patients in the shaded region are candidates for PRRT based on SSTR expression. PRRT: peptide receptor radionuclide therapy; SSTR: somatostatin transmembrane receptors; SSTR-RADS: Somatostatin Receptor Reporting and Data System; NET: neuroendocrine tumors. From *"Terapia con péptidos radiomarcados con [^{177}Lu]Lu-DOTA-TATE."* by S. Prado-Wohlwend, J.C. Bernal-Vergara et al. 2022. Copyright by Revista Española de Medicina Nuclear e Imagen Molecular.

Krenning Score	**Uptake**	**SSTR-RADS**	**Findings**
0	Absent	1	Benign lesion confirmed by biopsy or imaging
1	Very low	2	Atypical soft tissue or bone lesion for metastatic NET
2	Slightly lower than or equal to hepatic uptake	3	Lesion with uncertain malignancy in soft tissue or bone (due to either questionable uptake, intense uptake in an atypical location, or a lesion suggestive of malignancy but without uptake)
3	Greater than hepatic uptake	4	Intense uptake in a typical NET location without findings in conventional imaging
4	Greater than splenic uptake	5	Intense uptake in a typical NET location with findings in conventional imaging

Chapter 2

HYPOTHESIS AND OBJECTIVES

The hypothesis of this Thesis is that the extraction and analysis of quantitative data from different PET image strategies provide meaningful information that impacts clinical decisions. This hypothesis will be tested in two clinical studies (dementia and neuroendocrine tumors).

The aim of this work is to improve clinical decision-making in the management of dementia and neuroendocrine tumors by extracting relevant data from quantitative PET images and analyzing their clinically useful information. This objective will be achieved through the use of harmonization methods, artificial intelligence with neural networks, and the comparison of image quality metrics.

Dementia is widely recognized as a major public health issue that requires early detection, effective treatment, and prognosis assessment. The dementia clinical study will cover two applications. The first will focus on improving the early diagnosis of neurodegenerative diseases, while the second will focus on reducing of the neurological burden of conventional PET/CT with a brain-dedicated PET scanner, ensuring that both systems provide similar image quality and diagnostic capability.

Regarding neuroendocrine tumors, in the context of theragnosis it is critical not only to detect the lesions, but also to accurately quantify their uptake intensity. If Peptide Receptor Radionuclide Therapy is contemplated, a sufficient level of uptake is necessary. Nowadays, different PET systems provide varying quantitative values depending on a variety of scanner parameters. Due to the increasing number of PET procedures, several hospitals house different PET devices in the same center. As the detection of the intensity in the expression of somatostatin receptors may have therapeutic implications, the purpose of this analysis will focus on ensuring consis- tent treatment recommendations for each lesion, irrespective of the image acquisition device after the variable harmonization between PET/CT and PET/MR scanners.

Chapter 3

MATERIALS AND METHODS

This section describes both the materials as well as the procedures, techniques, and analyses employed to achieve the objectives of this thesis. To this end, since this thesis involves distinct interventions, the organization of this section, as well as the subsequent Results and Discussion sections, will follow a structured framework based on the following points:

- Dementia
  - Diagnosis of neurodegenerative diseases
    - Relationship between quantitative neuroimaging and emotion recognition
    - Neural Network validation for Alzheimer's Disease prediction
  - Brain-dedicated PET scanner evaluation
    - Objective PET image quality evaluation
    - Evaluation of brain-dedicated PET diagnostic capability
- Neuroendocrine tumors
    - Harmonization for consistent treatment recommendations

3.1 Materials

3.1.1 Dementia

The dementia study will explore two main applications. The first aims to enhance the early detection of neurodegenerative diseases. The second focuses on minimizing the neurological impact of traditional PET/CT scans by using a brain-dedicated PET

scanner, while ensuring that both imaging systems deliver comparable image quality and diagnostic accuracy. The next paragraphs detail the materials employed to achieve these expected outcomes.

3.1.1.1 Diagnosis of neurodegenerative diseases

For the former application focused on the early diagnosis of neurodegenerative diseases, the retrospectively recruited population was splitted in 2 groups. The first group comprises 124 patients with normal cognition, very mild, and mild cognitive impairment which undergone a [^{18}F]FDG PET acquisition on a PET/CT and the Reading the Mind in the Eyes Test. For this patients, the intervention consisted of analysing the relationship between brain [^{18}F]FDG PET imaging and cognitive status in patients with Mild Cognitive Impairment. This was supported by correlation studies to determine the potential of social cognition in early dementia detection. The second group comprises 90 patients with mild cognitive impairment which undergone a [^{18}F]FDG PET acquisition on a PET/CT. For this group of patients, the intervention consisted of validating a deep learning artificial intelligence algorithm using only [^{18}F]FDG PET images to identify neurodegenerative diseases within this cohort.

3.1.1.1.1 Relationship between neuroimaging and emotion recognition

All patients who participated in this analysis were retrospectively selected from the Hospital Universitari i Politècnic La Fe (HULAFE) in Valencia, Spain. The initial cohort included 310 individuals presenting with memory loss and other cognitive symptoms, who were evaluated in the Cognitive Disorders Unit of the Neurology Service. Diagnosis was based on neuropsychological assessments conducted over three years by certified neuropsychologists using tools such as the Clinical Dementia Rating Scale, Mini-Mental State Examination, Repeatable Battery for the Assessment of Neuropsychological Status, and RMET. Additionally, patients underwent brain imaging with [^{18}F]FDG PET scans within 12 months of the neuropsychological evaluation and were tested for cerebrospinal fluid biomarkers. At the time of performing CSF biomarkers and PET/CT imaging, all patients demonstrated mild cognitive impairment, defined according to the CDR evaluation criteria, with cognitive decline lasting at least six months and confirmed as objective.

MCI status was further characterized by impairments in two or more cognitive domains, representing a decline from previous levels of functioning as defined by the CIE-11 criteria for dementia. From the initial 310 individuals, 148 individuals without [18F]FDG PET scans were excluded. An additional 18 patients were also excluded because the time interval between their imaging and RMET testing exceeded one year, and another 18 individuals were excluded due to the absence of CSF molecular analysis. Two more patients with tumors or other brain abnormalities, such as basal ganglia cal-

cification, hemorrhages, or arteriovenous malformations, were removed from the study to avoid inaccuracies in brain image quantification.

Ultimately, the final dataset consisted of 124 participants. Figure 29 outlines the inclusion and exclusion criteria. This dataset comprised medical imaging data (SUVr from [^{18}F]FDG PET scans), CSF biomarker results, and neuropsychological test scores (CDR, MMSE, RBANS, RMET). Based on clinical classifications, all MCI patients had CDR scores of 0.5 or CDR 0 with impairments in other cognitive domains. Approximately half of the MCI cases were attributed to neurodegenerative diseases, indicated by abnormal CSF biomarkers or neuroimaging findings that met diagnostic criteria for neurodegeneration. The remaining cases did not meet such criteria, showing normal CSF biomarkers and neuroimaging results. Table 8 provides detailed information about the sample, including the distribution of clinical diagnoses, age, sex, and neuropsychological test results.

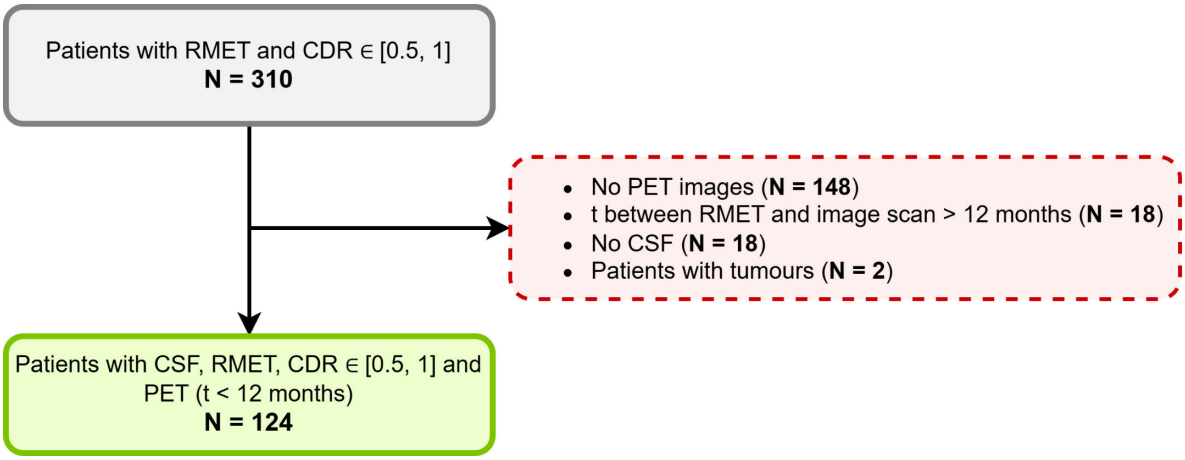

Figure 29: Inclusion and exclusion criteria for the study. RMET: Reading the Mind in the Eyes Test; CDR: Clinical Dementia Rating; PET: Positron Emission Tomography; CSF: Cerebrospinal Fluid.

Table 8: Demographical description of enrolled patients.

Clinical diagnosis	N	Age (years, mean ± sd)	Sex (female, N (%))	MMSE (mean ± sd)	RMET total (mean ± sd)	RBANS (sum of index, mean ± sd)
MCI due to neurodegenerative disease	58	68 ± 7	34 (59%)	22 ± 4	16 ± 5	326 ± 57
MCI not due to neurodegenerative disease	66	64 ± 8	37 (56%)	26 ± 3	18 ± 5	395 ± 69

Demographic and clinical data were retrieved from hospital clinical records and supplemented with the neuropsychological assessments. The study protocol was ap-

proved by the Ethics Committee (CEIC) at the Health Research Institute La Fe (reference: 2021–854-1, dated 22/12/2021), and all participants provided informed consent.

Regarding the [^{18}F]FDG image acquisitions, the protocol followed the European Association of Nuclear Medicine's [^{18}F]FDG procedural guidelines for brain PET imaging (version 2) [169]. Subjects fasted for at least 4 hours. Patients were positioned in a calm, dimly lit room for 20-30 minutes before [^{18}F]FDG administration and uptake phase. A 20-minute scan was acquired 20-30 minutes after injection. The injection dose was 155 $\pm$ 25 MBq [^{18}F]FDG. Prior to [^{18}F]FDG injection, glucose levels were tested and all subjects had less than 200 mg/dL.

Images with a resolution of 128 $\times$ 128 $\times$ 90 matrix and voxel dimensions of 2 $\times$ 2 $\times$ 2 mm were obtained in DICOM format from the PACS system. These images were acquired using a Philips Gemini TF 64 PET/CT scanner, which uses Ordered Subset Expectation Maximization (OSEM), a time-of-flight algorithm for 3D imaging. After image reconstruction, a nuclear medicine physician guaranteed the quality checks on the images.

Regarding the neuropsychological and emotion recognition evaluation, patients completed various neuropsychological assessments, which included an global dementia rating, an evaluation of general mental state, and a of different cognitive domains, functionality, and emotion recognition. The assessment began with the determination of the CDR scale to assess the severity of dementia. This was followed by the RBANS, which evaluated five cognitive domains for psychometric analysis. The MMSE was used to assess the general mental state of the patients.

Emotion recognition was assessed using the Spanish version of the RMET. In general, it's used to assess Theory of Mind. To understand another person's mental state, it's necessary to first recognize and integrate their emotions. The RMET includes 36 images of the eyes zone expressing various complicated emotions. The 36 pictures were divided into three valences: 8 positives (e.g., friendly), 12 negative (e.g., upset), and 16 neutral (e.g., reflecting). Participants selected the most appropriate adjective from four options (three incorrect and one correct) for each picture. Adjective definitions were provided as needed. The total score reflects the sum of right answers [95].

3.1.1.1.2 Neural Network validation for Alzheimer's Disease prediction

For this intervention, patients with MCI, identified through neuropsychological evaluations without functional impairment in daily activities, were retrospectively recruited. All cases were collected from the Cognitive Disorders Consultation of the Neurology Service of La Fe University and Polytechnic Hospital between 2013 and 2020. Patient data were sourced from the hospital's electronic clinical records, while imaging data were obtained from the PACS. The study initially included patients experiencing cognitive decline, primarily affecting memory, without impairments in daily function-

ing. However, those without a CDR score of 0.5 (MCI diagnosis), a final diagnosis, or FDG PET imaging were excluded. Figure 30 outlines the inclusion and exclusion criteria.

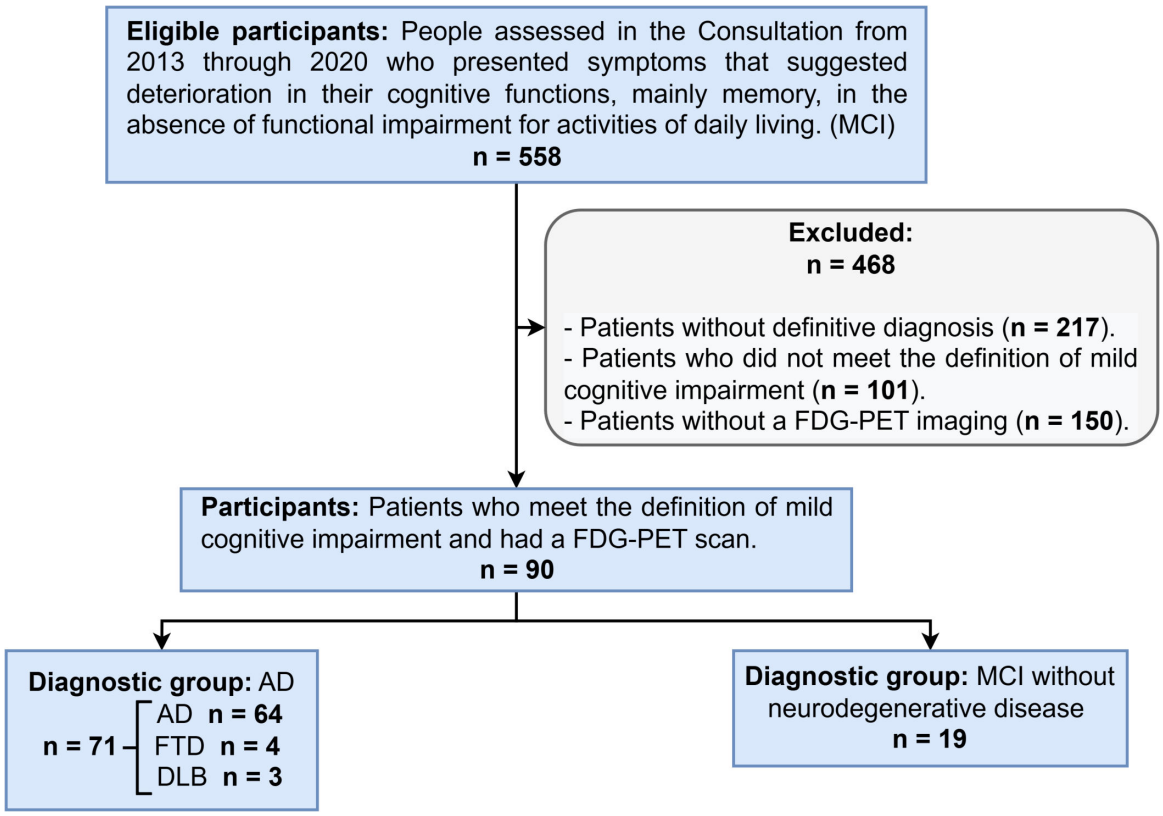

Figure 30: Eligibility criteria for the participants. From the 558 people assessed in the Consultation 90 participants who met the eligibility criteria were included (71 MCI with neurodegenerative disease and 19 MCI without neurodegenerative disease). All of them met the definition of MCI (Clinical Dementia Rating = 0.5) and had an FDG-PET scan. MCI = Mild Cognitive Impairment, AD = Alzheimer Disease, FTD = Frontotemporal Degeneration, DLB = Dementia with Lewy Bodies. From *"Artificial intelligence on fdg pet images identifies mild cognitive impairment patients with neurodegenerative disease."* by Joan Prats-Climent, Maria Teresa Gandia-Ferrero et al. 2022. Copyright by Journal of Medical Systems.

The study was approved by the Ethics Committee of La Fe University and Polytechnic Hospital, and informed consent was waived due to its retrospective, non-interventional observational design. A total of 90 subjects who met the eligibility criteria were included in the study. The final diagnosis was determined including physical and neuropsychological evaluations, FDG PET imaging, structural MR, and CSF molecular analysis from lumbar puncture.

After selecting patients retrospectively according to the inclusion criteria, the database was further reviewed to ensure greater precision in clinical diagnoses. Participants were categorized into two groups: 71 MCI cases associated with a neurodegenerative disease (64 with AD, 4 with FTD, and 3 with DLB) and 19 MCI cases without

an associated neurodegenerative disease (see Figure 30). The study included 52 women and 38 men, aged between 46 and 78 years. Regarding education levels, 14 had university degrees, 21 had secondary education, 54 had primary education, and one had no formal education. Table 9 presents the demographic and neuropsychological data [99].

Table 9: Demographical neuropsychological and cerebrospinal fluid characteristics of the independent sample. MCI: Mild Cognitive Impairment, US: university studies, SS: secondary studies, PS: primary studies, NS: no studies, MMSE: Mini-Mental State Examination, FAQ: Functional Activities Questionnaire, RBANs: Repeatable Battery for the Assessment of Neuropsychological Status, CSF: cerebrospinal fluid. $*$ Values are presented as mean $\pm$ standard deviation. From *"Artificial intelligence on fdg pet images identifies mild cognitive impairment patients with neurodegenerative disease."* by Joan Prats-Climent, Maria Teresa Gandia-Ferrero et al. 2022. Copyright by Journal of Medical Systems.

Groups	**MCI with neurodegenerative disease**	**MCI without neurodegenerative disease**
N subjects	71	19
Female/Male	41/3	11/8
Age$*$	71	19
US/SS/PS/NS	12/16/42/1	2/5/12/0
MMSE$*$	24 $\pm$ 5	25 $\pm$ 2
RBANs$*$	338 $\pm$ 61	357 $\pm$ 65
$A\beta_{42}$ CSF$*$	559 $\pm$ 267	1003 $\pm$ 384
p-tau CSF$*$	110 $\pm$ 65	43 $\pm$ 17
t-tau CSF$*$	735 $\pm$ 506	286 $\pm$ 113

Regarding the [^{18}F]FDG PET image acquisition, the protocol adhered to the European Association of Nuclear Medicine's [^{18}F]FDG procedural guidelines for brain PET imaging (version 2) [169]. Patients were comfortably positioned in a quiet, dimly lit room approximately 20–30 minutes before and during the uptake phase of 135–165 MBq [^{18}F]FDG administration. Imaging was conducted between 20 and 35 minutes post-injection, with scan durations ranging from 10 to 20 minutes. Three-dimensional images were reconstructed using the Ordered Subset Expectation Maximization algorithm with time-of-flight technology.

All scans were acquired using a Philips Gemini TF 64 PET/CT scanner and were assessed by a nuclear medicine physician to ensure quality. The images were downloaded in DICOM format with a matrix resolution of 128 $\times$ 128 $\times$ 90 and a voxel size of 2 $\times$ 2 $\times$ 2 mm.

3.1.1.2 Brain-dedicated PET scanner evaluation

For the latter application in dementia, which aimed to address the need to reduce the neurological burden of conventional PET/CT through a brain-dedicated PET scanner, the population was also divided into two groups. Both groups consisted of patients who attended the hospital for a diagnostic PET/CT scan and voluntarily participated in the validation of the brain-dedicated PET scanner. All patients were prospectively recruited. The first group comprised 80 patients with [^{18}F]FDG PET images. Here, the interventions involved comparing image quality between the two scanners using objective image quality metrics and assessing diagnostic prediction performance using a deep learning neural network. The second group consisted of 26 patients with amyloid PET images. For these patients, the intervention focused on evaluating the diagnostic capability of the brain-dedicated PET scanner using four different reconstructions and the Centiloid Scale.

PET systems

These two interventions are part of the clinical validation process for a a brain-dedicated PET (dPET) system named **CareMiBrain (CMB)**. The CMB scanner aims to facilitate the early diagnosis of neurodegenerative diseases. It is designed to maximize both spatial resolution and sensitivity by incorporating depth-of-interaction technology, reducing the scanner's diameter, and utilizing monolithic crystals. Patient comfort was a primary focus during development. Additionally, the scanner significantly reduces radiation exposure due to its high sensitivity and the absence of CT for attenuation correction. Instead, it generates an emission-based attenuation map for AC during each scan [60].

The CareMiBrain (Oncovision, Spain) scanner consists of three detector rings, each containing 16 detector modules, for a total of 48 modules. Each module is made up of a 12×12 array of silicon photomultipliers (SiPM) paired with continuous LYSO crystals measuring 50×50 mm^2. These monolithic crystals allow for precise depth-of-interaction (DOI) determination of gamma rays within the scintillation crystal, enhancing resolution. The scanner has a detector ring diameter of 260 mm, with an effective field of view of 220 mm in diameter and 150 mm axially. The spatial resolution (full-width at half maximum) for radial, tangential, and axial directions was measured using FBP reconstruction at distances of 10 mm and 100 mm from the center. The results were $1.87 \times 1.68 \times 1.39\ mm^3$ and $1.86 \times 1.91 \times 1.40\ mm^3$ (NU 2-2012) and $1.58 \times 1.45 \times 1.40\ mm^3$ and $1.64 \times 1.66 \times 1.44\ mm^3$ (NU 4-2008), respectively [128].

The emission-based attenuation map used in the CMB scanner is created during the reconstruction process from an estimated emission image. The different stages of this process are illustrated in Figure 31.

This image is generated using a single OSEM iteration with 12 subsets, without

applying attenuation or scatter corrections. To reduce noise near the detectors, the uncorrected image is radially cropped to a radius of 110 mm. A k-means clustering algorithm with four levels is then used for segmentation, where voxels in the lowest level are identified as noise and set to zero, while the remaining voxels are assigned a uniform value. Further mathematical processing is applied to fill internal gaps and smooth the contours, retaining only the largest connected component. Figure 31 shows the initial uncorrected emission image, the intermediate k-means segmented image, and the final volume used for attenuation correction. In the final attenuation map, all non-zero voxels are assigned the attenuation coefficient of grey matter [60].

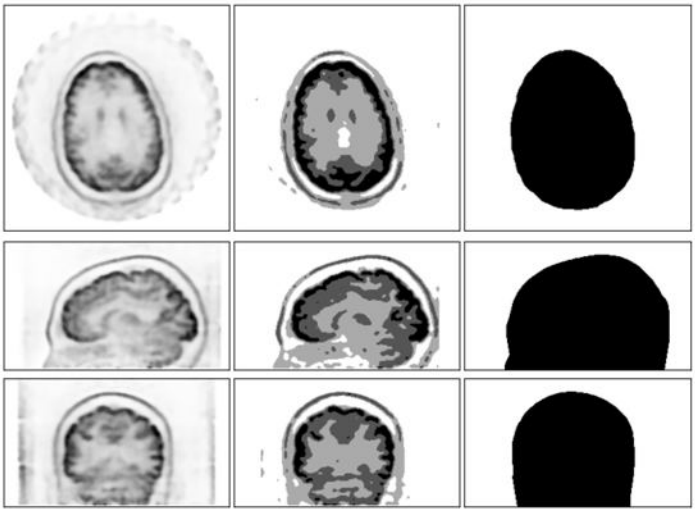

Figure 31: Generation of the emission-based attenuation map. The process consists of several steps: the uncorrected emission image (left), the k-means segmented image (middle), and the final attenuation map (right). The images are displayed in transversal, sagittal, and coronal views from top to bottom. From *"Objective image quality comparison between brain-dedicated PET and PET/CT scanners."* by Maria Teresa Gandia-Ferrero, Irene Torres-Espallardo et al. 2023. Copyright by Journal of Medical Systems.

The PET/CT scanner used for the comparison was **Philips Gemini TF 64 PET/CT**. This scanner features 28 flat detector modules, each consisting of a 23×44 array of discrete LYSO crystals measuring 4×4×22 mm^3. These crystals are arranged in an Anger-logic detector design to ensure uniform light distribution. The scanner has a detector ring diameter of 903.4 mm, with an active transverse field of view of 576 mm and an axial field of view of 180 mm. It is designed to function as a high-performance conventional PET scanner while also offering good timing resolution for time-of-flight PET imaging. The transverse and axial resolution near the center is 4.8 mm [170].

3.1.1.2.1 Objective PET image quality evaluation

For this application, both Hoffman Phantoms and patient acquisitions have been performed:

Dataset description for Hoffman Phantoms

During the validation study, three phantom scans of 20 minutes each were performed on separate days using both the CMB and PET/CT scanners. At the time of acquisition, the activity levels for the three Hoffman phantom scans on the PET/CT scanner were 9, 16, and 113 MBq of [^{18}F]FDG, while for the CMB scanner, they were 12, 13, and 22 MBq of [^{18}F]FDG. Additionally, a CT scan of the phantom was conducted using the PET/CT device. A total of 24 image sets were obtained to assess image quality, considering two scanners, three 20-minute acquisitions per scanner, and four different time frame reconstructions [60]. Since both systems recorded data in list mode, each 20-minute scan was divided into three sets of 10-minute images:

- **Total 20-minute reconstruction** ($t_0 = 00:00:00$, $t_1 = 00:20:00$)
- **Initial 10-minute reconstruction** ($t_0 = 00:00:00$, $t_1 = 00:10:00$)
- **Central 10-minute reconstruction** ($t_0 = 00:05:00$, $t_1 = 00:15:00$)
- **Final 10-minute reconstruction** ($t_0 = 00:10:00$, $t_1 = 00:20:00$)

These reconstructions were performed for both scanners, with three 20-minute scans on the CMB and three on the PET/CT. Figure 32 illustrates an example of a Hoffman phantom scan on both scanners. It is important to note that for the CMB scanner, a uniform cylindrical attenuation map was used during image reconstruction, whereas for the PET/CT scanner, a CT-based attenuation map was applied.

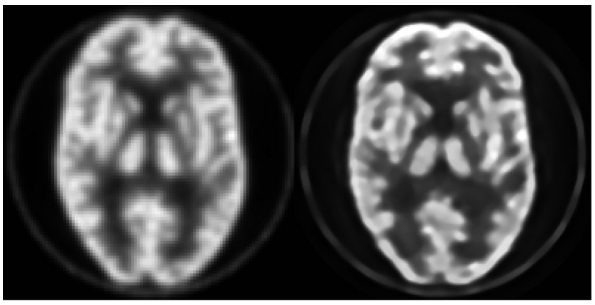

Figure 32: Reconstructed image of the Hoffman phantom on PET/CT (left) and on CMB (right). From *"Objective image quality comparison between brain-dedicated PET and PET/CT scanners."* by Maria Teresa Gandia-Ferrero, Irene Torres-Espallardo et al. 2023. Copyright by Journal of Medical Systems.

Dataset description for patients

The clinical validation of the CMB scanner at La Fe University and Polytechnic Hospital aimed to demonstrate that the image quality of CMB dPET is comparable to, or not inferior to, that of PET/CT. Patients scheduled for a diagnostic PET/CT

scan were invited to voluntarily participate in the validation study. The study received approval from the hospital's Ethics Committee (registration number: 2021-345-1). Once a patient agreed to participate, they underwent an additional scan using the CMB system with no additional radiopharmaceutical injection [60].

Between August 2021 and August 2022, a total of 127 FDG PET scans were performed on both scanners. The CMB scan was conducted for a total duration of 12 minutes, with images reconstructed for the full acquisition time. To maintain consistency in the evaluation, 16 patients who had PET scans for oncological purposes were excluded from the study. Additionally, due to the CMB scanner's axial field of view of 150 mm and the use of external anatomical references for patient positioning, the cerebellum was not always fully captured in the dedicated brain PET scan. As a result, 31 scans were excluded. Figure 33 presents the flowchart outlining the inclusion and exclusion criteria used for dataset selection [60].

The average age of the participants was 65 years, with a standard deviation of 13 years, and approximately 54% of them were female. Table 10 provides a summary of the clinical diagnoses of the 80 patients included in the study. For a comprehensive quantitative assessment of image quality, all CMB patient images were reconstructed using both the emission-based attenuation map generated by the device and the CT-based attenuation map derived from the PET/CT scan. Figure 34 illustrates an example of a patient scan acquired on both PET/CT and CMB.

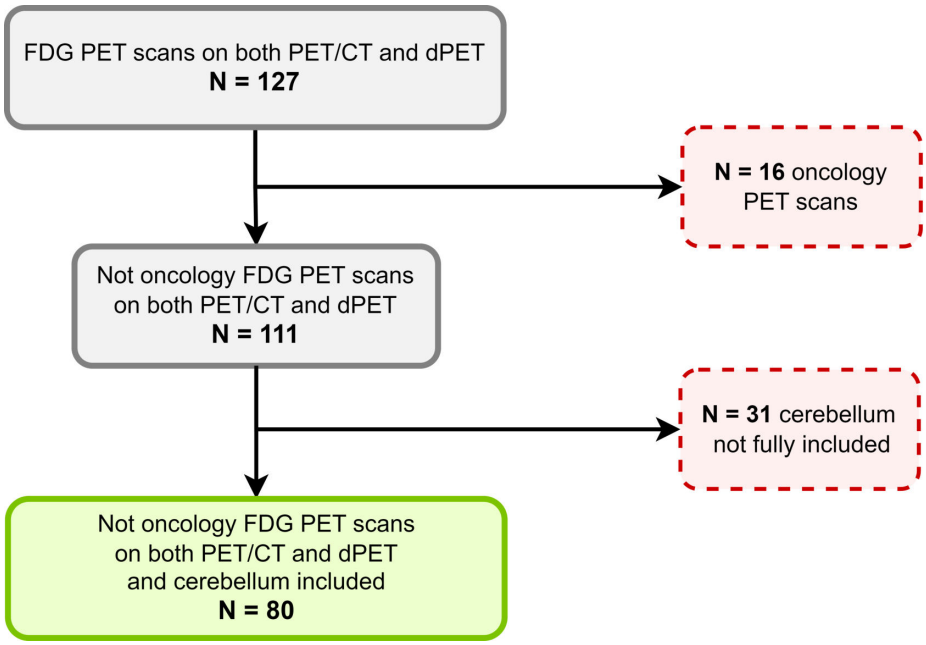

Figure 33: Flowchart of patient selection based on the inclusion and exclusion criteria for the image quality evaluation. From *"Objective image quality comparison between brain-dedicated PET and PET/CT scanners."* by Maria Teresa Gandia-Ferrero, Irene Torres-Espallardo et al. 2023. Copyright by Journal of Medical Systems.

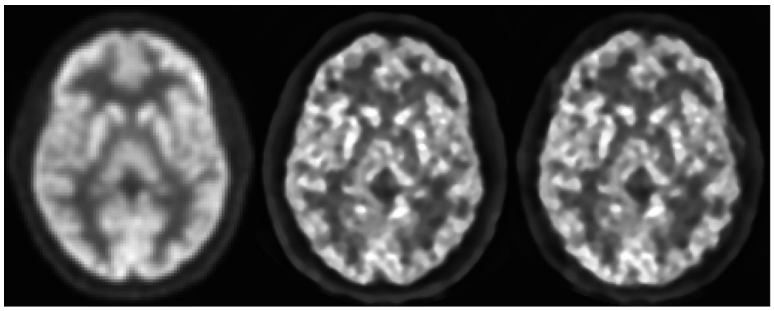

Figure 34: Example of a reconstructed image of a patient acquired on both scanners. Image acquired on PET/CT (left), on CMB reconstructed with emission-based attenuation map (middle) and on CMB reconstructed with CT-based attenuation map (right). From *"Objective image quality comparison between brain-dedicated PET and PET/CT scanners."* by Maria Teresa Gandia-Ferrero, Irene Torres-Espallardo et al. 2023. Copyright by Journal of Medical Systems.

Table 10: Clinical diagnosis summary of the 80 enrolled patients in the study. From *"Objective image quality comparison between brain-dedicated PET and PET/CT scanners."* by Maria Teresa Gandia-Ferrero, Irene Torres-Espallardo et al. 2023. Copyright by Journal of Medical Systems.

Clinical diagnosis	N
Mild cognitive impairment	55
Parkinsonism	9
Epilepsy	10
Others	6

The brain study acquisition protocol for patients followed the guidelines set by the European Association of Nuclear Medicine [169]. Patients were comfortably positioned in a quiet, dimly lit room approximately 20 minutes before the administration of [^{18}F]FDG and remained there during the uptake phase of 133–167 MBq [^{18}F]FDG. Image acquisition on the PET/CT scanner was performed around 20 minutes post-injection, lasting 20 minutes in a single bed position, with reconstruction covering the entire acquisition period. All images were reviewed and validated by a nuclear medicine physician.

For the CMB device, both phantom and patient images were reconstructed using the OSEM algorithm with 12 subsets and 4 iterations. The images were generated in DICOM format with a matrix size of 220 × 220 × 152 and a voxel size of 1 × 1 × 1 mm^3. For the PET/CT scanner, all images were reconstructed using the line-of-response row-action maximum likelihood algorithm (LOR-RAMLA). PET/CT images were generated in DICOM format with a matrix resolution of 128×128×90 and a voxel size of 2×2×2 mm^3. CT scans were also produced in DICOM format, with a matrix resolution of 512×512×179 and a voxel size of 1.17×1.17×2 mm^3.

3.1.1.2.2 Evaluation of brain-dedicated PET diagnostic capability

A comparative diagnosis analysis was conducted between PET/CT and CMB devices. This intervention, was divided into 2 subinterventions regarding the type of radiopharmaceutical employed for brain PET imaging (FDG and amyloid imaging).

For the former, the subintervention consisted of assessing the level of agreement in diagnosing a group of patients using the deep learning algorithm based on [^{18}F]FDG PET imaging that was previously validated on images from Hospital La Fe [99]. The initial database for this diagnostic comparison consisted of the same 80 patients analyzed in the previous image quality evaluation intervention. However, only 55 of these 80 patients were ultimately included in the analysis. These 55 patients were selected due to their cognitive impairment, as shown in Table 10, which aligned with the type of data on which the model was trained. Consequently, the deep learning model was tested on the images of these 55 patients from both devices.

As mentioned earlier, the brain study acquisition protocol for patients followed the guidelines outlined by the European Association of Nuclear Medicine [169]. For the CMB device, image reconstruction was performed using the OSEM algorithm with 12 subsets and 4 iterations. The images were produced in DICOM format, with a matrix size of $220 \times 220 \times 152$ and a voxel size of $1 \times 1 \times 1\ mm^3$. In contrast, the PET/CT scanner employed the line-of-response row-action maximum likelihood algorithm (LOR-RAMLA) for image reconstruction. The PET/CT images were generated in DICOM format, with a matrix resolution of $128 \times 128 \times 90$ and a voxel size of $2 \times 2 \times 2\ mm^3$.

For the latter, the subintervention consisted of assessing the level of agreement in diagnosing a group of patients using the Centiloid Scale. The hospital's Ethics Committee approved the study (registration number 2021-345-1), and all participants provided written informed consent. The patient recruitment process followed a structured approach: individuals with a possible AD diagnosis who visited the hospital for a diagnostic amyloid PET/CT were invited to participate in the validation of the brain-dedicated PET scanner. Those who consented to participate signed a formal agreement.

All enrolled patients underwent both a standard diagnostic PET/CT scan and an additional scan using the brain-dedicated CareMiBrain system. A total of 28 patients were scanned using amyloid tracers in both modalities. However, due to the 150 mm axial field of view and reliance on external anatomical references for patient positioning, the cerebellum was not fully captured in two CMB PET scans. These two cases were excluded from further analysis. Finally, amyloid PET images were successfully acquired for 26 patients, using the following tracers: 17 patients with [^{18}F]Flutemetamol, 5 with [^{18}F]Florbetaben, and 4 with [^{18}F]Florbetapir. Based on established criteria, patients were classified into two groups: those with Alzheimer's disease pathology (AD) and those without (No AD). All participants were assessed at the Cognitive Disorders Unit

within the Neurology Service due to symptoms of memory loss and other cognitive impairments. The diagnosis was determined using cerebrospinal fluid biomarkers, neuropsychological evaluations, and imaging studies, including [^{18}F]FDG PET/CT or MR brain scans.

In cases where lumbar puncture was contraindicated, such as in anticoagulated patients, or unavailable at referring hospitals, amyloid PET interpretation by nuclear medicine specialists was used as an alternative to CSF biomarker analysis. This substitution is a recognized and validated practice, as demonstrated in prior research by Palmqvist et al. [171]. The classification of patients into AD and No AD groups was based on these combined assessments. Table 11 presents the demographic and clinical characteristics of both groups.

Table 11: Demographic and clinical information in terms of the mean and standard deviation of participants in our study (number of patients (N), gender, age and Mini Mental State Examination (MMSE)). From *"Amyloid brain-dedicated PET images can diagnose Alzheimer's pathology with centiloid scale."* by Maria Teresa Gandia-Ferrero, Irene Torres-Espallardo et al. 2024. Copyright by Physica Medica.

	N	**Gender (F-M)**	**Age**	**MMSE**
AD	14	8-6	69 ± 7	24 ± 4
No AD	12	7-5	68 ± 8	27 ± 4

Regarding the Mini-Mental State Examination (MMSE), while various cutoff values have been applied in cognitive research, scores of ≤ 23 are generally considered indicative of cognitive impairment. Patients scoring between 23 and 26 are typically classified as having Mild Cognitive Impairment (MCI). However, for individuals with near-normal scores (28–30) and otherwise intact neurocognitive function, there is no clear clinical criterion for diagnosing MCI, particularly in elderly patients [172].

All images were acquired following the standardized procedures outlined in the SNMMI Procedure Standard and the EANM Practice Guideline for Amyloid PET brain imaging [173]. The waiting period before image acquisition adhered to these guidelines, except for four patients whose [^{18}F]Florbetapir PET images were obtained using the CMB scanner with an extended waiting period.

Although the guidelines recommend for [^{18}F]Florbetapir a waiting period of 30–50 minutes, its pharmacodynamics indicate that the time-activity curve increases steadily until 30 minutes post-injection and then stabilizes for at least 90 minutes thereafter [174]. This ensures that all acquisition times fall within the acceptable range. The specific waiting times and image acquisition durations for each of the three amyloid radiotracers are summarized in Table 12.

Initially, PET images were obtained using a Philips Gemini TF 64 PET/CT scanner. The PET/CT images were reconstructed following the standard brain imag-

ing protocol and saved in DICOM format with a matrix resolution of $128 \times 128 \times 90$ and a voxel size of $2 \times 2 \times 2$ mm^3. After PET/CT acquisition, additional PET images were collected using the CMB brain-dedicated PET scanner. All 3D images were reconstructed using the Ordered Subset Expectation Maximization (OSEM) algorithm with 12 subsets and 4 iterations, generating images in DICOM format with four different reconstruction settings:

- $110 \times 110 \times 76$ matrix size, $2 \times 2 \times 2$ mm^3 voxel size with Point Spread Function (2mmPSF).
- $110 \times 110 \times 76$ matrix size, $2 \times 2 \times 2$ mm^3 voxel size without PSF (2mmNoPSF).
- $220 \times 220 \times 152$ matrix size, $1 \times 1 \times 1$ mm^3 voxel size with PSF (1mmPSF).
- $220 \times 220 \times 152$ matrix size, $1 \times 1 \times 1$ mm^3 voxel size without PSF (1mmNoPSF).

Table 12: Waiting period after injection (mean ± standard deviation) and image acquisition duration for each PET scanner and radiotracer in minutes. From *"Amyloid brain-dedicated PET images can diagnose Alzheimer's pathology with centiloid scale."* by Maria Teresa Gandia-Ferrero, Irene Torres-Espallardo et al. 2024. Copyright by Physica Medica.

Scanner	Radiotracer	Waiting period	Image acquisition duration
PET/CT	[^{18}F]Flutemetamol	91 ± 8	20
	[^{18}F]Florbetaben	90 ± 1	20
	[^{18}F]Florbetapir	49 ± 2	10
CMB	[^{18}F]Flutemetamol	123 ± 9	10
	[^{18}F]Florbetaben	118 ± 13	20
	[^{18}F]Florbetapir	82 ± 2	10

3.1.2 Neuroendocrine tumors

In the context of neuroendocrine tumors, where precise quantification of lesion uptake is crucial for therapeutic decision-making, the analysis aims to guarantee uniform treatment recommendations for each lesion, regardless of the imaging device used, by the harmonization of variables between PET/CT and PET/MR scanners.

3.1.2.1 Harmonization for consistent treatment recommendations

PET systems

The PET/CT scanner used for the variables harmonization was **Philips Gemini TF 64 PET/CT**,which was described previously.

The PET/MR scanner used for the variables harmonization was **General Electric SIGNA™ PET/MR**. This system is a time-of-flight capable PET/MR scanner designed for simultaneous PET and MRI imaging. It features silicon photomultiplier (SiPM)-based detectors with lutetium-based scintillator crystals, optimized for high sensitivity and spatial resolution. The system has an axial field of view of 25 cm and a transverse FOV of 60 cm. The PET resolution near the center is approximately 4.2 mm, and the TOF capability enhances image quality and quantification by improving signal-to-noise ratio. The system is designed to ensure mutual compatibility between PET and MRI, minimizing interference and optimizing imaging performance.

Figure 35 presents an example of a reconstructed image from a patient scanned using both PET/CT and PET/MR scanners.

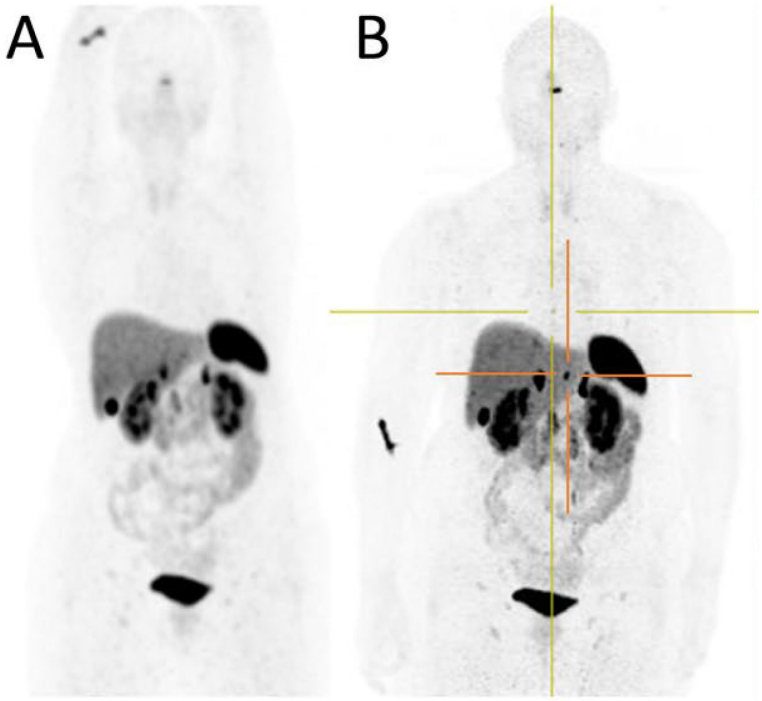

Figure 35: Example of a reconstructed image of a patient acquired on both scanners. (A) Maximum intensity projection (MIP) in PET/CT. (B) MIP in PET/MR. PET/MR revealed a new bone lesion (involvement of a new organ) and a new hepatic lesion (organ already affected). From *"Same-day comparative protocol PET/CT-PET/MRI [^{68}Ga]Ga-DOTA-TOC in paragangliomas and pheochromocytomas: an approach to personalized medicine"* by Prado-Wohlwend, S., Ballesta-Moratalla, M. et al. 2023. Copyright by Cancer Imaging.

Dataset description

This prospective study included patients diagnosed with locally advanced or metastatic histologically confirmed paragangliomas or pheochromocytomas. These patients were referred to our neuroendocrine tumors-accredited tertiary care center, officially recognized by the regional administration, for staging, follow-up, or therapeutic

decision-making between September 2020 and June 2022. The study was conducted with approval from the local ethics committee.

Exclusion criteria included pregnancy, age under 18, contraindications to MR, and an inability to comprehend the study protocol or provide informed consent. A same-day imaging protocol was carried out in 25 patients with metastatic or unresectable paragangliomas. PET/CT and PET/MR scans were performed consecutively following a single intravenous injection of approximately 185 MBq of [^{68}Ga]Ga-DOTA-TOC, without the use of radiological contrast. The whole-body PET/CT scan, covering the area from the skull to the upper thigh, was conducted first, immediately followed by a PET/MRI scan of the same region. The characteristics of the patients are summarized in Table 13.

Table 13: Overall characteristics of the study patients. From *"Same-day comparative protocol PET/CT-PET/MRI [^{68}Ga]Ga-DOTA-TOC in paragangliomas and pheochromocytomas: an approach to personalized medicine"* by Prado-Wohlwend, S., Ballesta-Moratalla, M. et al. 2023. Copyright by Cancer Imaging.

Gender	Female 12
	Male 13
Age	47.52 years (20–71)
Primary location	Pheochromocytoma 6
	Paraganglioma 17
	Synchronous pheochromocytoma and paraganglioma 2
Multifocality	Multifocal or metastatic 17
	Unifocal 8
Genetic syndrome	Sporadic 8
	SDHB 4
	SDHD 9
	SDHA 2
	FH 2
Scan purpose	Staging-initial diagnosis 4
	Follow-up 18
	Therapeutic decision 3
Number of patients with lesions located in	Cervical 15
	Bone 6
	Nodal 5
	Mediastinal 5
	Abdominal extra adrenal 4
	Liver 3
	Lung 2
	Adrenal 1

On average, 183.52 MBq of [^{68}Ga]Ga-DOTA-TOC was administered, with a range of 165.76 to 203.13 MBq. The mean interval between radiotracer injection and imaging was 65 minutes (ranging from 45 to 101 minutes) for PET/CT and 109 minutes (ranging from 81 to 165 minutes) for PET/MRI. After accounting for radioactive decay, the activity at the start of imaging was 93.61 MBq for PET/CT and 59.57 MBq for PET/MRI.

Figure 35 presents an example of a reconstructed image from a patient scanned using both imaging systems, PET/CT and PET/MR. Subfigure A shows the maximum intensity projection (MIP) in PET/CT while B shows MIP in PET/MR. The PET/MR scan identified an additional bone lesion in this patien, indicating the involvement of a previously unaffected organ, as well as a new hepatic lesion in an organ that was already affected.

3.2 Quantification of PET images

Recent improvements in digital computer technology allow to treat any image as an array of numbers representing the local values of the object property that was imaged, as well as to make quantitative measurements of body features based on their images [2].

In nuclear medicine, quantitative imaging is used either before or during certain radiopharmaceutical therapies. Quantification of activity throughout a scan after injecting a tracer amount of radioactivity is generally achieved by calibrating results using data from time zero, when whole-body activity matches injected activity [39].

Quantitative PET can range from simple to complex and laborious. This is significantly dependent on the objective of the imaging task. Static and dynamic PET are two distinct modalities of acquiring data from which relevant data is extracted and physiologically analyzed. Static images are typically acquired after the tracer is administered, and enough time is allowed for tracer clearance from plasma and accumulation in the tissue to increase the target-to-nontarget ratio. However, dynamic imaging captures metabolic information in real time, allowing one to infer useful physiological quantitative parameters [175]. All PET images analyzed in this work come from static acquisitions.

A primary goal of these quantitative or semiquantitative measures in PET image interpretation is to eliminate interreader variability. Another goal of having such a method of measurement is to allow for comparisons between different patient studies, which are often used in monitoring and assessing response to therapy. A strong, dependable, and distinct cutoff value of the response is suitable for supporting the decision-making process for a specific treatment line [176].

Additionally, it would be highly useful in predicting which therapy will be more successful than others, particularly in the early stages of a given therapeutic regimen. Conversely, an analysis of this kind can offer additional information on the spectrum and biological variability of a given illness, especially when comparing patients. The production of innovative targeted tracers demands the employment of a suitable or optimum quantitative approach, as traditional measurements are not always appropriate for extracting useful information [177].

Standardized imaging procedures and quantification techniques would also make it simple to compare data from various PET clinics and create a knowledge base with the least amount of observer variation and methodological bias. This can be possible if the procedure is well specified and imaging potential risks and technological error causes are identified and removed. Standardized quantification therefore assists the path towards personalized medicine and makes multicenter studies easier to compare across various PET centers [178, 179].

3.2.1 Dementia: data preprocessing and data extraction

Data preprocessing for dementia applications

Images from the same patient taken with different scanners might not necessarily be in the same reference space since patients are not positioned precisely the same. Therefore, it is frequently required to use mathematical transformations that can rewrite every image in the same reference space in order to create a point-to-point (voxel-to-voxel) correspondence between patients in order to compare them. Mathematical transformations are used to ensure that the same voxel in each image corresponds to the same anatomical area, as if the images were taken with the patient in the exact same position [180].

There are many different mathematical transformations that can be applied to medical images:

- Rotation: is an affine transformation that turns an image by a certain angle around its origin or centre. This transformation alters an image's orientation according on the angle it has been set to, while keeping the same shape and size.
- Translation: is an affine transformation that moves an image by a given number of pixels along the x and y axes. This process translates the image in such a way that each pixel is relocated to a new position while keeping the image's shape and size.
- Resampling: is a transformation that changes the spatial resolution of an image by interpolating pixel values to create a new image grid. This can involve upscaling (increasing resolution) or downscaling (decreasing resolution)
- Shearing: is an affine transformation that moves points that face a fixed direction

by a factor equal to their signed distance from a line that moves parallel to the direction in question.

- Warping: is a geometric transformation that alters the spatial configuration of an image, allowing for distortion or deformation to fit a desired shape or mapping.

These mathematical transformations of images (see Figure 36) can be grouped into different types of techniques according to the characteristics of the images to be processed: realignment, co-registration and spatial normalization.

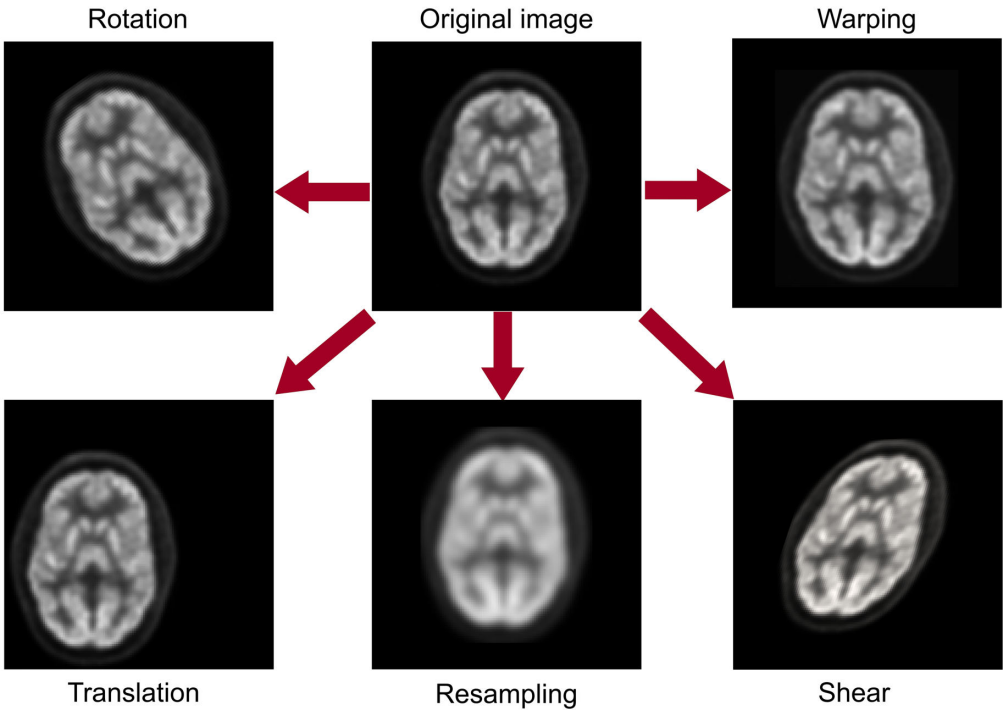

Figure 36: Geometric transformations in image processing. Images acquired at Hospital La Fe.

Realignment techniques are those mathematical transformations that rewrite many images of the same patient and modality in a single reference space. An example of a realignment of two amyloid brain PET images from different subjects can be observed in Figure 37. Realignment procedures should be used when comparing two PET images of the same patient acquired before and after therapy. In this situation, realigning the two PET images would allow for a pixel-by-pixel comparison to identify changes. A realignment procedure involves affine transformations of three-dimensional rotations and translations [180]. In order to minimize the disparities between a reference scan and each subsequent scan, parameters of an affine "rigid-body" transformation are estimated during the realignment process. The data is then resampled using an interpolation approach to apply the transformation. PET data analysis is often simpler since it does not have to deal with connected errors from one scan to the next [181].

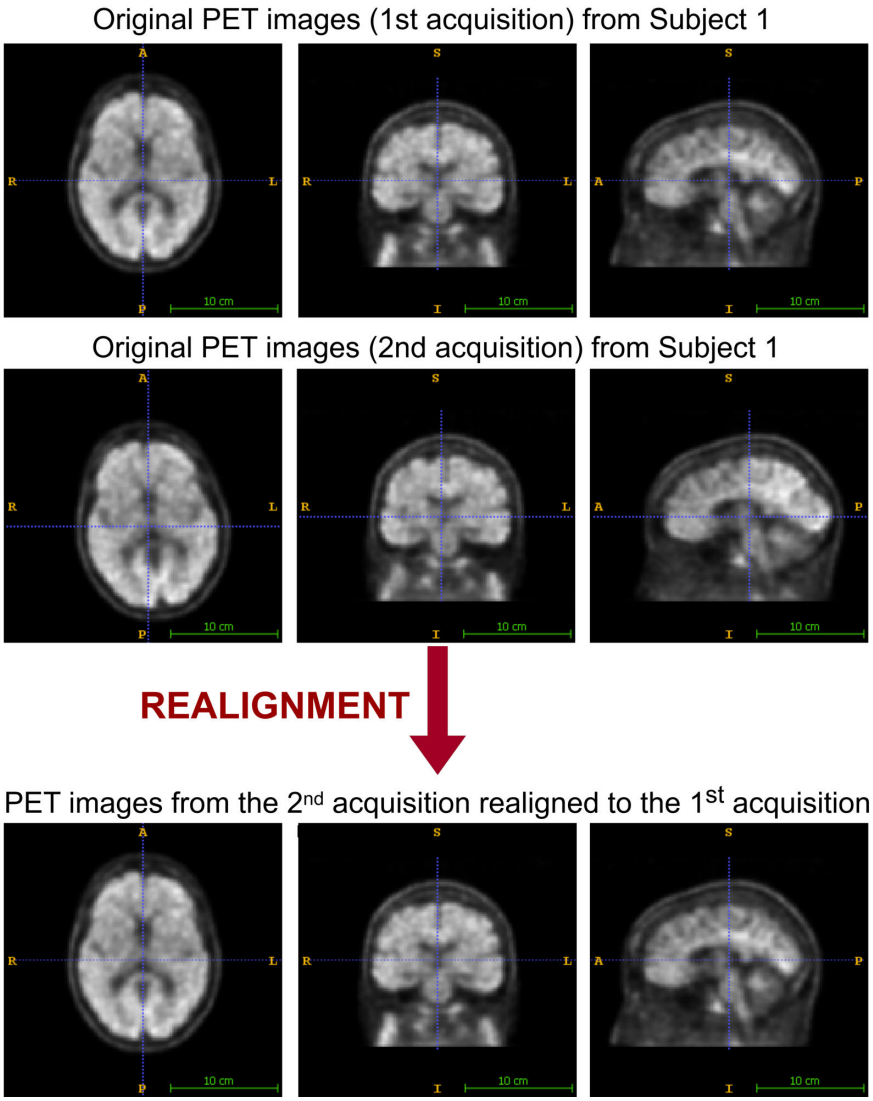

Figure 37: Example of a realignment of two amyloid brain PET images from 2 different subjects. Images acquired at Hospital La Fe.

Co-registration techniques involve mathematical modifications that employ the same reference space to rewrite images of the same patient from different modalities. The integration of different imaging modalities can give additional information that is not immediately obvious when studying individual image modalities. For research on a single subject, regions of activation can be precisely localized by superimposing them on a high resolution structural image of the subject. This involves the matching of functional images with structural images. Another possible use for this registration is to compute more exact spatial normalization from a more detailed structural image. Registration techniques can be used when integrating a PET scan with an MR image of the same subject. It is a similar technique to realignment. The difference between both procedures is that an MR image has smaller pixels than a PET image, requiring the addition of resampling transformations [180, 181]. Figure 38 illustrates an example of a co-registration of 2 brain images from the same subject but different modalities:

an amyloid PET image and a MR image.

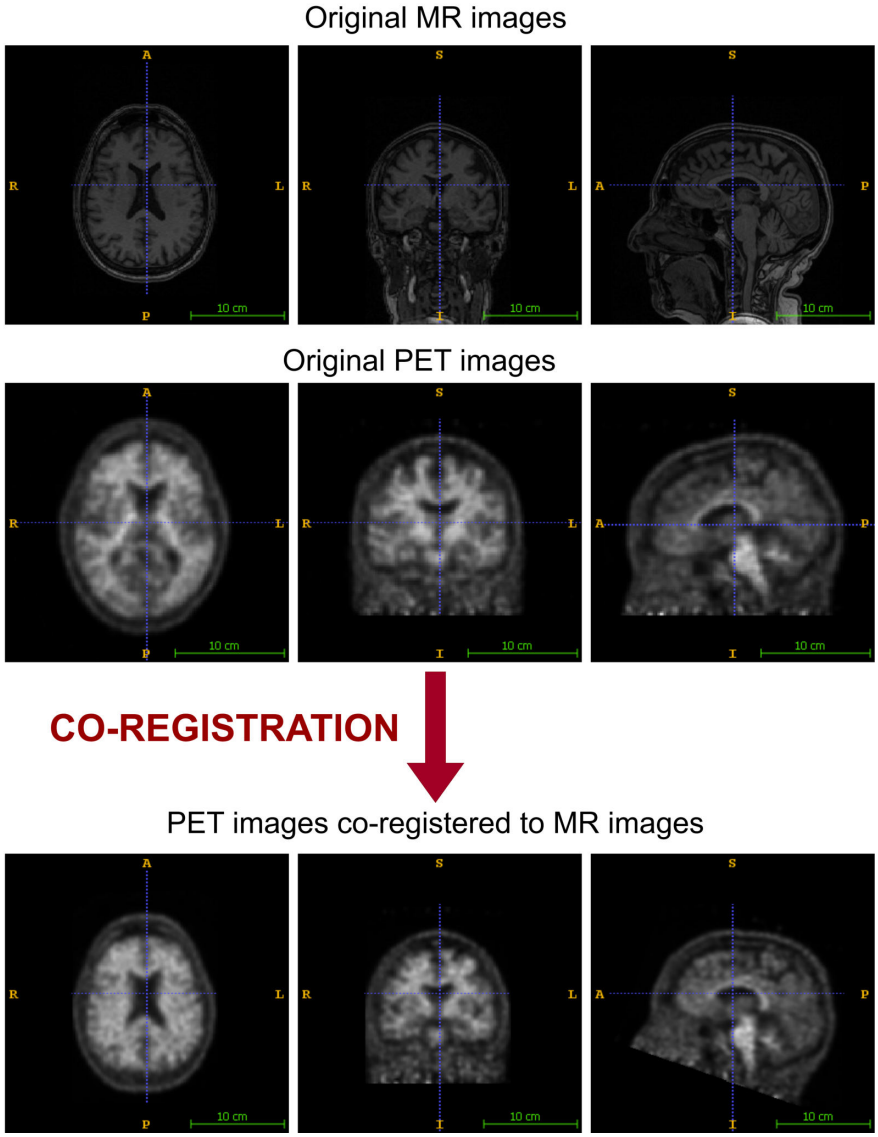

Figure 38: Example of a co-registration of 2 brain images from the same subject but different modalities: an amyloid PET image and a MR image. Images acquired at Hospital La Fe.

Spatial normalization is a technique that rewrites images from different subjects in the same reference space, from the same or different image modality. Figure 39 is an example of a spatial normalization of an MR and an amyloid brain PET image to Montreal Neurological Institute (MNI) space.

Spatial normalization is critical when comparing a patient's PET image to a reference PET image, such as an average from a database of normal patients. In realignment, the generative model for within-subject movements is a rigid-body displacement of the initial image. The generative model for spatial normalization is a canonical image or template that is altered to create a subject-specific image. Spatial normal-

ization inverts this model by undoing the warp using a template matching technique. This process includes rotations, three-dimensional translations, and deformations such as shear and warping [180, 181].

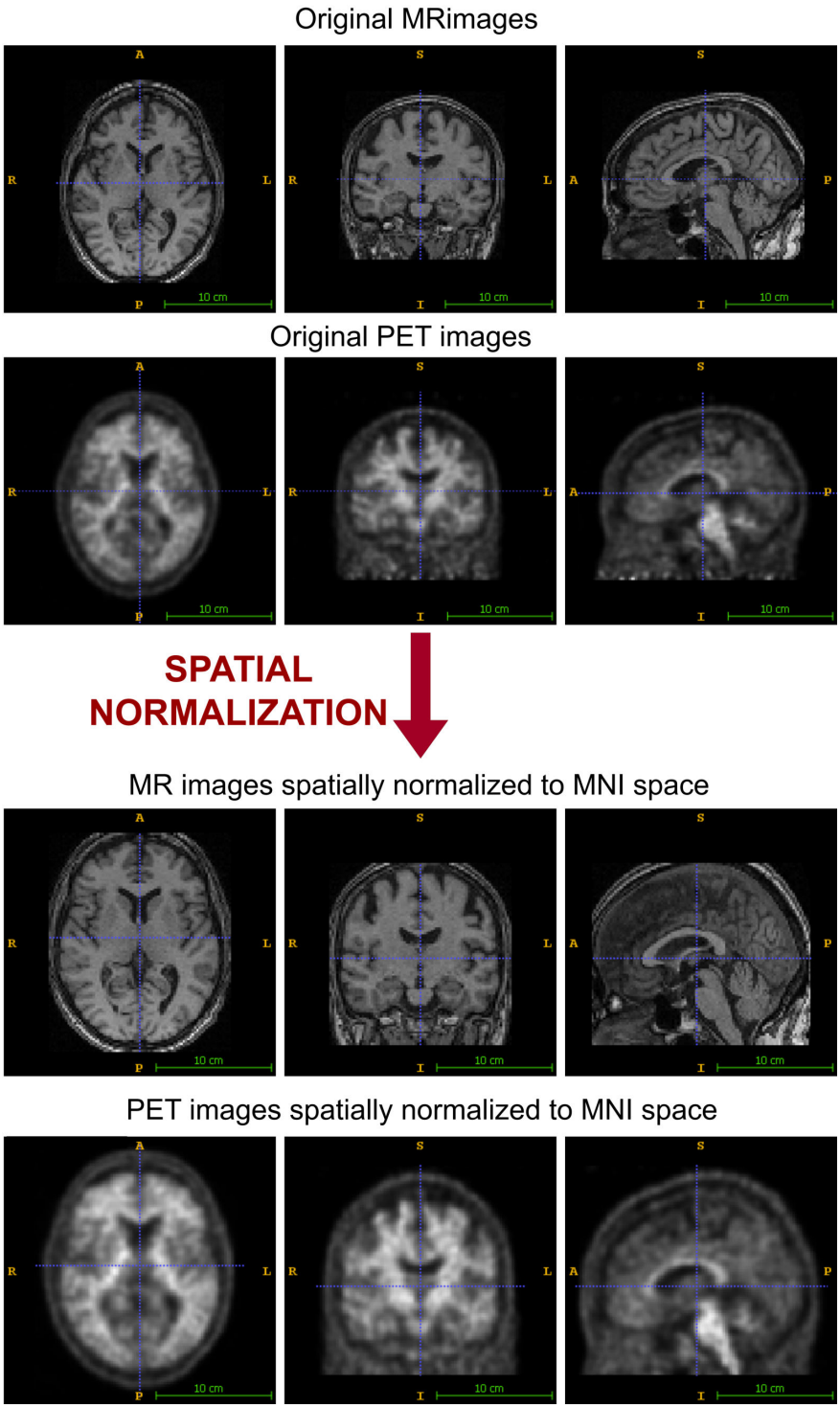

Figure 39: Example of a spatial normalization of an MR and a amyloid brain PET image to MNI space. Images acquired at Hospital La Fe.

Spatial normalization of PET images can be accomplished directly by identifying the mathematical transformation that rewrites the patient's PET image in the reference PET image space. However, the most suggested way is to estimate this transformation using the patient's MR scan, which gives more anatomical information and is more exact [180, 181].

For all the explained mathematical transformations, in this work, Statistical Parametric Mapping (SPM) was used. It is a well-documented software, freely available and strongly supported by many brain imaging researchers.

Apart form mathematical transformations, **intensity normalization** (or scaling) is required to account for biological and technological non-disease-related variables that might influence regional [^{18}F]FDG concentrations. Intensity normalization, in the field of brain imaging for example, can thus be achieved by normalising to the entire brain or to established reference regions that are known to be preserved in certain clinical contexts (for example, the cerebellum, brainstem, or pons). The fundamental premise is that the reference region has been unaffected by disease or method, which must be thoroughly evaluated. Intensity normalization is especially important when assessing individuals who may exhibit both hypermetabolism and hypometabolism [182].

PET can accurately quantify glucose metabolic rates due to the closeness to FDG. Glucose metabolic rates are not employed in clinical settings. The standardized uptake value (SUV) is a semiquantitative indicator of glucose metabolism that may be used to characterise lesions and monitor glucose metabolism [48]. The SUV represents the [^{18}F]FDG uptake within a volume normalized to the dose of [^{18}F]FDG administered and a factor (such as body weight) that accounts for distribution throughout the body [178]. The SUV normalized to body weight may be calculated using the equation below:

$$SUV = \frac{A_{C_{VOI}}(kBq/mL)}{\frac{A_{adm}(MBq)}{V(Kg)}} \tag{3.2.1}$$

where $A_{C_{VOI}}$ represents the average activity concentration, in kBq/mL, in the specified volume of interest, A_{adm} is the activity of [^{18}F]FDG administered in megabecquerels (corrected for physical decay); and V is the total volume (which is normally considered as the body weight), in kilograms.

However, this measurement is affected by a number of variables, including the patient's weight, the dose administered, the acquisition duration, and the plasma glucose level at the moment of the radiotracer injection. This leads to a significant degree of variety, even within the same subject. Evaluating the SUV ratio (SUVr) in this situation becomes particularly interesting since it facilitates the adjustment of this variability by normalizing the count values to, depending on the situation, the average uptake value of a particular organ. This will make the values that are acquired related to the

reference location and enable trustworthy comparisons across patients or within the same patient. However, it is important to remember that this index does not provide information on the absolute value of FDG uptake [180].

Data extraction from images for dementia applications

After obtaining preprocessed data, in the field of brain imaging, there are several ways to extract relevant patient data for the comparison with control (or normal) data. This comparison may be carried out using volumes of interest (VOIs), which can be defined in a standardized space to sample activity or parametric distributions automatically. Also, voxel-based techniques are frequently utilized for analysing functional (activation) images and are integrated into several software applications [39].

The **voxel-based quantification** compares a patient's PET image statistically to a set of PET images from control subjects. In this procedure, spatial normalization is needed in order to transform both images to the standard MNI space. The resultant parametric image shows the p-values, or statistical significance values, derived from the comparison of individual voxels. However, interpretation of this image requires two types of thresholding: defining a statistical significance threshold (usually set between 0.05 and 0.001) and applying spatial thresholding [180].

The goal of **VOI-based quantification** is to estimate the average concentration of radiopharmaceuticals in different brain volumes of interest. The indices obtained are frequently relative indices, such as the ratio of the average radiopharmaceutical in the VOI to a stable reference VOI, such as the cerebellum. The main advantage of these approaches is that the VOIs can be automatically delineated for each patient, since manual segmentation would be too time-consuming and operator-dependent. Since the VOI atlas is referenced to the MNI space, it can fit all PET images that are spatially normalized [180]. In the dementia applications of this study, VOI-based quantification will be performed in order to extract relevant information from PET images.

The state-of-the-art offers many different atlases. The Brodmann Atlas, Atlas Automated Anatomical Labelling (AAL), Desikan-Killiany Atlas, and Hammers Atlas are among the best-known and most extensively used atlases for quantifying PET scans. The Hammers Atlas is a probabilistic segmentation of the brain into 95 volumes of interest based on 30 MRI scans that were manually segmented [183, 184].

The dementia applications in this study employed a modified version of Hammers' VOI atlas in the MNI space. The modification consisted of combining some of the 95 brain areas contained in Hammer's VOI atlas, resulting in a new atlas (La Fe atlas) with 28 regions. This modification is consistent with the brain volumes of interest employed in CortexID Suite, a commercial clinical practice software (GE Healthcare, Marlborough, Massachusetts, USA). A nuclear medicine physician with over ten years of experience identified these volumes of interest [60]. Tables 14 and 15 depicts the name equivalence of the modified regions between Hammers and La Fe atlas, and Figure 40

shows this adjustment.

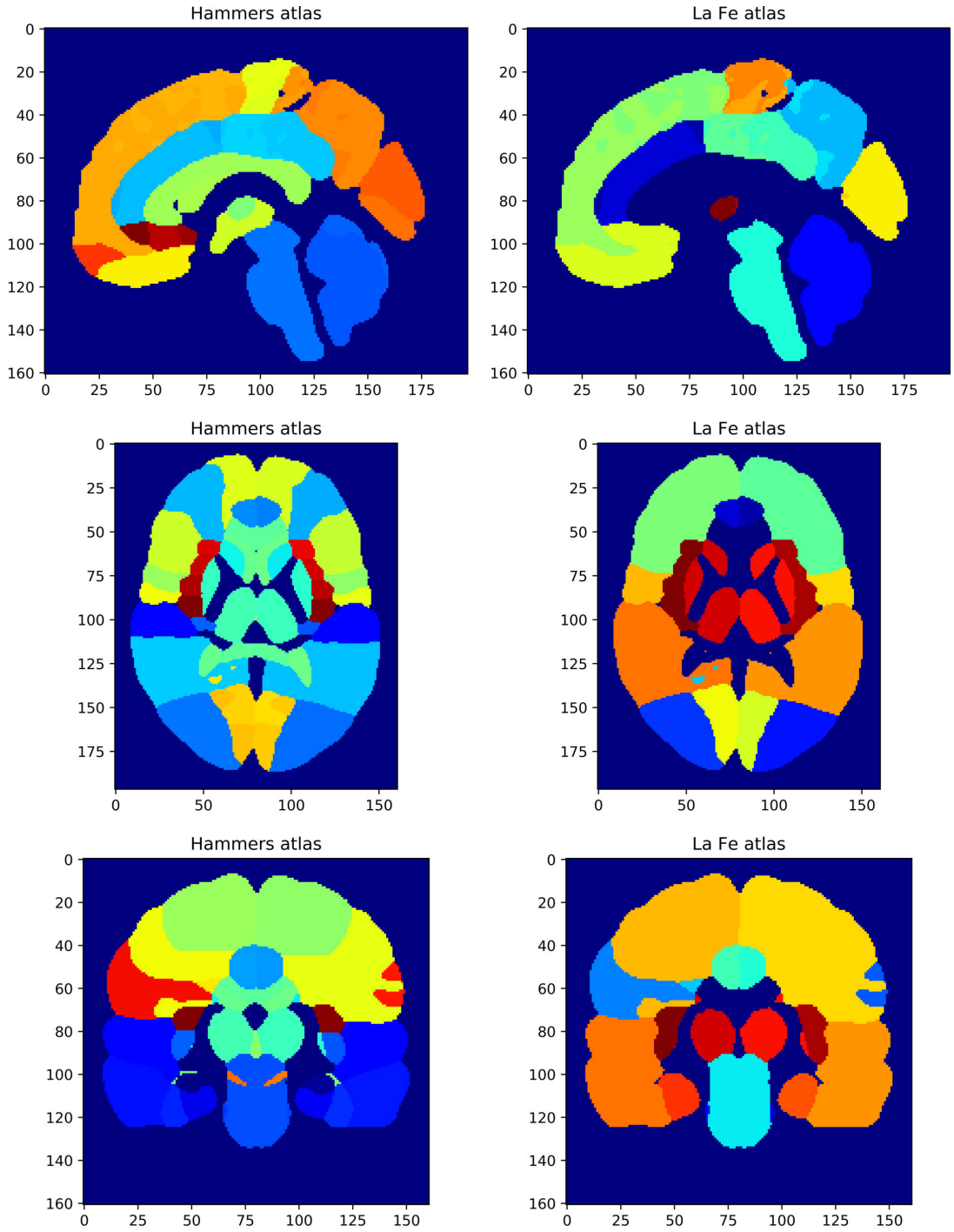

Figure 40: Modification of the Hammers VOI atlas (left) to La Fe atlas (right). From *"Objective image quality comparison between brain-dedicated PET and PET/CT scanners."* by Maria Teresa Gandia-Ferrero, Irene Torres-Espallardo et al. 2023. Copyright by Journal of Medical Systems.

Apart from brain atlases that can be used for measuring activity at different brain areas, segmenting the brain into grey matter (GM) and white matter (WM) is useful for assessing image quality in PET imaging. In the present research, grey matter and white matter were segmented using SPM, which divides the brain into distinct tissue classes using a modified Gaussian mixture model. Knowing the prior spatial probability of each voxel, that is grey matter, white matter or cerebrospinal fluid, it is possible to obtain quite robust classifications. The SPM algorithm selects voxels with a high probability of belonging to each class [181]. Figure 41 shows an example of a grey matter and white matter segmentation of a brain PET image.

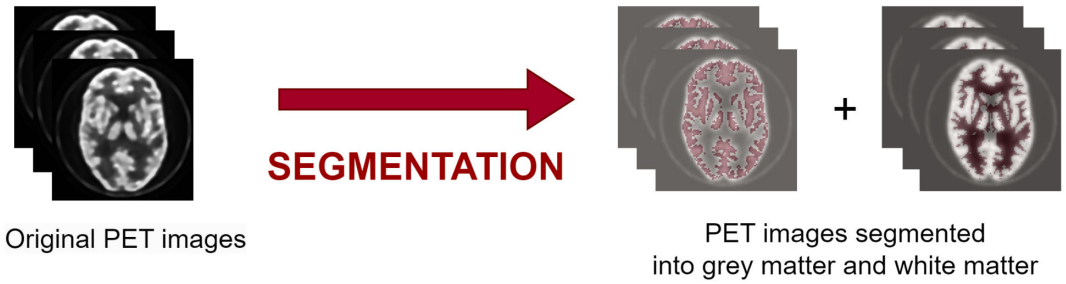

Figure 41: Example of a grey matter and white matter segmentation of a brain PET image.

Table 14: Modification of the Hammers VOI atlas to La Fe atlas (I).

La Fe Atlas VOI	Hammer Atlas VOIs correspondence
Anterior_Cingulate_L	CG anterior cingulate gyrus L
Anterior_Cingulate_R	CG anterior cingulate gyrus R
Cerebellum_Whole	cerebellum R + cerebellum L
Occipital_Lateral_L	OL lateral remainder occipital lobe L
Occipital_Lateral_R	OL lateral remainder occipital lobe R
Parietal_Inferior_L	PL angular gyrus L + PL supramarginal gyrus L
Parietal_Inferior_R	PL angular gyrus R + PL supramarginal gyrus R
Parietal_Superior_and_Precuneus_L	PL superior parietal gyrus L
Parietal_Superior_and_Precuneus_R	PL superior parietal gyrus R
Pons	brainstem excluding substantia nigra + substantia nigra L + substantia nigra R
Posterior_Cingulate_L	CG posterior cingulate gyrus L
Posterior_Cingulate_R	CG posterior cingulate gyrus R
Prefrontal_Lateral_L	FL middle frontal gyrus L + FL inferior frontal gyrus L + FL superior frontal gyrus L + FL lateral orbital gyrus L + FL posterior orbital gyrus L

It is important to remember that all of the image preprocessing and information extraction described above is applied on the image matrix. However, as mentioned in the earlier section (Medical Data Communication), images can include more information than just pixel data (DICOM tag: (7FE0, 0010)). DICOM images can additionally provide information about the equipment, acquisition date and time, the patient's sex and weight, the radionuclide administered for the acquisition, or additional acquisition and reconstruction parameters such as attenuation correction.

Table 15: Modification of the Hammers VOI atlas to La Fe atlas (II).

La Fe Atlas VOI	Hammer Atlas VOIs correspondence
Prefrontal_Lateral_R	FL middle frontal gyrus R + FL inferior frontal gyrus R + FL superior frontal gyrus R + FL lateral orbital gyrus R + FL posterior orbital gyrus R
Prefrontal_Medial_L	FL straight gyrus L + FL anterior orbital gyrus L + FL medial orbital gyrus L + FL subgenual frontal cortex L + FL subcallosal area L + FL pre-subgenual frontal cortex L
Prefrontal_Medial_R	FL straight gyrus R + FL anterior orbital gyrus R + FL medial orbital gyrus R + FL subgenual frontal cortex R + FL subcallosal area R + FL pre-subgenual frontal cortex R
Primary_Visual_L	OL lingual gyrus L + OL cuneus L
Primary_Visual_R	OL lingual gyrus R + OL cuneus R
Sensorimotor_L	FL precentral gyrus L + PL postcentral gyrus L
Sensorimotor_R	FL precentral gyrus R + PL postcentral gyrus R
Temporal_Lateral_L	TL anterior temporal lobe lateral part L + TL superior temporal gyrus middle part L + TL middle and inferior temporal gyrus L + TL fusiform gyrus L + TL posterior temporal lobe L + TL superior temporal gyrus anterior part L
Temporal_Lateral_R	TL anterior temporal lobe lateral part R + TL superior temporal gyrus middle part R + TL middle and inferior temporal gyrus R + TL fusiform gyrus R + TL posterior temporal lobe R + TL superior temporal gyrus anterior part R
Temporal_Mesial_L	TL hippocampus L + TL amygdala L + TL anterior temporal lobe medial part L + TL parahippocampal and ambient gyrus L
Temporal_Mesial_R	TL hippocampus R + TL amygdala R + TL anterior temporal lobe medial part R + TL parahippocampal and ambient gyrus R
Basal_ganglia_L	caudate nucleus L + nucleus accumbens L + putamen L + thalamus L + pallidum L
Basal_ganglia_R	caudate nucleus R + nucleus accumbens R + putamen R + thalamus R + pallidum R
Insula_L	insula posterior long gyrus L + insula anterior short gyrus L + insula middle short gyrus L + insula posterior short gyrus L + insula anterior inferior cortex L + insula anterior long gyrus L
Insula_R	insula posterior long gyrus R + insula anterior short gyrus R + insula middle short gyrus R + insula posterior short gyrus R + insula anterior inferior cortex R + insula anterior long gyrus R

3.2.2 Neuroendocrine tumors: data extraction

Experienced nuclear medicine physicians evaluated the imaging results. They assessed the Standard Uptake Value maximum and the target-to-liver ratio for all detected lesions. Additionally, SUVmax and SUVmean values were measured in both the liver and spleen. SUVmax was determined by generating isocontour volumes of interest, including all voxels exceeding 40% of the maximum uptake, both in lesions and in normal liver tissue. All these measurements were performed in software Philips IntelliSpace Portal and in GE Advantage Workstation (AW) with PET Volume Computer-Assisted Reading (VCAR) software.

Lesions were classified based on PET/CT and PET/MRI findings. Focal non-physiological uptakes on PET that correlated with abnormalities on CT or MR were identified as tumor lesions. Uptakes with confirmed benign features on CT or MR, as well as physiological uptakes without corresponding lesions, were classified as negative. Focal bone uptakes that could not be attributed to insertional or inflammatory processes were considered malignant. Non-physiological PET uptakes without corresponding CT or MR findings were interpreted on a case-by-case basis, particularly in patients with known small lesions. Lesion confirmation was based on prior and follow-up imaging studies, as well as histological data obtained from surgery or biopsy.

3.3 Data analysis

After quantification of PET images, different techniques have been employed for both dementia and neuroendocrine tumors applications. In this subsection, it will be discussed how raw data is converted into meaningful insights using modelling tools, allowing us to discover patterns, predict outcomes, and improve decision-making. A variety of methods will be introduced, starting with neural networks, which have transformed fields such as medical imaging and predictive modelling. Image quality metrics, which are critical for evaluating and enhancing the clarity and accuracy of visual data, will also be discussed. Additionally, harmonization techniques will be explored, with an emphasis on how they create uniformity across different PET scanner devices. Finally, statistical analysis will provide the basis for interpreting findings, verifying models, and making reliable conclusions.

3.3.1 Neural Networks

In this part of the Thesis, a validation of a Convolutional Neural Network (CNN) trained in order to classify patients who presented mild cognitive impairment with an associated neurodegenerative disease from those without it, was used. However,

before mentioning Convolutional Neural Networks, it is important to cover the basis by introducing many basic ideas in machine learning and neural networks. Therefore, this point includes a review of supervised and unsupervised learning, neural network structure and training, and the relevance of activation functions. Furthermore, the limitations of fully linked networks, notably in managing complicated image data, will be mentioned. All these points will give the framework for understanding CNNs and their importance in image processing applications.

3.3.1.1 Basic Concepts of Artificial intelligence

In today's rapidly advancing tech landscape, terms like artificial intelligence (AI), machine learning (ML), neural networks (NN), and deep learning (DL) are often used interchangeably, leading to confusion. While these concepts are closely related, each represents a distinct aspect of the field of AI, with unique characteristics and applications. Figure 42 represents the relationship between artificial intelligence, machine learning, neural networks, and deep learning.

Artificial intelligence is a word used to describe technologies or systems that simulate human intelligence when performing activities like problem solving, learning, and decision-making. AI capable of processing massive volumes of data and identifying trends that would be highly difficult for people to detect. It includes anything from basic decision-making systems to cutting-edge technology like self-driving automobiles [185].

Machine learning is a subset of AI that learns from data with minimal human interaction to classify categories or predict future or unknown conditions. Since ML is data-driven, it falls under the category of nonsymbolic AI and can predict from previously unseen data. ML tasks include regression, classification, detection, segmentation, and so forth. In general, machine learning data sets are made up of training, validation, and test sets. It learns data properties using the training dataset and validates them using the validation dataset. Finally, the test data set may be used to verify the accuracy of machine learning [186, 187].

Neural Networks are ML models inspired by the structure of the human brain. They are made up of interconnected "neurons" or nodes. Neural networks can process and classify data, and they are commonly employed for tasks such as image or speech recognition. Neural networks are essential for more complex ML models, but they require more data and computing than simple ML techniques [185, 188].

Deep Learning is a subset of neural networks that has a multi-layered structure that enables it to learn features from raw data without the need for manual input. This is what allows applications such as image recognition, language translation, and self-driving vehicles. Deep learning is more difficult than ordinary machine learning, requiring greater processing power and huge datasets [185, 187–189].

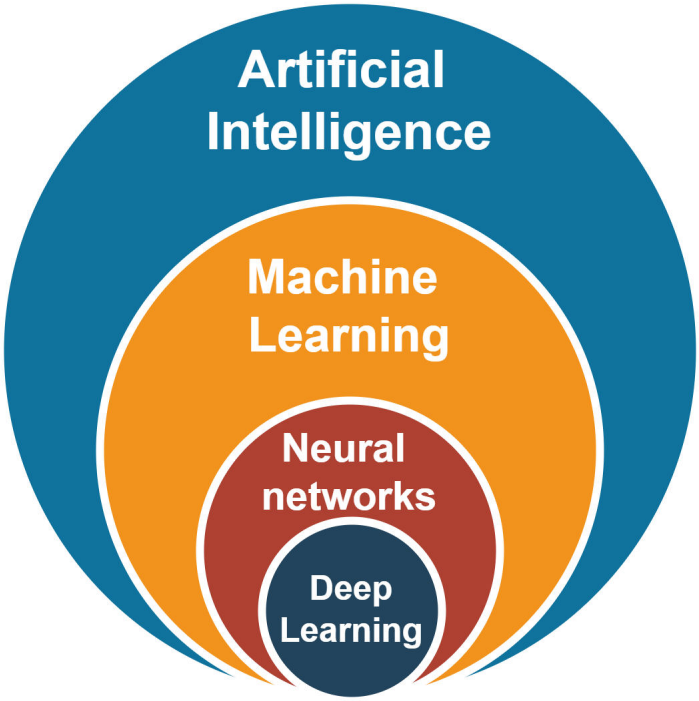

Figure 42: Relationship between artificial intelligence, machine learning, neural networks, and deep learning.

ML approaches are classified as supervised, unsupervised, and reinforcement learning. Reinforcement learning is not suitable for medical applications because to the impact on patients' health and treatment alternatives. As a result, long-term effects are difficult to predict [186]. Before differentiating between supervised and unsupervised learning is important to define the terms features and labels. The variables that a supervised model uses to predict the label are called features. The value we want the model to predict, or the answer, is the label.

The primary distinction between supervised and unsupervised learning is whether the training data set includes labelled outputs that match to input data. **Supervised learning** establishes a mathematical link between inputs and labelled outputs, whereas **unsupervised learning** infers a function to describe hidden qualities in input data. Supervised learning outputs might be categorised or numerical, depending on the job. When the output data is categorical, it becomes a classification or pattern recognition issue. For continuous numerical data, it becomes a regression problem. The classification task might be binary, multiclass, or multilabeled, with multilabeled indicating more than one class in each input data. Unsupervised learning involves clustering, principal component analysis, and generative adversarial networks (GANs) [186].

A supervised learning method, for instance, begins with PET images that have been classified as either normal or diseased. Machine learning will then generate a mathematical model that might associate PET images to diagnosis in both training and

test data. Clustering is an example of unsupervised learning in which the algorithm identifies subgroups within a given set of patients with the same condition [190].

3.3.1.2 Introduction to Neural Networks

Neural networks are a statistical machine learning approach based on brain mechanisms from neuroscience. Researchers developed a learning system that mimics how the brain processes information. A neuron is the basic element of the brain mechanism. Neurons are electrically excitable cells that receive, process, and transfer messages to other neurons. They activate and transfer signals when their input signal exceeds a specific threshold and constitute a network that controls the brain's process [190–192]. A perceptron represents the simplest type of neural network (Figure 43). It takes multiple input values, applies a set of weights, sums them, adds a bias, and passes the result through an activation function to produce a single output. The mathematical processing of the output can be described by the following equation:

$$\hat{y} = \varphi(w_0 + \sum_{i=1}^{n} x_i w_i) \tag{3.3.1}$$

where x_1 ... x_n is the vector of inputs passed to the algorithm, w_1 ... w_n represent the set of weights, w_0 is the bias, and φ the activation function.

An activation function in a neural network introduces non-linearity to the model, enabling it to learn and represent complex patterns. It transforms the weighted sum of inputs into an output for each neuron, determining whether the neuron should be activated or not. Some of the most common activation functions are the following:

$$\textbf{sigmoid: } \varphi(z) = \frac{1}{1 + e^{-z}} \tag{3.3.2}$$

$$\textbf{ReLU: } \varphi(z) = max(0, z) \tag{3.3.3}$$

$$\textbf{tanh: } \varphi(z) = \frac{e^{z} - e^{-z}}{e^{z} + e^{-z}} \tag{3.3.4}$$

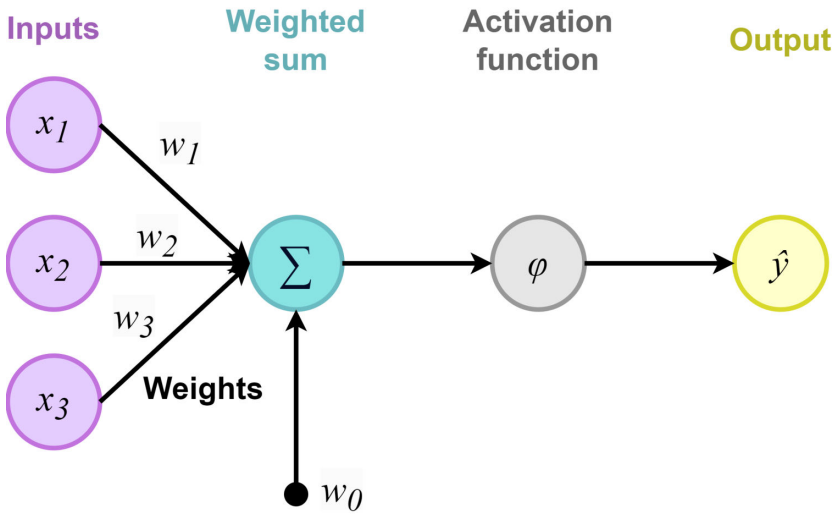

Figure 43: Example of a perceptron.

Figure 44 represents an example of a multilayer perceptron. An input layer that aggregates input signals from other linked neurons, a hidden layer that handles training, and an output layer make up an artificial neural network, which is an abstraction of an interconnected network of neurons with layers of nodes. Every node takes the activation function using the input from nodes in the preceding layer using different weights, and then relays the results to the nodes in the next layer. The activation function mimics a neuron's non-linear regulation of output strength [190–192].

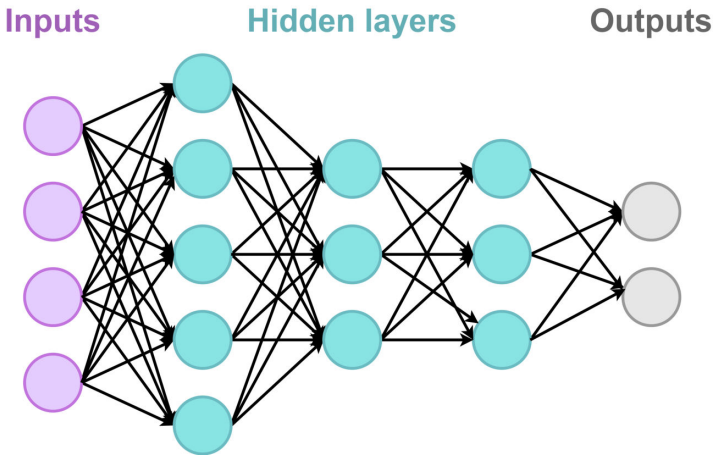

Figure 44: Example of a multilayer perceptron.

Since neural network includes 'hidden' layers between the input and output layers, the units of the neighbouring layers are fully connected to each other. Feedforward in neural networks is the process where data moves in one direction through the network, from input to output, without any loops or cycles. Each layer passes its output to the next layer until the final output is generated. This is the basic architecture for tasks like classification or regression [193].

Neural network training process involves updating weights across nodes to explain training data and minimise loss values. Backpropagation is a training algorithm for neural networks that adjusts the weights and biases by calculating the gradient of the loss function with respect to each parameter. It works by propagating the error backward from the output layer to the input layer, allowing the network to learn by minimizing the error through gradient descent. Back-propagation of losses modifies weights and biases in the network. As a consequence, NN components are updated to better represent target values [194, 195].

The fundamental concepts of neural network training are easy to comprehend: when training data is input into the network, perform the chain rule to calculate the gradient of the loss function relative to each weight, and use gradient descent to lower the loss by varying these weights. A neural network's weights are updated throughout training in order to optimise the network's outputs. This is accomplished by applying an optimization algorithm known as gradient descent to a cost function or loss function that measures how accurate the outputs are [196]. Some of the most common loss functions, which measure the error between the predicted output ($\hat{y}$) and the true target (y), are the following:

$$\textbf{Mean Squared Error: } MSE = \frac{1}{n}\sum_{i=1}^{n}(y_i - \hat{y}_i)^2 \tag{3.3.5}$$

$$\textbf{Cross Entropy Loss: } CE = -\frac{1}{n}\sum_{i=1}^{n}(y_i log(\hat{y}_i) + (1 - y_i) log(1 - \hat{y}_i)) \tag{3.3.6}$$

Training neural networks is truly an art. The model is sometimes overparametrized, making the optimization problem nonconvex and unstable unless specific rules are followed. Some of the most popular issues include overfitting, the number of hidden units and layers, and input scaling.

Overfitting in neural networks happens when a model learns the training data too well, accumulating noise as well as specific patterns that are not relevant to new, unseen data. This occurs when the model gets excessively complex, with too many parameters compared to the quantity of training data, causing it to "memorise" rather than learn general patterns. As a result, the model performs well on the training set but fails on validation or test data. Regularization, dropout, and the use of extra data can all assist to prevent overfitting and increase generalization [197].

Regarding the number of hidden units and layers, it is typically preferable to have too many than too few. Using too few hidden units may limit the model's ability to capture nonlinearities in data, while using too many might reduce excess weights to zero with proper regularization. Typically, the number of hidden units ranges from 5 to 100, growing with inputs and training cases. Typically, a large number of units are put down and trained using regularization methods. The number of hidden layers is determined by background knowledge and experimentation. Each layer extracts features from the

input for regression or classification. Using multiple hidden layers allows construction of hierarchical features with different levels of resolution [198].

Finally, scaling inputs has a substantial impact on the quality of the final result. Standardizing all inputs to have a mean of zero and a standard deviation of one provides equal treatment in the regularization process while also providing a reasonable range for the random starting weights [198].

3.3.1.3 Convolutional neural networks

Convolutional neural networks are a state-of-the-art technique for computer vision applications, having notably profited from the recent development and availability of high-performance computing systems as well as large-scale data repositories. They are especially effective in image classification [199].

CNN is a network architecture composed of many stacked convolutional layers. Convolution is a mathematical process involving addition and multiplication. Convolution is ideal for image identification as it considers local information, such as neighbouring voxels or pixels. CNN was the initial driver for broad use of deep learning. LeNet-5 and other well-known designs, such as AlexNet, GoogLeNet, VGG-Net, and ResNET, have significantly advanced machine learning algorithms for recognizing handwritten digits. Convolutional neural networks (CNNs) are being used in computer vision for both supervised and unsupervised learning tasks as part of deep learning techniques. CNN has broken all-time records for traditional vision tasks [186, 190]. CNNs consist of the following building blocks [196]:

- **Convolutional layers** in neural networks involve convolving previous layers' actions with small parameterized filters, often of size 3×3, to achieve translational equivariance and reduce the number of weights needed for learning. This is because features appearing in one part of the image likely also appear in other parts. Applying all convolutional filters at all input locations produces a tensor of feature maps.

- The **activation layer** feeds feature maps from a convolutional layer through nonlinear activation functions, allowing the entire neural network to approximate almost any nonlinear function. These functions are typically simple regularized linear units (ReLUs) or variants like leaky ReLUs or parametric ReLUs.

- A **pooling layer** is used to reduce the spatial dimensions (width and height) of feature maps, making the network more computationally efficient and helping prevent overfitting. It works by summarizing regions of the input, typically using operations like max pooling or average pooling. Max pooling selects the maximum value from a patch of the feature map, while average pooling calculates the average

value. Pooling layers help retain important features while reducing the overall size of the data as it moves through the network.

- **Dropout regularization** is another common element in CNNs, which averaging several models in an ensemble leads to better performance than using single models. By randomly removing neurons during training one ends up using slightly different networks for each batch of training data, and the weights of the trained network are tuned based on optimization of multiple variations of the network.

- **Batch normalization** is a technique where layers are placed after activation layers, producing normalized activation maps by subtracting the mean and dividing by the standard deviation for each training batch. This forces the network to periodically change its activations to zero mean and unit standard deviation, speeding up training and making it less dependent on careful parameter initialization.

- **Fully Connected (Dense) Layers** are used in the final stages of the CNN. These layers connect all neurons from the previous layer to every neuron in the next, often leading to a classification output.

In the design of new and improved CNN architectures, these components are combined in increasingly complicated and interconnected ways, or even replaced by other more convenient operations. When architecting a CNN for a particular task there are multiple factors to consider, including under-standing the task to be solved and the requirements to be met,figuring out how to best feed the data to the network, and optimally utilizing one's budget for computation and memory consumption [196].

The CNN design may include millions of training parameters because to its many layers. Acquiring adequate accuracy requires a significant amount of data during training. The amount of data collected depends on the task and image attributes. Data gathering can be challenging, especially when labelling is required. To address this issue, data augmentation can build graphics from limited data using image manipulation techniques including rotation, translation, scaling, and flipping [190].

3.3.2 Image Quality metrics

The past few decades have seen significant advancements in image research and development, leading to improved image quality performance. Therefore, there is a need for a good standard of image quality evaluation for assessing any newly designed hardware, software, higher field strength (in MR) or radiation (in CT, X-ray or PET), image reconstruction techniques and image processing algorithm, among others. A high-quality image will boost diagnostic confidence and help determine the best strategy for treatment [200].

For the PET image quality evaluation in this work, the following metrics were employed:

- **Contrast**: The contrast of an image represents the difference in signal intensity that differentiates objects from one another. High contrast images show strong differences between light and dark areas, whilst low contrast images indicate more gradual transitions and less differentiation between tones. The following equation can be used to calculate the contrast between GM and WM:

$$Contrast = \frac{Mean(GM) - Mean(WM)}{Mean(WM)} \tag{3.3.7}$$

where

$$Mean(VOI) = \frac{\sum_{i \in VOI} A_{\text{con}}(i)}{N_{\text{VOI}}} \tag{3.3.8}$$

i is a voxel that belongs to the VOI and N is the total number of voxels.

- **Recovery coefficient** (RC): The recovery coefficient in PET imaging measures the accuracy of the detected radioactivity in a region of interest compared to the actual radioactivity present. It reflects how successfully the imaging system retrieves the true signal, with 1 representing complete recovery and values less than 1 suggesting some degree of underestimating. It isdefined as the ratio between the measured activity and the theoretical activity.

$$RC(GM) = \frac{A_{\text{con}_\text{M}}(GM)}{A_{\text{con}_\text{T}}(GM)} \tag{3.3.9}$$

where A_{con_M} is the measured A_{con} and A_{con_T} is the theoretical A_{con}.

- **Signal to noise ratio** (SNR): An image's signal-to-noise ratio measures the quantity of desirable signal in comparison to the level of background noise. A higher SNR indicates a better image quality with less noise, whereas a lower SNR indicates more noise, which could mask important details of the image. This metric can be calculated for both GM and WM VOIs, separately.

$$SNR(VOI) = \frac{Mean(VOI)}{SD(VOI)} \tag{3.3.10}$$

where

$$SD(VOI) = \sqrt{\frac{\sum_{i \in VOI} A_{\text{con}}(i) - Mean(VOI)}{N(VOI)}} \tag{3.3.11}$$

- **Contrast to noise ratio** (CNR): The contrast-to-noise ratio in an image evaluates the clarity of the signal (contrast) compared to background noise. A higher CNR means that features are more visible, whereas a lower CNR implies that noise could hide important details.

$$CNR = \frac{Mean(GM) - Mean(WM)}{SD(WM)} \tag{3.3.12}$$

- **Coefficient of variation** ($COV_{10\text{min}}$): The coefficient of variation is another metric that allows the description of the image noise. It quantifies the relative variability of pixel intensity values. A higher COV indicates greater noise relative to the signal, while a lower COV suggests more uniformity in pixel values, reflecting less noise in the image. This metric can be calculated for both GM and WM VOIs, separately.

$$COV_{10\text{min}} = \frac{Mean_{\text{SD}_{10\text{min}}}(VOI)}{Mean_{\text{mean}_{10\text{min}}}(VOI)} \tag{3.3.13}$$

- **Standardized Uptake Value ratio** ($SUVr$): Since the potential of PET is the capability to reproduce the image activity concentration, image quantification is crucial. Consequently, SUVr comparison between the same brain areas in two different devices could be an important image quality metric, considering that SUVr it is an essential parameter employed in the brain imaging studies. In this work, for the SUVr calculation the cerebellum whole was selected as the region of reference. Therefore, this metric was calculated for the remaining 27 VOIs of La Fe atlas [60].

$$SUVr = \frac{SUV_{\text{VOI}}}{SUV_{\text{referenceregion}}} \tag{3.3.14}$$

where

$$SUV_{\text{VOI}} = \frac{A_{\text{con}}^{VOI}}{A_{\text{con}}^{adm}} \tag{3.3.15}$$

and A_{con}^{adm} is the administered activity concentration.

3.3.3 Harmonization methods

One of the advantages of PET imaging, as discussed previously, is its high quantitative accuracy [201]. Depending on the goal of each PET imaging, different quantitative metrics are adopted. In treatment response evaluation studies, quantitative metrics like SUVs and their percentage change can be used as an a surrogate marker to evaluate the therapeutic response [202–204]. Many studies and trials have used changes in tumor SUVs as primary and secondary endpoints for evaluating the treatment response using pre-therapy and follow-up PET [203, 205, 206]. SUVs would be one of the most significant biomarkers for clinical decision-making in such situations [207].

Nevertheless, technological variables (such as quality control and quality assurance for a PET system and other instruments, cross calibration between a PET system and dose calibrator; residual radioactivity in syringes and tubes; synchronization of clocks between a PET system and dose calibrator; or decay correction of injected radioactivity), biological variables (such as uptake duration; patient motion and breathing; patient preparation; or blood glucose level), and physical variables (such as acquisition duration; image reconstruction parameters; VOI definition; normalization

factors for SUV; or attenuation correction position mismatch) might affect the quantitative data obtained from PET [178, 207–209]. Moreover, when quantitative metrics are used in multicenter research, the metrics' variability might significantly affect the study outcomes [210, 211].

All these effects are detrimental to the design and validation of predictive or prognostic models, limiting their potential for use with large multicenter cohorts. Harmonising image acquisition and reconstruction processes is crucial to decrease multicenter variability when pooling data from many sites, as many quantitative biomarkers and radiomic characteristics are sensitive to scanner or protocol effects, often known as the site effect [212–216]. Similarly, when a novel radiomic or quantitative image analysis approach is established at one site and used to images from another, it must first be verified that the images from both locations are comparable. Harmonization strategies are an urgent need to mitigate the effects of this variability.

In this work, two methods are employed to both harmonize quantitative variables (ComBat) and to standardize quantitative estimations from PET images (Centiloid Scale) across different PET scanners.

3.3.3.1 ComBat

ComBat harmonization is a statistical method designed to reduce batch effects and other undesired variations in data. It was first proposed in the field of genomics [217], and nowadays is widely used in neuroimaging, and many other clinical investigations [218–222].

When datasets gather information from multiple sources or scanners, they may have inherent biases that might mask truly biological or experimental signals. ComBat corrects these biases by adjusting for known batch factors, allowing data from many different sources to be compared more directly and meaningfully. The method models and adjusts data using an empirical Bayesian framework while preserving important biological variations across groups. ComBat directly applies to quantitative values derived from PET images. Therefore, additional image data processing and any phantom data acquisition are not mandatory [207].

An example of ComBat harmonization can be observed in Figure 45. This example shows the distribution of the SUVr in the right basal ganglia of a group of patients acquired on a PET/CT device and a brain-dedicated scanner (CMB) before (on the left) and after (on the right) ComBat harmonization.

ComBat assumes that:

$$y_{ij} = \alpha + \gamma_i + \delta_i \varepsilon_{ij} \tag{3.3.16}$$

where j represents the specific measurement of feature y, i denotes the setting, α is the average value of the feature of interest y, ε_{ij} is an error term, and γ_i and δ_i represent an additive and multiplicative batch effect, respectively.

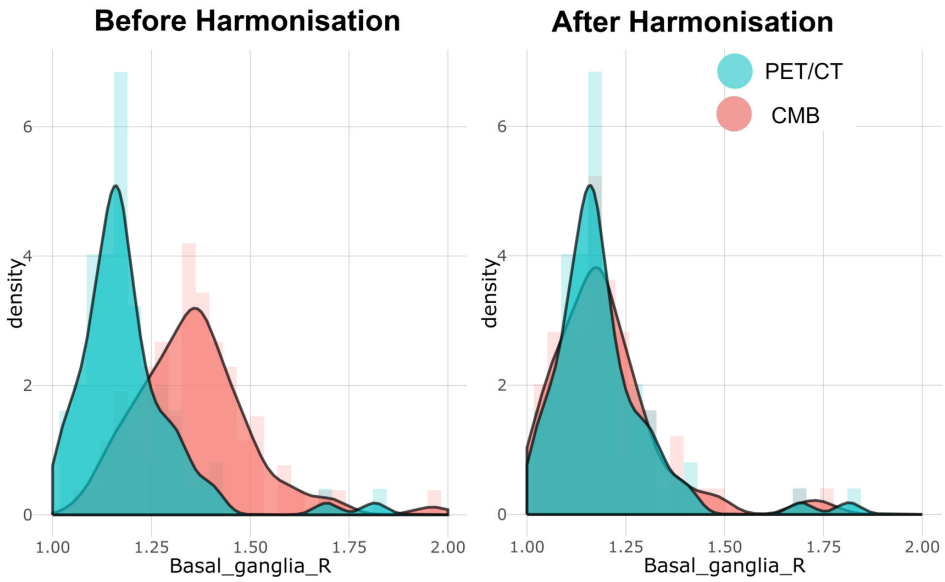

Figure 45: Example of ComBat harmonization of right basal ganglia SUVr between 2 different scanners: PET/CT (green) and CMB (red).

In medical imaging, y represents an image feature (e.g., SUV), i represents the scanner, protocol effect, or observer effect (sometimes known as the site effect), and j represents the measurement, usually the volume of interest. The model therefore considers that the value of measurement i of a particular feature y in volume of interest j may be influenced by additive and multiplicative effects that vary depending on the scanner, procedure, or even observer who took the measurement. These effects apply to all measurements j of the same amount y obtained with the same scanner, methodology, or observer [223]. Multiple measurements y_{ij} of the same feature y made in volume of interest j in different images acquired from independent scanners i, the site effects γ_i and δ_i may be assessed using conditional posterior means and then corrected using the following equation:

$$y_{ij}^{ComBat} = \frac{\hat{y}_{ij} - \hat{\alpha} - \hat{\gamma}_i}{\hat{\delta}_i} + \hat{\alpha} \tag{3.3.17}$$

where $\hat{\alpha}$, $\hat{\gamma}_i$ and $\hat{\delta}_i$ are estimators of α, γ_i and δ_i and y_{ij}^{ComBat} is the transformed y_{ij} measurement without the site i effect [223].

In neuroimaging, for example, ComBat harmonization has been modified to address site-specific effects across imaging centers, allowing for more consistent brain imaging measures across different datasets. ComBat harmonization improves data comparability, which is important for large-scale research when collecting data from several different sources is required for reliable outcomes. In this work, neuroCombat package in R was used for the harmonization methods [224].

3.3.3.2 Centiloid Scale

The centiloid scale (CL) is a widely used data-driven harmonization technique. It was proposed by Klunk et al., as a standardized metric for assessing amyloid plaque levels in the brain that is frequently related with Alzheimer's disease [225]. The Centiloid scale measures amyloid levels from 0 to 100, with 0 representing a healthy, amyloid-negative brain without Alzheimer's disease, and 100 reflects the typical amyloid level found in Alzheimer's disease individuals with severe plaque accumulation [207].

The Centiloid Project developed a standardized amyloid measurement scale using two key subject groups. The first group, the Young Control 0-Anchor (YC-0), consisted of 34 cognitively normal adults under 45 years old, with an average age of 31.5 years. These individuals were chosen to be amyloid-negative, as they rarely exhibit amyloid buildup. The data from these subjects provided a baseline amyloid level of 0 on the Centiloid scale. The second group, the Alzheimer's Disease 100-Anchor (AD-100), consisted of 45 individuals diagnosed with Alzheimer's disease, with an upper reference point of 100 on the scale. These two anchor groups provided a reliable scale that ranged from no detectable amyloid to high levels of amyloid plaque, providing a robust reference framework for amyloid pathology across cognitive health and Alzheimer's disease [225].

The standard SPM8-based processing system as well as the volumes of interest, PiB PET, and T1 3D MRI imaging datasets, all of which are available for download, are described by Klunk et al [225]. Additionally, they offer the standard uptake value ratios that their data should generate. Before using this method, users need to develop their own code by following the instructions provided by Klunk et al. and test it employing the original data in order to use the Centiloid scale.

First, the software must be validated employing the GAAIN dataset (https://www.gaain.org/centiloid-project) and using the pipeline created by Klunk et al. (replication of the Level-1 analysis). All MR images must be coregistered and spatially normalized to the Montreal Neurosciences Institute-152 template using MATLAB's SPM unified segmentation method. All PET scans are then coregistered to each patient's MR images and spatially normalized to Montreal Neurosciences Institute space using transformation parameters that were computed from the MR images. SUVr values were used to calculate CL values. The global cortical target (CTX) is the VOI employed in

the present study (see Figure 46). According to the original study, the four VOIs that corresponded to the reference VOIs were Cerebellum Gray, Pons, Whole Cerebellum, and Whole Cerebellum plus Brainstem (see Figure 47).

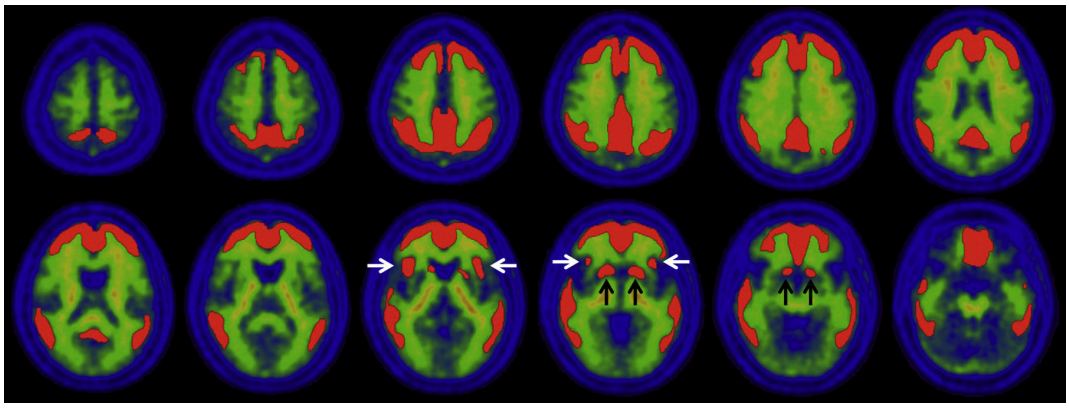

Figure 46: The global cortical target (CTX) VOI (red). From *"The centiloid project: Standardizing quantitative amyloid plaque estimation by PET."* by William E. Klunk et al. 2015. Copyright by Alzheimer's and Dementia.

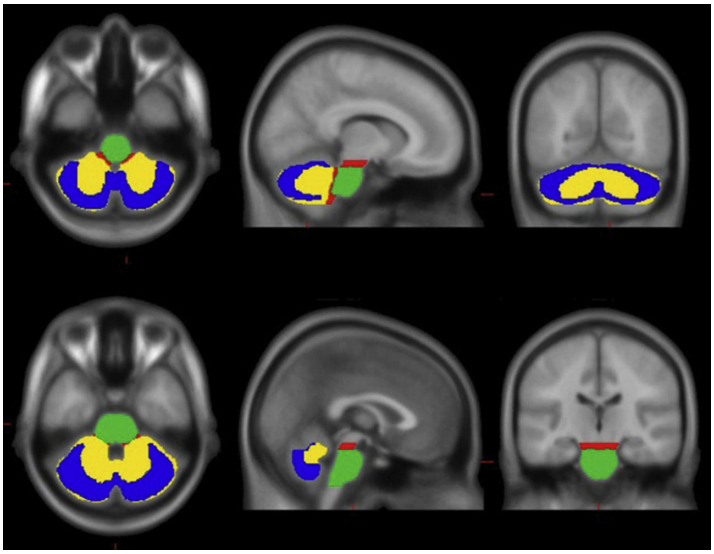

Figure 47: The reference VOIs: Cerebellum Gray (blue), Pons (green), Whole Cerebellum (blue + yellow), and Whole Cerebellum plus Brainstem (which would be represented by all colors combined where the red area represents that part of the Whole Cerebellum plus Brainstem that does not overlap either the WC or the Pons). From *"The centiloid project: Standardizing quantitative amyloid plaque estimation by PET."* by William E. Klunk et al. 2015. Copyright by Alzheimer's and Dementia.

It is required to calculate the normalized PET image CL values and establish a linear correlation with the original CL values. This analysis must be done by comparing the original results provided by Klunk et al. with the obtained results on the analysis of the 34 YC-0 and 45 AD-100 subject data. The expectations of Klunk et al. must be

satisfied (slope between 0.98 and 1.02, intercept between -2 and 2 CL and $R^2 > 0.98$) in order to validate the replication of the Level-1 analysis.

Once the replication of the Level-1 analysis is validated, the equations to convert SUVr into CL units can be applied to the images of the centers themselves. Since the Cerebellum Whole (CW) it is the reference region employed in the previously calibrated methods [19,20,21], it was chosen as the reference region. Based on the previously calibrated procedures [19,20,21], the standard equations to convert SUVr data into CL units applied to each individual for the three amyloid radiotracers used in this study was as follows:

$$[^{18}F]Flutemetamol : CL = 121.42 \cdot SUV_{\mathrm{r}} - 121.16 \tag{3.3.18}$$

$$[^{18}F]Florbetaben : CL = 153.4 \cdot SUV_{\mathrm{r}} - 154.9 \tag{3.3.19}$$

$$[^{18}F]Florbetapir : CL = 183 \cdot SUV_{\mathrm{r}} - 177 \tag{3.3.20}$$

3.3.4 Statistical analysis

In this subsection of the methodology, we will describe the methods that were used to analyze, validate, and interpret data in this study. These approaches give an appropriate basis for evaluating reliability, agreement, and diagnostic accuracy, with each addressing a distinct analytical need throughout the case study. Agreement measurements, such as the kappa index and Youden's index, determine the reliability and usefulness of diagnostic classifications, whereas distribution tests and comparative studies evaluate group differences. Correlation, regression, and agreement analyses, such as Spearman's rank correlation, Passing-Bablok regression and Bland-Altman plots, provide insights into variable relationships and are powerful tools for evaluating bias and agreement. Furthermore, classification metrics generated from confusion matrices and ROC curves aid in the evaluation of prediction accuracy, while neural network attention maps improve interpretability for image-based models. This variety of methods guarantees both statistical consistency and a full understanding of the data's relationships and patterns.

3.3.4.1 Comparative analysis of groups

For the comparison analysis of different groups, parametric and non-parametric tests can be used depending on the samples distribution. Parametric tests are those

that make assumptions about the parameters of the population distribution from which the sample is drawn. The parametric statistical inference assumes that the data are a random sample from a population with a known probability distribution, which is often dependent on unknown parameters. This type of inference is valid only if the probability distribution used accurately describes the probabilistic behavior of the data. The literature has a wide range of goodness-of-fit tests that address the issue of determining if a parametric family of distributions provides an adequate fit to the data. The normal distribution, commonly known as the Gaussian distribution, is one of the most often used distributions because of its simplicity. It is suitable for modelling symmetric data sets. Non-parametric tests are "distribution-free" and, as such, can be used for non-normal variables [226].

Shapiro-Wilk Test is a robust method for testing data normality. It was published in 1965 by Samuel Sanford Shapiro and Martin Wilk. The test calculates a W statistic based on how closely the data points follow a theoretical normal distribution [227]. The W statistic formula is:

$$W = \frac{(\sum_{i=1}^{n} a_i X_{(i)})^2}{\sum_{i=1}^{n}(X_{(i)} - \bar{X})^2} \tag{3.3.21}$$

where $X_{(i)}$ are the ordered statistics corresponding to the random sample $X_{(1)}$, $X_{(2)}$, ..., $X_{(n)}$, $\bar{X}$ is the sample mean, and a_i are the Shapiro-Wilk coefficients, based on expected values from a normal distribution [226].

The null hypothesis for this test is that the population is normaly distributed. Thus, if the p-value is smaller than the chosen alpha level, the null hypothesis is rejected, indicating that the data studied are not normally distributed. On the other hand, if the p value is greater than the chosen alpha level, then the null hypothesis (that the data came from a normally distributed population) cannot be rejected.

In this study, for the comparative analysis between groups, two statistical tests have been used depending on the distribution of the analyzed samples: the t-test (parametric test) and the Mann-Whitney-Wilcoxon test (non-parametric test).

The **t-test**, additionally referred to as the student's t-test, is a popular statistical hypothesis test that assesses whether two sets of data differ significantly by comparing the means of two groups while accounting for possible variability. It is a method applied to basic and clinical science research in all areas of medicine. Clinicians and researchers can benefit from a basic understanding of the t-test in order to conduct relevant experiments and interpret data accurately. The one-sample t-test, two-sample t-test, and two-sample paired t-test are the three types of the t-test [228].

Understanding the assumptions and limitations for each variation of the t-test is essential to avoid major errors due to the incorrect use of statistical tests in medical

research, particularly when using the commonly employed t-test analysis. In order to produce valuable findings, the t-test depends on a number of assumptions on the sample under analysis. In t-tests, the sample standard deviation is used to compare the difference in means since the population standard deviation is unknown [229–231]. Being a parametric procedure, t-tests are often applicable when the sample meets the assumptions of data independence, normality and equal variances.

To determine whether a sample mean deviates significantly from the population mean or a specified constant, **one sample t-test** is employed. In contrast to the independent samples t-test, which compares the means of two defined samples, the one-sample t-test is based on a reference mean. When evaluating the impact of a novel treatment on a single patient group, the one sample t-test is frequently employed [232, 233].

The null (H_0) and alternative H_1 hypothesis for the one sample t-test are: H_0: the population mean is equal to some value (μ_0). H_1: the mean is greater or less than μ_0.

The t-statistic for the one sample t-test is calculated as [228]:

$$t = \frac{\bar{x} - \mu_0}{\frac{s}{\sqrt{n}}} \tag{3.3.22}$$

where $\bar{x}$ is the sample mean, μ_0 is the reference mean, n is the sample size, and s is the standard deviation calculated as:

$$s = \sqrt{\frac{\sum_{i=1}^{n}(x_i - \bar{x})^2}{n-1}} \tag{3.3.23}$$

When the dependent variable is continuous and normally distributed and the two independent variables are discrete levels or groups, the **independent sample t-test**, additionally known as an unpaired two-sample t-test, is frequently used. The purpose of this test is to determine whether the means of the two distinct populations under comparison are identical. The main difference is that the one-sample t-test is used to test whether the mean of a normally distributed population is different from a specified value, whereas the two-sample t-test is used in toder to test whether the means of two populations are significantly different from one another. In this work, the two-sample t-test was used. Unless the samples are large enough to satisfy the central limit theorem, this t-test assumes that samples were independently chosen from their population and that the populations have a normal distribution. It does not assume that the population has equal variance [234, 235].

The null (H_0) and alternative H_1 hypothesis for the independent sample t-test are:

H_0: the means of the two populations are equal ($\mu_1 = \mu_2$). H_1: the means of the two populations are unequal ($\mu_1 < \mu_2$ or $\mu_1 > \mu_2$).

The t-statistic for the independent sample t-test is calculated as [228]:

$$t = \frac{(\bar{x_1} - \bar{x_2}) - (\mu_1 - \mu_2)}{\sqrt{S_p^2(\frac{1}{n_1} + \frac{1}{n_2})}} \tag{3.3.24}$$

where $\bar{x_1}$ is the mean of sample 1, $\bar{x_2}$ is the mean of sample 2, μ_1 and μ_2 are the mean of populations 1 and 2, n_1 and n_2 are the sample sizes, and S_p^2 is the pooled variance which is calculated as:

$$S_p^2 = \frac{(n_1 - 1)S_1^2 + (n_2 - 1)S_2^2}{n_1 + n_2 - 2} \tag{3.3.25}$$

The **paired t-test** is employed when data in a sample assumes the form of matched pairs, as opposed to the independent sample t-test, which evaluates the means of two statistically independent samples. The paired t-test basically assumes that the data is normally distributed, as compared to a two-sample t-test that makes the assumptions that the data from both samples are independent, normally distributed, and do not assume equal variances [234].

The null (H_0) and alternative H_1 hypothesis for the paired sample t-test are:

H_0: the average of the differences between the paired observations in the two samples is zero. H_1: the average of the differences between the paired observations in the two samples is not zero.

The t-statistic for the paired sample t-test is calculated as [228]:

$$t = \frac{\bar{d} - (\mu_1 - \mu_2)}{\frac{s_d}{\sqrt{n}}} \tag{3.3.26}$$

where $\bar{d}$ is the mean of difference in scores, μ_1 and μ_2 are the means of populations 1 and 2, n is the sample size, and s_d is the standard deviation of difference in scores.

Non-parametric statistics are often known as "distribution-free statistical procedures." This indicates that, in contrast to parametric tests, which assume a normal distribution, no assumptions are made on the data's distribution. A non-parametric test alternative to independent t-test is **Mann-Whitney-Wilcoxon test**, ant to paired t-test is **Wilcoxon Signed-Rank**.

Mann-Whitney-Wilcoxon test, also called the **Mann–Whitney U test** or the **Wilcoxon rank-sum test**, is a non-parametric alternative to the independent t-test for comparing medians when data does not meet normality assumptions. This test assumes that both groups' observations are independent, and responses are at least ordinal (i.e., one can at least say, which is the larger between two observations), and he distributions of the two groups are similar in shape (although they can differ in location or spread) [236, 237].

The null (H_0) and alternative H_1 hypothesis for the Mann-Whitney-Wilcoxon test are:

H_0: the two groups have the same distribution. This implies that the likelihood of an observation from one group being greater than an observation from the other group is equal.

H_1: The distributions of the two groups are different.

The U-statistic for the Mann-Whitney U test is defined as the smaller of [238]:

$$U_1 = n_1 n_2 \frac{n_1(n_1+1)}{2} - R_1 and U_2 = n_1 n_2 \frac{n_2(n_2+1)}{2} - R_2 \tag{3.3.27}$$

where R_1 and R_2 are the sum of the ranks in groups 1 and 2, after ranking all samples from both groups such that the smallest value obtains rank 1 and the largest, rank $n_1 + n_2$.

The **Wilcoxon Signed-Rank test** is a non-parametric statistical test that compares two related or paired samples. It is a nonparametric alternative to the paired t-test for data that are not normally distributed or have an ordinal scale of measurement [239].

The null (H_0) and alternative H_1 hypothesis for the Wilcoxon Signed-Rank test are:

H_0: The median difference between paired observations is zero. H_1: The median difference between paired observations is not equal zero.

The statistic for the Wilcoxon Signed-Rank test is defined as the smaller between T^+ (the sum of the ranks for the positive differences) and T^- (the sum of the ranks for the negative differences).

3.3.4.2 Correlation analysis

Correlation refers to a statistical relationship between two variables, indicating the strength and direction of their association. It helps to quantify how changes in one variable are related to changes in another. When both variables are continuous and follow a linear relationship, the Pearson correlation coefficient is typically used. However, when the data are ordinal, or when the relationship between the variables is not linear, Spearman's rank correlation coefficient is often more appropriate. This nonparametric measure assesses the strength and direction of the association between two variables by evaluating the ranks of the data rather than the actual values, making it particularly useful for ordinal data or data that does not meet the assumptions of normality [240]. In this work, the Spearman's rank correlation coefficient was used to evaluate the relationship between two variables.

Spearman's rank correlation coefficient is a nonparametric statistic used to assess the strength of an association between two variables. Spearman's coefficient does not measure the linear relationship between two variables. This test evaluates the ability of an arbitrary monotonic function to accurately explain the relationship between two variables without relying on their frequency distribution. Unlike Pearson's correlation coefficient, this method does not require a linear relationship between variables or interval scales. It can be applied to variables measured at the ordinal level [240, 241].

The Spearman rank correlation coefficient is calculated as [242]:

$$r_s = 1 - \frac{6 \sum_{i=1}^{n} d_i^2}{n(n^2 - 1)} \tag{3.3.28}$$

where $\sum_{i=1}^{n} d_i^2$ represents the sum of the squared rank differences, and n is the number of paired observations.

The sign of the Spearman correlation provides the direction of the association between X (the independent variable) and Y (the dependent variable). If Y tends to increase when X does, the Spearman correlation coefficient is positive. If Y tends to drop as X increases, the Spearman correlation coefficient is negative. A Spearman correlation of 0 means that Y has no tendency to increase or decrease as X increases. When X and Y are exactly monotonically associated, the Spearman correlation coefficient equals 1 [241].

3.3.4.3 Classification and Performance Evaluation

In the following part, classification and performance evaluation methods will be covered, which are critical for determining how effectively a prediction model or

classifier is doing.

The **Confusion Matrix** is an important tool for performance evaluation since it gives a detailed breakdown of the model's predictions vs the actual results. The confusion matrix, as displayed in Table 16, can be used to describe the discrimination evaluation of the optimal solution during classification training for binary classification problems. The predicted class is shown in the table's row, while the actual class is shown in the column. The number of correctly identified positive and negative examples is shown by the symbols TP and TN in this confusion matrix, whereas the numbers of incorrectly identified positive and negative cases are shown by FP and FN, respectively. The confusion matrix can be used to calculate a variety of performance metrics, which provide information about the model's strengths and weaknesses [243].

Table 16: Confusion matrix for classification.

		True diagnosis		
		Positive	Negative	Total
Predicted class	Positive	TP	FN	$TP + FN$
	Negative	FP	TN	$FP + TN$
	Total	$TP + FP$	$FN + TN$	N

Some of the most widely used performance metrics are the following [243]:

- **Accuracy**: is a metric that measures the ratio of correct predictions over the total number of instances evaluated.

$$Accuracy = \frac{TP + TN}{TP + FP + TN + FN} \tag{3.3.29}$$

- **Error Rate**: misclassification error measures the ratio of incorrect predictions over the total number of instances evaluated.

$$ErrorRate = \frac{FP + FN}{TP + FP + TN + FN} \tag{3.3.30}$$

- **Sensitivity**: is a metric used to measure the fraction of positive patterns that are correctly classified

$$Sensitivity = \frac{TP}{TP + FN} \tag{3.3.31}$$

- **Specificity**: is a metric used to measure the fraction of negative patterns that are correctly classified

$$Specificity = \frac{TN}{TN + FP} \tag{3.3.32}$$

- **Precision**: is a metric used to measure the positive patterns that are correctly predicted from the total predicted patterns in a positive class.

$$Precision = \frac{TP + T}{TP + FP} \tag{3.3.33}$$

- **Recall**: is a metric that measures the fraction of positive patterns that are correctly classified.

$$Recall = \frac{TP}{TP + TN} \tag{3.3.34}$$

- **Area Under the Curve (AUC)**: is one of the popular ranking type metrics. It represents the area under the Receiver Operating Characteristic (ROC) curve, which is a graph that plots the True Positive Rate (sensitivity) against the False Positive Rate (1-specificity) to illustrate how well a classification model performs at different threshold values. For two-class problem, the AUC can be calculated using the following equation:

$$AUC = \frac{S_p - n_p(n_n + 1)/2}{n_p n_n} \tag{3.3.35}$$

where S_p is the sum of all positive observations ranked, while n_p and n_n refer to the number of positive and negative observations respectively.

3.3.4.4 Diagnostic effectiveness metrics

One metric for assessing a diagnostic test's efficacy is the **Youden's Index**, sometimes referred to as Youden's J statistic. It can be defined as: $J = sensitivity + specificity - 1$. In a classification model, the Youden Index is particularly useful for determining the cutoffs that maximise a diagnostic test's overall accuracy while balancing sensitivity and specificity. The Youden Index ranges from -1 to 1, with a negative value indicating a poor test with performance inferior to random guessing, a value of 0 indicating a test with no discriminatory power, and a higher J value indicating that the model performs more successfully in distinguishing between positive and negative cases. It is widely employed in medical diagnostics to determine a threshold that provides a reasonable balance between false positives and false negatives [244, 245].

3.3.4.5 Agreement and Bias Assessment

Next, statistical approaches for determining agreement and bias among various measurements or raters will be covered. These approaches are critical for determining the consistency and reliability of measures in medical diagnostics. The Cohen's Kappa coefficient will be dicussed, which measures the level of agreement between categorical data, as well as the Bland-Altman plot, which evaluates the agreement between two continuous variables. In addition, we will go over the Passing-Bablok regression, which

is a graphical tool for assessing the relationship and potential bias between two measurements. And finally, it will be explained how neural networks could help on the diagnosis comparison between two devices.

Cohen's kappa Index, represented by the Greek letter κ, is a reliable statistic for both inter- and intra- rater reliability assessment. It can be calculated as [246]:

$$\kappa = \frac{observedagreement - chanceagreement}{1 - chanceagreement} \tag{3.3.36}$$

Similar to correlation coefficients, it can range from -1 to $+1$, with 0 indicating random chance and 1 indicating perfect agreement between raters. Cohen suggests that kappa values below 0 are unlikely to occur in practice. The kappa coefficient, like all correlation statistics, is standardized and may be interpreted consistently across research. Cohen recommended interpreting Kappa results as follows: values ≤ 0 indicate no agreement, $0.01 - 0.20$ indicate none to minor agreement, $0.21 - 0.40$ indicate fair agreement, $0.41 - 0.60$ indicate moderate agreement, $0.61 - 0.80$ indicate substantial agreement, and $0.81 - 1.00$ indicate nearly perfect agreement [247].

The comparison of method experiments is a crucial step in the validation of analytical methods and devices. **Passing-Bablok regression analysis** is an algorithm of statistics that allows for the accurate evaluation of analytical method agreement and any systematic bias between them. It is robust, non-parametric, and non sensitive to error distributions and data outliers. The effective implementation of Passing-Bablok regression assumes constantly distributed data and a linear relationship between data evaluated using two analytical approaches. The results are shown as a scatter plot, a regression line, and a regression equation in which the intercept represents constant and the slope proportional measurement error. Confidence intervals of 95% of intercept and slope explain if their values deviate from zero (intercept) and one (slope) merely by chance, allowing the conclusion of method agreement and correction action if necessary [248].

Figure 48 represents an example of Passing-Bablok regression analysis between scanner A and scanner B. The blue points represent the data measured in scanner A and B, the red dotted line represents the case where the two methods perfectly agree, (the points would align along a 45 degree line passing through the origin, representing $x = y$), the blue line represents the Passing-Bablock regression adjustment. The slope of this line reflects proportional bias between the methods (values of slope = 1 indicate that there is no bias; if slope < 1, scanner B tends to have greater values than scanner A).

The intercept reflects any constant bias between the two methods (if the intercept = 0, there is no constant bias, if the intercept < 0, scanner B gives consistently lower results than scanner A). The grey-shaded areas surrounding the regression line reflect

the slope and intercept confidence intervals. These ranges give insight into the estimated parameters uncertainty, allowing to evaluate the reliability of the observed bias.

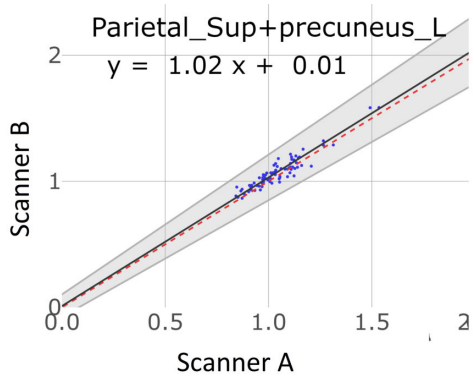

Figure 48: Passing-Bablock regression example.

To sum up, the slope and intercept of the Passing-Bablock regression line reflect the level of agreement between two methods.. If it's close to the equality line, there is minimal bias, showing excellent agreement. If it diverges, it means there is a proportional or constant bias, as shown by the slope and intercept.

The best statistical methodology for determining the degree of agreement between two quantitative methods of measurement is not evident. Altman and Bland provided an alternate technique in 1983 that quantified the agreement between two quantitative measurements using the mean difference and limits of agreement. The **Bland-Altman plot analysis** is a straightforward approach for evaluating a bias in mean differences and estimating an agreement interval within which 95% of the differences between the second and first methods lie. The Bland-Altman plot just defines the intervals of agreement; it does not specify whether such limits are acceptable or not. Acceptable limits must be established beforehand, based on clinical necessity, biological factors, or other goals. Data can be analyzed both as unit differences plot and as percentage differences plot. In this study, the Bland-Altman percentage plots are used [249].

Figure 49 depicts 5 examples of Bland-Altman percentage plots. The position of each point on the x-axis represents the average of the two techniques measurements for a specific sample. It allows find out whether the discrepancies between the two methods vary over the measurement range. The y-axis shows the percentage difference between the two methods for each sample. A difference of 0 indicates complete agreement for that specific measurement. This plot has three lines: a horizontal line at the mean of all differences, known as the bias line. This line depicts the average difference between both methods, which may be used to measure overall bias. If this line is near to 0, it indicates that there is no systematic bias. The 95% limits of agreement are represented by two extra horizontal lines at mean $\pm$ 1.96 SD of thestandard deviations (SD) . If the differences are normally distributed, about 95% of the data points should fall between these ranges. Each point on the plot shows a single sample measure comparing

both methods. Outliers, or points that fall beyond the range of agreement, represent measurements where the two methods disagree considerably [250–252].

In this figure, there are 5 examples which could represent general behaviors of agreement analysis. The first example, case in point A, compares strongly correlated measurements. The Bland-Altman figure highlights differences between the two measurements.The bias decreases as concentration increases. Furthermore, the discrepancies appear to be continuous. The bias is -0.5%, and the agreement range is ± 11% (from -11.5% to 10.5%), mainly due to lower measurements. Above 500 units, the agreement range appears to be under 5%. If the variability of the differences between the two measuring procedures is constant, the plot will look like in example B: the spread of the differences grows significantly as concentration decreases on the percentage difference plot [249].

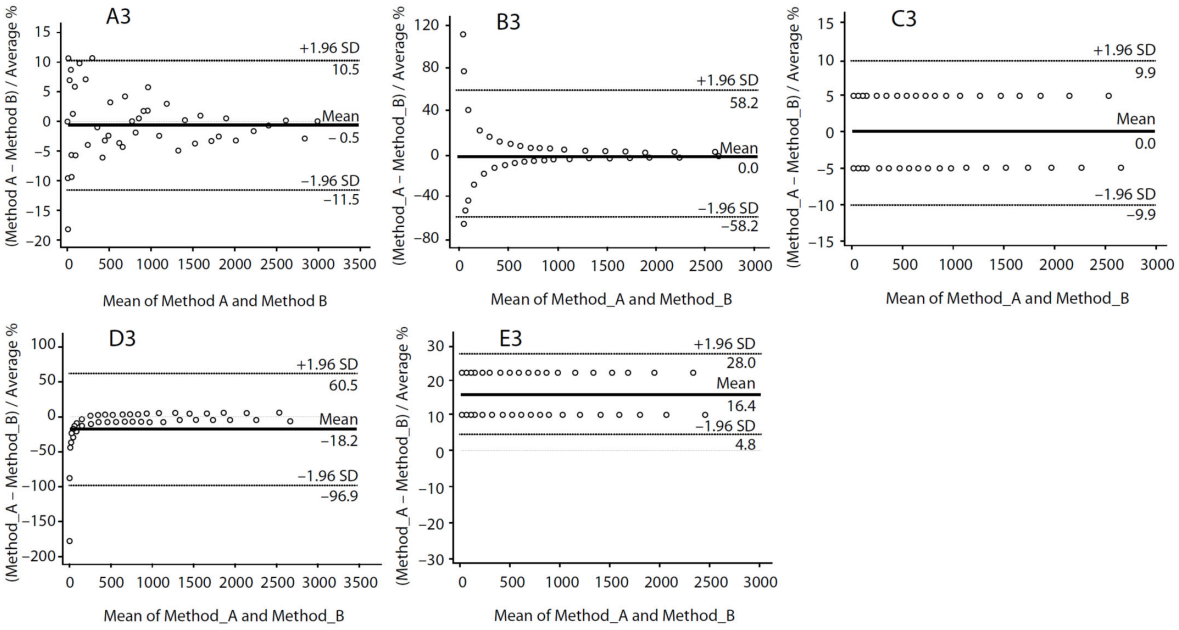

Figure 49: Different Bland-Altman percentage plot cases example. From *"Understanding Bland Altman analysis"* by Davide Giavarina. 2015. Copyright by Biochemia Medica.

When there is a proportional difference variability between measurements, i.e. constant coefficient of variation across the range of concentration, the Bland-Altman percentage plot shows a parallel trend with the x axis (example C). Additional errors can overlap these sources of variability adding their effects to the previous one. For example, in example D, we hypothesized a constant error plus 15 units with the same proportional variability of 5% as in case C. The percentage difference plot shows how this error had a greater impact on measurements of low concentrations, whereas higher concentrations showed no bias. Finally, case E, hypothesizes a proportional constant error, overlapped with the same proportional variability (CV%) of 5%, as in case C. An example could be a calibration error in one method, or a problem in some constants in an equation when computing the final results. [249].

Another technique employed in this work is the use of **neural networks for the diagnosis comparison between two devices**. In order to evaluate and compare the diagnostic performance of two imaging devices, an analysis could be performed using a deep learning algorithm. The goal is to assess the degree of agreement between the two devices in predicting the diagnosis for a cohort of patients. In this study, this approach was proposed since the accuracy of diagnosis is an essential factor when validating new imaging devices [60].

The proposed method consists of employing a neural network model to process the PET images produced by both scanners. The neural network model employed needs to be trained previously to classify the images into categories based on the patient's diagnosis, with the ground truth labels provided by clinical diagnosis, with its performance previously validated. The neural network's outputs, which represent the diagnostic predictions, can then be compared across the two device modalities. The degree of agreement between the device-based predictions can be evaluated using the Cohen's kappa coefficient. This allows for an objective assessment of the concordance between the predictions made by the two devices. By using this neural network-based approach, an unbiased, data-driven evaluation of the diagnostic performance of the two devices can be provided [60].

3.3.4.6 Interpretability in Neural Network Models

Deep neural networks have made significant advances in numerous computer vision tasks, including image classification. However, DNNs are hard to understand and behave like black boxes. When constructing a deep neural network model, most researchers focus on the model's framework and the model's many internal parameters, but they are unable to offer a clear explanation of the model's output when errors occur. This also prevents users from trusting the network's decisions. It is essential that models are transparent so that users understand their reasoning. This will aid in analyzing errors, troubleshooting, and detecting potential biases in training data [253].

Therefore, **neural network attention maps** in Convolutional Neural Networks for image classification are critical for improving model interpretability by graphically showing which regions of an image contribute the most to the network's predictions. These maps can implement spatial attention, which focusses on critical visual areas, or channel attention, which prioritizes feature channels depending on their importance. These techniques significantly enhanced CNN interpretability, making model decisions clearer and more actionable in computer vision applications [254].

In this work, three neural network attention maps have been used: Saliency maps, Grad-CAM and SmoothGrad. Saliency maps compute the gradient of the output with respect to the input pixels, emphasizing critical pixels by intensity [255]. SmoothGrad improves saliency maps by averaging gradients across several noisy input

samples, resulting in a cleaner and denoised visualization [256]. Grad-CAM improves interpretability by using gradients to weight feature maps in the final convolutional layer, resulting in a class-discriminative heatmap that emphasizes key regions for a given prediction [257].

Chapter 4

RESULTS

4.1 Dementia

PET imaging has become an essential technique in the study of neurological diseases, providing novel insights into the brain's metabolism and function. This section looks into two essential aspects of PET applications in brain imaging: the PET vital role in the early diagnosis of neurodegenerative diseases and the evaluation of a new brain-dedicated PET scanner. These approaches not only improve the trustworthiness of imaging data but also lead to early strategies that may influence the course of degenerative neurological diseases.

4.1.1 Diagnosis of neurodegenerative diseases

For the early diagnosis of neurodegenerative diseases application two interventions were proposed:

- To analyze the relationship between brain [^{18}F]FDG PET imaging and cognitive status in Mild Cognitive Impairment patients, to explore if social cognition may be useful in early detection of dementia.
- To validate a Deep Learning algorithm based on [^{18}F]FDG PET images that can detect patients with a neurodegenerative disease among patients with Mild Cognitive Impairment.

4.1.1.1 Relationship between neuroimaging and emotion recognition

This analysis assessed the correlation between brain [^{18}F]FDG PET imaging and a sensitive neuropsychological evaluation based on emotion recognition to identify potential physiopathological mechanisms associated with MCI, which could aid in understanding dementia development. This could help determine whether including RMET in the neuropsychological test battery improves the accuracy of AD diagnosis or not.

In this analysis, the PET images were spatially normalized to the Montreal Neurological Institute space. As part of this process, all scans were resized to a resolution of $121 \times 145 \times 121$ and voxel size of $1.5 \times 1.5 \times 1.5$ mm to align with the resolution and voxel size of the probability map. The voxel values of the PET images were converted into standardized uptake values. To calculate the mean SUV for different PET volumes of interest, La Fe atlas was employed. The SUVr was then determined by using the brainstem as the reference region [95].

The statistical analysis was performed using the software R. Correlations between various variables were explored using Spearman's rank correlation coefficient. These correlation coefficients were visualized using correlogram plots, organized by the variables of interest. The original plots included a color bar to indicate the actual correlation values.

To simplify interpretation, the correlation coefficients were grouped based on their strength: values between 0.5 and 1 were categorized as strong (assigned a value of 1), those between 0.3 and 0.5 as moderate (assigned a value of 0.5), and those between 0 and 0.3 as weak or negligible (assigned a value of 0). Even though correlograms examine straightforward correlations and do not require adjustments for Type I errors, only correlations with a statistical significance of $p < 0.001$ were included in the report. Figure 50 shows the correlogram plot of this analysis.

The study found strong relationships between standard neuropsychological evaluations (RBANS, CDR, MMSE) and CSF biomarker values ($A\beta_{42}$, Tau, and p-Tau). RMET scores did not correlate with CSF biomarkers, but did show some correlations with other cognitive tests (CDR, MMSE, and RBANS).

The [^{18}F]FDG PET SUVr revealed significant correlations with CSF biomarkers and cognitive tests. Correlation analysis between [^{18}F]FDG PET and RMET data also revealed some correlations. There was a positive correlation between RMET (total score and negative group) and SUVr in the following areas: prefrontal medial L and R (r = 0.36), posterior cingulate L and R (r = 0.34), parietal inferior L and R (r = 0.31), anterior cingulate L and R (r = 0.33), prefrontal lateral L and R (r = 0.33), temporal lateral R (r = 0.33), insula R (r = 0.31), and basal ganglia R (r = 0.30). Therefore, reduced metabolic activity in these areas was found to be linked to disfunction in emotion detection in MCI patients.

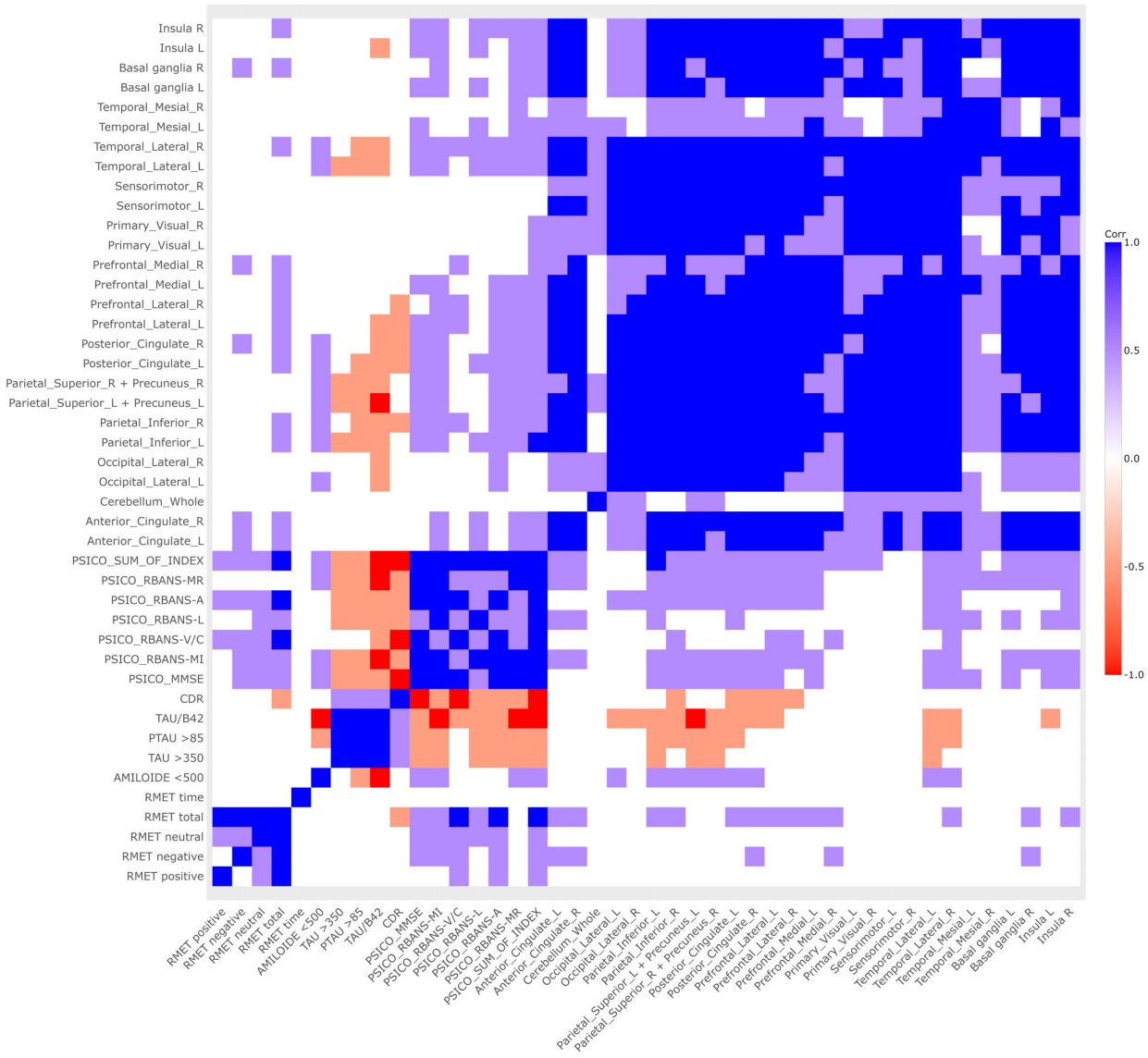

Figure 50: Correlogram plot of the CSF, neuropsychological and FDG-PET SUVr data with categorized coefficients according to the magnitude of the correlation. From *"Relationship between neuroimaging and emotion recognition in mild cognitive impairment patients."* by Maria Teresa Gandia-Ferrero, Jesús Adrián-Ventura et al. 2024. Copyright by Elsevier.

4.1.1.2 Neural Network validation for Alzheimer's Disease prediction

As mentioned, subjective differentiating between MCI and neurodegenerative diseases can sometimes be challenging. To enhance the accuracy and predictive power of [^{18}F]FDG PET in this context, a Deep Neural Network model was validated with images from Hospital La Fe to identify patients with neurodegenerative disease among those diagnosed with MCI.

For this analysis, images were co-registered to a Dementia-Specific FDG PET

template from the Montreal Neurological Institute and smoothed using a 4 mm FWHM filter. To align with the template's resolution and voxel size, all scans were resized to $110 \times 92 \times 92$, maintaining a $2 \times 2 \times 2$ mm voxel size. Additionally, two extra voxels with a zero value were added at the borders of the z-axis [99].

The Deep Learning neural network used in this analysis had already been trained on FDG PET brain images from 822 patients (472 AD, 350 MCI), acquired at the baseline visit of each subject and downloaded from the Alzheimer's Disease Neuroimaging Initiative (ADNI) database (http://adni.loni.usc.edu).

The goal of the 3D CNN was to distinguish between MCI cases with and without an associated neurodegenerative disease. The network architecture includes three convolutional and pooling blocks, followed by a fully connected layer with rectified linear unit (ReLU) activation functions.

A convolutional filter size of $3 \times 3 \times 3$ was used, along with the Adam optimizer set to a learning rate of 1.510^{-3} and a binary cross-entropy loss function. The batch size was set to 8, and dropout layers were incorporated after both the convolutional blocks and the fully connected layer. ADNI test dataset achieved a sensitivity of 88% and specificity of 71% with an accuracy of 79% in classifying AD from MCI patients. The neural network architecture is illustrated in Figure 51, and additional details on its training and design can be found in [99]. In this study, the network was not trained but rather validated to assess its reproducibility using external images from La Fe University and Polytechnic Hospital.

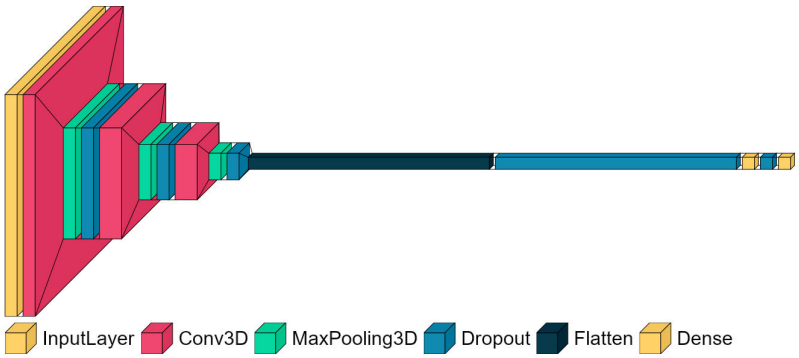

Figure 51: Neural network architecture. The CNN consists of 3 convolutional and pooling blocks (Conv3D + Max-Pooling3D + Dropout) attached to a fully connected layer after a flatten layer. From *"Artificial intelligence on fdg pet images identifies mild cognitive impairment patients with neurodegenerative disease."* by Joan Prats-Climent, Maria Teresa Gandia-Ferrero et al. 2022. Copyright by Journal of Medical Systems.

The model was applied to the hospital independent set of images to perform the external validation of the CNN performance. To assess its performance, various classification metrics were analyzed, including Sensitivity, Specificity, Balanced Accuracy, and the Area Under the Receiver Operating Characteristic curve (AUC). This analysis

was performed using the software Python. The receiver operating characteristic curve and the confusion matrix for the validation dataset are shown in Figures 52 and 53, respectively.

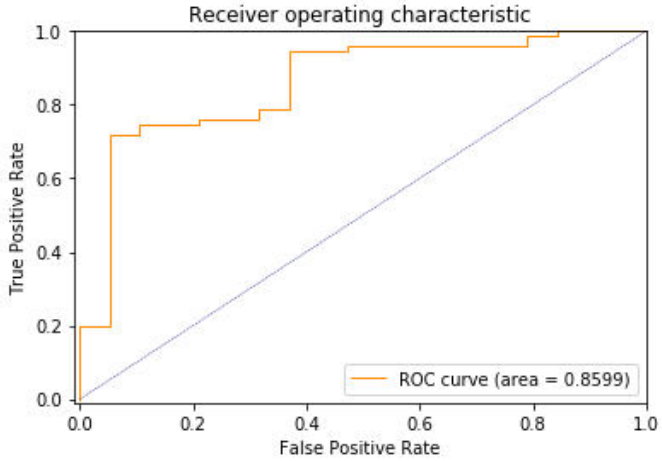

Figure 52: ROC curves for La Fe dataset. The model performance can be evaluated from the area under the receiver operating characteristic curve (AUC). For La Fe dataset the AUC obtained is 0.897. From *"Artificial intelligence on fdg pet images identifies mild cognitive impairment patients with neurodegenerative disease."* by Joan Prats-Climent, Maria Teresa Gandia-Ferrero et al. 2022. Copyright by Journal of Medical Systems.

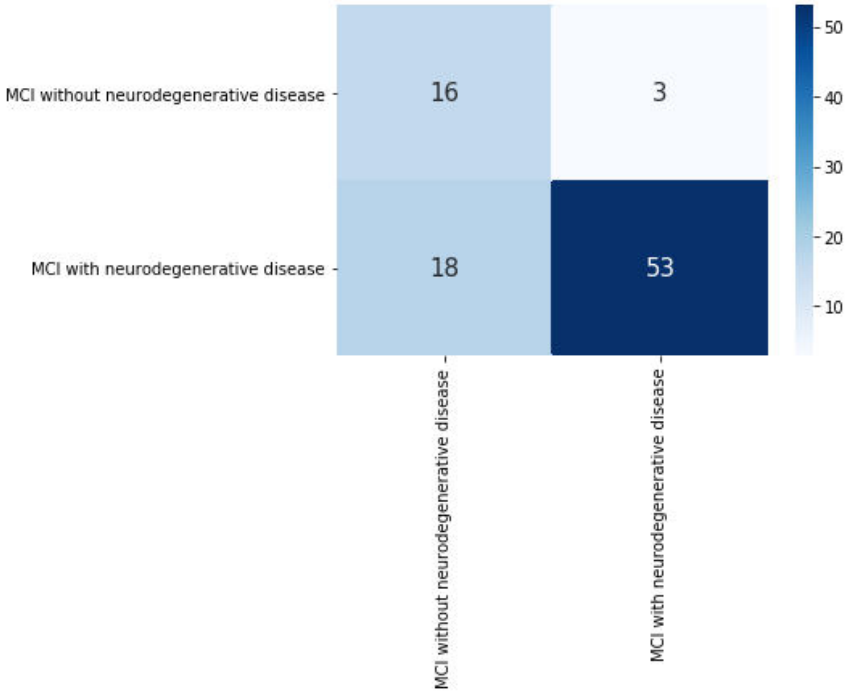

Figure 53: Confusion matrix for La Fe dataset. From *"Artificial intelligence on fdg pet images identifies mild cognitive impairment patients with neurodegenerative disease."* by Joan Prats-Climent, Maria Teresa Gandia-Ferrero et al. 2022. Copyright by Journal of Medical Systems.

The model achieved a sensitivity of 75% (correctly identifying 53 out of 71 MCI cases with an associated neurodegenerative disease) and a specificity of 84% (correctly identifying 16 out of 19 MCI cases without an associated neurodegenerative disease). This resulted in a balanced accuracy of 80% and an AUC of 0.8599. Specifically, within the MCI group with an associated neurodegenerative disease, the model correctly classified 48 out of 64 AD cases, all 4 FTD cases, and 1 out of 3 DLB cases.

Additionally, to assess the interpretability of the developed model, various visualization techniques were explored to generate network attention maps. These maps highlight key features of the input image that the model considers in its final prediction. Saliency maps, SmoothGrad, and Grad-CAM visualization algorithms were applied. These visualization algorithms are depicted in Figures 54 - 56. Both Saliency maps and SmoothGrad seem to highlight the posterior cingulate and superior parietal regions. These brain areas align with the FDG endophenotype of AD [258]. However, the Grad-CAM method focuses on the right prefrontal brain area, which is not typically associated with AD. This suggests that SmoothGrad might be the most reliable method for this study, as it aligns with the FDG endophenotype of AD.

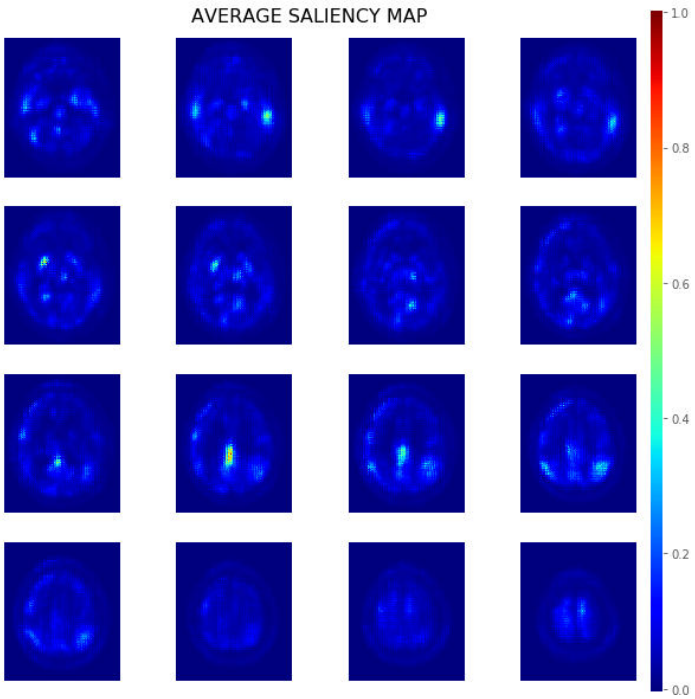

Figure 54: Saliency maps visualization algorithm computed and averaged on the external validation dataset. From *"Artificial intelligence on fdg pet images identifies mild cognitive impairment patients with neurodegenerative disease."* by Joan Prats-Climent, Maria Teresa Gandia-Ferrero et al. 2022. Copyright by Journal of Medical Systems.

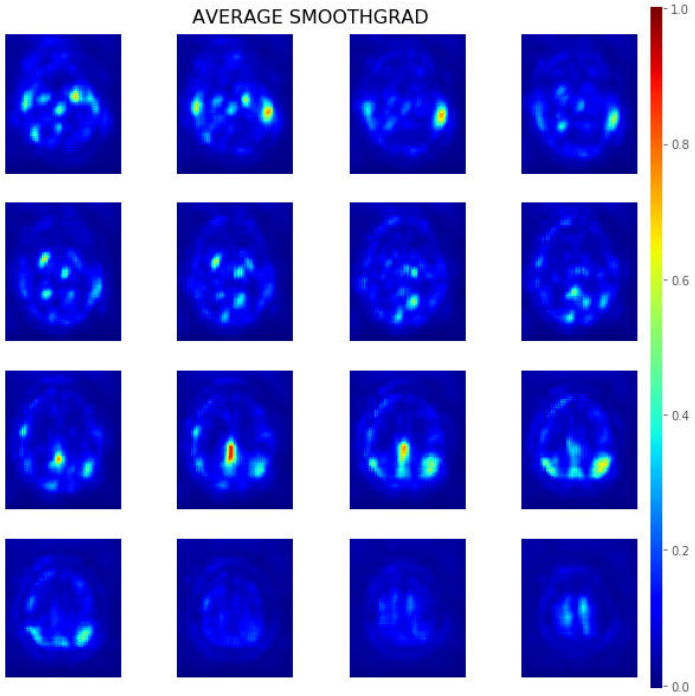

Figure 55: SmoothGrad visualization algorithm computed and averaged on the external validation dataset. From *"Artificial intelligence on fdg pet images identifies mild cognitive impairment patients with neurodegenerative disease."* by Joan Prats-Climent, Maria Teresa Gandia-Ferrero et al. 2022. Copyright by Journal of Medical Systems.

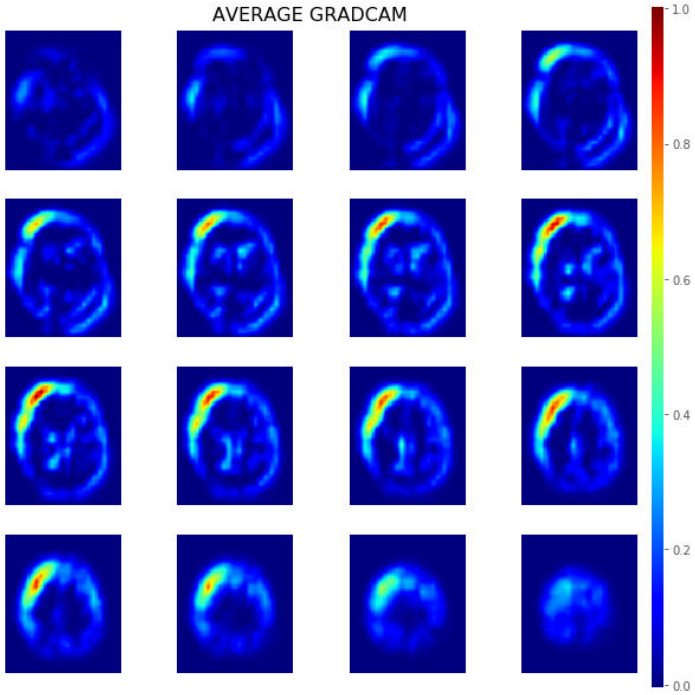

Figure 56: Grad-CAM visualization algorithm computed and averaged on the external validation dataset. From *"Artificial intelligence on fdg pet images identifies mild cognitive impairment patients with neurodegenerative disease."* by Joan Prats-Climent, Maria Teresa Gandia-Ferrero et al. 2022. Copyright by Journal of Medical Systems.

4.1.2 Brain-dedicated PET scanner evaluation

In order to reduce the neurological burden of conventional PET/CT, a brain-dedicated PET scanner could be an alternative. However, it is crucial to ensure that both systems provide similar image quality and diagnostic capability. For this reason, for the brain-dedicated PET scanner evaluation application two interventions are proposed:

- To compare PET image quality evaluation between PET/CT and brain-dedicated PET scanners.
- To compare the diagnostic capability of the brain-dedicated PET against PET/CT.

4.1.2.1 Objective PET image quality evaluation

The first purpose of this intervention is to evaluate the image quality of a novel brain-dedicated PET system in comparison to a whole-body PET/CT scanner using objective metrics derived from both Hoffman phantom and patient data.

Since this new scanner does not use a CT for attenuation correction, a key part of the image quality evaluation will focus on evaluating how the emission-based AC impacts the quality of CMB PET images. This will be done by comparing the PET images produced by the CMB scanner using emission-based AC with the images that would have been obtained if the scanner had a CT for AC. To achieve this, patient PET images from a PET/CT system and the CMB scanner will be compared using both emission-based and CT-based attenuation maps [60].

To evaluate image quality, both for phantom and patient FDG images of a PET/CT and a dPET device, two different sets of volume-of-interest (VOI) regions were defined. The first set, which included gray matter (GM) and white matter (WM), was used to assess contrast, noise, and other metrics related to signal properties within the images. The second set, consisting of 28 brain regions from the La Fe atlas, was used to validate the accuracy of the quantitative data. Figures 57 and 58 illustrate the analysis for the Hoffman phantom and patient data, respectively [60].

For the GM and WM segmentation in the Hoffman phantom, the CT image was co-registered with each reconstructed PET image to ensure matching resolution and voxel size. This co-registered CT was then used for GM and WM segmentation using the SPM software.

Although SPM12 is optimized for segmenting MR T1 weighted images, it was necessary to use the CT image because the plastic materials of the Hoffman phantom do not accurately represent GM and WM. As a result, probability maps for GM and

WM were obtained.

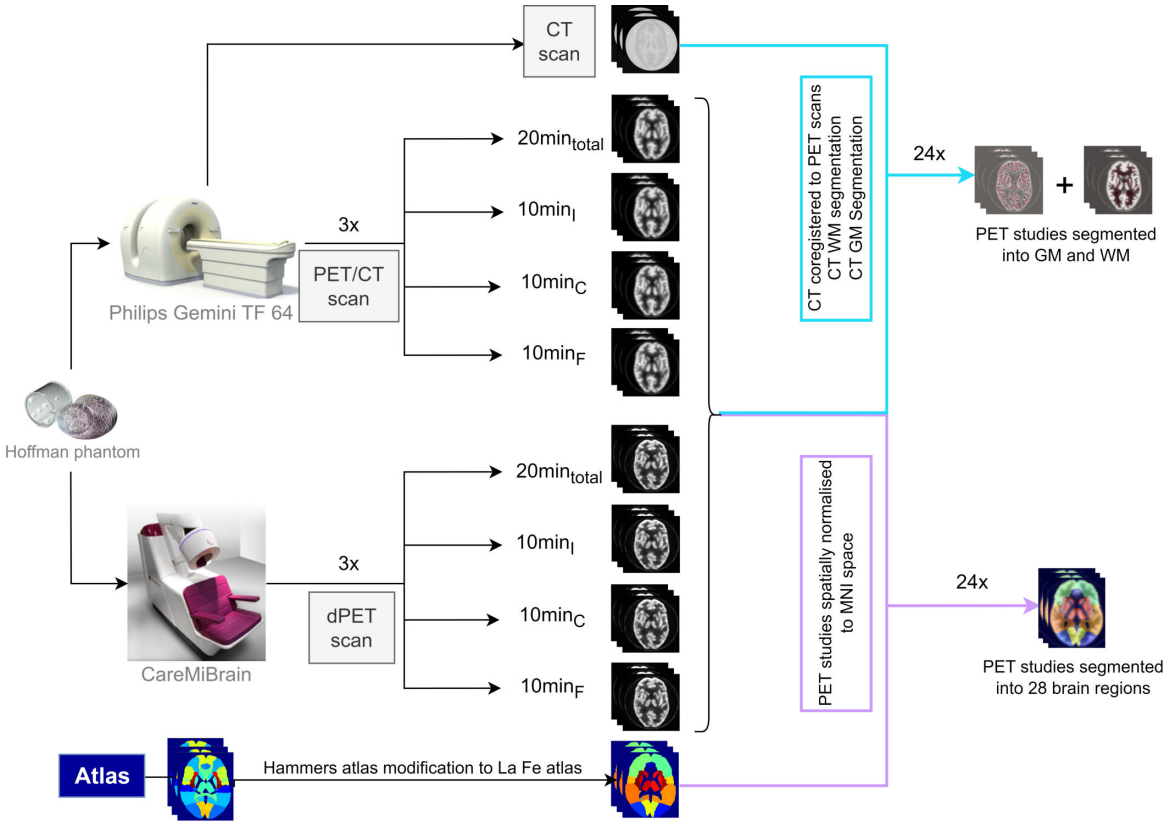

Figure 57: Flowchart of the imaging acquisition and analysis for the Hoffman phantom. From *"Objective image quality comparison between brain-dedicated PET and PET/CT scanners."* by Maria Teresa Gandia-Ferrero, Irene Torres-Espallardo et al. 2023. Copyright by Journal of Medical Systems.

For patient data, the GM and WM segmentation probability maps were generated directly from the PET images rather than the CT scan. This was because the PET/CT scans were acquired using a low-dose CT protocol, making it difficult to distinguish between GM and WM. Additionally, not all patients included in the study had MR scans available for segmentation. However, all segmentations, both for the Hoffman phantom and patient data, were supervised by a nuclear medicine physicist.

Using these probability maps as masks, the mean and standard deviation of GM and WM values were calculated for each reconstructed PET image. These values were then used to compute several image quality metrics, including: contrast, recovery coefficient, signal to noise ratio, contrast to noise ratio and coefficient of variation.

For the segmentation of 28 brain regions, all reconstructed PET images were spatially normalized to a dementia-specific FDG PET template from the MNI using SPM12. To ensure consistency, all images were resized to a voxel resolution of $1.5 \times 1.5 \times 1.5\ mm^3$, matching the template dimensions.

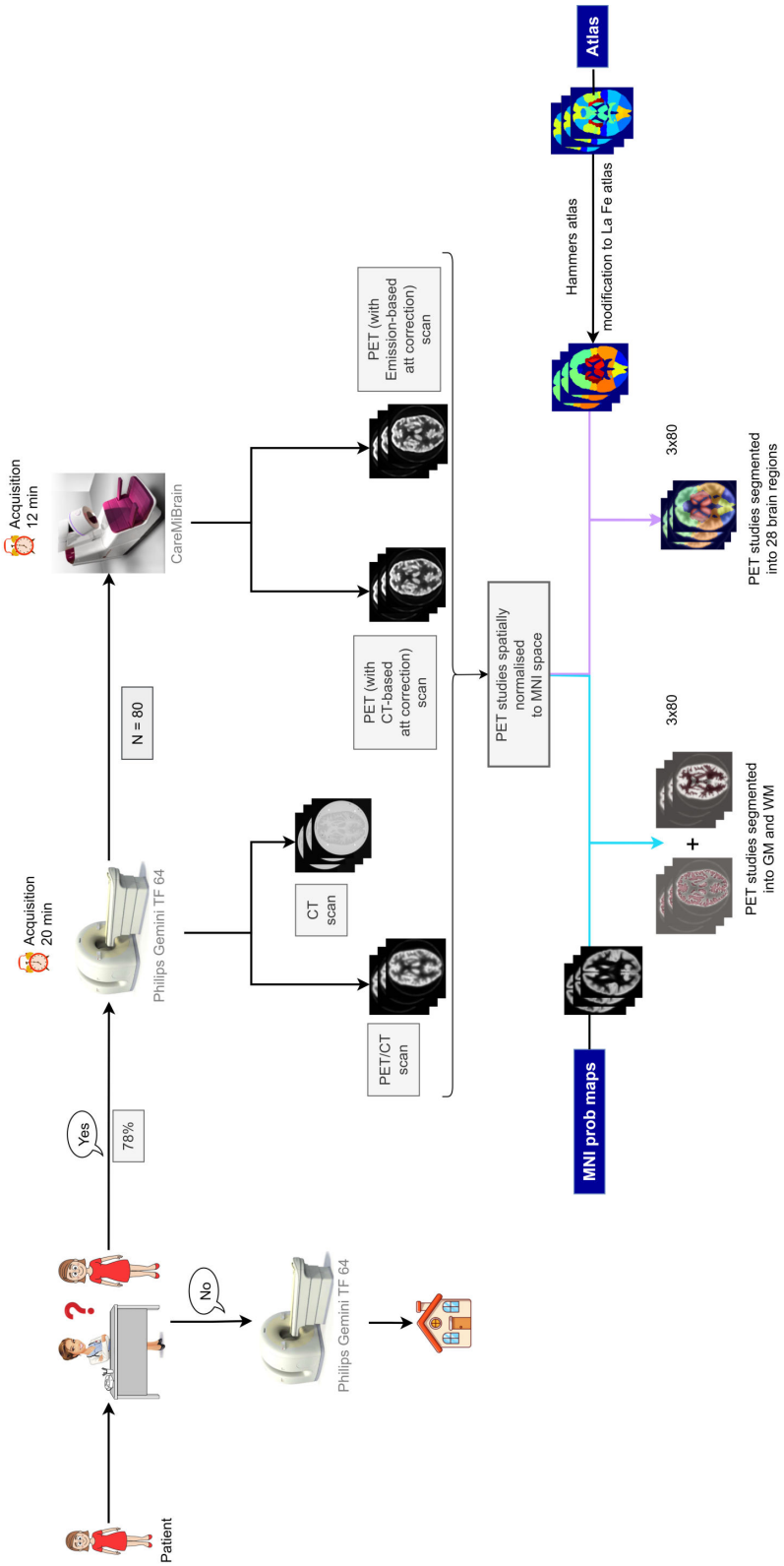

Figure 58: Flowchart of the imaging acquisition and analysis for patients. From *"Objective image quality comparison between brain-dedicated PET and PET/CT scanners."* by Maria Teresa Gandia-Ferrero, Irene Torres-Espallardo et al. 2023. Copyright by Journal of Medical Systems.

After spatial normalization, the La Fe atlas was used to extract the mean SUV for different brain regions. Since PET imaging is primarily used to measure activity concentration, quantification is critical. A key quality metric in this study was the comparison of SUVr between corresponding brain regions in the two different scanners. SUVr is an essential parameter in neurological imaging studies, as it allows for a relative assessment of metabolic activity across brain regions. For this analysis, the whole cerebellum was chosen as the reference region. The SUVr was then calculated for the remaining 27 brain regions in the La Fe atlas.

In this intervention, three different sets of comparisons were used to evaluate the image quality of PET scans from the new brain-dedicated scanner. The first comparison set included PET images from both the PET/CT scanner and the new CMB scanner, analyzed for both Hoffman phantom images and patient scans to assess the overall image quality of the new device.

Since the new scanner does not use a CT-based attenuation correction and this correction is crucial for PET image quality, a second comparison was performed. This set included patient PET images from PET/CT and CMB, both reconstructed using CT-based attenuation correction to analize the impact of using a standard CT AC method. The third set focused on comparing different attenuation correction methods within the CMB scanner itself, including patient PET images from CMB reconstructed with both emission-based AC and CT-based AC to evaluate the differences between these two correction techniques. The Hoffman phantom was excluded from the attenuation correction comparisons because, unlike human tissue, its material composition does not significantly affect attenuation. While patients have different tissues with distinct attenuation coefficients such as cortical bone, gray matter, white matter, and air, the plastic and water materials in the Hoffman phantom have very similar attenuation properties.

For the first seven image quality metrics, including contrast, recovery coefficient, signal-to-noise ratio in white matter, signal-to-noise ratio in gray matter, contrast-to-noise ratio, and coefficient of variation for 10-minute scans in both white and gray matter, the mean and standard deviation were calculated.

For the 27 SUV ratio metrics, the relative differences between PET/CT and CMB images were analized. A statistical analysis was conducted to determine whether there were significant differences in SUVr across brain regions. The Shapiro-Wilk test was used to check if the data followed a normal distribution, and depending on the result, either a paired t-test for normally distributed data or the Wilcoxon signed-rank test for non-normally distributed data was applied. A p-value of 0.05 was set as the significance threshold.

Additionally, the Passing-Bablok regression analysis was applied to the 27 SUVr metrics to evaluate the agreement between PET images from both scanners, PET/CT and CMB. The Bland-Altman analysis was also used to assess whether there were

systematic differences, or bias, between the two devices and to define the limits of agreement for SUVr measurements in patients. Finally, ComBat method was performed to harmonise SUVr results between PET/CT and CMB images.

A total of 34 metrics were taken to assess image quality in the Hoffman phantom, including contrast, recovery coefficient, signal to noise ratio in white and gray matter, contrast to noise ratio, coefficient of variation over 10 minutes in both tissues, and SUVr across 27 specific regions. For patient images, 31 image quality metrics were calculated, including contrast, signal to noise ratio in white and gray matter, contrast to noise ratio, and SUVr of the 27 VOIs.

When evaluating image quality based on the segmentation of gray and white matter, absolute values might change slightly depending on the segmented area, but the overall trend remains consistent. Since this study aims to compare two imaging devices, the main goal is to determine whether PET images maintain equal or not inferior quality.

The evaluation of image quality for the **Hoffman phantom** is detailed below. Figure 59 presents a box-plot distribution of several image quality metrics, including CNR of GM, contrast, SNR of GM and WM, RC of GM, and COV_{10min} for GM and WM in PET images. The distributions are categorized based on the imaging device, where the blue distribution corresponds to PET/CT images and the green distribution represents CMB images. Table 17 summarizes the mean and standard deviation (mean ± SD) of these four metrics. The results indicate that while CMB images exhibit higher contrast between GM and WM and a higher RC of GM compared to PET/CT, they also have lower SNR and higher COV_{10min}. This increased variability in CMB images is primarily due to the higher noise levels.

Table 17: Image quality metrics evaluated on Hoffman phantom (I). Mean ± standard deviation of contrast to noise ratio of grey matter: CNR(GM), contrast, signal to noise ratio of grey matter: SNR(GM), signal to noise ratio of white matter: SNR(WM), recovery coefficient of grey matter RC(GM), and coefficients of variation of grey matter: COV_{10min}(GM) and white matter: COV_{10min}(WM) distributions of PET/CT images and CMB PET images on Hoffman phantom. From *"Objective image quality comparison between brain-dedicated PET and PET/CT scanners."* by Maria Teresa Gandia-Ferrero, Irene Torres-Espallardo et al. 2023. Copyright by Journal of Medical Systems.

	PET/CT	**CMB**
CNR (GM)	2.14 ± 0.04	2.92 ± 0.12
contrast	0.78 ± 0.00	1.53 ± 0.06
SNR (GM)	5.39 ± 0.14	3.32 ± 0.19
SNR (WM)	2.74 ± 0.05	1.92 ± 0.09
RC (GM)	0.74 ± 0.03	0.94 ± 0.03
COV_{10min}(GM)	0.19 ± 0.01	0.31 ± 0.02
COV_{10min} (WM)	0.37 ± 0.01	0.53 ± 0.03

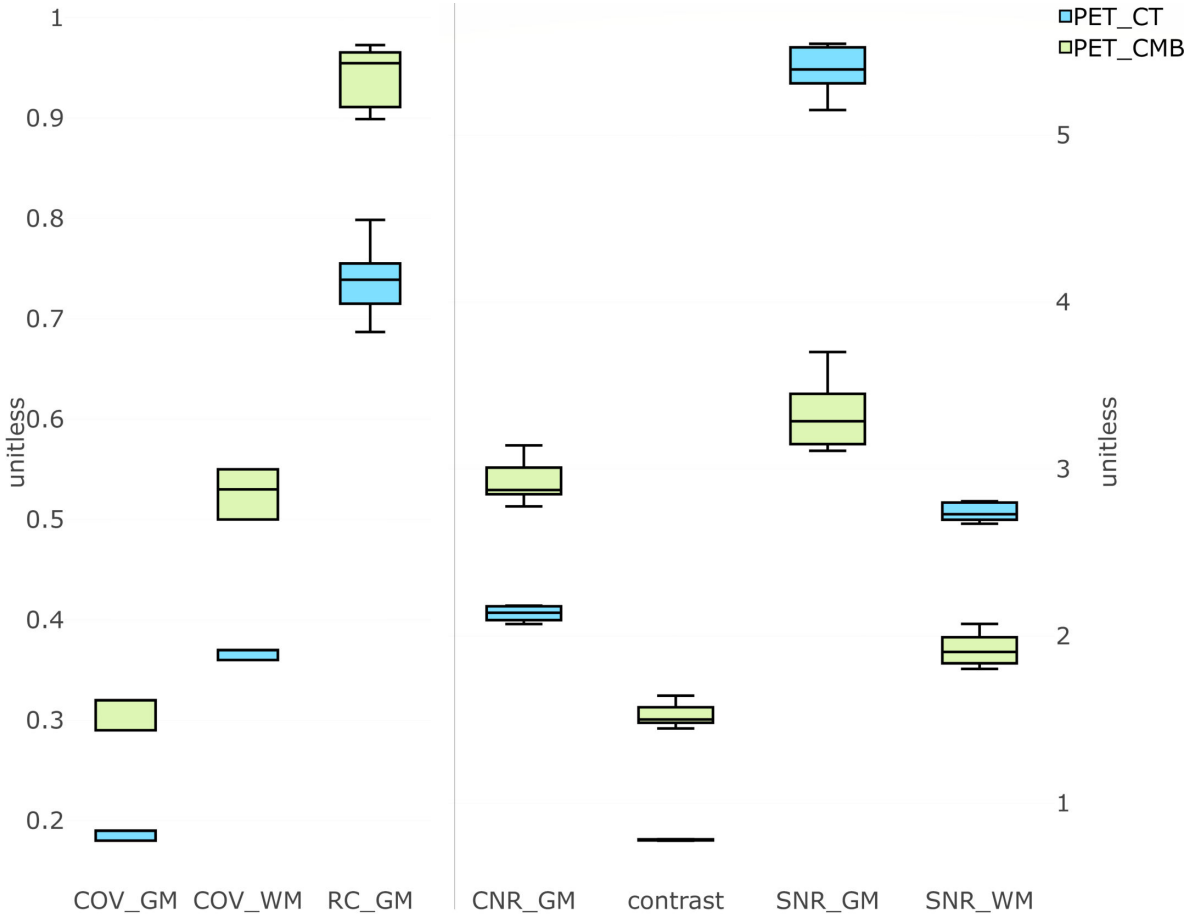

Figure 59: Image quality metrics evaluated on Hoffman phantom (I). Contrast to noise ratio of grey matter: CNR(GM), contrast, signal to noise ratio of grey matter: SNR(GM) and signal to noise ratio of white matter; SNR(WM), recovery coefficient of grey matter RC(GM), and coefficients of variation of grey matter COV10min(GM) and white matter distributions: COV10min(WM) of PET/CT images (blue) CMB PET images (green) on Hoffman. From *"Objective image quality comparison between brain-dedicated PET and PET/CT scanners."* by Maria Teresa Gandia-Ferrero, Irene Torres-Espallardo et al. 2023. Copyright by Journal of Medical Systems.

Figure 60 shows the distributions of the 27 SUVr metrics for all brain regions. These distributions are also grouped by device, with PET/CT images shown in blue and CMB images in green. Relative differences between PET images from both scanners were computed for all PET scans. The mean relative difference across acquisitions for these 27 metrics is presented in Table 18, where metrics that show statistically significant differences between both imaging modalities are marked with an *.

Statistical analysis revealed that nearly all SUVr metrics demonstrated significant differences when comparing PET images from PET/CT and CMB. However, despite these differences, the mean relative differences between both devices remained below 10%.

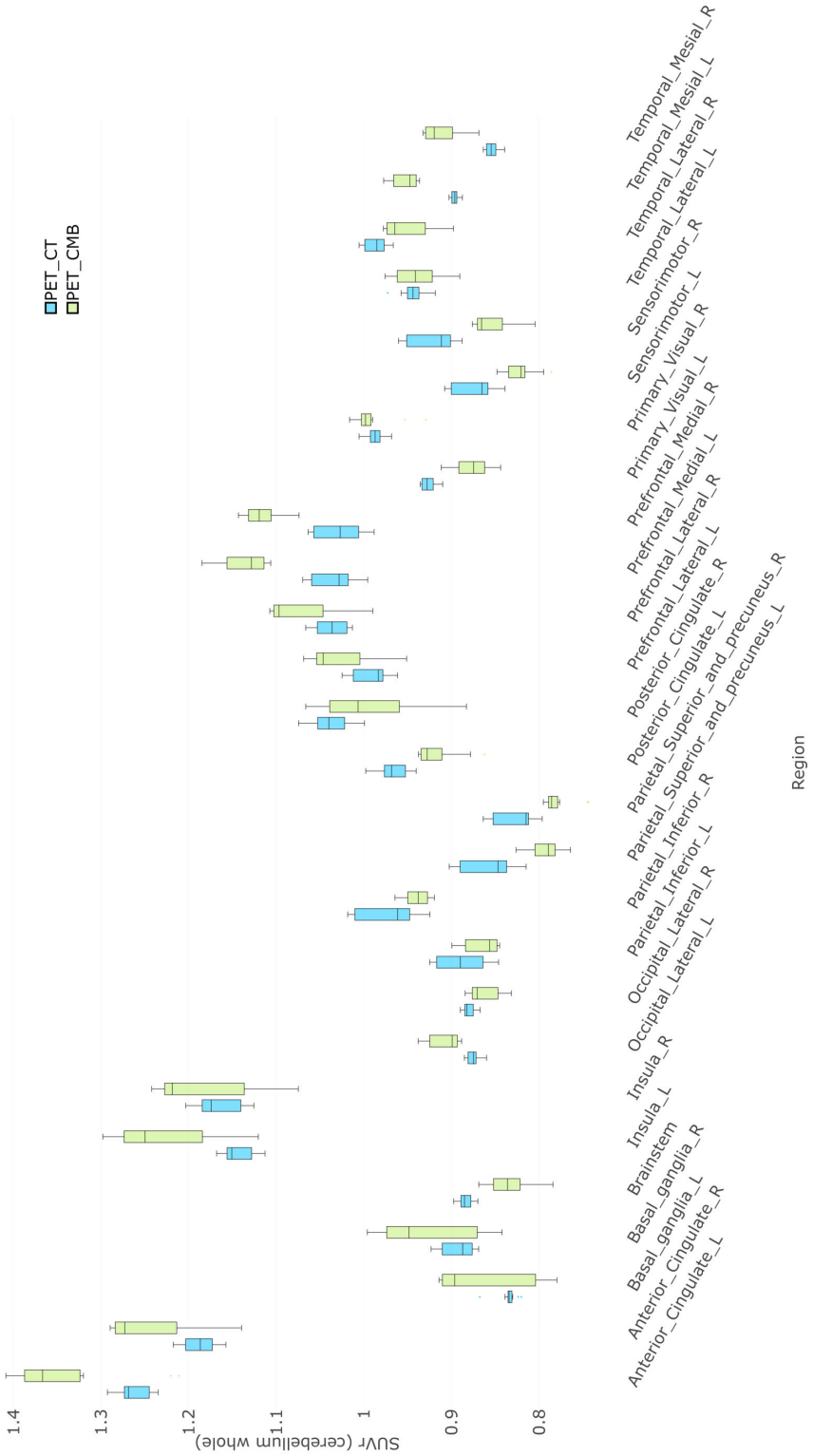

Figure 60: Image quality metrics evaluated on Hoffman phantom (II). Hoffman SUVr distribution of PET/CT images (blue) CMB PET images (green) for each brain region. From *"Objective image quality comparison between brain-dedicated PET and PET/CT scanners."* by Maria Teresa Gandia-Ferrero, Irene Torres-Espallardo et al. 2023. Copyright by Journal of Medical Systems.

Table 18: Image quality metrics evaluated on Hoffman phantom (II). Relative differences of mean SUVr across all the Hoffman phantom measurements between PET/CT and CMB. Values with * correspond to brain regions that presented statistically significant differences. From *"Objective image quality comparison between brain-dedicated PET and PET/CT scanners."* by Maria Teresa Gandia-Ferrero, Irene Torres-Espallardo et al. 2023. Copyright by Journal of Medical Systems.

Region	Relative difference
Anterior_Cingulate_L	0.06*
Anterior_Cingulate_R	0.05*
Basal_ganglia_L	0.04
Basal_ganglia_R	0.04
Brainstem	0.06*
Insula_L	0.07*
Insula_R	0.02
Occipital_Lateral_L	0.04*
Occipital_Lateral_R	0.02*
Parietal_Inferior_L	0.03*
Parietal_Inferior_R	0.04*
Parietal_Sup+precuneus_L	0.08*
Parietal_Sup+precuneus_R	0.06*
Posterior_Cingulate_L	0.05*
Posterior_Cingulate_R	0.04*
Prefrontal_Lateral_L	0.04*
Prefrontal_Lateral_R	0.04*
Prefrontal_Medial_L	0.10*
Prefrontal_Medial_R	0.08*
Primary_Visual_L	0.05*
Primary_Visual_R	0.00
Sensorimotor_L	0.06*
Sensorimotor_R	0.07*
Temporal_Lateral_L	0.01
Temporal_Lateral_R	0.04*
Temporal_Mesial_L	0.06*
Temporal_Mesial_R	0.07*
MEAN	**0.05**

The evaluation of image quality for the **Patients** is detailed below. Figure 61 presents the distribution of several image quality metrics, including CNR of GM, contrast, SNR of GM, and SNR of WM. These distributions are visualized using three separate box plots: one representing images acquired on PET/CT (blue), another for images acquired on CMB reconstructed using the emission attenuation map (green), and a third for images acquired on CMB reconstructed using the CT attenuation map (pink). The mean and standard deviation (mean ± SD) for these metrics are summarized in Table 19. The results indicate that, while CMB images exhibit higher contrast between GM and WM compared to PET/CT, they also have lower SNR values.

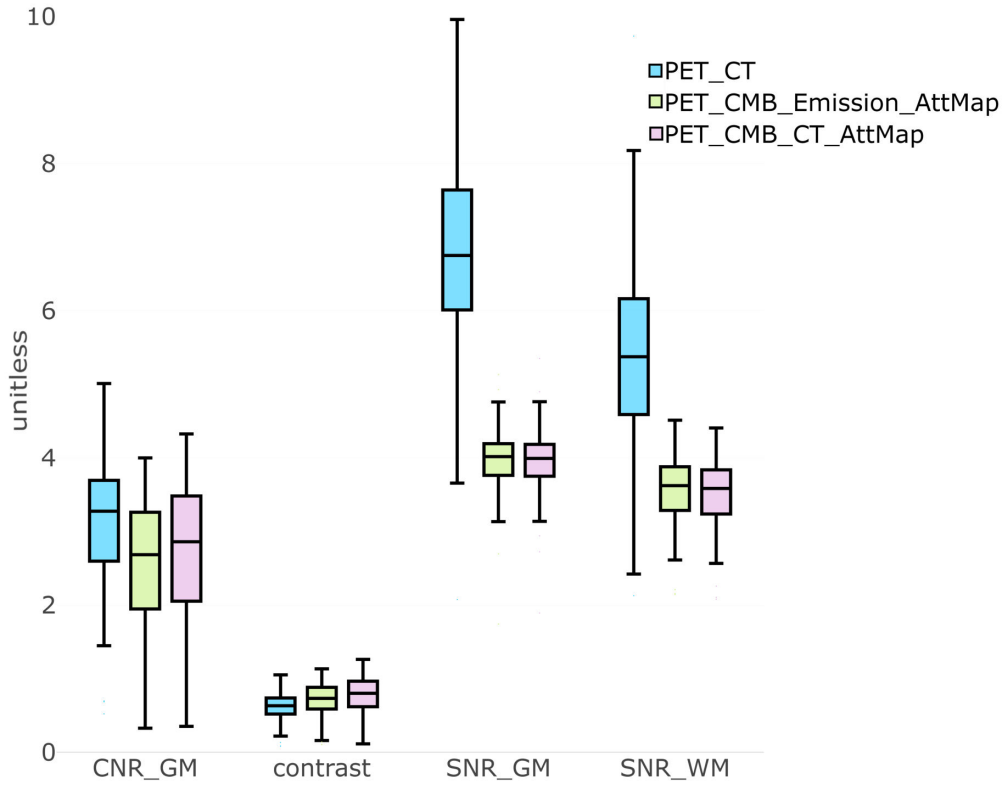

Figure 61: Image quality metrics evaluated on patients (I). Contrast to noise ratio of grey matter: CNR(GM), contrast, signal to noise ratio of grey matter: SNR(GM) and signal to noise ratio of white matter; SNR(WM) distributions of PET/CT images (blue), CMB PET images reconstructed using Emission-based attenuation map (green) and CMB PET images reconstructed using CT-based attenuation map (pink) on patients. From *"Objective image quality comparison between brain-dedicated PET and PET/CT scanners."* by Maria Teresa Gandia-Ferrero, Irene Torres-Espallardo et al. 2023. Copyright by Journal of Medical Systems.

Table 19: Image quality metrics evaluated on patients (I). Mean ± standard deviation of contrast to noise ratio of grey matter: CNR(GM), contrast, signal to noise ratio of grey matter: SNR(GM) and signal to noise ratio of white matter: SNR(WM) distributions of PET/CT images, CMB PET images reconstructed using Emission-based attenuation map and CMB PET images reconstructed using CT-based attenuation map on patients. From *"Objective image quality comparison between brain-dedicated PET and PET/CT scanners."* by Maria Teresa Gandia-Ferrero, Irene Torres-Espallardo et al. 2023. Copyright by Journal of Medical Systems.

	PET/CT	**CMB Emission-based AC**	**CMB CT-based AC**
CNR(GM)	3.03 ± 1.17	2.49 ± 1.00	2.65 ± 1.08
contrast	0.60 ± 0.24	0.70 ± 0.26	0.75 ± 0.29
SNR(GM)	7.04 ± 1.78	3.95 ± 0.49	3.95 ± 0.49
SNR(WM)	5.39 ± 1.35	3.56 ± 0.47	3.51 ± 0.49

Table 20: Image quality metrics evaluated on patients (II). Relative differences of mean SUVr across all the patients measurements between PET/CT and CMB. Values with * correspond to brain regions that presented statistically significant differences. CTAC: Computed Tomography Attenuation Correction; EmissionAC: Emission-based Attenuation Correction. From *"Objective image quality comparison between brain-dedicated PET and PET/CT scanners."* by Maria Teresa Gandia-Ferrero, Irene Torres-Espallardo et al. 2023. Copyright by Journal of Medical Systems.

Region	CMB: CTAC – EmissionAC	PET/CT – CMB CTAC	PET/CT – CMB EmissionAC
Anterior_Cingulate_L	0.04	0.04*	0.04
Anterior_Cingulate_R	0.04	0.04	0.04
Basal_ganglia_L	0.05*	0.09*	0.14*
Basal_ganglia_R	0.04*	0.12*	0.16*
Brainstem	0.07*	0.05*	0.13*
Insula_L	0.05*	0.06*	0.04
Insula_R	0.04*	0.03	0.04
Occipital_Lateral_L	0.07*	0.05*	0.11*
Occipital_Lateral_R	0.06*	0.03	0.05*
Parietal_Inferior_L	0.06*	0.06*	0.11*
Parietal_Inferior_R	0.06*	0.03	0.06*
Pariet_Sup+precun_L	0.03	0.04*	0.03
Pariet_Sup+precun_R	0.03	0.06*	0.05
Posterior_Cingulate_L	0.03	0.05	0.06*
Posterior_Cingulate_R	0.03	0.04	0.06*
Prefrontal_Lateral_L	0.03	0.09*	0.10*
Prefrontal_Lateral_R	0.04	0.05*	0.08*
Prefrontal_Medial_L	0.03	0.04	0.05
Prefrontal_Medial_R	0.04	0.04	0.05*
Primary_Visual_L	0.02	0.03	0.03
Primary_Visual_R	0.02	0.03	0.04
Sensorimotor_L	0.04*	0.04*	0.08*
Sensorimotor_R	0.04*	0.03	0.05*
Temporal_Lateral_L	0.03	0.07*	0.10*
Temporal_Lateral_R	0.02	0.02	0.02
Temporal_Mesial_L	0.04	0.04	0.04
Temporal_Mesial_R	0.03	0.05*	0.08*
MEAN	**0.04**	**0.05**	**0.07**

Figure 62 displays the distributions of the 27 SUVr quality metrics, corresponding to different brain regions. Similar to Figure 61, these distributions are grouped into three box plots: blue for PET/CT, green for CMB reconstructed with the emission attenuation map, and pink for CMB reconstructed with the CT attenuation map. Relative differences between these three PET image sets were computed for all patients. Table 20 provides the mean relative differences across all patients for each of the 27 SUVr quality metrics. Metrics that show statistically significant differences between image types are marked with an asterisk (*).

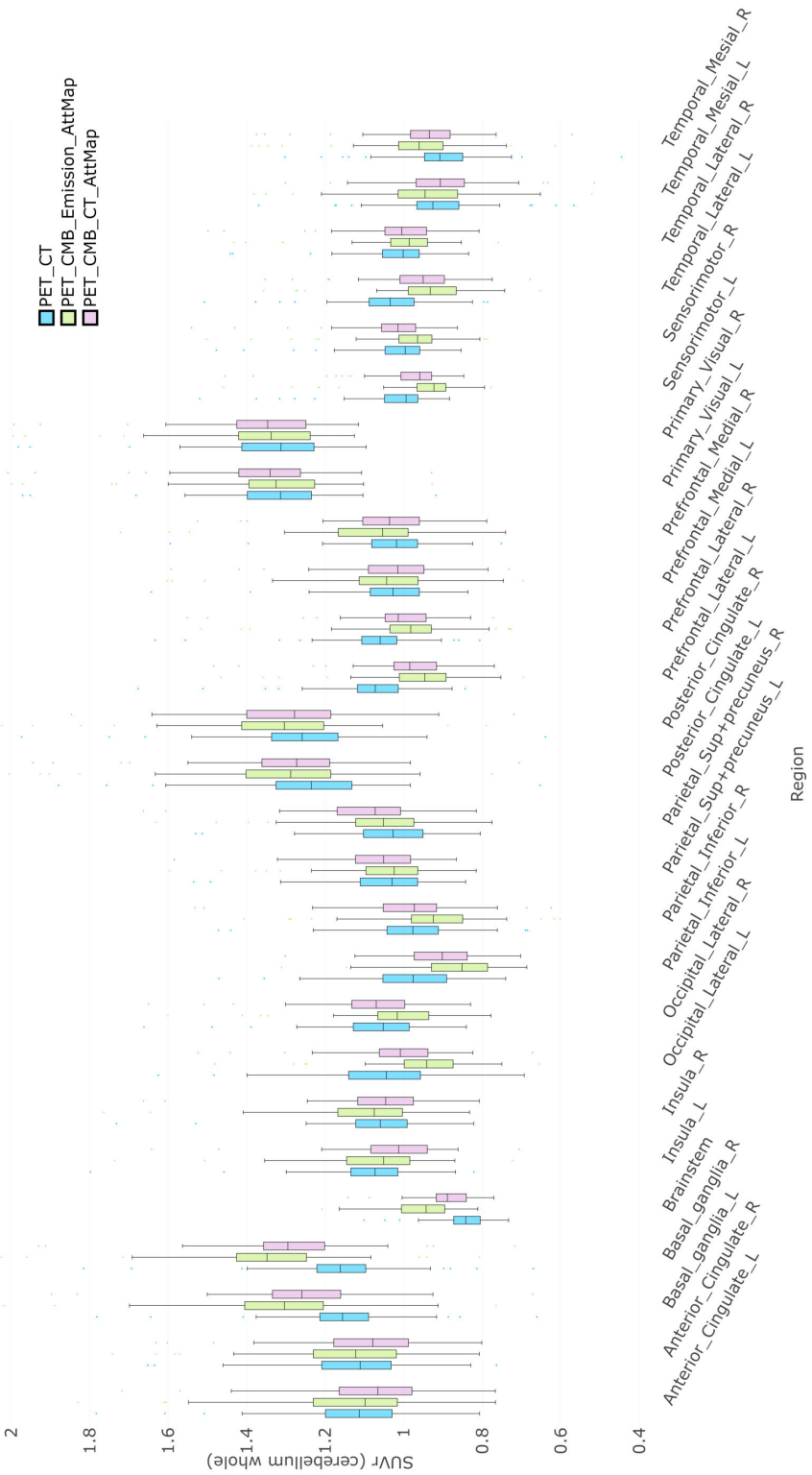

Figure 62: Image quality metrics evaluated on patients (II). SUVr distribution of PET/CT images (blue) CMB PET images reconstructed using Emission-based attenuation map (green) and CMB PET images reconstructed using CT-based attenuation map (pink) for each brain region. From *"Objective image quality comparison between brain-dedicated PET and PET/CT scanners."* by Maria Teresa Gandia-Ferrero, Irene Torres-Espallardo et al. 2023. Copyright by Journal of Medical Systems.

The box-plot distributions indicate that images acquired on CMB reconstructed using the CT attenuation map are generally more similar to PET/CT images across almost all 27 SUVr metrics than images reconstructed using the emission attenuation map. Statistical analysis revealed that 11 out of the 27 SUVr metrics exhibited statistically significant differences when comparing CMB images reconstructed with CT-based and emission-based AC.

Additionally, when comparing CMB to PET/CT, more SUVr metrics showed statistically significant differences for CMB reconstructed with CT AC (16 out of 27) than for CMB reconstructed with emission AC (14 out of 27). These relative differences align with the statistical results, as the differences between PET/CT and CMB with CT-based AC are generally smaller than those between PET/CT and CMB with emission-based AC (see Table 20). Despite these statistically significant differences, most relative differences between groups remain below 10%.

The Passing-Bablok regression results for SUVr values across different brain regions are presented in Figures 63 and 64. These results are visualized using scatter plots, along with the corresponding regression line and equation, which includes an intercept and a slope that account for measurement error. The 95% confidence intervals for both the intercept and slope are also provided to determine whether their values deviate from zero (intercept) and one (slope) due to random variation. These regression plots assess the agreement in SUVr values between PET/CT and CMB and help identify any systematic bias between the two imaging modalities. Since this is a non-parametric method, it remains unaffected by error distribution or data outliers. A stronger agreement between devices is indicated when the slope approaches 1 and the intercept nears 0. Results demonstrate that, for almost all brain regions, the SUVr regression between PET/CT and CMB images reconstructed with CT-based attenuation correction shows a better fit (slope ≈ 1, intercept ≈ 0) compared to the regression between PET/CT and CMB images reconstructed with emission-based attenuation correction.

Results of the Bland-Altman analysis of the 27 SUVr quality metrics measured in patient images are shown in Figures 65, 67, and 69. Specifically, Figure 65 compares PET/CT and CMB with emission-based AC, Figure 67, CMB images reconstructed with CT-based AC and emission-based AC, and Figure 69, PET/CT and CMB with CT-based AC. The results indicate that systematic differences across all brain regions remain below 15%, and nearly all data points fall within the limits of agreement. For improved visual representation, Figures 66, 68, and 70 depict the percentage difference between measurements by coloring the different brain regions of the Atlas La Fe.

The findings of the Bland-Altman analysis reveal that when comparing PET/CT and CMB, there is an observable asymmetry between the left and right hemispheres (see Figures 66 and 70). However, this asymmetry is not present when comparing CMB images alone, as shown in Figure 68. Despite this asymmetry, the overall differences between PET/CT and CMB remain small.

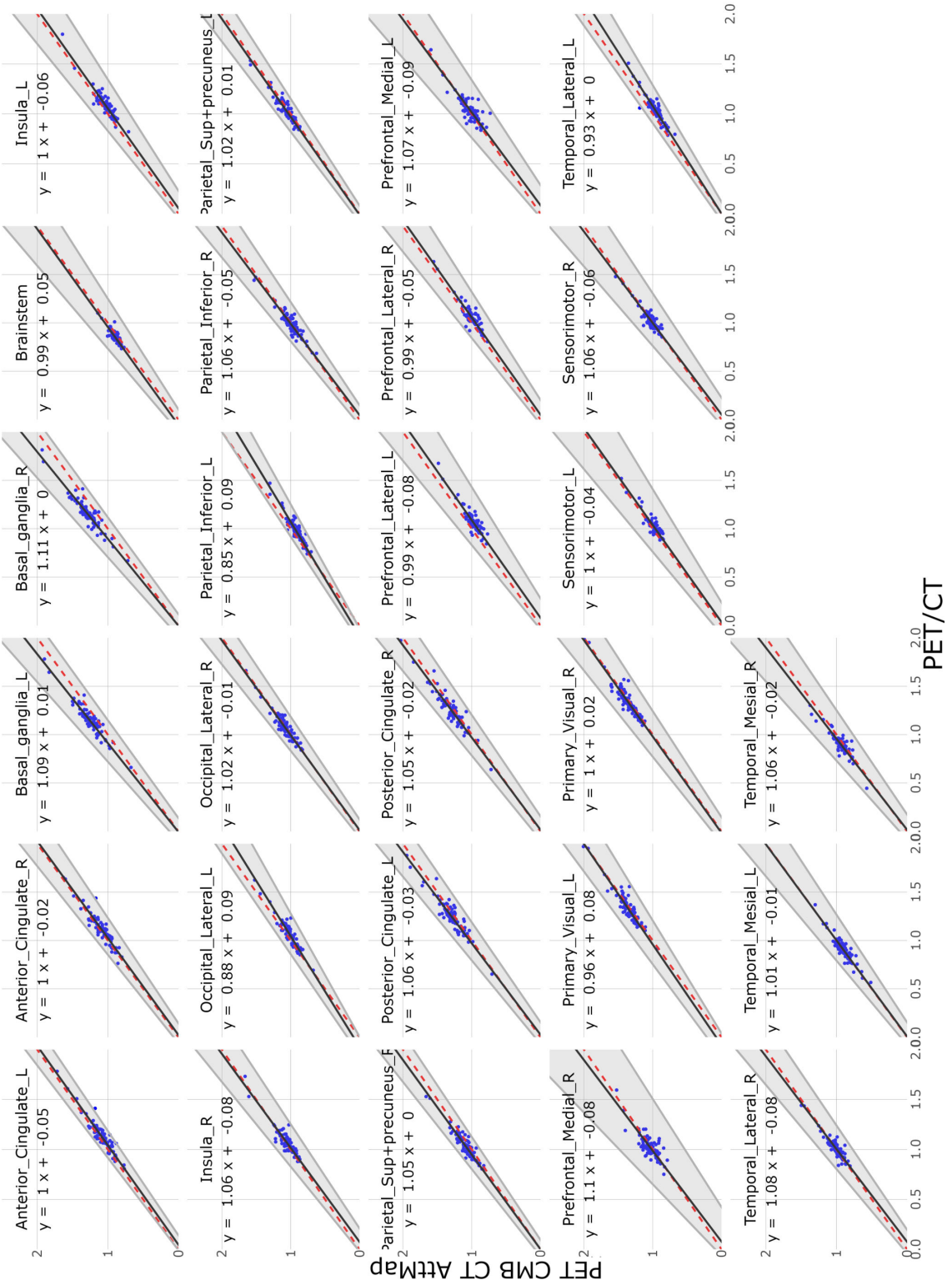

Figure 63: SUVr Passing-Bablok regression plots between images from PET/CT and CMB with emission-based attenuation map grouped by brain regions. From *"Objective image quality comparison between brain-dedicated PET and PET/CT scanners."* by Maria Teresa Gandia-Ferrero, Irene Torres-Espallardo et al. 2023. Copyright by Journal of Medical Systems.

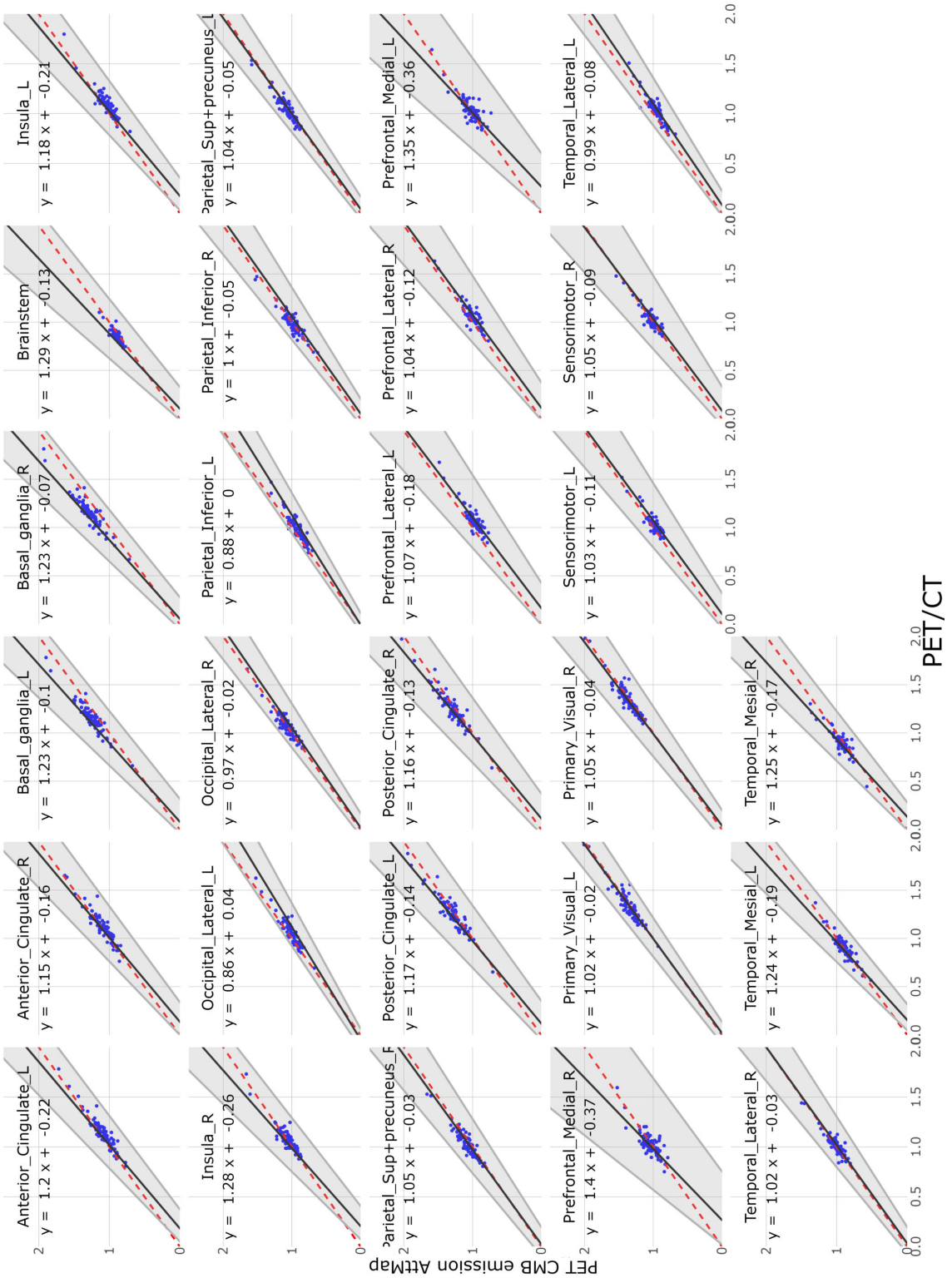

Figure 64: SUVr Passing-Bablok regression plots between images from PET/CT and CMB with CT-based attenuation map grouped by brain regions. From *"Objective image quality comparison between brain-dedicated PET and PET/CT scanners."* by Maria Teresa Gandia-Ferrero, Irene Torres-Espallardo et al. 2023. Copyright by Journal of Medical Systems.

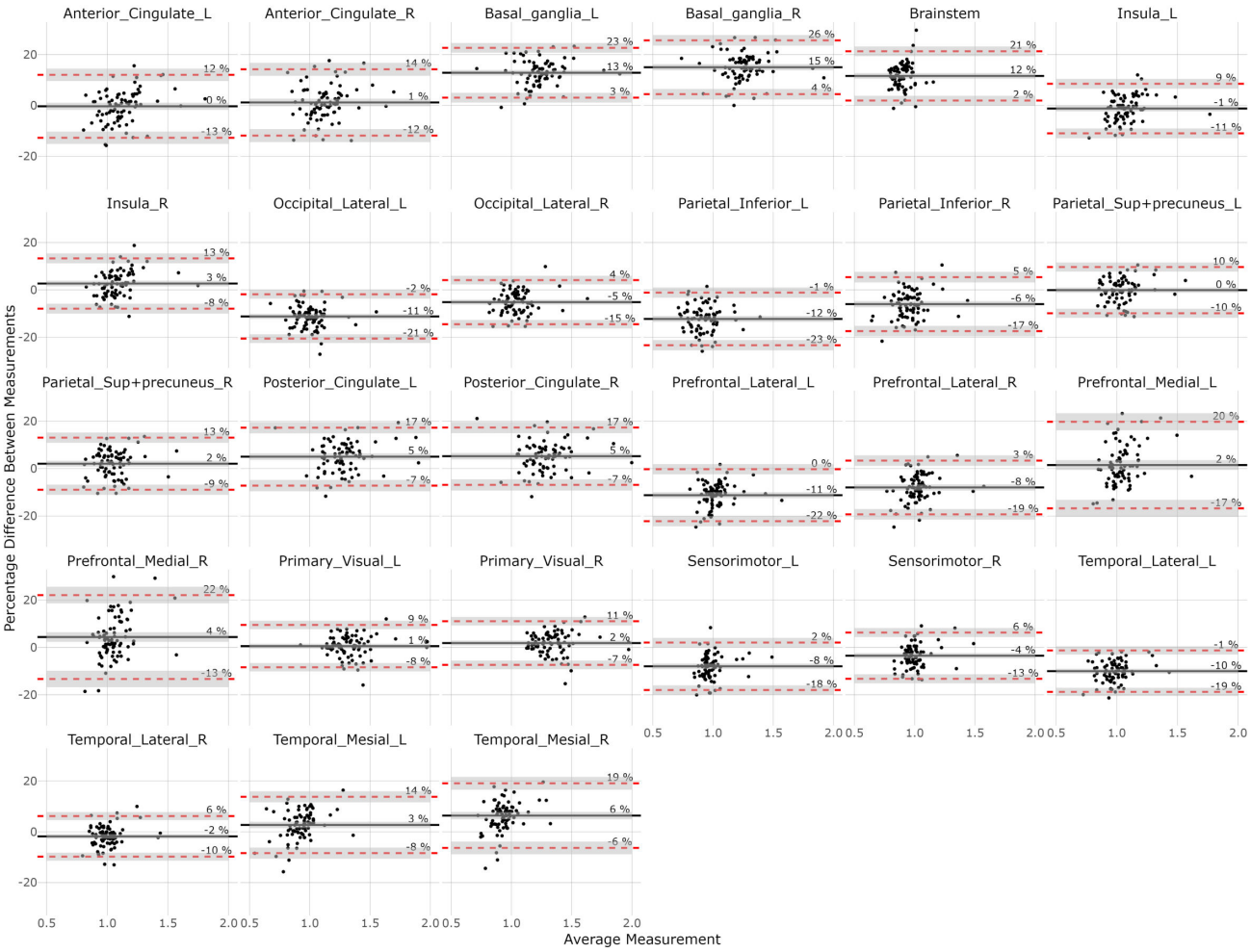

Figure 65: Bland-Altman plot of the 27 SUVr quality metrics evaluated in patients for the comparison of PET images between PET/CT and CMB with emission-based AC. From *"Objective image quality comparison between brain-dedicated PET and PET/CT scanners."* by Maria Teresa Gandia-Ferrero, Irene Torres-Espallardo et al. 2023. Copyright by Journal of Medical Systems.

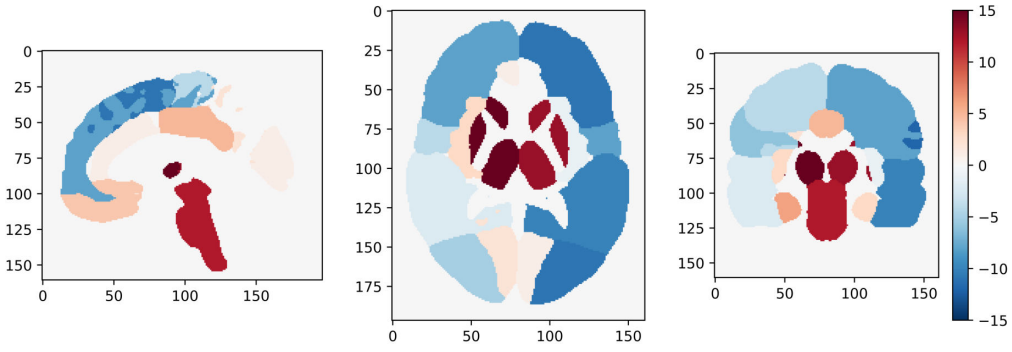

Figure 66: Atlas La Fe plot with its regions colored by the Bland-Altman percentage differences of the 27 SUVr quality metrics evaluated in patients between PET/CT and CMB with emission-based AC. From *"Objective image quality comparison between brain-dedicated PET and PET/CT scanners."* by Maria Teresa Gandia-Ferrero, Irene Torres-Espallardo et al. 2023. Copyright by Journal of Medical Systems.

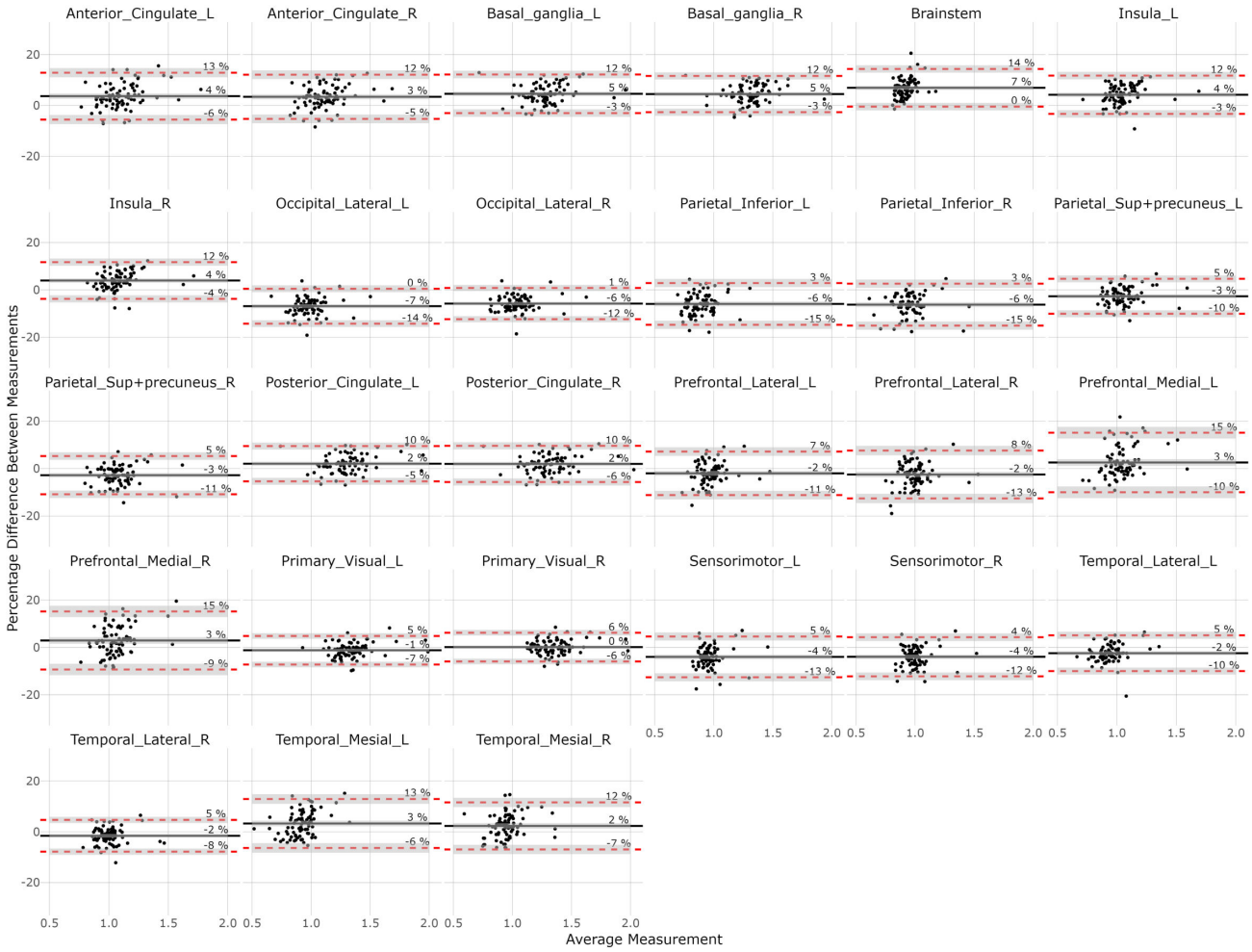

Figure 67: Bland-Altman plot of the 27 SUVr quality metrics evaluated in patients for the comparison of PET images between CMB with CT-based AC and CMB with emission-based AC. From *"Objective image quality comparison between brain-dedicated PET and PET/CT scanners."* by Maria Teresa Gandia-Ferrero, Irene Torres-Espallardo et al. 2023. Copyright by Journal of Medical Systems.

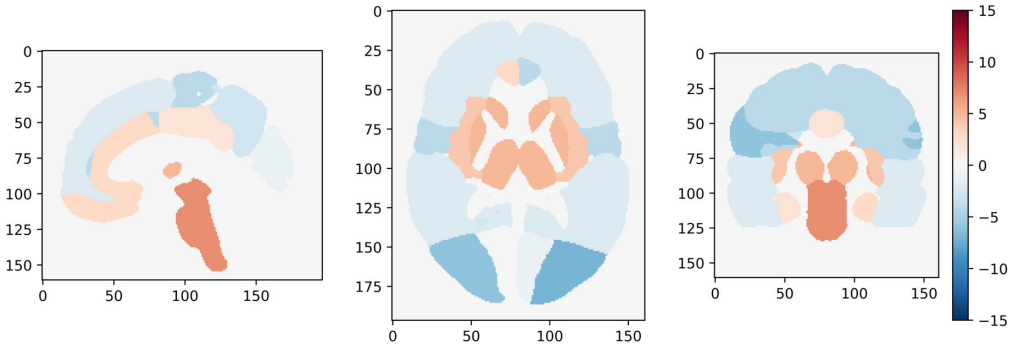

Figure 68: Atlas La Fe plot with its regions colored by the Bland-Altman percentage differences of the 27 SUVr quality metrics evaluated in patients between CMB with CT-based AC and CMB with emission-based AC. From *"Objective image quality comparison between brain-dedicated PET and PET/CT scanners."* by Maria Teresa Gandia-Ferrero, Irene Torres-Espallardo et al. 2023. Copyright by Journal of Medical Systems.

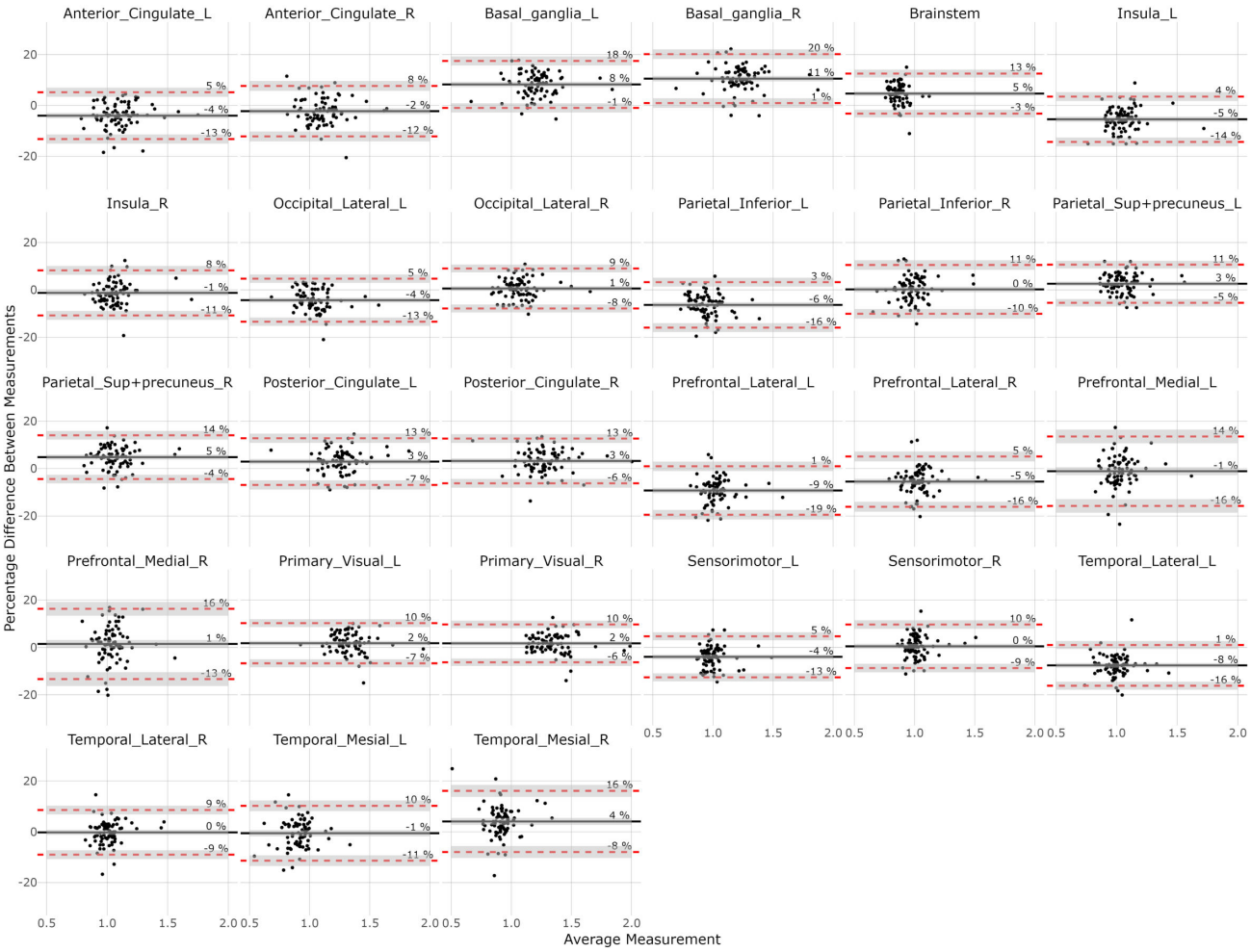

Figure 69: Bland-Altman plot of the 27 SUVr quality metrics evaluated in patients for the comparison of PET images between PET/CT and CMB with CT-based AC. From *"Objective image quality comparison between brain-dedicated PET and PET/CT scanners."* by Maria Teresa Gandia-Ferrero, Irene Torres-Espallardo et al. 2023. Copyright by Journal of Medical Systems.

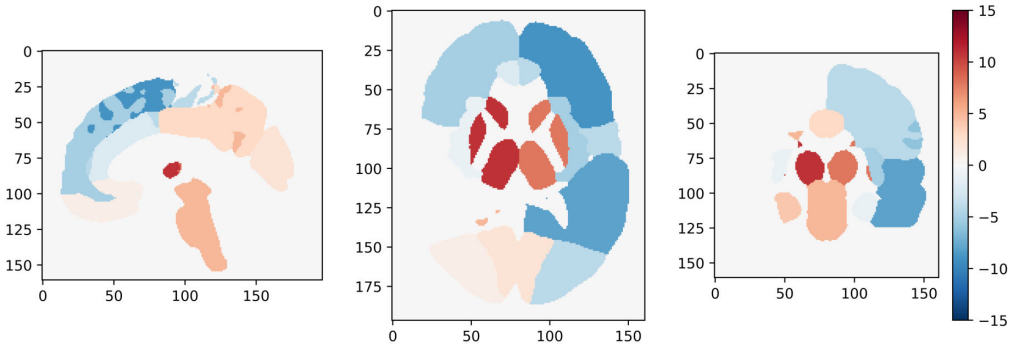

Figure 70: Atlas La Fe plot with its regions colored by the Bland-Altman percentage differences of the 27 SUVr quality metrics evaluated in patients between PET/CT and CMB with CT-based AC. From *"Objective image quality comparison between brain-dedicated PET and PET/CT scanners."* by Maria Teresa Gandia-Ferrero, Irene Torres-Espallardo et al. 2023. Copyright by Journal of Medical Systems.

The harmonization results of the 27 VOI SUVr values between PET/CT and CMB using emission-based attenuation correction, are illustrated in Figures 71 and 72. Figure 71 presents a density plot for a specific VOI, the left and right basal ganglia, before and after harmonization. In this plot, PET/CT data is shown in green, while CMB data is represented in red. Before harmonization, the distributions of both devices were noticeably different. However, after harmonization, the distributions became much more similar, indicating improved alignment between the systems.

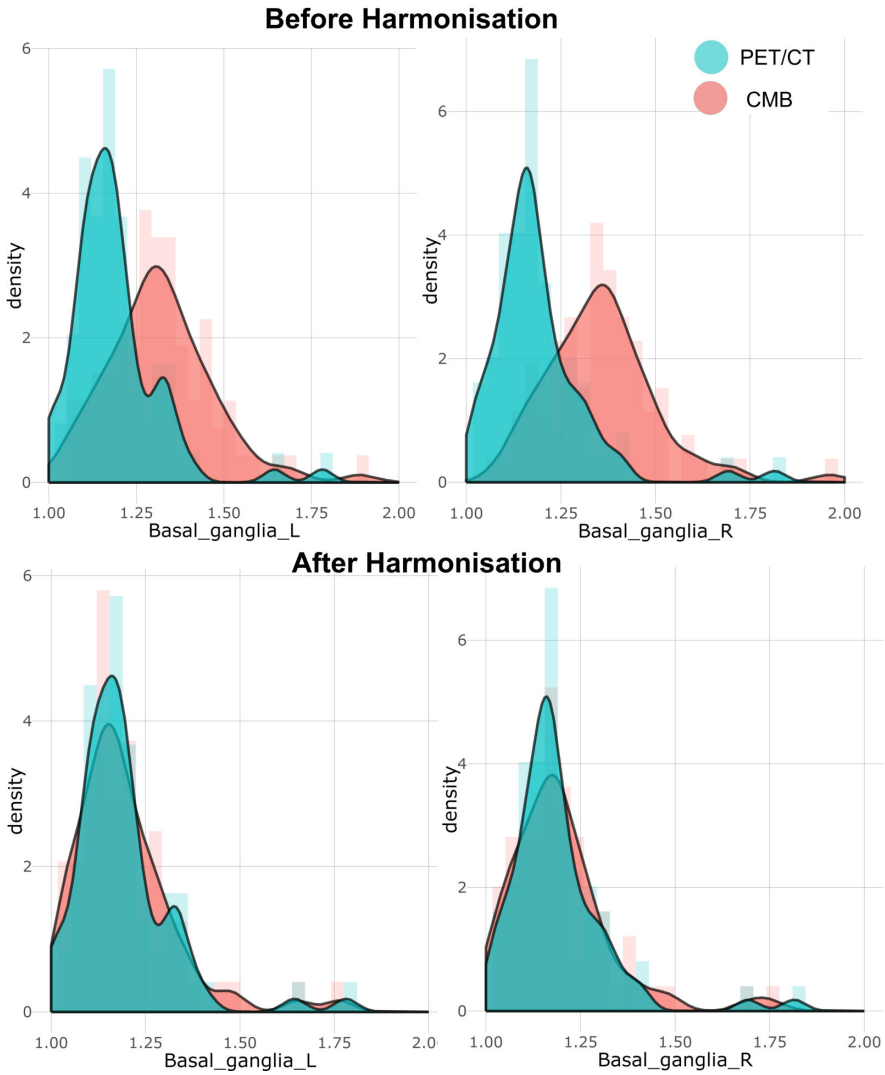

Figure 71: Density plot of the left (on the left) and right basal ganglia (on the right) before (up) and after (down) harmonization for images from PET/CT (green) and CMB with emission-based AC (red).

Figure 72 displays the Bland-Altman analysis for PET/CT and CMB after applying ComBat harmonization. Prior to harmonization (as seen in Figure 65), the analysis revealed differences between the two devices, such as a 15% difference in the right basal ganglia. However, after harmonization, results improved significantly, with an average

difference of 0%, demonstrating the effectiveness of the harmonization process.

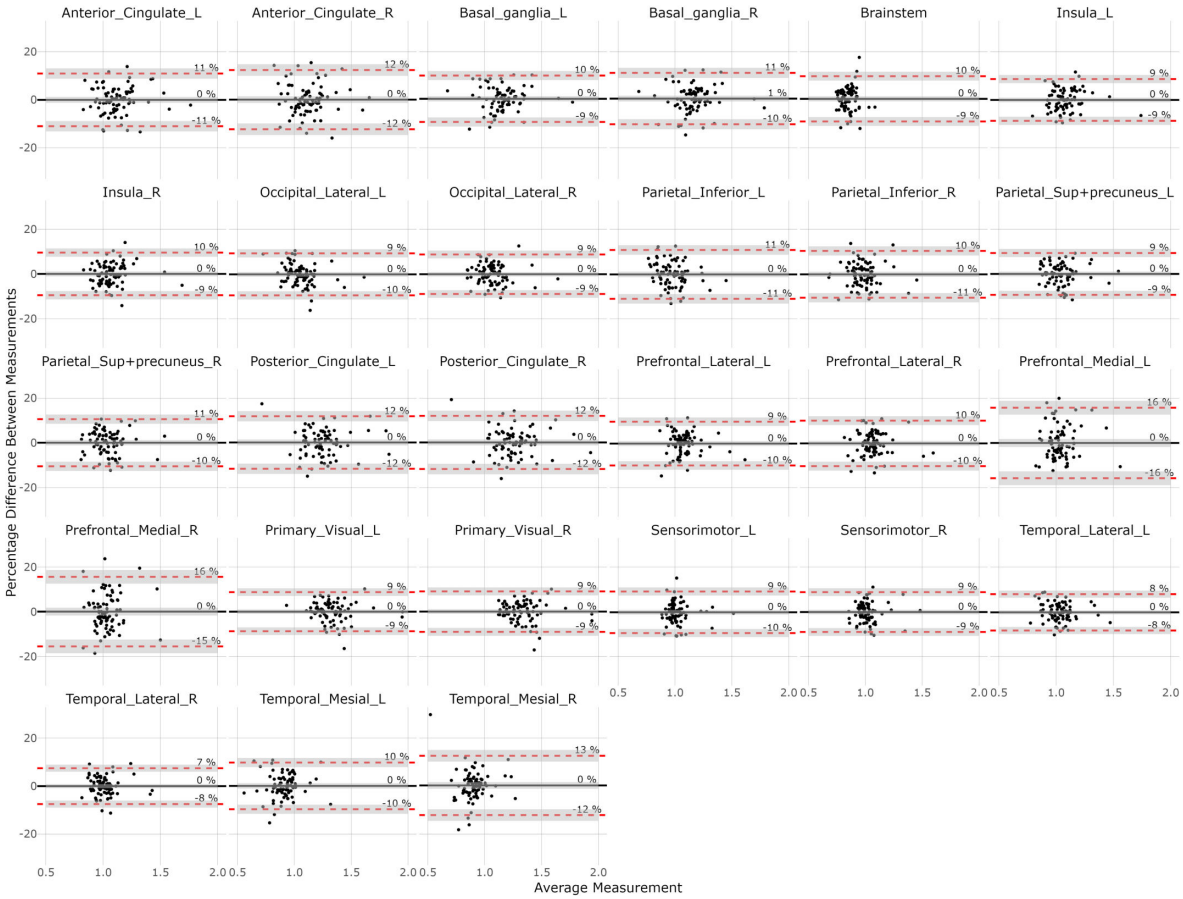

Figure 72: Bland-Altman plot of the 27 SUVr VOIs evaluated in patients for the comparison of PET images between PET/CT and CMB with emission-based AC after harmonization.

4.1.2.2 Evaluation of brain-dedicated PET diagnostic capability

The second purpose of this intervention is to evaluate the diagnostic capability of CMB, in comparison to Philips Gemini TF 64 PET/CT scanner on both FDG and amyloid PET images. For the former evaluation, a prevalidated neural network will be used, and for the latter, the Centiloid Scale will be performed.

4.1.2.2.1 Based on neural networks for FDG images

Since accurate patient diagnosis is crucial when validating a new device, a comparative analysis was conducted between PET/CT and CMB devices. This analysis assessed the level of agreement in diagnosing a group of patients using the deep learning algorithm based on [^{18}F]FDG PET imaging that was previously validated on images from Hospital La Fe which demonstrated strong accuracy [99].

All scans were co-registered to a Dementia-Specific FDG PET template from the MNI and smoothed using a 4 mm FWHM filter. To match the resolution and voxel size of the template, the scans were resized to 110 × 92 × 92, preserving the 2 × 2 × 2 mm voxel size. Additionally, two extra voxels with zero values were included at the edges of the z-axis [99].

The Deep Learning neural network used in this analysis was described earlier (see section 1.1.1.2 Neural Network validation for Alzheimer's Disease prediction). The model was applied to images from both the PET/CT and CMB, reconstructed with the two attenuation correction methods.

To compare the diagnostic predictions between the two different scanners, confusion matrices generated as a result of the neural network predictions were used. The neural network classified patients with MCI as 0 and those with a neurodegenerative disease as 1. The level of agreement between the PET/CT and CMB images (with both AC methods) was evaluated using the kappa coefficient. Table 21 presents the confusion matrices for the neural network predictions based on PET images.

The matrix on the left compares the predictions between PET/CT and CMB with emission-based AC, while the matrix on the right shows the comparison between PET/CT and CMB with CT-based AC. Results indicate that the agreement between PET/CT and CMB with emission-based AC has a kappa coefficient of $k = 0.34$. However, when comparing PET/CT with CMB using CT-based AC, kappa coefficient improves substantially $k = 0.60$.

Table 21: Confusion matrices of the PET images predicted by the deep learning model between predictions from PET/CT images and from CMB images with emission-based AC (left) and with CT-based AC (right) and the resulting Cohen's kappa coefficients. From *"Objective image quality comparison between brain-dedicated PET and PET/CT scanners."* by Maria Teresa Gandia-Ferrero, Irene Torres-Espallardo et al. 2023. Copyright by Journal of Medical Systems.

PET/CT - CMB Emission-based AC			**PET/CT - CMB CT-based AC**		
	PET/CT 0	**PET/CT 1**		**PET/CT 0**	**PET/CT 1**
CMB Emiss-based AC 0	12	0	**CMB CT-based AC 0**	19	0
CMB Emiss-based AC 1	15	28	**CMB CT-based AC 1**	8	28
	***k* = 0.34**			***k* = 0.60**	

4.1.2.2.2 Based on the Centiloid Scale for Amyloid images

The following data analysis aims to demonstrate that the Centiloid scale, without the requirement for other imaging modalities other than amyloid PET from a brain-dedicated PET scanner, is a suitable method for diagnosing Alzheimer's Disease pathology.

The GAAIN dataset was utilized to validate the developed software by replicating the Level-1 analysis, as proposed by Klunk et al. The validation process involved analyzing data from 34 YC-0 and 45 AD-100 subjects, following the methodology described by Klunk et al. Figure 73 illustrates the correlation between the original Pittsburgh analysis and the locally calculated analysis at La Fe hospital.

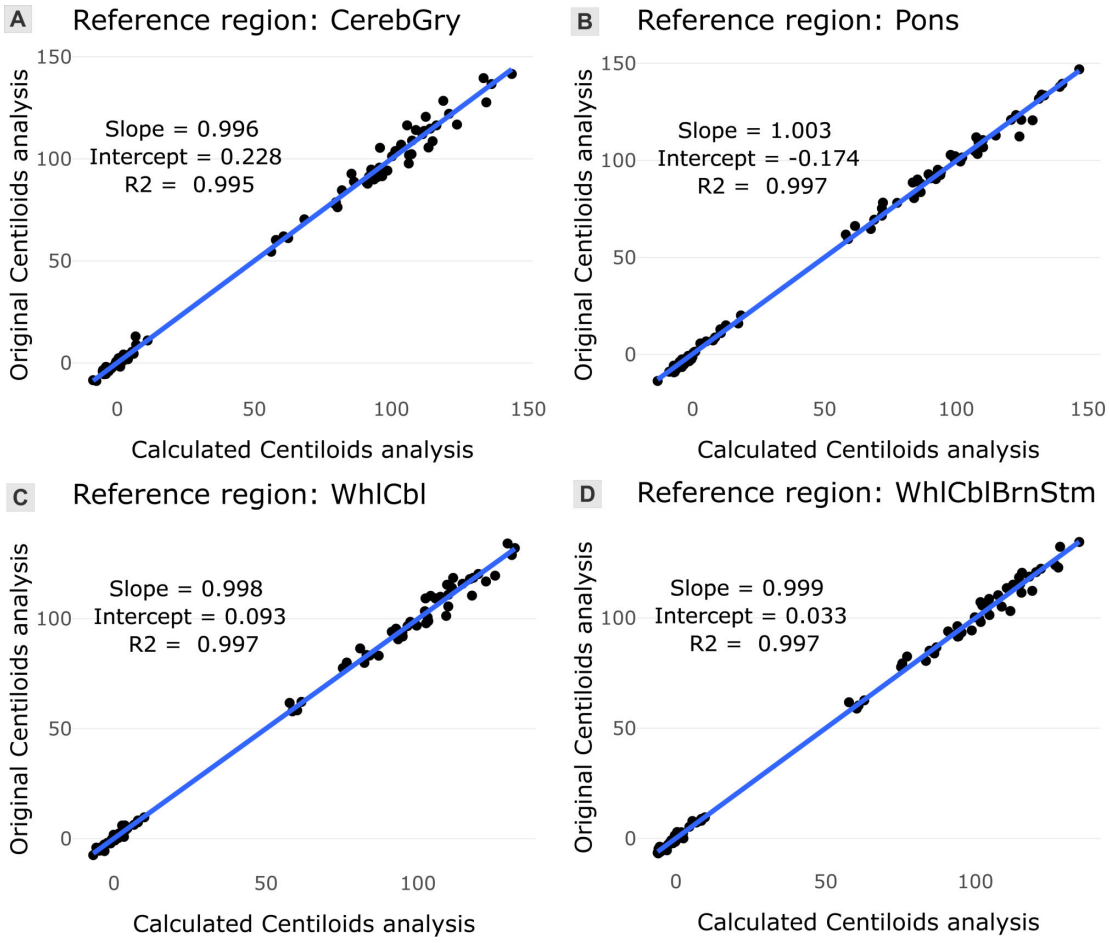

Figure 73: Replication of the Centiloid Scale Level-1 analysis. Correlation of the Pittsburgh (original) and La Fe (calculated) analysis of the 34 YC-0 and 45 AD-100 subject data using 4 reference VOIs: (A) Cerebellum Gray, (B) Pons, (C) Whole Cerebellum and (D) Whole Cerebellum plus brainstem. From *"Amyloid brain-dedicated PET images can diagnose Alzheimer's pathology with centiloid scale."* by Maria Teresa Gandia-Ferrero, Irene Torres-Espallardo et al. 2024. Copyright by Physica Medica.

Additionally, a boxplot distribution of the scaled data grouped by diagnosis is shown in Figure 74. The results indicate that for all reference VOIs (Cerebellum Gray, Pons, Whole Cerebellum, and Whole Cerebellum plus Brainstem), the expected criteria were met (slope between 0.98 and 1.02, intercept between -2 and 2 CL, and $R^2 > 0.98$). Consequently, the validation process for the Centiloid Scale Level-1 replication was successfully completed.

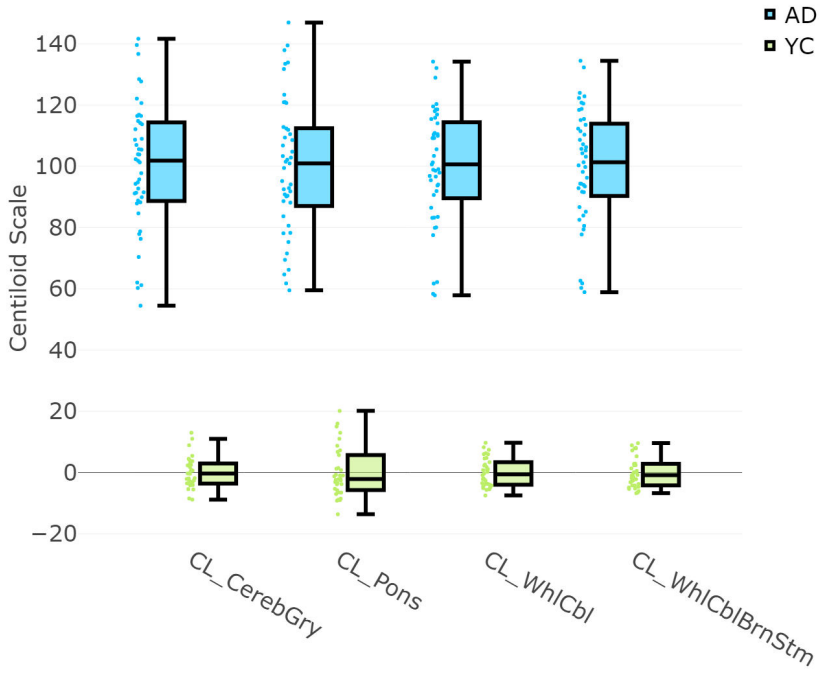

Figure 74: Replication of the Centiloid Scale Level-1 analysis. Boxplots distribution of Scaled data for each reference VOI of La Fe analysis of the 34 YC-0 and 45 AD-100 subject data (from Klunk et al.) for the 4 reference VOIs grouped by diagnosis (blue: Alzheimer's Disease and green: Young Controls). From *"Amyloid brain-dedicated PET images can diagnose Alzheimer's pathology with centiloid scale."* by Maria Teresa Gandia-Ferrero, Irene Torres-Espallardo et al. 2024. Copyright by Physica Medica.

The original pipeline included the use of MR images; however, not all patients undergoing amyloid PET scans have corresponding MR scans. In this study, only 21 out of 26 patients had available MR exams, with 2 patients not undergoing MR scans and 3 scans inaccessible due to being performed at different hospitals. To develop a more general approach, the pipeline was modified to exclude MR images. Instead of coregistering PET to MR images, PET images were directly coregistered and spatially normalized to the Montreal Neurosciences Institute-152 template. This PET-only pipeline was validated by ensuring compliance with the predefined criteria established by Klunk et al. and comparing its results to the standard pipeline. No statistically significant differences were observed between the two methods [259].

Figure 75 presents the correlation results between the PET-only pipeline and the original Centiloid analysis for the Whole Cerebellum reference region. Figure 76

displays the scaled data distribution for the 34 YC-0 and 45 AD-100 subjects, grouped by diagnosis. The statistical comparison (t-test) between the distributions showed p-values greater than 0.05, confirming no significant differences between the pipelines. This validated the elimination of MR image dependency.

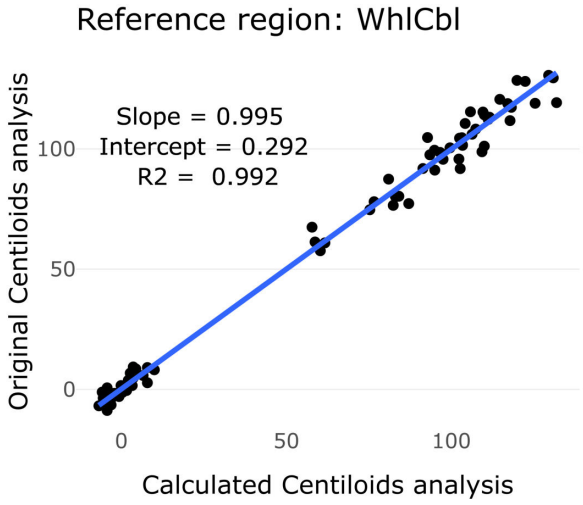

Figure 75: Replication of the Centiloid Scale Level-1 analysis. Correlation of the Pittsburgh (original) and La Fe (calculated) analysis only with PET images of the 34 YC-0 and 45 AD-100 subject data using the Whole Cerebellum as the reference VOI. From *"Amyloid brain-dedicated PET images can diagnose Alzheimer's pathology with centiloid scale."* by Maria Teresa Gandia-Ferrero, Irene Torres-Espallardo et al. 2024. Copyright by Physica Medica.

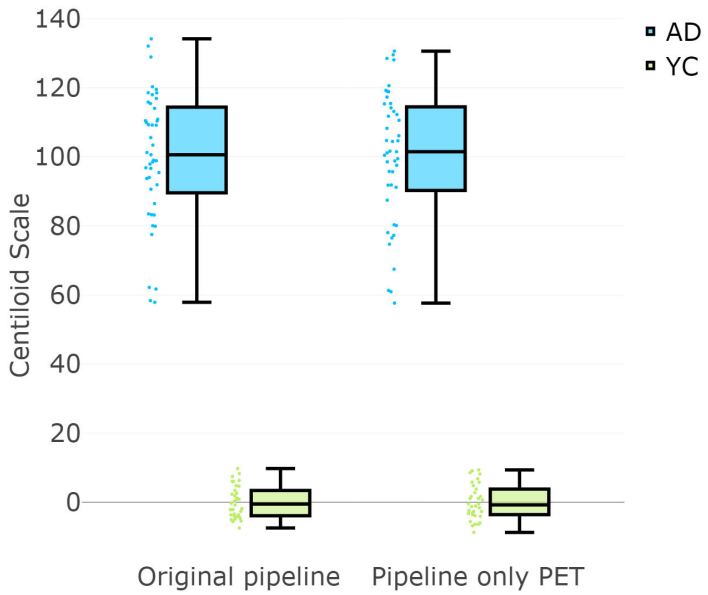

Figure 76: Replication of the Centiloid Scale Level-1 analysis. Boxplots distribution of Scaled data of the Pittsburgh (Original pipeline) and La Fe analysis of the 34 YC-0 and 45 AD-100 subject data for the pipeline with only PET images (Pipeline only PET) grouped by diagnosis (blue: Alzheimer's Disease and green: Young Controls). From *"Amyloid brain-dedicated PET images can diagnose Alzheimer's pathology with centiloid scale."* by Maria Teresa Gandia-Ferrero, Irene Torres-Espallardo et al. 2024. Copyright by Physica Medica.

Although the PET-only pipeline met the expected validation criteria, a Bland-Altman analysis was performed on the subset of patients with available MR images. Figure 77 presents the comparison between the original Pittsburgh pipeline and the La Fe PET-only pipeline.

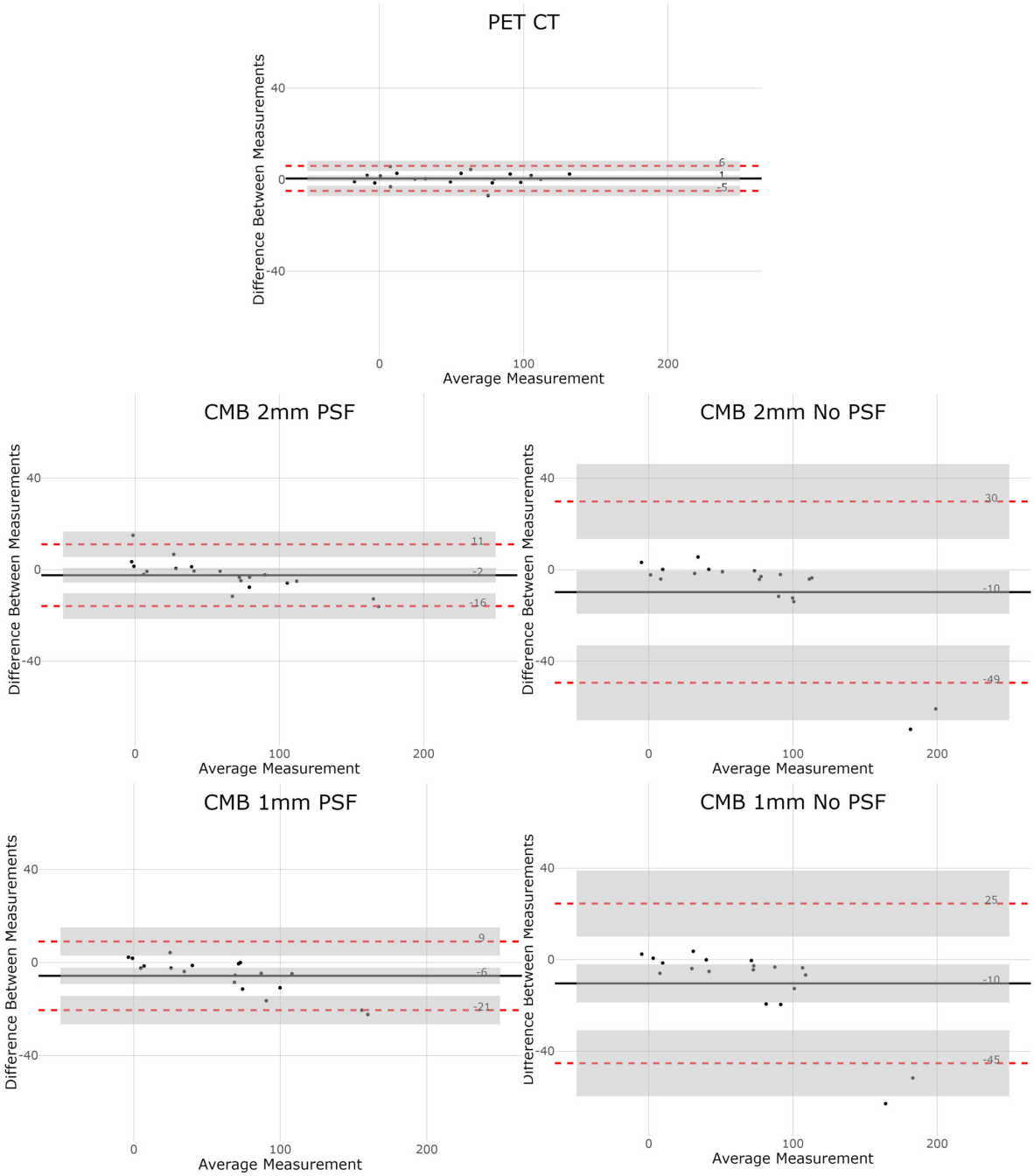

Figure 77: Bland Altman plots of the Centiloid Scale comparing the Pittsburgh (Original pipeline) and La Fe (Pipeline only PET) analysis of the subgroup of subjects that had an MR. From *"Amyloid brain-dedicated PET images can diagnose Alzheimer's pathology with centiloid scale."* by Maria Teresa Gandia-Ferrero, Irene Torres-Espallardo et al. 2024. Copyright by Physica Medica.

Results demonstrated that for PET/CT, no systematic differences were found between the two pipelines. However, for CMB reconstructions, a bias was detected, particularly in No-PSF reconstructions. The observed bias was more pronounced at the extreme Centiloid values. To further investigate this, a Bland-Altman plot excluding values outside the 0-100 CL range was created (Figure 78).

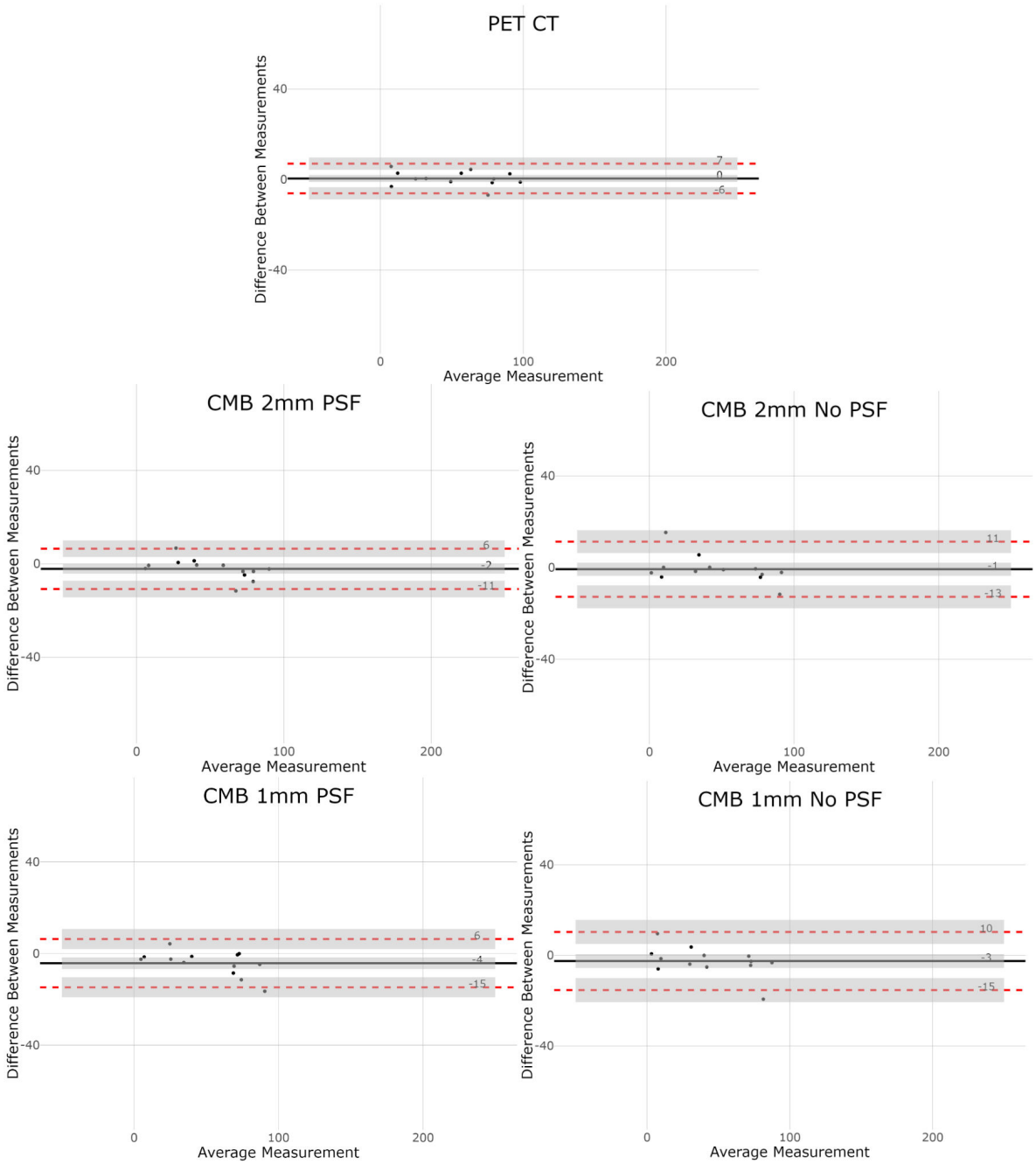

Figure 78: Bland Altman plots of the Centiloid Scale (only values from 0 to 100 CL) comparing the Pittsburgh (Original pipeline) and La Fe (Pipeline only PET) analysis of the subgroup of subjects that had an MR. From *"Amyloid brain-dedicated PET images can diagnose Alzheimer's pathology with centiloid scale."* by Maria Teresa Gandia-Ferrero, Irene Torres-Espallardo et al. 2024. Copyright by Physica Medica.

The exclusion of these extreme values reduced the bias significantly, confirming that it does not impact the clinical interpretation of AD pathology.

Following pipeline validation, PET images from 26 patients acquired on both PET/CT and CMB scanners were processed using the validated PET-only pipeline. The standard equations (refer to Materials and Methods) were applied to convert the acquired data into CL units for three amyloid radiotracers.

Figure 79 illustrates the CL distributions for AD and No-AD patients using different CMB image reconstruction methods (1mmNoPSF, 1mmPSF, 2mmNoPSF, and 2mmPSF) and the PET/CT device. Table 22 presents the confusion matrices for AD diagnosis, determined using the optimal cutoff maximizing the Youden Index. All performance metrics (AUC, accuracy, precision, and recall) were equal to 1 for PET/CT and CMB (1mmNoPSF, 2mmNoPSF, and 2mmPSF). For CMB 1mmPSF, precision remained 1, but recall was 0.93, and AUC and accuracy were 0.96.

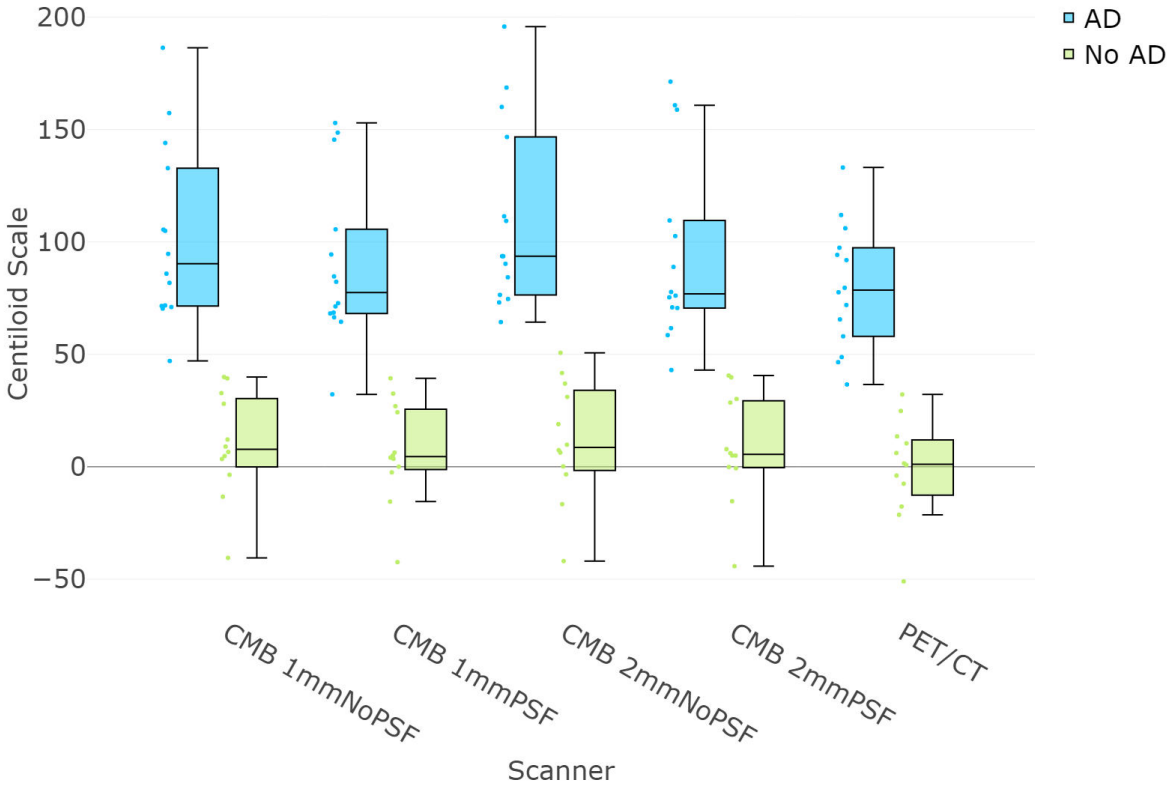

Figure 79: Boxplots distribution of La Fe Scaled data for the PET/CT and the four different reconstructions of CMB scanners grouped by diagnosis (blue: AD and green: No AD). From *"Amyloid brain-dedicated PET images can diagnose Alzheimer's pathology with centiloid scale."* by Maria Teresa Gandia-Ferrero, Irene Torres-Espallardo et al. 2024. Copyright by Physica Medica.

Although the primary goal was to validate the Centiloid Scale for PET images from a brain-dedicated PET scanner, a comparison between PET/CT and CMB recon-

structions was also performed. Figure 80 displays an example of PET/CT and PET CMB images with different reconstruction methods. Notably, the 1mmNoPSF reconstruction appears noisier, with less differentiation between brain structures. Excluding this reconstruction, CMB images were visually comparable to PET/CT images. However, higher amyloid accumulation near the ventricles was observed in CMB images, potentially due to attenuation correction artifacts since CMB does not include a CT component. Despite minor distributional differences, the Centiloid Scale effectively diagnosed AD pathology from CMB dPET images.

Additionally, a nuclear medicine physician with 18 years of experience visually assessed the 26 amyloid brain-dedicated PET images. Table 23 presents the confusion matrices comparing visual assessment with ground truth diagnoses. The kappa coefficient ($\kappa = 0.7$) indicated substantial agreement.

Table 22: Confusion matrices of the diagnosis predicted by the Centiloid Scale. From *"Amyloid brain-dedicated PET images can diagnose Alzheimer's pathology with centiloid scale."* by Maria Teresa Gandia-Ferrero, Irene Torres-Espallardo et al. 2024. Copyright by Physica Medica.

PET/CT **Cutoff (CL):** 34.4 ± 2.2		
	AD	**No AD**
AD	14	0
No AD	0	12

CMB - 1mmNoPSF **Cutoff (CL):** 43.5 ± 3.5		
	AD	**No AD**
AD	14	0
No AD	0	12

CMB - 1mmPSF **Cutoff (CL):** 51.9 ± 12.5		
	AD	**No AD**
AD	13	0
No AD	1	12

CMB - 2mmNoPSF **Cutoff (CL):** 57.5 ± 6.8		
	AD	**No AD**
AD	14	0
No AD	0	12

CMB - 2mmPSF **Cutoff (CL):** 41.8 ± 1.2		
	AD	**No AD**
AD	14	0
No AD	0	12

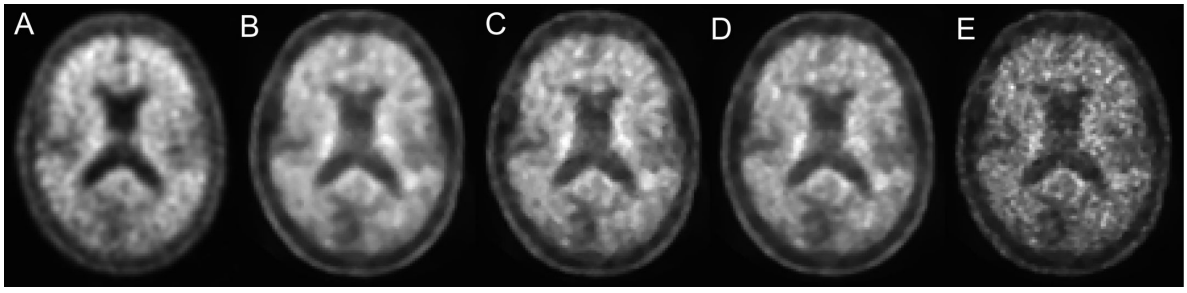

Figure 80: Example of a patient with AD pathology acquired on (A) PET/CT, (B) CMB with 2mmPSF, (C) CMB with 2mmNoPSF, (D) CMB with 1mmPSF, (E) CMB with 1mmNoPSF. The Centiloid values were equal to: (A) 106, (B) 103, (C) 111, (D) 94, (E) 105. From *"Amyloid brain-dedicated PET images can diagnose Alzheimer's pathology with centiloid scale."* by Maria Teresa Gandia-Ferrero, Irene Torres-Espallardo et al. 2024. Copyright by Physica Medica.

Table 23: Confusion matrices of the AD diagnosis of brain-dedicated PET images between predictions from the visual assessment and the true diagnosis. From *"Amyloid brain-dedicated PET images can diagnose Alzheimer's pathology with centiloid scale."* by Maria Teresa Gandia-Ferrero, Irene Torres-Espallardo et al. 2024. Copyright by Physica Medica.

		True diagnosis	
		AD	No AD
CMB visual assessment	AD	11	1
	No AD	3	11

Figure 81 presents the Passing-Bablok regression analysis comparing SUVr values between PET/CT and different CMB reconstructions. While SUVr values were similar across all reconstructions, the regression was more accurate for PSF-based CMB reconstructions (slope ≈ 1, intercept ≈ 0) than for No-PSF reconstructions. This suggests that PSF reconstructions better align with PET/CT results.

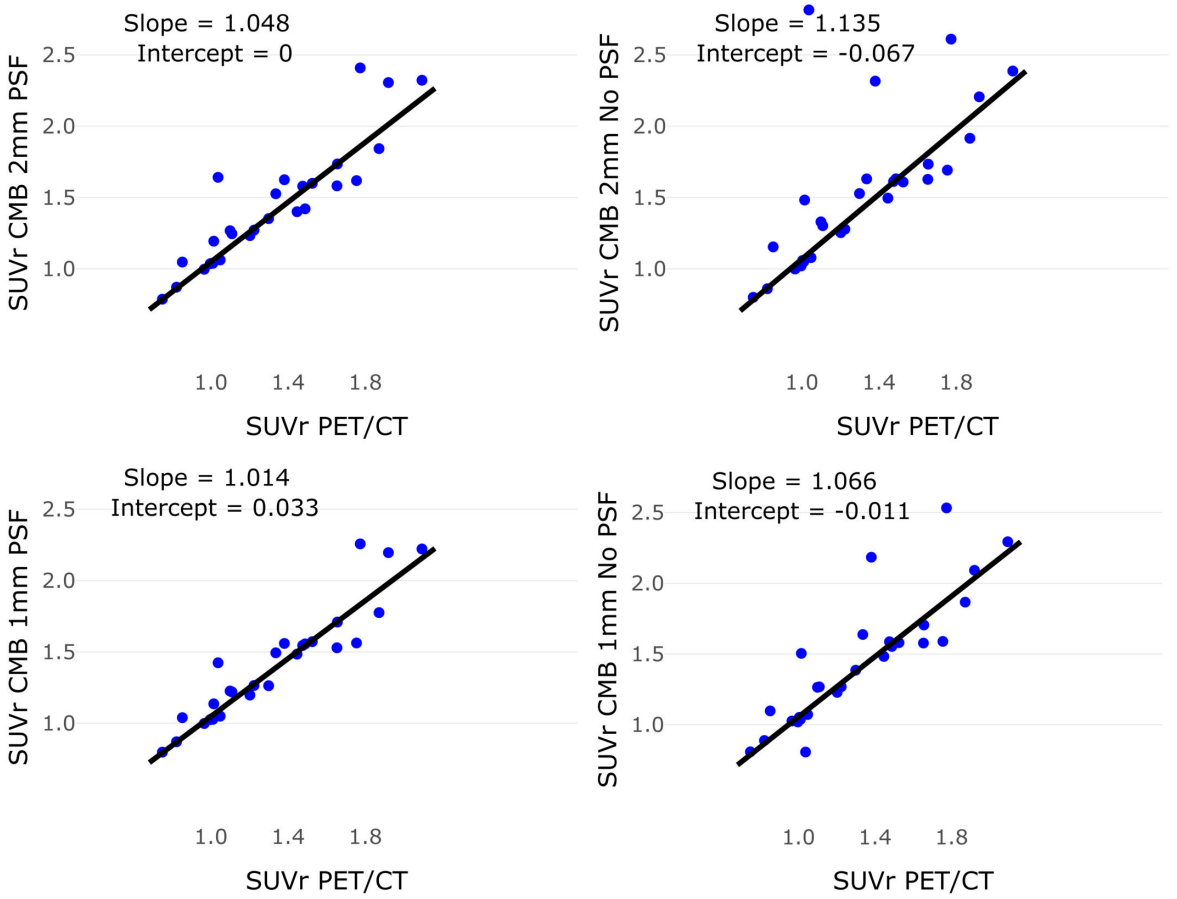

Figure 81: Passing-Bablok regression plots comparing the SUVr values of the 4 different reconstructions of CMB vs PET/CT. From *"Amyloid brain-dedicated PET images can diagnose Alzheimer's pathology with centiloid scale."* by Maria Teresa Gandia-Ferrero, Irene Torres-Espallardo et al. 2024. Copyright by Physica Medica.

4.2 Neuroendocrine tumors

This section looks into the PET vital role in the therapeutical decisions for neuroendocrine tumors. When considering Peptide Receptor Radionuclide Therapy, a sufficient uptake intensity is required, typically corresponding to a Krenning Score $\geq$ 3. Consequently, improved detection of SSR expression intensity may have significant therapeutic implications. Given that different PET scanners produce varying quantitative values, harmonization between different devices is a must. This work will adress the harmonization application between a PET/CT and a PET/MR scanner to achieve reliable results regardless of the device.

4.2.1 Harmonization for consistent treatment recommendations

To assess the impact of harmonization on SUV_{max} values, we first examined the differences between PET/CT and PET/MR measurements. Before harmonization, key observations from [^{68}Ga]Ga-DOTA-TOC PET images of 25 patients acquired on both devices revealed notable scanner-dependent variations. PET/CT identified 109 lesions, whereas PET/MR detected 125. Additionally, tumor SUV_{max} values were consistently higher in PET/MR than in PET/CT. In 29 out of 125 lesions, the KS $\geq$ 3 classification differed between imaging systems, highlighting the potential influence of these discrepancies on treatment decisions. Table 24 represents the characteristics of each of the patients included in the study along with the results of the total number of detected lesions in both PET/CT and PET/MR devices.

In this intervention, the ComBat harmonization method was implemented to harmonise variables between PET/CT and PET/MR scanners. Three different reference systems were used for harmonization: PET/MR as the reference system, PET/CT as the reference system, an arbitrarily chosen reference system. Figure 82 shows a 3D scatter plot of the SUV_{max} values before and after harmonization.

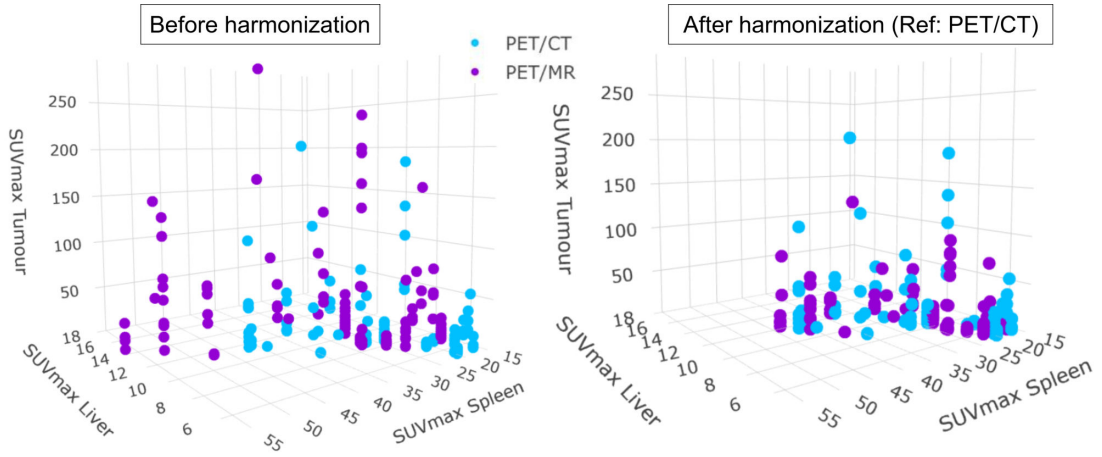

Figure 82: 3D scatter plot where each point represents the SUV_{max} of the liver, spleen and tumor for the PET/CT (blue) and the PET/MR (purple) before harmonization (left) and after harmonization (right) selecting the PET/CT scanner as the reference system.

The figure, shows SUV_{max} values of the liver, spleen, and tumor, with each point representing measurements from PET/CT (blue) and PET/MR (purple). The left side of the figure represents the data before harmonization, highlighting differences between the two imaging systems. The right side displays the data after harmonization, where PET/CT was used as the reference, illustrating how the harmonization reduces discrepancies between PET/CT and PET/MR measurements.

Table 24: Characteristics of each patient included in the series. MF = Multifocality, PHEO = Pheochromocytoma, PGL = Paraganglioma. From *"Same-day comparative protocol PET/CT-PET/MRI [^{68}Ga]Ga-DOTA-TOC in paragangliomas and pheochromocytomas: an approach to personalized medicine"* by Prado-Wohlwend, S., Ballesta-Moratalla, M. et al. 2023. Copyright by Cancer Imaging.

Patient	Gender - Age	Initial diagnosis	MF	PET/CT lesions	PET/MR lesions
1	M - 48	PHEO	Yes	16	16
2	F - 71	Cervical PGL	Yes	4	5
3	F - 38	Cervical PGL	No	1	1
4	M - 38	Retroperitoneal PGL	Yes	5	5
5	M - 54	Cervical PGL	Yes	4	4
6	F - 53	Cervical PGL	Yes	8	8
7	M - 60	Sella Turcica PGL	No	1	1
8	M - 46	PHEO	Yes	11	16
9	F - 50	Cervical PGL	Yes	4	4
10	M - 53	PHEO	Yes	14	19
11	M - 46	PHEO and cervical PGL	Yes	2	2
12	M - 58	PHEO and cervical PGL	Yes	5	5
13	M - 38	Mediastinal PGL	No	1	1
14	M - 59	Cervical PGL	Yes	3	4
15	F - 54	Cervical PGL	Yes	5	7
16	M - 31	Retroperitoneal PGL	Yes	3	4
17	F - 52	Cervical PGL	No	1	1
18	M - 51	PHEO	Yes	3	3
19	M - 44	PHEO	No	1	1
20	M - 51	Cervical PGL	Yes	7	8
21	M - 20	PHEO	No	1	1
22	M - 25	Retroperitoneal PGL	Yes	4	4
23	F - 27	Cervical PGL	No	1	1
24	M - 36	PHEO	Yes	3	3
25	F - 56	Cervical PGL	No	1	1

Table 25 depicts the concordance matrices between PET/CT and PET/MR of the tumors classification based on KS ≥ 3 or not before and after harmonization using the 3 different reference systems. The impact of harmonization on treatment decisions

was then assessed through kappa coefficient. Before harmonization, SUV_{max} values varied between PET/CT and PET/MR for certain lesions, leading to a kappa coefficient of 0.54, which indicates moderate agreement between the two imaging modalities. After harmonization, the level of agreement depended on the reference system used. When PET/MR was set as the reference, the kappa value dropped to 0.04, and when an arbitrary system was used, it was 0.19, both of which indicate insignificant agreement. However, when PET/CT was chosen as the reference system, the kappa value increased to 0.68, reflecting substantial agreement between the measurements.

Table 25: Concordance matrices between PET/CT and PET/MR of the tumors classification based on KS $\geq$ 3 or not before and after harmonization for the three different reference systems.

Before harmonization			**After harmonization PET/MR reference**		
	PET/CT (KS < 3)	**PET/CT (KS ≥ 3)**		**PET/CT (KS < 3)**	**PET/CT (KS ≥ 3)**
PET/MR (KS < 3)	35	0	**PET/MR (KS < 3)**	1	34
PET/MR (KS ≥ 3)	29	61	**PET/MR (KS ≥ 3)**	0	90
	***k* = 0.54**			***k* = 0.04**	

After harmonization PET/CT reference			**After harmonization Standard reference**		
	PET/CT (KS < 3)	**PET/CT (KS ≥ 3)**		**PET/CT (KS < 3)**	**PET/CT (KS ≥ 3)**
PET/MR (KS < 3)	57	13	**PET/MR (KS < 3)**	11	33
PET/MR (KS ≥ 3)	7	48	**PET/MR (KS ≥ 3)**	2	69
	***k* = 0.68**			***k* = 0.19**	

Since the results after harmonization did not align with the expectations, we analyzed the distribution plots of the variables before and after harmonization to better understand the underlying discrepancies. This analysis yielded the following results: Figure 83 displays density plots of SUV_{max} values for the liver and lesion, and target to liver ratio (TLR), with each row representing the distribution of one of these variables, respectively. The columns illustrate how these distributions change before and after harmonization across the three different reference systems. TLR, calculated as the ratio between lesion SUV_{max} and liver SUV_{max}, is particularly relevant as it determines whether KS $\geq$ 3. The vertical red dotted line (TLR > 1) marks the threshold for KS $\geq$ 3, highlighting shifts in classification after harmonization. To further explore these changes, we deeply analyzed the distributions of the TLR before and after harmonization, which is represented in Figure 84.

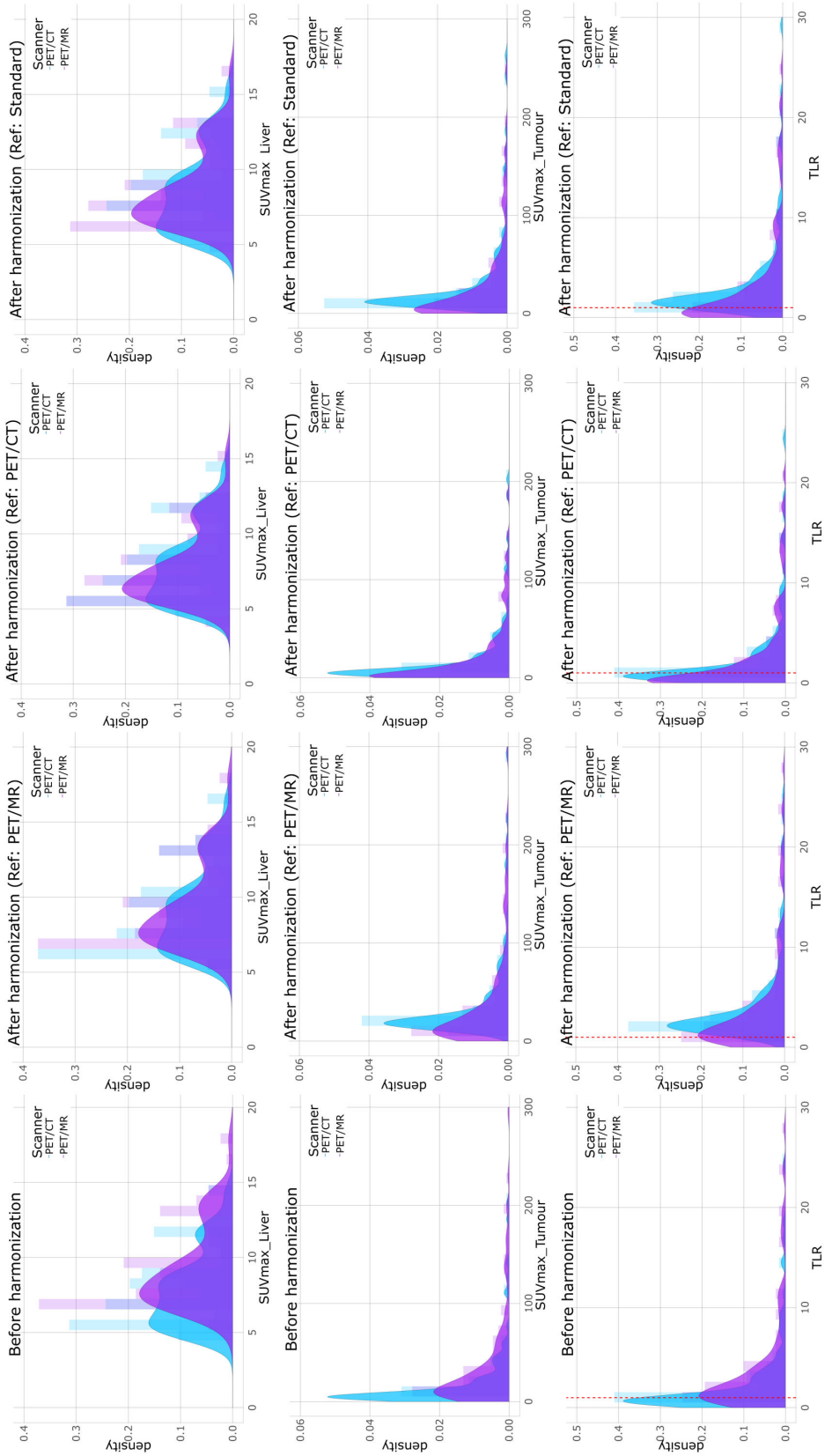

Figure 83: Density plot of the distribution of the SUV_{max} of the liver, the SUV_{max} of the tumor and the TLR before and after harmonization for the three different reference systems. PET/CT distributions are colored in blue while PET/MR, in purple.

A closer look at the TLR distribution in Figure 84 revealed that, after harmonization, except in the case where PET/CT was the reference system, the blue distribution (PET/CT) shifts noticeably to the right, causing nearly all lesions to be classified as KS ≥ 3. This explains the poor agreement observed when the PET/MR or the standard reference systems were chosen. Additionally, the Mann–Whitney–Wilcoxon test confirmed that these distributions showed statistically significant differences.

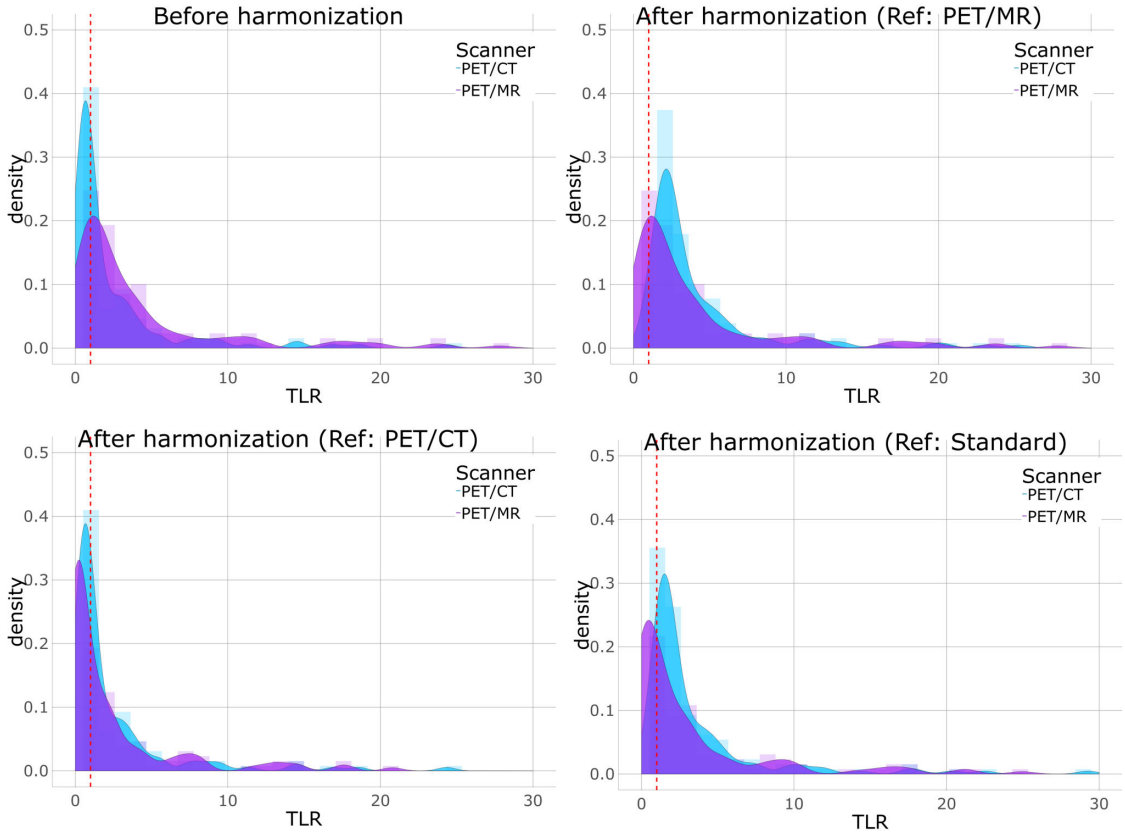

Figure 84: Density plot of the distribution of the TLR before and after harmonization for the three different reference systems. PET/CT distributions are colored in blue while PET/MR, in purple.

A particularly interesting finding was that SUV_{max} values for lesions did not harmonise well using the standard ComBat method. While SUV_{max} values for the liver and spleen aligned well after harmonization, SUV_{max} for lesions remained problematic. Since this variable followed an inverse gamma distribution, a logarithmic transformation was applied before harmonization, followed by an inverse transformation afterward. An example of this process for the PET/CT reference is described in Figure 85.

This step significantly improved the results: Figure 86 illustrates the distributions of the target to liver ratio after applying the transformation, both before and after harmonization, across the three reference systems.

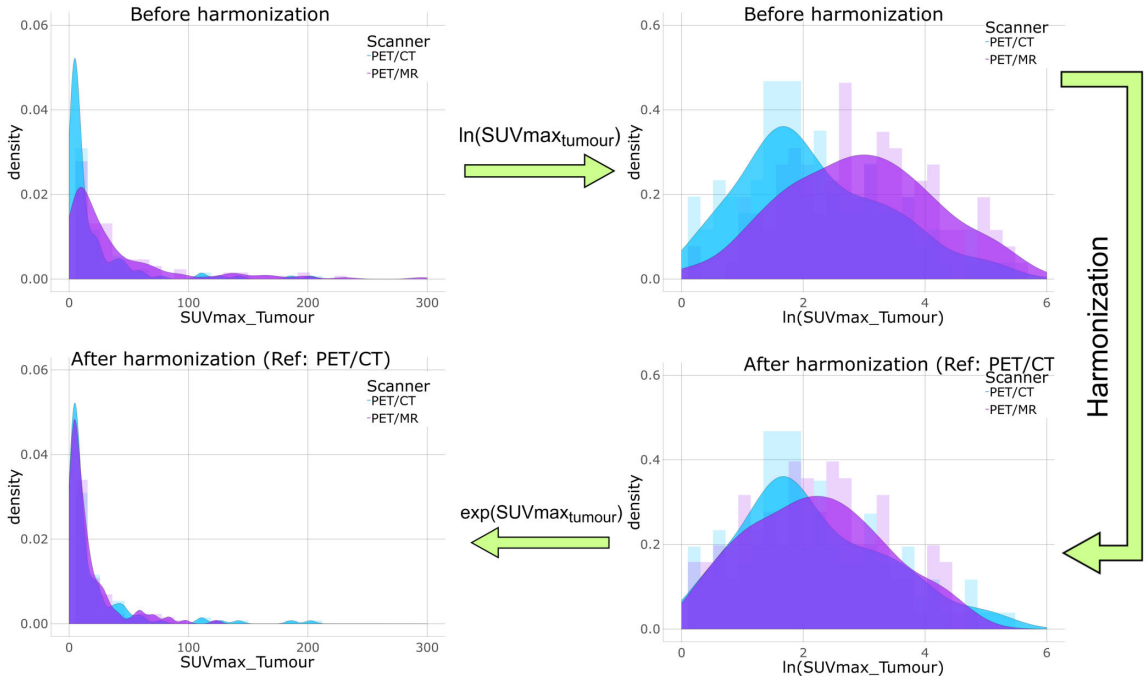

Figure 85: Distributions of the logarithmic transformation of the tumor SUV_{max} before harmonization and exponential transformation after harmonization.

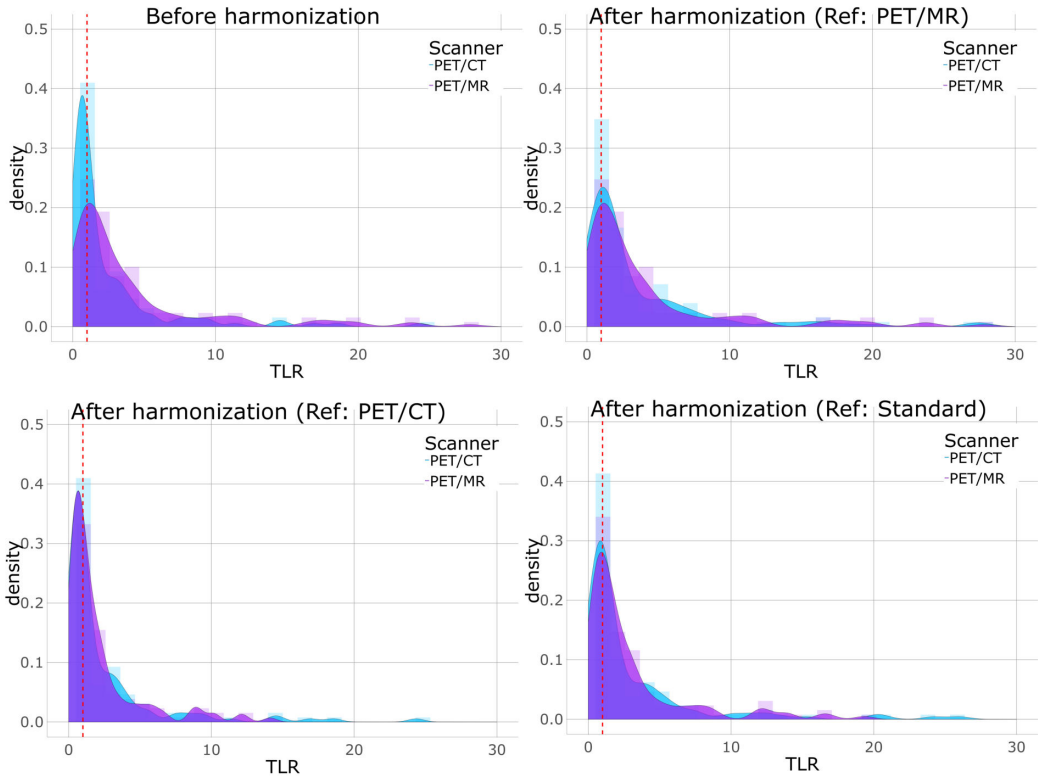

Figure 86: Density plot of the distribution of the TLR before and after harmonization for the three different reference systems after logarithmic transformation of the tumor SUV_{max}. PET/CT distributions are colored in blue while PET/MR, in purple.

In comparison to Figure 84, Figure 86 shows that the harmonization process resulted in significantly better alignment of the distributions between the two devices. The statistical analysis confirmed that, after applying this correction, there were no longer significant differences between the two distributions, meaning that the harmonization process had worked effectively.

Table 26 depicts the concordance matrices, following the log transformation of tumor SUV_{max}, comparing PET/CT and PET/MR for tumor classification based on whether KS ≥ 3, both before and after harmonization across three different reference systems. Similarly, Table 27 displays the concordance matrices, also after log transformation of tumor SUV_{max}, assessing the agreement between PET/CT and PET/MR in PRRT treatment decisions for patients, before and after harmonization across the three reference systems.

Table 26: Concordance matrices (after the log transformation for the tumor SUV_{max}) between PET/CT and PET/MR of the tumors classification based on KS ≥ 3 or not before and after harmonization for the three different reference systems.

Before harmonization			**After harmonization PET/MR reference**		
	PET/CT (KS < 3)	**PET/CT (KS ≥ 3)**		**PET/CT (KS < 3)**	**PET/CT (KS ≥ 3)**
PET/MR (KS < 3)	35	0	**PET/MR (KS < 3)**	25	10
PET/MR (KS ≥ 3)	29	61	**PET/MR (KS ≥ 3)**	10	80
	$k = 0.54$			**$k = 0.60$**	
After harmonization PET/CT reference			**After harmonization Standard reference**		
	PET/CT (KS < 3)	**PET/CT (KS ≥ 3)**		**PET/CT (KS < 3)**	**PET/CT (KS ≥ 3)**
PET/MR (KS < 3)	52	4	**PET/MR (KS < 3)**	39	3
PET/MR (KS ≥ 3)	12	57	**PET/MR (KS ≥ 3)**	18	65
	$k = 0.74$			**$k = 0.65$**	

As previously mentioned, prior to harmonization, SUV_{max} values varied between PET/CT and PET/MR for certain lesions, resulting in a kappa coefficient of 0.54, indicating moderate agreement between the two imaging modalities. Following harmonization, which included log transformation of tumor SUV_{max}, the kappa coefficient increased to 0.60 when PET/MR was used as the reference system, 0.74 when PET/CT was the reference system, and 0.65 for the arbitrary reference system. These findings demonstrate an improvement in agreement, reaching a substantial level regardless of

the PET system used.

With regard to the therapeutic implications, as shown in Table 27, before harmonization, PET/MR would have altered the therapeutic decision in 8 out of 25 patients (32%), resulting in a kappa coefficient of 0.40, indicating fair agreement between the two PET scanners. Following harmonization, the kappa coefficient increased to 0.53 when either PET/MR or PET/CT was used as the reference system and to 0.51 for the arbitrary reference system. These findings highlight an improvement in patient management, with therapeutic agreement reaching a moderate level regardless of the PET system used.

Table 27: Concordance matrices (after the log transformation for the tumor SUV_{max}) between PET/CT and PET/MR of the patient's PRRT treatment decision before and after harmonization for the three different reference systems.

Before harmonization			**After harmonization PET/CT reference**		
	PET/CT No PRRT	**PET/CT PRRT**		**PET/CT No PRRT**	**PET/CT PRRT**
PET/MR No PRRT	6	0	**PET/MR No PRRT**	5	1
PET/MR PRRT	8	11	**PET/MR PRRT**	4	15
	***k* = 0.40**			***k* = 0.53**	
After harmonization PET/MR reference			**After harmonization Standard reference**		
	PET/CT No PRRT	**PET/CT PRRT**		**PET/CT No PRRT**	**PET/CT PRRT**
PET/MR No PRRT	8	1	**PET/MR No PRRT**	5	0
PET/MR PRRT	5	11	**PET/MR PRRT**	6	13
	***k* = 0.53**			***k* = 0.51**	

Chapter 5

DISCUSSION

5.1 Dementia

5.1.1 Diagnosis of neurodegenerative diseases

5.1.1.1 Relationship between neuroimaging and emotion recognition

Recent neuropsychology research in dementia has centered on social cognition impairment, which impacts social relationships [260]. Research indicates that FDT is associated with more severe impairment in social cognition compared to AD [261]. A recent study found that social cognition deficiencies may be more significant in AD than other types of dementia [262]. Assessing social cognition may aid in the differential diagnosis of AD [263]. A recent meta-analysis found that emotion recognition may be impaired in early AD stages [264, 265], even if overall cognition remains unaltered [266]. However, there is some debate in this field. The Reading the Mind in the Eyes Test (RMET) [267, 268] can assess dysfunction in recognizing complex social emotions.

The RMET, originally designed to detect subtle impairments in positive, negative, and neutral emotion recognition in autism, is frequently used [269, 270]. Neuroanatomical alterations in MCI and AD, including the anterior medial frontal cortex, medial temporal cortex, and amygdala, have been linked to social and cognitive problems in patients [271]. DLB and AD patients have shown higher atrophy in the medial temporal lobes and regions associated with Theory of Mind (ToM), such as the prefrontal and orbitofrontal cortex, temporoparietal junction, precuneus, and insula [272].

Future research should combine social cognitive indicators such as RMET with brain structure and function parameters to improve AD prediction accuracy [273] and

evaluate its relationship with MCI. Using emotion recognition tests like the RMET can help increase the understanding of this subject.

This intervention investigated the correlation between brain [^{18}F]FDG PET imaging and cognitive tests. By analyzing clinical markers like cerebrospinal fluid biomarkers and neuropsychological tests, this analysis helped to understand the underlying mechanisms of MCI. Importantly, the potential of exploring socio-cognitive abilities, such as emotion recognition and Theory of Mind, areas often overlooked in MCI and PET imaging research were highlighted. To address this gap, the study examined the connection between [^{18}F]FDG PET findings and socio-cognitive performance, specifically using the Reading the Mind in the Eyes Test, in a group of MCI patients aged 50–80 years. This appears to be the first large-scale study involving MCI from different causes, both neurodegenerative and non-neurodegenerative.

Socio-cognitive abilities underlying individual differences in ToM are a key area of focus in AD continuum research [261, 265], highlighting domain-specific deficits during the MCI stage. In this context, findings in this study demonstrated a consistent relationship between RMET scores and neuropsychological tests assessing cognitive status in MCI, such as the CDR, MMSE, and RBANS using a correlational methodology.

Recent analyses have further suggested that AD patients exhibit impaired abilities to recognize facial expressions [274]. However, no association between RMET performance and cerebrospinal fluid (CSF) biomarkers of Alzheimer's disease was observed in this investigation. As a result, the social cognitive deficit reported in MCI was not specific to AD. Thus, the RMET could show that an early significant impairment in emotion recognition is not particular to Alzheimer's disease. All of these findings give additional evidence and underline the significance of social cognitive assessment in neuropsychological evaluations regarding individuals at risk of dementia [275, 276].

[^{18}F]FDG PET imaging results showed that MCI patients with low RMET scores had reduced glucose metabolism (lower SUVr values) in key brain areas, including medial and lateral prefrontal regions, anterior and posterior cingulate cortices, lateral parietal and temporal regions, the insula, and basal ganglia. These results align with earlier research by Orso et al. [277], which found hypometabolism in some of these areas in AD and frontotemporal dementia patients. Additionally, the negative relationship between Tau protein levels in CSF and glucose metabolism in certain brain regions supports existing findings [278].

The study, however, had some limitations. For instance, primary emotion recognition was not evaluated, and traumatic brain injuries were not systematically recorded. Furthermore, while the study explores correlations between [^{18}F]FDG PET and social cognition, more in-depth studies are needed to delineate neuropathological pathways in specific conditions, such as distinguishing between MCI due to AD and non-AD causes. Larger subgroup samples would be required for these analyses. Despite these limitations, the study provides valuable insights into the role of social cognition in MCI and

it paves the way for future research.

To sum up, the findings from this study showed a correlation between social cognition impairment and changes in the brain's function, particularly in regions important for cognitive and emotional processing, such as the prefrontal cortex, insula, and anterior cingulate cortex. The study identified brain patterns associated with differences in social cognitive abilities among MCI patients, highlight an important step in understanding neurodegeneration. However, it it was found that this early significant impairment in emotion recognition is not particular to Alzheimer's disease.

5.1.1.2 Neural Network validation for Alzheimer's Disease prediction

Our study externally validated a Deep Learning algorithm designed to classify patients with mild cognitive impairment into two diagnostic categories based on FDG PET imaging. The validation was conducted using a dataset of 90 patients whose scans were acquired at Hospital La Fe. The classification differentiates between patients with an underlying neurodegenerative disease and those without. Out of the 90 patients in the validation dataset, 71 were diagnosed with MCI without an associated neurodegenerative disease. Results indicate that the model trained using the ADNI dataset can be effectively applied to hospital images, maintaining 80% balanced accuracy in diagnosing patients. This validation confirms that the network, which was trained on ADNI data, can produce consistent results when tested on an external dataset. The model performs well on both datasets, demonstrating its ability to recognize the key features in brain images for classification.

It must be mentioned that for the external validation of this model, cognitively unimpaired participants were excluded, as they can be more easily identified through other assessments, making an imaging scan unnecessary. Similarly, patients with a higher clinical dementia rating, indicating moderate to severe dementia, were also excluded. While other studies may include them, it was felt that the most challenging classification in clinical practice is distinguishing patients with MCI who have an associated neurodegenerative disease from those in the early stages of cognitive impairment.

This selection bias could have been one potential source of error. Specifically, all ADNI subjects did not have a CDR of 0.5, meaning their cognitive impairment may not have been in the early stages, whereas all patients in the validation dataset had a CDR of 0.5. Additionally, the ADNI dataset only included patients with AD, while the validation dataset included DLB and FTD patients in the MCI group with an associated neurodegenerative disease. Although 100% of FTD patients were correctly identified as distinct from those without a neurodegenerative disease, DLB patients were not identified as accurately. While the model was not trained on images from these other conditions, this study aimed to reflect real world hospital scenarios, where DLB and FTD patients are often together with AD patients in the MCI group [99].

A major limitation of this study is the relatively small dataset size compared to other research, which often involves thousands of images. The dataset was constrained by selection criteria and data availability, considering only the first scan at baseline for each patient. Despite this limitation, the model exhibited reasonable performance. Visualization techniques such as Saliency maps and SmoothGrad highlighted the posterior cingulate and superior parietal areas, aligning with the FDG endophenotype of AD. However, Grad-CAM focused on the right prefrontal cortex, which is not typical of AD. This suggests that SmoothGrad may be the most reliable method in this context. Nonetheless, these visualization techniques for interpreting the neural network should be used cautiously, as they can be highly sensitive to small changes in the input image [279]. Other studies have reported similar findings. For example, Ding et al. [280] observed that the Saliency map indicated their model was considering the entire brain when making predictions. Further research is needed to improve the reliability and interpretation of neural network results.

Several AI studies aim to classify neurodegenerative diseases [63, 88, 280–284]. While some achieve higher accuracy, specificity, or sensitivity, few rely solely on PET imaging; most incorporate MRI and other biomarkers. Furthermore, many studies do not focus on classifying patients with CDR = 0.5, which presents a significant clinical challenge. For instance, Manhua et al. [284] achieved higher balanced accuracy using FDG PET for differentiating AD/MCI from healthy controls (HC). However, their dataset allowed perfect classification based on CDR values alone, unlike this study, where all patients had CDR = 0.5.

Moreover, external validation is uncommonly done. Ding et al. [280] validated an ADNI-trained deep learning model on an independent dataset but included cognitively unimpaired individuals, performing a three-class classification. Unlike their study, our research excluded patients with advanced dementia, focusing solely on MCI classification. While their model achieved 59% balanced accuracy on an independent dataset, our study reached 80%. Additionally, Ding et al. compared model performance to radiologists, showing that their deep learning model outperformed human readers. This study, however, took a step further by validating the algorithm against the final clinical diagnosis, incorporating neuropsychological assessments and CSF biomarker analysis, which provides a more stringent ground truth.

To sum up, the external validation results of the binary classifier model, which was based on a 3D Convolutional Neural Network using FDG PET images, reinforce the value of deep learning models as effective tools for assisting nuclear medicine physicians in classifying neurodegenerative diseases. Unlike simply comparing the model's performance with radiologists' interpretations, this study evaluated the Deep Learning algorithm against the final diagnosis, which was determined through a combination of radiologists' reports, neuropsychological assessments, and CSF molecular analysis. Using the final diagnosis as the reference for comparison is a more rigorous and dependable approach, making it a more robust objective for the study.

The model shows potential in aiding the early, non-invasive detection of neurodegenerative diseases in patients with MCI. While it is not yet implemented in the hospital, it could serve as an experimental decision-support tool for nuclear medicine physicians in daily clinical settings. To enhance the model for future use, new neural network architectures should be explored to improve performance. Incorporating additional non-image variables, such as biometric data, could also lead to more accurate classification results by enhance the model's performance.

5.1.2 Brain-dedicated PET scanner evaluation

In order to reduce the neurological burden of conventional PET/CT, a brain-dedicated PET scanner could be an alternative. However, it is crucial to ensure that both systems provide similar image quality and diagnostic capability. For this reason, for the brain-dedicated PET scanner evaluation application two interventions were proposed, comparing PET/CT and dPET image quality and diagnostic capability.

5.1.2.1 Objective PET image quality evaluation

The analysis of the Hoffman phantom results indicates that CMB images exhibit higher contrast and RC but also lower SNR and higher COV compared to PET/CT images. These trends observed in the phantom reconstructions are also seen in patient data, with the exception that contrast values between CMB and PET/CT images are similar (slightly higher for CMB, but within the error bars).

The lower SNR in CMB images suggests greater variability among voxels in uniform image regions, which can be attributed to the smaller voxel size used in CMB imaging ($1 \times 1 \times 1$ mm^3). CMB reconstruction settings are optimized for high-resolution imaging, with a measured spatial resolution of 1.5 mm at the center of the field of view (FOV) [128], whereas the Philips Gemini TF PET/CT system reports a spatial resolution of 4.8 mm [170]. The smaller voxel size results in sharper images but also more heterogeneous activity distributions. The CNR and SNR values measured in this study align with these expected characteristics. Overall, the analysis confirms that CMB images do not exhibit lower quality metrics than conventional PET/CT images.

When comparing SUVr between CMB images reconstructed using emission-based AC and those using CT-based AC, significant differences were observed. These differences are largely due to the simplified assumption in the emission-based approach, which models the head as a homogeneous volume. Although statistically significant differences were detected in various brain regions when comparing PET/CT images with CT-based AC CMB images, the relative differences remained small, with a mean of 4% across all 27 regions and a maximum difference of 7% in the occipital lateral

region.

These values are lower than those reported in similar studies evaluating attenuation correction techniques on commercial PET/MR systems. For instance, an analysis of MR-based AC accuracy in the Philips Ingenuity TF whole-body PET/MR found differences of up to 20% [285], whereas the values in this study align with those obtained using Atlas-based correction techniques such as the Mean Atlas approach [286]. Ongoing research is focusing on improving emission-based attenuation maps through convolutional neural networks, which have previously demonstrated superior performance compared to Atlas-based techniques [127, 287].

Relative SUVr differences remain within a similar range (5% mean) when comparing CMB images reconstructed with CT-based AC to PET/CT images. These discrepancies could be attributed to differences in system specifications, including FOV, detector proximity, and reconstruction algorithms. However, the observed variations are consistent with the expected scanner-to-scanner variability [288]. In contrast, when comparing emission-based CMB images with PET/CT, the number of regions showing statistically significant differences increases, and the mean relative difference exceeds 5%, with some regions exceeding 10%.

The results of the Passing-Bablok regression analysis further support the observed differences, providing a measure of agreement between the two imaging devices. The findings indicate that PET/CT images are more closely aligned with CMB images using CT-based AC than with CMB images using emission-based AC. These results highlight the importance of improving attenuation correction maps to enhance image consistency across different devices.

The Bland-Altman analysis revealed an asymmetry between the left and right hemispheres when comparing images from the two devices. However, this asymmetry was not present when comparing CMB images reconstructed using different attenuation correction methods. Despite this asymmetry, the differences between PET/CT and CMB remain minimal.

Finally, it is well known that different PET systems provide varying quantitative values due to differences in scanner parameters. This variability has been demonstrated in Bland-Altman plots comparing PET/CT and CMB dPET systems. Since standardized uptake value ratios are crucial for diagnosing neurological diseases, it is essential to harmonize SUVr measurements across both devices to ensure consistency. The results of ComBat harmonization between PET/CT and CMB indicate that this method is highly effective in aligning data from different scanners. Using harmonization techniques like ComBat allows for more reliable and reproducible analyses, making scanner comparisons more accurate.

It is worth noting that due to the current system design (an inclined cylinder), the device requires a stabilization mechanism when acquiring phantom images. Addi-

tionally, 28% of the patients were excluded from this study because their cerebellum was not fully captured within the axial field of view. Although not addressed in this study, an extended axial FOV is recommended to resolve this limitation.

It is also worth mentioning that a clinical comparison of CMB images and brain PET/CT was previously conducted by Cabrera-Martin et al. [289]. In that study, nuclear medicine specialists visually assessed image quality by classifying scans as normal or abnormal and ranked CMB images into five categories based on quality relative to brain PET/CT images. The ranking scale ranged from Category 1 (CMB image quality significantly lower than PET/CT) to Category 5 (CMB image quality significantly higher than PET/CT). The first analysis demonstrated complete agreement (kappa coefficient = 1), while the second analysis showed a good level of agreement (kappa coefficient = 0.70). Most cases (19 out of 40) were classified as having image quality similar to PET/CT. The authors concluded that CMB images are qualitatively comparable to brain PET/CT images.

5.1.2.2 Evaluation of brain-dedicated PET diagnostic capability

5.1.2.2.1 Based on neural networks for FDG images

Considering results from the previous intervention regarding image quality evaluation, clinical assessment was necessary to determine whether small differences between the devices impact the final diagnosis. Since a patient's diagnosis is the key factor in validating a new medical device, the comparison was conducted between PET/CT and CMB by analyzing the consistency of diagnosis predictions made using this previously explained deep learning algorithm. This algorithm was applied to the $[^{18}F]$FDG PET images of the 55 patients with cognitive impairment acquired on both PET scanners.

The kappa coefficient findings indicate that the agreement between PET/CT and CMB with emission-based attenuation correction is fair, whereas the agreement improves to a substantial level when comparing PET/CT with CMB using CT-based AC. This confirms that CMB images using CT-based attenuation correction closely resemble conventional PET/CT images compared to CMB images that use emission-based attenuation correction.

On the other hand, a clinical comparison of CMB images and brain PET/CT was previously conducted by Cabrera-Martin et al. [289]. In that study, nuclear medicine specialists visually assessed image quality by classifying scans as normal or abnormal relative to brain PET/CT images. The analysis demonstrated complete agreement (kappa coefficient = 1) between normal and abnormal brain PET images, thus concluding that CMB images are qualitatively comparable to brain PET/CT images.

5.1.2.2.2 Based on the Centiloid Scale for Amyloid images

The recent authorization of two drugs for AD by the FDA (aducanumab and lecanemab), which may also receive approval from the EMA in the near future, has brought attention to a significant rise in the demand for amyloid brain PET/CT scans within the nuclear medicine community. Estimates suggest that the number of amyloid brain PET-CT studies could increase by approximately 20 times [112]. This surge is attributed to the fact that PET/CT scans will not only be utilized for patient selection in treatment but may also play a role in therapy guidance, including determining treatment duration, adjusting doses, and identifying non-responders [113].

Given this pressing need to manage the burden of neurodegenerative diseases, the development of brain-dedicated imaging devices has become essential. Compared to whole-body PET scanners, dedicated brain PET systems aim to enhance performance by improving spatial resolution and increasing sensitivity, which facilitates the imaging of small brain regions. Additionally, dedicated PET scanners offer advantages such as enhanced portability, mobility, and cost-effectiveness [75].

Furthermore, there is an urgent necessity for a standardized approach to diagnosing AD pathology through amyloid imaging across different medical centers. Variability in amyloid PET results arises due to differences in factors such as the specific amyloid tracer used, acquisition duration, attenuation correction techniques, analysis methods, target and reference regions, partial volume correction strategies, and variations in scanners, imaging protocols, and reconstruction algorithms. Standardization of these aspects is crucial to ensuring consistency and reliability in amyloid PET imaging outcomes.

To achieve standardized measurements across different medical centers, Klunk et al. [225] introduced the Centiloid method. This approach linearly scales the measurements of a specific tracer to standard Centiloid units (CL). The CL scale ranges from 0 to 100, where a value of 0 corresponds to the average uptake in young control patients, while a value of 100 represents the average uptake observed in typical Alzheimer's Disease (AD) patients at the dementia stage.

The objective of this intervention was to demonstrate that the Centiloid scale, when applied using only PET imaging from a brain-dedicated PET scanner, serves as a reliable and effective method for diagnosing AD pathology without the necessity of additional imaging modalities.

This study confirmed the suitability of the Centiloid methodology for predicting Alzheimer's disease pathology using a brain-dedicated PET scanner, even without requiring MR images for spatial normalization. The optimal Centiloid cutoff values, determined as those maximizing the Youden Index, yielded excellent performance in identifying patients with AD pathology. The only CMB reconstruction where perfor-

mance metrics did not reach their maximum was the 1mmPSF configuration. This discrepancy was due to one patient, predicted as not having AD, who was later diagnosed with AD. This particular case corresponds to the lowest blue data point among all AD (blue) distributions (see Fig. 79). The patient had preclinical AD, which is characterized by neuropathological lesions preceding clinical symptoms [290]. The patient scored 28 on the MMSE neuropsychological test, and the nuclear medicine physician's evaluation was inconclusive regarding Aβ plaque accumulation. However, cerebrospinal fluid analysis confirmed abnormal Aβ levels.

Several studies have reported optimal Centiloid cutoff values for Aβ positivity. Salvadó et al. [291] suggested that a cutoff around 12 CL indicates the transition from no pathology to subtle pathology, while a value of approximately 30 CL marks established pathology. Bullich et al. [292] identified cutoffs at 13.5 CL for early amyloid pathology and 35.7 CL for established pathology. Amadoru et al. [293] found that values below 10 CL accurately reflected an absence of neuritic plaques, values above 20 CL indicated moderate plaque density, and values of 50 CL or more confirmed neuropathological and clinicopathological diagnoses of AD. The cutoff values obtained in this study for the 26 patient PET images align with these established values.

Nevertheless, differences in cutoff values were observed between PET/CT (34.4 ± 2.2) and the four CMB reconstructions (2mmPSF: 41.8 ± 1.2, 2mmNoPSF: 57.5 ± 6.8, 1mmPSF: 51.9 ± 12.5, and 1mmNoPSF: 43.5 ± 3.5). It is well known that different PET systems produce variations in quantitative values due to scanner parameters, affecting objective threshold values. Therefore, standardization across centers is crucial to ensure consistent results, irrespective of the equipment used. Klunk et al. [225] introduced the Centiloid scale to provide a standardized method for diagnosing AD pathology via amyloid imaging. Despite slight differences in AD pathology thresholds due to scanner parameters, the ability to identify AD pathology remains intact. Among the CMB reconstructions, the 2mmPSF reconstruction yielded the most comparable cutoff to the PET/CT scanner.

It is noteworthy that the RSNA QIBA Profile for Amyloid PET as an Imaging Biomarker for Cerebral Amyloid Quantification [294] does not recommend the use of the PSF filter for amyloid image quantification when employing SUVr as a biomarker. However, our study demonstrates that reconstructions with and without PSF produce equivalent results in confusion matrices, validating the use of PSF reconstruction with the Centiloid Scale.

To our knowledge, no previous studies have compared the Centiloid scale on PET images acquired from the same patient cohort using two different scanners. However, given the variability of AD pathology in the population, the relatively small sample size (26 patients) represents a limitation. Future studies with larger sample sizes are necessary to further investigate the impact of scanner parameters and improve confidence in Centiloid cutoff values. Despite recognizing that Centiloid cutoffs may slightly vary depending on the scanner, the Centiloid scale remains a valuable clinical tool, provided

that appropriate cutoffs are established for specific scanner protocols.

Another limitation of this study was the exclusion of two patients due to incomplete cerebellum coverage in the PET scan, preventing the application of the Centiloid Scale methodology. In clinical practice, it is essential to ensure that the cerebellum is fully captured in PET images. Additionally, the CMB device is expected to be upgraded with an extra detection ring to enhance axial field-of-view coverage.

Finally, based on both quantitative analysis and visual assessment, the 2mmPSF reconstruction appears to be the most suitable configuration for amyloid imaging using the CMB device. Overall, the Centiloid Scale proved to be a reliable method for diagnosing AD pathology using brain-dedicated PET imaging, independent of additional imaging modalities.

5.2 Neuroendocrine tumors

5.2.1 Harmonization for consistent treatment recommendations

In the context of of metastatic or unresectable paragangliomas and phaeochromocytomas, [^{68}Ga]Ga-DOTA-TOC PET imaging plays a crucial role in both diagnosis and treatment planning (theranostics). Patient eligibility for peptide receptor radionuclide therapy with [^{177}Lu]Lu-DOTA-TATE is determined by assessing uptake intensity, which is quantified using the Krenning Score. A KS value of ≥ 3, indicating that lesion uptake exceeds that of the liver, is required for therapy consideration. However, variations in PET systems may result in differing quantitative values due to differences in hardware, reconstruction algorithms, and correction methodologies.

Owing to inherent discrepancies in SUV measurements across PET/CT and PET/MR systems, these lesions would change from being unsuitable for SSR-targeted therapies to being appropriate for them from a theragnostic perspective. Before harmonization, 29 out of 125 lesions (23%) were classified differently depending on whether the scan was done with PET/CT or PET/MR. This lack of agreement between scanners was reflected in a kappa coefficient of 0.54, indicating only a moderate level of agreement.

This variation highlights the necessity for harmonization to ensure consistency in clinical decision-making, regardless of the imaging system. In this study, the ComBat harmonization method was applied to SUV_{max} values obtained from PET/CT and PET/MR and evaluated its impact on lesion classification.

Following the implementation of the ComBat harmonization method, three different reference systems were evaluated: PET/MR as the reference, PET/CT as the reference, and an arbitrary reference system. The results indicated that harmonization significantly reduced scanner-dependent variability when PET/CT was used as the reference, achieving a kappa coefficient of 0.68, indicating substantial agreement. However, when PET/MR was the reference or an arbitrary system was used, agreement levels were significantly lower, with kappa values of 0.04 and 0.19, respectively.

Despite successful harmonization of SUV_{max} values for liver and spleen tissues, lesion SUV_{max} values remained problematic. The observed discrepancies were attributed to the non-Gaussian distribution of lesion SUV_{max}, which followed an inverse gamma distribution. To address this, a logarithmic transformation was applied before harmonization, followed by an inverse transformation afterward.

After this adjustment, following harmonization, the agreement improved across all reference systems, with kappa values increasing to 0.60 for PET/MR reference, 0.74 choosing PET/CT as references and 0.65 for the arbitrary system. These findings suggest that harmonization enhances the consistency of PRRT eligibility assessments, potentially reducing variability in clinical decision-making.

A limitation of this study is the small sample size. A validation in larger, multicenter cohorts will be needed to confirm the generalizability of these findings. Investigating the integration of deep-learning-based harmonization methods could further enhance standardization across imaging modalities.

To sum up, these results emphasize the importance of verifying harmonization outcomes variable by variable. Although ComBat provides a valuable tool for harmonization, its application requires careful validation to avoid misclassifications. With careful selection of the reference system and appropriate data transformations, the ComBat method can successfully harmonize PET data across different scanners, reducing equipment-based variability. This approach facilitates reliable cross-system comparisons, ensuring that patients receive consistent and accurate theragnostic evaluations regardless of the PET imaging system used.

Chapter 6

GENERAL CONCLUSIONS

Impact of Advanced PET Imaging Analysis on Clinical Decision-Making:

- Quantitative PET image analysis enhances diagnostic precision and reliability in treatment decisions for patients with dementia and neuroendocrine tumors.
- Optimizing imaging technology is essential for improving clinical outcomes.

Applications in Dementia Diagnosis:

- The combination of FDG PET with social cognition assessment (*Reading the Mind in the Eyes Test*) provides additional insights for early diagnosis of MCI since emotional recognition deficits are present in MCI patients. However, these are not exclusive to Alzheimer's disease, and therefore, it does not improve accuracy in identifying Alzheimer's disease.
- An externally validated deep learning-based classification algorithm achieved 80% accuracy in identifying mild cognitive impairment (MCI) associated with neurodegenerative diseases.
- A comparison between dedicated brain PET scanners and conventional PET/CT systems demonstrated that brain-dedicated scanners can reduce the burden on general PET/CT scanners while maintaining image quality and diagnostic reliability.

Applications in Neuroendocrine Tumours:

- Differences in PET scanner parameters significantly impact SUV measurements, directly affecting patient eligibility for peptide receptor radionuclide therapy, highlighting the need for data harmonization to standardize clinical practice.

- ComBat harmonization aligns SUV values between PET/CT and PET/MR scanners, reducing variability in lesion classification and improving consistency in treatment recommendations.

Challenges and Future Perspectives:

- While advanced computational methods have demonstrated improved diagnostic accuracy and treatment planning, challenges remain, including the need for larger datasets and multicenter studies to validate harmonization techniques.
- Standardizing PET imaging techniques in nuclear medicine is crucial to ensure consistent clinical decisions across different imaging devices.
- The findings of this study support the continued development of quantitative PET imaging tools and reinforce their role in precision medicine.

Publications derived from the thesis

Original Papers:

- Gandia-Ferrero, M. T., Torres-Espallardo, I., Martínez-Sanchis, B., Muñoz, E., Morera-Ballester, C., Sopena-Novales, P., AlvarezSanchez, L., BaqueroToledo, M., & Martí-Bonmatí, L. (2024). Amyloid brain-dedicated PET images can diagnose Alzheimer's pathology with Centiloid Scale. *Physica Medica*. https://doi.org/10.1016/j.ejmp.2024.103345.
- Gandia-Ferrero, M. T., Adrián-Ventura, J., Cháfer-Pericás, C., AlvarezSanchez, L., Ferrer-Cairols, I., MartinezSanchis, B., TorresEspallardo, I., BaqueroToledo, M., & MartiBonmati, L. (2024). Relationship between neuroimaging and emotion recognition in mild cognitive impairment patients. *Behavioural Brain Research, 461*. https://doi.org/10.1016/j.bbr.2023.114844.
- Gandia-Ferrero, M. T., Torres-Espallardo, I., Martínez-Sanchis, B., Morera-Ballester, C., Muñoz, E., Sopena-Novales, P., González-Pavón, G., & Martí-Bonmatí, L. (2023). Objective Image Quality Comparison Between Brain-Dedicated PET and PET/CT Scanners. *Journal of Medical Systems, 47(1), 88*. https://doi.org/10.1007/S10916-023-01984-7.
- Prats-Climent, J., Gandia-Ferrero, M. T., Torres-Espallardo, I., Álvarez-Sanchez, L., Martínez-Sanchis, B., Cháfer-Pericás, C., Gómez-Rico, I., Cerdá-Alberich, L., Aparici-Robles, F., Baquero-Toledo, M., Rodríguez-Álvarez, M. J., & Martí-Bonmatí, L. (2022). Artificial Intelligence on FDG PET Images Identifies Mild Cognitive Impairment Patients with Neurodegenerative Disease. *Journal of Medical Systems, 46(8)*. https://doi.org/10.1007/s10916-022-01836-w.

Congresses:

- Gandia-Ferrero, M. T., Torres-Espallardo, I., Martínez-Sanchis, B., Muñoz, E., Morera-Ballester, C., Sopena-Novales, P., AlvarezSanchez, L., BaqueroToledo, M., & Martí-Bonmatí, L. (2024). Las imágenes PET amiloide dedicadas al cerebro pueden diagnosticar Alzheimer con la escala Centiloide. *40 Congreso de la*

Sociedad Española de Medicina Nuclear e Imagen Molecular 2024. https://www.elsevier.es/es-revista-revista-espanola-medicina-nuclear-e-125-congresos-40-congreso-sociedad-espanola-medicina-166-sesion-comunicaciones-orales-8283. CO013 Oral Presentation

- Gandia-Ferrero, M. T., Torres-Espallardo, I., Prado-Wohlwend, S., Bello-Arques, P., Vázquez-Martínez, M., Ginés-Cárdenas, S., Almendros-Riaza, Á., & Martí-Bonmatí, L. (2023). Armonización en equipos PET/CT y PET/RM aplicado a estudios con 68Ga. *8º Congreso Conjunto de la SEFM-SEPR 2023*. (Pages 179-180) https://congresosefmsepr.es/oviedo2023/libros-resumenes/. **1st prize oral communication SEFM**.

- Gandia-Ferrero, M. T., Torres-Espallardo, I., Prado-Wohlwend, S., Bello-Arques, P., Vázquez-Martínez, M., Ginés-Cárdenas, S., Almendros-Riaza, Á., & Martí-Bonmatí, L. (2023). ComBat harmonization in different PET imaging scenarios. *Congress of the European Association of Nuclear Medicine 2023*. https://doi.org/10.1007/s00259-023-06333-x. EPS-096 Eposter presentation.

- Gandia-Ferrero, M. T., Torres-Espallardo, I., Martínez-Sanchis, B., Morera-Ballester, C., Muñoz, E., Sopena-Novales, P., González-Pavón, G., & Martí-Bonmatí, L. (2022). Quantitative evaluation of a non-CT based attenuation correction method for a new dedicated brain PET. *Congress of the European Association of Nuclear Medicine 2022*. https://doi.org/10.1007/s00259-022-05924-4. OP-500 Top Rated Oral Presentation.

Bibliography

[1] US Food and Drug Administration medical imaging definition. https://www.fda.gov/radiation-emitting-products/radiation-emitting-products-and-procedures/medical-imaging. Accessed: 2024-05-08.

[2] Miles N. Wernick and John N. Aarsvold. *Emission Tomography. The Fundamentals of PET and SPECT*. Elsevier, 2004.

[3] Stewart C. Bushong and Geoffrey Clarke. *Magnetic Resonance Imaging*. Elsevier, 2015.

[4] Mark A Haidekker. *Medical Imaging Technology*. SpringerBriefs in Physics, 2013.

[5] Jerrold T Bushberg, Anthony J Seibert, Edwin M Leidholdt, and John M Boone. *The essential physics of medical imaging*. Lippincott Williams and Wilkins, Philadelphia, PA, 2012.

[6] Shah Hussain, Iqra Mubeen, Niamat Ullah, Syed Shahab Ud Din Shah, Bakhtawar Abduljalil Khan, Muhammad Zahoor, Riaz Ullah, Farhat Ali Khan, and Mujeeb A. Sultan. Modern diagnostic imaging technique applications and risk factors in the medical field: A review, 2022.

[7] Dale L Bailey, David W Townsend, Peter E Valk, and Michael N Maisey. *Positron Emission Tomography. Basic Sciences*. Springer, 2004.

[8] Simon R. Cherry, James A. Sorenson, and Michael E. Phelps. *Physics in Nuclear Medicine*. Elsevier, 2012.

[9] Paul Suetens. *Fundamentals of Medical Imaging*. Cambridge, 2009.

[10] Liang Zhou, Mengjie Fan, Charles Hansen, Chris R. Johnson, and Daniel Weiskopf. A review of three-dimensional medical image visualization. *Health Data Science*, 2022:9840519, 2022.

[11] Saxby Brown, Dale L. Bailey, Kathy Willowson, and Clive Baldock. Investigation of the relationship between linear attenuation coefficients and ct hounsfield units using radionuclides for spect. *Applied Radiation and Isotopes*, 66:1206–1212, 9 2008.

[12] P. Mah, T. E. Reeves, and W. D. McDavid. Deriving hounsfield units using grey levels in cone beam computed tomography. *Dentomaxillofacial Radiology*, 39:323–335, 9 2010.

[13] Stewart C Bushong. *Manual De Radiología Para Técnicos: Física, Biología Y Protección Radiológica*. 2010.

[14] Richard Bibb, Dominic Eggbeer, and Abby Paterson. 2 - medical imaging. In Richard Bibb, Dominic Eggbeer, and Abby Paterson, editors, *Medical Modelling (Second Edition)*, pages 7–34. Woodhead Publishing, Oxford, second edition edition, 2015.

[15] M. A. Flower. *Webb's Physics of Medical Imaging, Second Edition*. 2016.

[16] Sociedad Española de Radiología Médica (SERAM). *Radiología esencial*. Ed. Médica Panamericana, 2010.

[17] Sociedad Española de Física Médica (SEFM). *Fundamentos de la física médica. Volumen 10. Radiaciones no ionizantes II*. ADI, 2017.

[18] Suryansh Bajaj, Avneesh Chhabra, and Atul Kumar Taneja. 3d isotropic mri of ankle: review of literature with comparison to 2d mri, 5 2024.

[19] Shivani Ahlawat, Neil M. Kumar, Ali Ghasemi, and Laura M. Fayad. Three-dimensional magnetic resonance imaging in the musculoskeletal system: Clinical applications and opportunities to improve imaging speed and resolution, 3 2024.

[20] Richard Kijowski and Garry E. Gold. Routine 3d magnetic resonance imaging of joints, 4 2011.

[21] G.B. Chavhan. *MRI Made Easy*. Made Easy Series. Jaypee Brothers, 2007.

[22] C. Westbrook and J. Talbot. *MRI in Practice*. Wiley, 2018.

[23] Juan José Vaquero and Paul Kinahan. Positron emission tomography: Current challenges and opportunities for technological advances in clinical and preclinical imaging systems, 2015.

[24] I. Torres Espallardo. Pet/tac: bases físicas, instrumentación y avances. *Radiología*, 59(5):431–445, 2017.

[25] Ramesh Chandra. *Nuclear Medicine Physics: The Basics.* 2004.

[26] S.R. Cherry, J.A. Sorenson, and M.E. Phelps. *Physics in Nuclear Medicine*. ClinicalKey 2012. Elsevier Health Sciences, 2012.

[27] W. N. Cottingham and D. A. Greenwood. *An Introduction to Nuclear Physics*. 2001.

[28] Kenneth S. Krane and William G. Lynch. Introductory nuclear physics. *Physics Today*, 42, 1989.

[29] C.W. Lerche, U. Pietrzyk, and M. Lenz. *Hybrid MR-PET Imaging: Systems, Methods and Applications*. 2019.

[30] Vanessa Nadig, Katrin Herweg, Mitch M.C. Chou, Jack W.C. Lin, Edmund Chin, Chu An Li, Volkmar Schulz, and Stefan Gundacker. Timing advances of commercial divalent-ion co-doped lyso:ce and sipms in sub-100 ps time-of-flight positron emission tomography. *Physics in Medicine and Biology*, 68, 4 2023.

[31] Charles L. Melcher. Scintillation crystals for pet. *Journal of Nuclear Medicine*, 41:1051–1055, 6 2000.

[32] Rachel A. Powsner, Matthew R. Palmer, and Edward R. Powsner. *Essentials of Nuclear Medicine Physics and Instrumentation: Third Edition*. 2013.

[33] W. W. Moses. Time of flight in pet revisited. *IEEE Transactions on Nuclear Science*, 50, 2003.

[34] Suleman Surti and Joel S. Karp. Update on latest advances in time-of-flight pet, 2020.

[35] David Brasse, Paul E. Kinahan, Carole Lartizien, Claude Comtat, Mike Casey, and Christian Michel. Correction methods for random coincidences in fully 3d whole-body pet: Impact on data and image quality. *Journal of Nuclear Medicine*, 46, 2005.

[36] Habib Zaidi and Marie Louise Montandon. Scatter compensation techniques in pet, 2007.

[37] Olivier Rousset, Arman Rahmim, Abass Alavi, and Habib Zaidi. Partial volume correction strategies in pet. *PET Clinics*, 2(2):235–249, 2007. PET Instrumentation and Quantification.

[38] Marine Soret, Stephen L. Bacharach, and Irène Buvat. Partial-volume effect in pet tumor imaging, 2007.

[39] Mark Madsen. Quantitative analysis in nuclear medicine imaging. *Medical Physics*, 34, 2007.

[40] European Association of Nuclear Medicine. *Principles and practice of PET/CT: part 1: a technologists guide*. 2010. Depositing User : Hogg, P Comments and Notes (inc. copyright restrictions) : 23/9/11 email sent requesting permissions SH Themes : Health and Wellbeing.

[41] H.A. Ziessman, J.P. O'Malley, and J.H. Thrall. *Nuclear Medicine: The Requisites*. Requisites in Radiology. Elsevier Health Sciences, 2013.

[42] W. Wadsak and M. Mitterhauser. Basics and principles of radiopharmaceuticals for pet/ct. *European Journal of Radiology*, 73(3):461–469, 2010. PET/CT - An Imaging Challenge.

[43] Giorgio Treglia and Luca Giovanella. *Evidence-based Positron Emission Tomography Summary of Recent Meta-analyses on PET: Summary of Recent Meta-analyses on PET*. 01 2020.

[44] Kathy P. Willowson. Production of radionuclides for clinical nuclear medicine, 2019.

[45] Ferdinando Calabria and Orazio Schillaci. 2019, month = 10, pages = , title = Radiopharmaceuticals. A Guide to PET/CT and PET/MRI, isbn = 978-3-030-27781-9, doi = 10.1007/978-3-030-27779-6 editor = Springer.

[46] Clemens Kratochwil, Paul Flechsig, Thomas Lindner, Labidi Abderrahim, Annette Altmann, Walter Mier, Sebastian Adeberg, Hendrik Rathke, Manuel Röhrich, Hauke Winter, Peter K. Plinkert, Frederik Marme, Matthias Lang, Hans Ulrich Kauczor, Dirk Jäger, Jürgen Debus, Uwe Haberkorn, and Frederik L. Giesel. 68ga-fapi pet/ct: Tracer uptake in 28 different kinds of cancer. *Journal of Nuclear Medicine*, 60, 2019.

[47] Vandana Dhingra, Abhishek Mahajan, and Sandip Basu. Emerging clinical applications of pet based molecular imaging in oncology: The promising future potential for evolving personalized cancer care. *Indian Journal of Radiology and Imaging*, 25, 2015.

[48] Eric M. Rohren, Timothy G. Turkington, and R. Edward Coleman. Clinical applications of pet in oncology, 5 2004.

[49] Stefan Prado-Wohlwend, Mónica Ballesta-Moratalla, Irene Torres-Espallardo, María Isabel del Olmo-García, Pilar Bello-Arques, Consuelo Olivas-Arroyo, and Juan Francisco Merino-Torres. Same-day comparative protocol pet/ct-pet/mri [68 ga]ga-dota-toc in paragangliomas and pheochromocytomas: an approach to personalized medicine. *Cancer Imaging*, 23, 2023.

[50] Rudi A.J.O. Dierckx, Klaus L. Leenders, Erik F.J. De Vries, and Aren Van Waarde. *PET and SPECT in neurology*. 2014.

[51] Paul Shreve and David W. Townsend. *Clinical PET-CT in radiology: Integrated imaging in oncology*. 2011.

[52] Raj Mohan Paspulati, Sasan Partovi, Karin A. Herrmann, Smitha Krishnamurthi, Conor P. Delaney, and Nghi C. Nguyen. Comparison of hybrid fdg pet/mri compared with pet/ct in colorectal cancer staging and restaging: a pilot study. *Abdominal Imaging*, 40, 2015.

[53] Borjana Bogdanovic, Esteban Lucas Solari, Alberto Villagran Asiares, Lachlan McIntosh, Sandra van Marwick, Sylvia Schachoff, and Stephan G. Nekolla. Pet/mr technology: Advancement and challenges, 2022.

[54] Sikkandhar Musafargani, Krishna Kanta Ghosh, Sachin Mishra, Pachaiyappan Mahalakshmi, Parasuraman Padmanabhan, and Balázs Gulyás. Pet/mri: a frontier in era of complementary hybrid imaging, 2018.

[55] Zhenhua Hu, Weidong Yang, Haixiao Liu, Kun Wang, Chengpeng Bao, Tianming Song, Jing Wang, and Jie Tian. From pet/ct to pet/mri: Advances in instrumentation and clinical applications. *Molecular Pharmaceutics*, 11, 2014.

[56] Ciprian Catana, Richard Laforest, Hongyu An, Fernando Boada, Tuoyu Cao, David Faul, Bjoern Jakoby, Floris P. Jansen, Bradley J. Kemp, Paul E. Kinahan, Peder Larson, Michael A. Levine, Piotr Maniawski, Osama Mawlawi, Jonathan E. McConathy, Alan B. McMillan, Julie C. Price, Abhejit Rajagopal, John Sunderland, Patrick Veit-Haibach, Kristen A. Wangerin, Chunwei Ying, and Thomas A. Hope. A path to qualification of pet/mri scanners for multicenter brain imaging studies: Evaluation of mri-based attenuation correction methods using a patient phantom. *Journal of Nuclear Medicine*, 63, 2022.

[57] Matthias K. Werner, Holger Schmidt, and Nina F. Schwenzer. Mr/pet: A new challenge in hybrid imaging, 2012.

[58] Miguel Gallach, Miriam Mikhail Lette, May Abdel-Wahab, Francesco Giammarile, Olivier Pellet, and Diana Paez. Addressing global inequities in positron emission tomography-computed tomography (pet-ct) for cancer management: A statistical model to guide strategic planning. *Medical Science Monitor*, 26, 2020.

[59] Amirhossein Sanaat, Mehdi Amini, Hossein Arabi, and Habib Zaidi. The quest for multifunctional and dedicated pet instrumentation with irregular geometries, 2024.

[60] Maria Teresa Gandia-Ferrero, Irene Torres-Espallardo, Begoña Martínez-Sanchis, Constantino Morera-Ballester, Enrique Muñoz, Pablo Sopena-Novales, Gabriel González-Pavón, and Luis Martí-Bonmatí. Objective image quality comparison between brain-dedicated pet and pet/ct scanners. *Journal of medical systems*, 47:88, 12 2023.

[61] Martina Moglioni, Aafke Christine Kraan, Guido Baroni, Giuseppe Battistoni, Nicola Belcari, Andrea Berti, Pietro Carra, Piergiorgio Cerello, Mario Ciocca, Angelica De Gregorio, Micol De Simoni, Damiano Del Sarto, Marco Donetti, Yunsheng Dong, Alessia Embriaco, Maria Evelina Fantacci, Veronica Ferrero, Elisa Fiorina, Marta Fischetti, Gaia Franciosini, Giuseppe Giraudo, Francesco Laruina, Davide Maestri, Marco Magi, Giuseppe Magro, Etesam Malekzadeh, Michela Marafini, Ilaria Mattei, Enrico Mazzoni, Paolo Mereu, Alfredo Mirandola, Matteo Morrocchi, Silvia Muraro, Ester Orlandi, Vincenzo Patera, Francesco Pennazio,

Marco Pullia, Alessandra Retico, Angelo Rivetti, Manuel Dionisio Da Rocha Rolo, Valeria Rosso, Alessio Sarti, Angelo Schiavi, Adalberto Sciubba, Giancarlo Sportelli, Sara Tampellini, Marco Toppi, Giacomo Traini, Antonio Trigilio, Serena Marta Valle, Francesca Valvo, Barbara Vischioni, Viviana Vitolo, Richard Wheadon, and Maria Giuseppina Bisogni. In-vivo range verification analysis with in-beam pet data for patients treated with proton therapy at cnao. *Frontiers in Oncology*, 12, 2022.

[62] Tonke L. de Jong, Daniëlle Koopman, Jorn A. van Dalen, Aline Tegelaar, Joris D. van Dijk, Henk Stevens, and Pieter L. Jager. Performance of digital pet/ct compared with conventional pet/ct in oncologic patients: a prospective comparison study. *Annals of Nuclear Medicine*, 36, 2022.

[63] Fang Liu, Hyungseok Jang, Richard Kijowski, Gengyan Zhao, Tyler Bradshaw, and Alan B. McMillan. A deep learning approach for18 f-fdg pet attenuation correction. *EJNMMI Physics*, 5, 2018.

[64] Karl D. Spuhler, John Gardus, Yi Gao, Christine DeLorenzo, Ramin Parsey, and Chuan Huang. Synthesis of patient-specific transmission data for pet attenuation correction for pet/mri neuroimaging using a convolutional neural network. *Journal of Nuclear Medicine*, 60, 2019.

[65] Jaewon Yang, Dookun Park, Grant T. Gullberg, and Youngho Seo. Joint correction of attenuation and scatter in image space using deep convolutional neural networks for dedicated brain 18f-fdg pet. *Physics in Medicine and Biology*, 64, 2019.

[66] Hanan Aldosari, Basema Saddik, and Khulud Al Kadi. Impact of picture archiving and communication system (pacs) on radiology staff. *Informatics in Medicine Unlocked*, 10:1–16, 1 2018.

[67] Oleg S. Pianykh. Digital imaging and communications in medicine (dicom). *Digital Imaging and Communications in Medicine (DICOM)*, 2012.

[68] T. Kanchan. Medical records, access to. *Encyclopedia of Forensic and Legal Medicine: Second Edition*, pages 520–525, 1 2016.

[69] José Manuel Fonseca, André Damas Mora, and Pedro Barroso. The web and the new generation of medical information systems. *Outcome Prediction in Cancer*, pages 391–414, 1 2007.

[70] Ira J. Kalet. Medical data communication. *Principles of Biomedical Informatics*, pages 349–391, 1 2009.

[71] Richard Bibb, Dominic Eggbeer, and Abby Paterson. Medical imaging. *Medical Modelling*, pages 7–34, 1 2015.

[72] Michele Larobina. Thirty years of the dicom standard, 2023.

[73] Martin Prince, Adelina Comas-Herrera, Martin Knapp, Maëlenn Guerchet, and Maria Karagiannidou. World alzheimer report 2016 improving healthcare for people living with dementia coverage, quality and costs now and in the future.

[74] 2020 alzheimer's disease facts and figures. *Alzheimer's and Dementia*, 16, 2020.

[75] Ciprian Catana. Development of dedicated brain pet imaging devices: Recent advances and future perspectives. *Journal of Nuclear Medicine*, 60, 2019.

[76] Clifford R Jack, David A Bennett, Kaj Blennow, Maria C Carrillo, Billy Dunn, Samantha Budd Haeberlein, David M Holtzman, William Jagust, Frank Jessen, Jason Karlawish, Enchi Liu, Jose Luis Molinuevo, Thomas Montine, Creighton Phelps, Katherine P Rankin, Christopher C Rowe, Philip Scheltens, Eric Siemers, Heather M Snyder, Reisa Sperling, Cerise Elliott, Eliezer Masliah, Laurie Ryan, and Nina Silverberg. National institute on aging-alzheimer's association (nia-aa) research framework nia-aa research framework: Toward a biological definition of alzheimer's disease. *Alzheimer's and Dementia*, 14, 2018.

[77] Michael A. Deture and Dennis W. Dickson. The neuropathological diagnosis of alzheimer's disease, 2019.

[78] Maileen Gloriane Ulep, Simrit Kaur Saraon, and Samantha McLea. Alzheimer disease. *Journal for Nurse Practitioners*, 14:129–135, 3 2018.

[79] Reisa A. Sperling, Paul S. Aisen, Laurel A. Beckett, David A. Bennett, Suzanne Craft, Anne M. Fagan, Takeshi Iwatsubo, Clifford R. Jack, Jeffrey Kaye, Thomas J. Montine, Denise C. Park, Eric M. Reiman, Christopher C. Rowe, Eric Siemers, Yaakov Stern, Kristine Yaffe, Maria C. Carrillo, Bill Thies, Marcelle Morrison-Bogorad, Molly V. Wagster, and Creighton H. Phelps. Toward defining the preclinical stages of alzheimer's disease: Recommendations from the national institute on aging-alzheimer's association workgroups on diagnostic guidelines for alzheimer's disease. *Alzheimer's and Dementia*, 7, 2011.

[80] Adam M. Staffaroni, Fanny M. Elahi, Dana McDermott, Kacey Marton, Elissaios Karageorgiou, Simone Sacco, Matteo Paoletti, Eduardo Caverzasi, Christopher P. Hess, Howard J. Rosen, and Michael D. Geschwind. Neuroimaging in dementia. *Seminars in Neurology*, 37:510–537, 10 2017.

[81] M. A. Lambert, H. Bickel, M. Prince, L. Fratiglioni, E. Von Strauss, D. Frydecka, A. Kiejna, J. Georges, and E. L. Reynish. Estimating the burden of early onset dementia; systematic review of disease prevalence, 4 2014.

[82] Jee Bang, Salvatore Spina, and Bruce L. Miller. Frontotemporal dementia, 10 2015.

[83] Clive Holmes and Jay Amin. Dementia, 2020.

[84] Jared S. Katzeff, Fiona Bright, Katherine Phan, Jillian J. Kril, Lars M. Ittner, Michael Kassiou, John R. Hodges, Olivier Piguet, Matthew C. Kiernan, Glenda M. Halliday, and Woojin Scott Kim. Biomarker discovery and development for frontotemporal dementia and amyotrophic lateral sclerosis, 2022.

[85] Serge Gauthier, Barry Reisberg, Michael Zaudig, Ronald C. Petersen, Karen Ritchie, Karl Broich, Sylvie Belleville, Henry Brodaty, David Bennett, Howard Chertkow, Jeffrey L. Cummings, Mony de Leon, Howard Feldman, Mary Ganguli, Harald Hampel, Philip Scheltens, Mary C. Tierney, Peter Whitehouse, and Bengt Winblad. Mild cognitive impairment. *Lancet*, 367:1262–1270, 4 2006.

[86] A. Villarejo Galende, M. Eimil Ortiz, S. Llamas Velasco, M. Llanero Luque, C. López de Silanes de Miguel, and C. Prieto Jurczynska. Report by the spanish foundation of the brain on the social impact of alzheimer disease and other types of dementia, 1 2021.

[87] J. C. Morris, M. Storandt, J. P. Miller, D. W. McKeel, J. L. Price, E. H. Rubin, and L. Berg. Mild cognitive impairment represents early-stage alzheimer disease. *Archives of Neurology*, 58, 2001.

[88] Yubraj Gupta, Ramesh Kumar Lama, and Goo Rak Kwon. Prediction and classification of alzheimer's disease based on combined features from apolipoprotein-e genotype, cerebrospinal fluid, mr, and fdg-pet imaging biomarkers. *Frontiers in Computational Neuroscience*, 13, 10 2019.

[89] Kaj Blennow. A review of fluid biomarkers for alzheimer's disease: Moving from csf to blood, 2017.

[90] K. Blennow and H. Zetterberg. Biomarkers for alzheimer's disease: current status and prospects for the future, 2018.

[91] Carmen Peña-Bautista, Lourdes Álvarez Sánchez, Rosa Pascual, Maria José Moreno, Miguel Baquero, and Consuelo Cháfer-Pericás. Clinical usefulness of cerebrospinal fluid biomarkers in alzheimer's disease. *European Journal of Clinical Investigation*, 53, 2023.

[92] Oskar Hansson, Sylvain Lehmann, Markus Otto, Henrik Zetterberg, and Piotr Lewczuk. Advantages and disadvantages of the use of the csf amyloid β (aβ) 42/40 ratio in the diagnosis of alzheimer's disease, 2019.

[93] C. P. Hughes, L. Berg, W. L. Danziger, L. A. Coben, and R. L. Martin. A new clinical scale for the staging of dementia. *British Journal of Psychiatry*, 140, 1982.

[94] John C. Morris. The clinical dementia rating (cdr): Current version and scoring rules. *Neurology*, 43:2412–2414, 1993.

[95] Maria Teresa Gandia-Ferrero, Jesús Adrián-Ventura, Consuelo Cháfer-Pericás, Lourdes Alvarez-Sanchez, Inés Ferrer-Cairols, Begoña Martinez-Sanchis, Irene

Torres-Espallardo, Miquel Baquero-Toledo, and Luis Marti-Bonmati. Relationship between neuroimaging and emotion recognition in mild cognitive impairment patients. *Behavioural Brain Research*, 461, 2024.

[96] Christopher Randolph, Michael C. Tierney, Erich Mohr, and Thomas N. Chase. The repeatable battery for the assessment of neuropsychological status (rbans): Preliminary clinical validity. *Journal of Clinical and Experimental Neuropsychology*, 20, 1998.

[97] Marshal F. Folstein, Susan E. Folstein, and Paul R. McHugh. "mini-mental state". a practical method for grading the cognitive state of patients for the clinician. *Journal of Psychiatric Research*, 12, 1975.

[98] Colin L. Masters, Randall Bateman, Kaj Blennow, Christopher C. Rowe, Reisa A. Sperling, and Jeffrey L. Cummings. Alzheimer's disease, 10 2015.

[99] Joan Prats-Climent, Maria Teresa Gandia-Ferrero, Irene Torres-Espallardo, Lourdes Álvarez Sanchez, Begoña Martínez-Sanchis, Consuelo Cháfer-Pericás, Ignacio Gómez-Rico, Leonor Cerdá-Alberich, Fernando Aparici-Robles, Miquel Baquero-Toledo, María José Rodríguez-Álvarez, and Luis Martí-Bonmatí. Artificial intelligence on fdg pet images identifies mild cognitive impairment patients with neurodegenerative disease. *Journal of Medical Systems*, 46, 8 2022.

[100] Maria Ricci, Andrea Cimini, Agostino Chiaravalloti, Luca Filippi, and Orazio Schillaci. Positron emission tomography (pet) and neuroimaging in the personalized approach to neurodegenerative causes of dementia, 2020.

[101] C Gamez-Cenzano, J J Robles-Barba, L Rodriguez-Bel, J Gascon-Bayarri, M Cortes-Romera, A Sabate-Llobera, L M Gracia-Sanchez, I Romero-Zayas, M Rocaengronyat, J L Vercher-Conejero, C Majos-Torro, C Soriano-Mas, C Aguileragrijalvo, I Rico-Pons, and R Reñe-Ramirez. Impact of pet brain imaging using f18-fdg and f18-florbetapir in patients with cognitive impairment. *European Journal of Nuclear Medicine and Molecular Imaging*, 42:S554, 2015.

[102] Sowmya Mahalingam and Ming Kai Chen. Neuroimaging in dementias. *Seminars in Neurology*, 39, 2019.

[103] Matteo Cotta Ramusino, Giulia Perini, Daniele Altomare, Paola Barbarino, Wendy Weidner, Gabriella Salvini Porro, Frederik Barkhof, Gil D. Rabinovici, Wiesje M. van der Flier, Giovanni B. Frisoni, Valentina Garibotto, Stefan Teipel, and Marina Boccardi. Outcomes of clinical utility in amyloid-pet studies: state of art and future perspectives, 2021.

[104] Michael Schöll, Samuel N. Lockhart, Daniel R. Schonhaut, James P. O'Neil, Mustafa Janabi, Rik Ossenkoppele, Suzanne L. Baker, Jacob W. Vogel, Jamie Faria, Henry D. Schwimmer, Gil D. Rabinovici, and William J. Jagust. Pet imaging of tau deposition in the aging human brain. *Neuron*, 89, 2016.

[105] Henryk Barthel and Osama Sabri. Clinical use and utility of amyloid imaging. *Journal of Nuclear Medicine*, 58, 2017.

[106] Peter N.E. Young, Mar Estarellas, Emma Coomans, Meera Srikrishna, Helen Beaumont, Anne Maass, Ashwin V. Venkataraman, Rikki Lissaman, Daniel Jiménez, Matthew J. Betts, Eimear McGlinchey, David Berron, Antoinette O'Connor, Nick C. Fox, Joana B. Pereira, William Jagust, Stephen F. Carter, Ross W. Paterson, and Michael Schöll. Imaging biomarkers in neurodegeneration: Current and future practices, 2020.

[107] Marianne Chapleau, Leonardo Iaccarino, David Soleimani-Meigooni, and Gil D. Rabinovici. The role of amyloid pet in imaging neurodegenerative disorders: A review. *Journal of Nuclear Medicine*, 63:13S–19S, 6 2022.

[108] William E. Klunk, Henry Engler, Agneta Nordberg, Yanming Wang, Gunnar Blomqvist, Daniel P. Holt, Mats Bergström, Irina Savitcheva, Guo Feng Huang, Sergio Estrada, Birgitta Ausén, Manik L. Debnath, Julien Barletta, Julie C. Price, Johan Sandell, Brian J. Lopresti, Anders Wall, Pernilla Koivisto, Gunnar Antoni, Chester A. Mathis, and Bengt Långström. Imaging brain amyloid in alzheimer's disease with pittsburgh compound-b. *Annals of Neurology*, 55, 2004.

[109] Milos D. Ikonomovic, William E. Klunk, Eric E. Abrahamson, Chester A. Mathis, Julie C. Price, Nicholas D. Tsopelas, Brian J. Lopresti, Scott Ziolko, Wenzhu Bi, William R. Paljug, Manik L. Debnath, Caroline E. Hope, Barbara A. Isanski, Ronald L. Hamilton, and Steven T. DeKosky. Post-mortem correlates of in vivo pib-pet amyloid imaging in a typical case of alzheimer's disease. *Brain*, 131, 2008.

[110] Natalie Nelissen, Koen Van Laere, Lennart Thurfjell, Rikard Owenius, Mathieu Vandenbulcke, Michel Koole, Guy Bormans, David J. Brooks, and Rik Vandenberghe. Phase 1 study of the pittsburgh compound b derivative18f- flutemetamol in healthy volunteers and patients with probable alzheimer disease. *Journal of Nuclear Medicine*, 50, 2009.

[111] David A. Wolk, Zheng Zhang, Sanaa Boudhar, Christopher M. Clark, Michael J. Pontecorvo, and Steven E. Arnold. Amyloid imaging in alzheimer's disease: Comparison of florbetapir and pittsburgh compound-b positron emission tomography. *Journal of Neurology, Neurosurgery and Psychiatry*, 83, 2012.

[112] Valentina Garibotto, Nathalie L. Albert, Henryk Barthel, Bart van Berckel, Ronald Boellaard, Matthias Brendel, Diego Cecchin, Ozgul Ekmekcioglu, Elsmarieke van de Giessen, Eric Guedj, Adriaan A. Lammerstma, Franck Semah, Tatjana Traub-Weidinger, Donatienne Van Weehaeghe, and Silvia Morbelli. The approval of a disease-modifying treatment for alzheimer's disease: impact and consequences for the nuclear medicine community, 2021.

[113] Antoine Verger, Igor Yakushev, Nathalie L. Albert, Bart van Berckel, Matthias Brendel, Diego Cecchin, Pablo Aguiar Fernandez, Francesco Fraioli, Eric Guedj,

Silvia Morbelli, Nelleke Tolboom, Tatjana Traub-Weidinger, Donatienne Van Weehaeghe, and Henryk Barthel. Fda approval of lecanemab: the real start of widespread amyloid pet use? — the eanm neuroimaging committee perspective, 2023.

[114] F. Nobili, J. Arbizu, F. Bouwman, A. Drzezga, F. Agosta, P. Nestor, Z. Walker, M. Boccardi, Cristina Festari, Daniele Altomare, Federica Gandolfo, and Stefania Orini. European association of nuclear medicine and european academy of neurology recommendations for the use of brain 18 f-fluorodeoxyglucose positron emission tomography in neurodegenerative cognitive impairment and dementia: Delphi consensus, 2018.

[115] Atman Dave, Neil Hansen, Ryan Downey, and Craig Johnson. Fdg-pet imaging of dementia and neurodegenerative disease. *Seminars in Ultrasound, CT and MRI*, 41, 2020.

[116] Anne B. Rocher, Françoise Chapon, Xavier Blaizot, Jean Claude Baron, and Chantal Chavoix. Resting-state brain glucose utilization as measured by pet is directly related to regional synaptophysin levels: A study in baboons. *NeuroImage*, 20, 2003.

[117] Daniel H S Silverman, Lisa Mosconi, Linda Ercoli, W Chen, and Gary W Small. Pet scans obtained for evaluation of cognitive dysfunction. *Seminars in nuclear medicine*, 38, 2008.

[118] Charles Marcus, Esther Mena, and Rathan M. Subramaniam. Brain pet in the diagnosis of alzheimer's disease, 2014.

[119] Gámez-Cenzano C., Rodríguez-Bel L., Gascón-Bayarri J., Reñé-Ramírez R., Campdelacreu-Fumado J., Turón-Sans J., Soriano-Mas C., Vercher-Conejero J., Gràcia-Sánchez L., Llinares-Tello E., Pons-Escoda A., Majós-Torro C., and Aguilera-Grijalvo C. Role of 18f-fdg-pet and amyloid-pet imaging on patient management in mild cognitive impairment or dementia. *European Journal of Nuclear Medicine and Molecular Imaging*, 43:S117, 2016.

[120] M. Schmand. Performance results of a new doi detector block for a high resolution pet - lso research tomograph hrrt. *IEEE Transactions on Nuclear Science*, 45, 1998.

[121] Taiga Yamaya, Eiji Yoshida, Keishi Kitamura, Takashi Obi, Katsuyuki Tanimoto, Kyosan Yoshikawa, Hiroshi Ito, and Hideo Murayama. First human brain images of the jpet-d4 using 3d os-em with a pre-computed system matrix. pages 3384–3387, 5 2007.

[122] Kira S. Grogg, Terrence Toole, Jinsong Ouyang, Xuping Zhu, Marc D. Normandin, Quanzheng Li, Keith Johnson, Nathaniel M. Alpert, and Georges El Fakhri. National electrical manufacturers association and clinical evaluation of a novel brain pet/ct scanner. *Journal of Nuclear Medicine*, 57, 2016.

[123] Mitsuo Watanabe, Akinori Saito, Takashi Isobe, Kibo Ote, Ryoko Yamada, Takahiro Moriya, and Tomohide Omura. Performance evaluation of a high-resolution brain pet scanner using four-layer mppc doi detectors. *Physics in Medicine and Biology*, 62, 2017.

[124] Seiichi Yamamoto, Manabu Honda, Tutomu Oohashi, Keiji Shimizu, and Michio Senda. Development of a brain pet system, pet-hat: A wearable pet system for brain research. *IEEE Transactions on Nuclear Science*, 58, 2011.

[125] Christopher E. Bauer, Julie Brefczynski-Lewis, Gary Marano, Mary Beth Mandich, Alexander Stolin, Peter Martone, James W. Lewis, Gangadhar Jaliparthi, Raymond R. Raylman, and Stan Majewski. Concept of an upright wearable positron emission tomography imager in humans. *Brain and Behavior*, 6, 2016.

[126] Jianfeng Xu, Zhixiang Zhao, Siwei Xie, Dawei Shi, Qiu Huang, and Qiyu Peng. Mind-tracker pet: A wearable pet camera for brain imaging. 2018.

[127] Markus Jehl, Ekaterina Mikhaylova, Valerie Treyer, Marlena Hofbauer, Martin Hullner, Philipp A. Kaufmann, Alfred Buck, Geoff Warnock, Viet Dao, Charalampos Tsoumpas, Daniel Deidda, Kris Thielemans, Max Ludwig Ahnen, and Jannis Fischer. Attenuation correction using template pet registration for brain pet: A proof-of-concept study. *Journal of Imaging*, 9:2, 12 2022.

[128] Laura Moliner, Maria J. Rodríguez-Álvarez, Juan V. Catret, Antonio González, Víctor Ilisie, and José M. Benlloch. Nema performance evaluation of caremibrain dedicated brain pet and comparison with the whole-body and dedicated brain pet systems. *Scientific Reports*, 9, 2019.

[129] Katherine A. Morgan, Stacey E. Rudd, Asif Noor, and Paul S. Donnelly. Theranostic nuclear medicine with gallium-68, lutetium-177, copper-64/67, actinium-225, and lead-212/203 radionuclides, 2023.

[130] Manisha H. Shah, Whitney S. Goldner, Al B. Benson, Emily Bergsland, Lawrence S. Blaszkowsky, Pamela Brock, Jennifer Chan, Satya Das, Paxton V. Dickson, Paul Fanta, Thomas Giordano, Thorvardur R. Halfdanarson, Daniel Halperin, Jin He, Anthony Heaney, Martin J. Heslin, Fouad Kandeel, Arash Kardan, Sajid A. Khan, Boris W. Kuvshinoff, Christopher Lieu, Kimberly Miller, Venu G. Pillarisetty, Diane Reidy, Sarimar Agosto Salgado, Shagufta Shaheen, Heloisa P. Soares, Michael C. Soulen, Jonathan R. Strosberg, Craig R. Sussman, Nikolaos A. Trikalinos, Nataliya A. Uboha, Namrata Vijayvergia, Terence Wong, Beth Lynn, and Cindy Hochstetler. Neuroendocrine and adrenal tumors, version 2.2021, nccn clinical practice guidelines in oncology. *Journal of the National Comprehensive Cancer Network*, 19, 2021.

[131] Jacques W.M. Lenders, Quan Yang Duh, Graeme Eisenhofer, Anne Paule Gimenez-Roqueplo, Stefan K.G. Grebe, Mohammad Hassan Murad, Mitsuhide

Naruse, Karel Pacak, and William F. Young. Pheochromocytoma and paraganglioma: An endocrine society clinical practice guideline, 2014.

[132] Stefan Prado-Wohlwend, María Isabel del Olmo-García, Pilar Bello-Arques, and Juan Francisco Merino-Torres. [177lu]lu-dota-tate and [131i]mibg phenotypic imaging-based therapy in metastatic/inoperable pheochromocytomas and paragangliomas: Comparative results in a single center. *Frontiers in Endocrinology*, 13, 2022.

[133] Joakim Crona, David Taïeb, and Karel Pacak. New perspectives on pheochromocytoma and paraganglioma: Toward a molecular classification, 2017.

[134] Daniel J. Cuthbertson, Rebecca Shankland, and Raj Srirajaskanthan. Diagnosis and management of neuroendocrine tumours. *Clinical Medicine, Journal of the Royal College of Physicians of London*, 23, 2023.

[135] Mauro Cives and Jonathan R. Strosberg. Gastroenteropancreatic neuroendocrine tumors. *CA: A Cancer Journal for Clinicians*, 68, 2018.

[136] Abhishek Jha, David Taïeb, Jorge A. Carrasquillo, Daniel A. Pryma, Mayank Patel, Corina Millo, Wouter W. de Herder, Jaydira Del Rivero, Joakim Crona, Barry L. Shulkin, Irene Virgolini, Alice P. Chen, Bhagwant R. Mittal, Sandip Basu, Joseph S. Dillon, Thomas A. Hope, Carina Mari Aparici, Andrei H. Iagaru, Rodney J. Hicks, Anca M. Avram, Jonathan R. Strosberg, Ali Cahid Civelek, Frank I. Lin, Neeta Pandit-Taskar, and Karel Pacak. High-specific-activity-131i-mibg versus 177lu-dotatate targeted radionuclide therapy for metastatic pheochromocytoma and paraganglioma, 2021.

[137] David Taïeb, Rodney J. Hicks, Elif Hindié, Benjamin A. Guillet, Anca Avram, Pietro Ghedini, Henri J. Timmers, Aaron T. Scott, Saeed Elojeimy, Domenico Rubello, Irène J. Virgolini, Stefano Fanti, Sona Balogova, Neeta Pandit-Taskar, and Karel Pacak. European association of nuclear medicine practice guideline/society of nuclear medicine and molecular imaging procedure standard 2019 for radionuclide imaging of phaeochromocytoma and paraganglioma. *European Journal of Nuclear Medicine and Molecular Imaging*, 46, 2019.

[138] Stephen S.F. Yip and Hugo J.W.L. Aerts. Applications and limitations of radiomics, 2016.

[139] S. Warner. Diagnostics + therapy = theranostics. *Scientist*, 18:38–39, 08 2004.

[140] David Taïeb, Rodney J. Hicks, and Karel Pacak. Nuclear medicine in cancer theranostics: Beyond the target, 2016.

[141] Richard P. Baum and Harshad R. Kulkarni. Theranostics: From molecular imaging using ga-68 labeled tracers and pet/ct to personalized radionuclide therapy - the bad berka experience, 2012.

[142] Baran Sumer and Jinming Gao. Theranostic nanomedicine for cancer, 2008.

[143] José Flávio Gomes Marin, Rafael F. Nunes, Artur M. Coutinho, Elaine C. Zaniboni, Larissa B. Costa, Felipe G. Barbosa, Marcelo A. Queiroz, Giovanni G. Cerri, and Carlos A. Buchpiguel. Theranostics in nuclear medicine: Emerging and re-emerging integrated imaging and therapies in the era of precision oncology. *Radiographics*, 40, 2020.

[144] S. Del Vecchio, A. Zannetti, R. Fonti, L. Pace, and M. Salvatore. Nuclear imaging in cancer theranostics, 2007.

[145] Hossein Jadvar, Xiaoyuan Chen, Weibo Cai, and Umar Mahmood. Radiotheranostics in cancer diagnosis and management, 2018.

[146] Jin Xie, Seulki Lee, and Xiaoyuan Chen. Nanoparticle-based theranostic agents, 2010.

[147] Daniel Y. Lee and King C.P. Li. Molecular theranostics: A primer for the imaging professional, 2011.

[148] Irvin M. Modlin, Kjell Oberg, Daniel C. Chung, Robert T. Jensen, Wouter W. de Herder, Rajesh V. Thakker, Martyn Caplin, Gianfranco Delle Fave, Greg A. Kaltsas, Eric P. Krenning, Steven F. Moss, Ola Nilsson, Guido Rindi, Ramon Salazar, Philippe Ruszniewski, and Anders Sundin. Gastroenteropancreatic neuroendocrine tumours, 2008.

[149] E. P. Krenning, D. J. Kwekkeboom, W. H. Bakker, W. A.P. Breeman, P. P.M. Kooij, H. Y. Oei, M. van Hagen, P. T.E. Postema, M. de Jong, J. C. Reubi, T. J. Visser, A. E.M. Reijs, L. J. Hofland, J. W. Koper, and S. W.J. Lamberts. Somatostatin receptor scintigraphy with [111in-dtpa-d-phe1]- and [123i-tyr3]-octreotide: the rotterdam experience with more than 1000 patients. *European Journal of Nuclear Medicine*, 20, 1993.

[150] I. Buchmann, M. Henze, S. Engelbrecht, M. Eisenhut, A. Runz, M. Schäfer, T. Schilling, S. Haufe, T. Herrmann, and U. Haberkorn. Comparison of 68ga-dotatoc pet and 111in-dtpaoc (octreoscan) spect in patients with neuroendocrine tumours. *European Journal of Nuclear Medicine and Molecular Imaging*, 34, 2007.

[151] M. Hofmann, H. Maecke, A. R. Börner, E. Weckesser, P. Schöffski, M. L. Oei, J. Schumacher, M. Henze, A. Heppeler, G. J. Meyer, and W. H. Knapp. Biokinetics and imaging with the somatostatin receptor pet radioligand 68ga-dotatoc: Preliminary data. *European Journal of Nuclear Medicine*, 28, 2001.

[152] Simron Singh, Raymond Poon, Rebecca Wong, and Ur Metser. 68ga pet imaging in patients with neuroendocrine tumors: A systematic review and meta-analysis. *Clinical Nuclear Medicine*, 43, 2018.

[153] Rachel Levine and Eric P. Krenning. Clinical history of the theranostic radionuclide approach to neuroendocrine tumors and other types of cancer: Historical review based on an interview of eric p. krenning by rachel levine, 2017.

[154] K. Öberg, U. Knigge, D. Kwekkeboom, and A. Perren. Neuroendocrine gastro-entero-pancreatic tumors: Esmo clinical practice guidelines for diagnosis, treatment and follow-up. *Annals of Oncology*, 23, 2012.

[155] Manisha H. Shah, Whitney S. Goldner, Thorvardur R. Halfdanarson, Emily Bergsland, Jordan D. Berlin, Daniel Halperin, Jennifer Chan, Matthew H. Kulke, Al B. Benson, Lawrence S. Blaszkowsky, Jennifer Eads, Paul F. Engstrom, Paul Fanta, Thomas Giordano, Jin He, Martin J. Heslin, Gregory P. Kalemkerian, Fouad Kandeel, Sajid A. Khan, Wajih Zaheer Kidwai, Pamela L. Kunz, Boris W. Kuvshinoff, Christopher Lieu, Venu G. Pillarisetty, Leonard Saltz, Julie Ann Sosa, Jonathan R. Strosberg, Craig A. Sussman, Nikolaos A. Trikalinos, Nataliya A. Uboha, Jonathan Whisenant, Terence Wong, James C. Yao, Jennifer L. Burns, Ndiya Ogba, and Griselda Zuccarino-Catania. Nccn guidelines insights: Neuroendocrine and adrenal tumors, version 2.2018. *Journal of the National Comprehensive Cancer Network*, 16, 2018.

[156] Thomas A. Hope, Emily K. Bergsland, Murat Fani Bozkurt, Michael Graham, Anthony P. Heaney, Ken Herrmann, James R. Howe, Matthew H. Kulke, Pamela L. Kunz, Josh Mailman, Lawrence May, David C. Metz, Corina Millo, Sue O'Dorisio, Diane L. Reidy-Lagunes, Michael C. Soulen, and Jonathan R. Strosberg. Appropriate use criteria for somatostatin receptor pet imaging in neuroendocrine tumors. *Journal of Nuclear Medicine*, 59, 2018.

[157] Sangwon Han, Chong Hyun Suh, Sungmin Woo, Yeon Joo Kim, and Jong Jin Lee. Performance of 68 ga-dota–conjugated somatostatin receptor–targeting peptide pet in detection of pheochromocytoma and paraganglioma: A systematic review and metaanalysis. *Journal of Nuclear Medicine*, 60, 2019.

[158] Romain Eychenne, Christelle Bouvry, Mickael Bourgeois, Pascal Loyer, Eric Benoist, and Nicolas Lepareur. Overview of radiolabeled somatostatin analogs for cancer imaging and therapy, 2020.

[159] Roberto Baldelli, A. Barnabei, L. Rizza, A. M. Isidori, F. Rota, P. Di Giacinto, A. Paoloni, F. Torino, S. M. Corsello, A. Lenzi, and M. Appetecchia. Somatostatin analogs therapy in gastroenteropancreatic neuroendocrine tumors: Current aspects and new perspectives, 2014.

[160] E. P. KRENNING, P. P.M. KOOIJ, W. H. BAKKER, W. A.P. BREEMAN, P. T.E. POSTEMA, D. J. KWEKKEBOOM, H. Y. OEI, M. de JONG, T. J. VISSER, A. E.M. REIJS, and S. W.J. LAMBERTS. Radiotherapy with a radiolabeled somatostatin analogue, [111in-dtpa-d-phe1]-octreotide: A case history. *Annals of the New York Academy of Sciences*, 733, 1994.

[161] A. Otte, R. Herrmann, A. Heppeler, M. Behe, E. Jermann, P. Powell, H. R. Maecke, and J. Muller. Yttrium-90 dotatoc: First clinical results. *European Journal of Nuclear Medicine*, 26, 1999.

[162] Barbara Stolz, Gisbert Weckbecker, Peter M. Smith-Jones, Rainer Albert, Friedrich Raulf, and Christian Bruns. The somatostatin receptor-targeted radiotherapeutic [90y-dota-dphe1,tyr3]octreotide (90y-smt 487) eradicates experimental rat pancreatic ca 20948 tumours. *European Journal of Nuclear Medicine*, 25, 1998.

[163] Eric P. Krenning, Dik J. Kwekkeboom, Roelf Valkema, Stanislas Pauwels, Larry K. Kvols, and Marion De Jong. Peptide receptor radionuclide therapy, 2004.

[164] D. J. Kwekkeboom, W. H. Bakker, B. L. Kam, J. J.M. Teunissen, P. P.M. Kooij, W. W. Herder, R. A. Feelders, C. H.J. Eijck, M. Jong, A. Srinivasan, J. L. Erion, and E. P. Krenning. Treatment of patients with gastro-entero-pancreatic (gep) tumours with the novel radiolabelled somatostatin analogue [177lu-dota0,tyr3]octreotate. *European Journal of Nuclear Medicine and Molecular Imaging*, 30, 2003.

[165] Lisa Bodei, Mark Kidd, Giovanni Paganelli, Chiara M. Grana, Ignat Drozdov, Marta Cremonesi, Christopher Lepensky, Dik J. Kwekkeboom, Richard P. Baum, Eric P. Krenning, and Irvin M. Modlin. Long-term tolerability of prrt in 807 patients with neuroendocrine tumours: the value and limitations of clinical factors. *European Journal of Nuclear Medicine and Molecular Imaging*, 42, 2015.

[166] S. Prado-Wohlwend, J.C. Bernal-Vergara, A. Utrera-Costero, J.R. Cañón-Sánchez, M. Agudelo-Cifuentes, and P. Bello-Arques. Terapia con péptidos radiomarcados con [177lu]lu-dota-tate. *Revista Española de Medicina Nuclear e Imagen Molecular*, 41, 2022.

[167] Thomas A. Hope, Jeremie Calais, Li Zhang, William Dieckmann, and Corina Millo. 111in-pentetreotide scintigraphy versus 68ga-dotatate pet: Impact on krenning scores and effect of tumor burden. *Journal of Nuclear Medicine*, 60, 2019.

[168] Rudolf A. Werner, Ralph A. Bundschuh, Lena Bundschuh, Mehrbod S. Javadi, Takahiro Higuchi, Alexander Weich, Sara Sheikhbahaei, Kenneth J. Pienta, Andreas K. Buck, Martin G. Pomper, Michael A. Gorin, Constantin Lapa, and Steven P. Rowe. Molecular imaging reporting and data systems (mi-rads): a generalizable framework for targeted radiotracers with theranostic implications, 2018.

[169] Eric Guedj, Andrea Varrone, Ronald Boellaard, Nathalie L. Albert, Henryk Barthel, Bart van Berckel, Matthias Brendel, Diego Cecchin, Ozgul Ekmekcioglu, Valentina Garibotto, Adriaan A. Lammertsma, Ian Law, Iván Peñuelas, Franck Semah, Tatjana Traub-Weidinger, Elsmarieke van de Giessen, Donatienne Van Weehaeghe, and Silvia Morbelli. Eanm procedure guidelines for brain pet imaging using [18f]fdg, version 3. *European Journal of Nuclear Medicine and Molecular Imaging 2021 49:2*, 49:632–651, 12 2021.

[170] Suleman Surti, Austin Kuhn, Matthew E. Werner, Amy E. Perkins, Jeffrey Kolthammer, and Joel S. Karp. Performance of philips gemini tf pet/ct scanner with special consideration for its time-of-flight imaging capabilities. *Journal of Nuclear Medicine*, 48, 2007.

[171] Sebastian Palmqvist, Henrik Zetterberg, Niklas Mattsson, Per Johansson, Lennart Minthon, Kaj Blennow, Mattias Olsson, and Oskar Hansson. Detailed comparison of amyloid pet and csf biomarkers for identifying early alzheimer disease. *Neurology*, 85:1240–1249, 10 2015.

[172] Kelvin K.F. Tsoi, Joyce Y.C. Chan, Hoyee W. Hirai, Samuel Y.S. Wong, and Timothy C.Y. Kwok. Cognitive tests to detect dementia a systematic review and meta-analysis. *JAMA Internal Medicine*, 175, 2015.

[173] Satoshi Minoshima, Alexander E. Drzezga, Henryk Barthel, Nicolaas Bohnen, Mehdi Djekidel, David H. Lewis, Chester A. Mathis, Jonathan McConathy, Agneta Nordberg, Osama Sabri, John P. Seibyl, Margaret K. Stokes, and Koen Van Laere. Snmmi procedure standard/eanm practice guideline for amyloid pet imaging of the brain 1.0. *Journal of Nuclear Medicine*, 57, 2016.

[174] European Medicines Agency. Ema/30808/2013 amyvid—assessment report. 2013.

[175] Magdy M. Khalil. *Basic science of PET imaging*. Springer, 2016.

[176] Angelina Cistaro, Natale Quartuccio, Alireza Mojtahedi, Piercarlo Fania, Pier Luigi Filosso, Alfredo Campenni, Umberto Ficola, and Sergio Baldari. Prediction of 2 years-survival in patients with stage i and ii non-small cell lung cancer utilizing 18f-fdg pet/ct suv quantification. *Radiology and Oncology*, 47, 2013.

[177] Giampaolo Tomasi, Federico Turkheimer, and Eric Aboagye. Importance of quantification for the analysis of pet data in oncology: Review of current methods and trends for the future, 2012.

[178] Ronald Boellaard. Standards for pet image acquisition and quantitative data analysis, 2009.

[179] Søren Hess, Björn A. Blomberg, Rajan Rakheja, Kent Friedman, Thomas C. Kwee, Poul Flemming Høilund-Carlsen, and Abass Alavi. A brief overview of novel approaches to fdg pet imaging and quantification, 2014.

[180] A. Niñerola-Baizán, P. Aguiar, M.N. Cabrera-Martín, C. Vigil, A. Gómez-Grande, C. Lorenzo, S. Rubí, P. Sopena, and V. Camacho. Relevancia de la cuantificación en los estudios pet cerebrales con 18f-fdg. *Revista Española de Medicina Nuclear e Imagen Molecular*, 39, 2020.

[181] William D.. Penny, Karl J.. Friston, John T.. Ashburner, Stefan J.. Kiebel, and Thomas E.. Nichols. Statistical parametric mapping: the analysis of functional brain images. 2006.

[182] Eric Guedj, Andrea Varrone, Ronald Boellaard, Nathalie L. Albert, Henryk Barthel, Bart van Berckel, Matthias Brendel, Diego Cecchin, Ozgul Ekmekcioglu, Valentina Garibotto, Adriaan A. Lammertsma, Ian Law, Iván Peñuelas, Franck Semah, Tatjana Traub-Weidinger, Elsmarieke van de Giessen, Donatienne Van Weehaeghe, and Silvia Morbelli. Eanm procedure guidelines for brain pet imaging using [18f]fdg, version 3. *European Journal of Nuclear Medicine and Molecular Imaging 2021 49:2*, 49:632–651, 12 2021.

[183] Alexander Hammers, Richard Allom, Matthias J. Koepp, Samantha L. Free, Ralph Myers, Louis Lemieux, Tejal N. Mitchell, David J. Brooks, and John S. Duncan. Three-dimensional maximum probability atlas of the human brain, with particular reference to the temporal lobe. *Human Brain Mapping*, 19:224–247, 8 2003.

[184] Ioannis S. Gousias, Daniel Rueckert, Rolf A. Heckemann, Leigh E. Dyet, James P. Boardman, A. David Edwards, and Alexander Hammers. Automatic segmentation of brain mris of 2-year-olds into 83 regions of interest. *NeuroImage*, 40:672–684, 4 2008.

[185] Abhishek Mahajan, Nivedita Chakrabarty, Jinita Majithia, Ankita Ahuja, Ujjwal Agarwal, Shubham Suryavanshi, Mahesh Biradar, Prerit Sharma, Bagyam Raghavan, Rasheed Arafath, and Shreya Shukla. Multisystem imaging recommendations/guidelines: In the pursuit of precision oncology, 2023.

[186] Mingyu Kim, Jihye Yun, Yongwon Cho, Keewon Shin, Ryoungwoo Jang, Hyun Jin Bae, and Namkug Kim. Deep learning in medical imaging, 2019.

[187] Shijun Wang and Ronald M. Summers. Machine learning and radiology. *Medical Image Analysis*, 16:933–951, 7 2012.

[188] Huan Hsin Tseng, Lise Wei, Sunan Cui, Yi Luo, Randall K. Ten Haken, and Issam El Naqa. Machine learning and imaging informatics in oncology, 2020.

[189] Garry Choy, Omid Khalilzadeh, Mark Michalski, Synho Do, Anthony E. Samir, Oleg S. Pianykh, J. Raymond Geis, Pari V. Pandharipande, James A. Brink, and Keith J. Dreyer. Current applications and future impact of machine learning in radiology, 2018.

[190] Jonghoon Kim, Jisu Hong, and Hyunjin Park. Prospects of deep learning for medical imaging. *Precision and Future Medicine*, 2, 2018.

[191] M T Hagan, H B Demuth, and M H Beale. Neural network design. *Boston Massachusetts PWS*, 2, 1995.

[192] The perceptron — a perceiving and recognizing automaton – brain wars.

[193] Earl Brill and Harry P. Schultz. *Christopher M. Bishop - Pattern Recognition and Machine Learning*, volume 29. 1964.

[194] Quoc V. Le, Jiquan Ngiam, Adam Coates, Abhik Lahiri, Bobby Prochnow, and Andrew Y. Ng. On optimization methods for deep learning. In *Proceedings of the 28th International Conference on Machine Learning, ICML 2011*, 2011.

[195] David E. Rumelhart, Geoffrey E. Hinton, and Ronald J. Williams. Learning representations by back-propagating errors. *Nature*, 323, 1986.

[196] Alexander Selvikvåg Lundervold and Arvid Lundervold. An overview of deep learning in medical imaging focusing on mri. *Zeitschrift fur medizinische Physik*, 29:102–127, 5 2019.

[197] Ian Goodfellow, Yoshua Bengio, and Aaron Courville. *Deep Learning*. MIT Press, 2016. http://www.deeplearningbook.org.

[198] Trevor Hastie, Robert Tibshirani, and Jerome Friedman. The elements of statistical learning. 2009.

[199] Karen Simonyan and Andrew Zisserman. Very deep convolutional networks for large-scale image recognition. In *3rd International Conference on Learning Representations, ICLR 2015 - Conference Track Proceedings*, 2015.

[200] Li Sze Chow and Raveendran Paramesran. Review of medical image quality assessment, 2016.

[201] Steven R Meikle, Vesna Sossi, Emilie Roncali, Simon R Cherry, Richard Banati, David Mankoff, Terry Jones, Michelle James, Julie Sutcliffe, Jinsong Ouyang, Yoann Petibon, Chao Ma, Georges El Fakhri, Suleman Surti, Joel S Karp, Ramsey D Badawi, Taiga Yamaya, Georg Schramm, Ahmadreza Rezaei, Johan Nuyts, Roger Fulton, André Kyme, Cristina Lois, Hasan Sari, Julie Price, Ronald Boellaard, Robert Jeraj, Dale L Bailey, Enid Eslick, Kathy P Willowson, and Joyita Dutta. Quantitative pet in the 2020s: a roadmap. *Phys. Med. Biol*, 66:6–7, 2021.

[202] Wolfgang A. Weber. Positron emission tomography as an imaging biomarker, 2006.

[203] James P.B. O'Connor, Eric O. Aboagye, Judith E. Adams, Hugo J.W.L. Aerts, Sally F. Barrington, Ambros J. Beer, Ronald Boellaard, Sarah E. Bohndiek, Michael Brady, Gina Brown, David L. Buckley, Thomas L. Chenevert, Laurence P. Clarke, Sandra Collette, Gary J. Cook, Nandita M. Desouza, John C. Dickson, Caroline Dive, Jeffrey L. Evelhoch, Corinne Faivre-Finn, Ferdia A. Gallagher, Fiona J. Gilbert, Robert J. Gillies, Vicky Goh, John R. Griffiths, Ashley M. Groves, Steve Halligan, Adrian L. Harris, David J. Hawkes, Otto S. Hoekstra, Erich P. Huang, Brian F. Hutton, Edward F. Jackson, Gordon C. Jayson, Andrew Jones, Dow Mu Koh, Denis Lacombe, Philippe Lambin, Nathalie Lassau, Martin O. Leach, Ting Yim Lee, Edward L. Leen, Jason S. Lewis, Yan Liu, Mark F. Lythgoe, Prakash Manoharan, Ross J. Maxwell, Kenneth A. Miles, Bruno Morgan, Steve Morris, Tony Ng, Anwar R. Padhani, Geoff J.M. Parker, Mike Partridge, Arvind P. Pathak, Andrew C. Peet, Shonit Punwani, Andrew R.

Reynolds, Simon P. Robinson, Lalitha K. Shankar, Ricky A. Sharma, Dmitry Soloviev, Sigrid Stroobants, Daniel C. Sullivan, Stuart A. Taylor, Paul S. Tofts, Gillian M. Tozer, Marcel Van Herk, Simon Walker-Samuel, James Wason, Kaye J. Williams, Paul Workman, Thomas E. Yankeelov, Kevin M. Brindle, Lisa M. McShane, Alan Jackson, and John C. Waterton. Imaging biomarker roadmap for cancer studies. *Nature Reviews Clinical Oncology*, 14, 2017.

[204] David L. Raunig, Lisa M. McShane, Gene Pennello, Constantine Gatsonis, Paul L. Carson, James T. Voyvodic, Richard L. Wahl, Brenda F. Kurland, Adam J. Schwarz, Mithat Gönen, Gudrun Zahlmann, Marina V. Kondratovich, Kevin O'Donnell, Nicholas Petrick, Patricia E. Cole, Brian Garra, and Daniel C. Sullivan. Quantitative imaging biomarkers: A review of statistical methods for technical performance assessment, 2015.

[205] David A. Mankoff, Daniel A. Pryma, and Amy S. Clark. Molecular imaging biomarkers for oncology clinical trials. *Journal of Nuclear Medicine*, 55, 2014.

[206] Sangwon Han, Yong il Kim, Sungmin Woo, Tae Hyung Kim, and Jin Sook Ryu. Prognostic and predictive values of interim 18f-fdg pet during neoadjuvant chemoradiotherapy for esophageal cancer: a systematic review and meta-analysis. *Annals of Nuclear Medicine*, 35, 2021.

[207] Go Akamatsu, Yuji Tsutsui, Hiromitsu Daisaki, Katsuhiko Mitsumoto, Shingo Baba, and Masayuki Sasaki. A review of harmonization strategies for quantitative pet, 2023.

[208] Frederic H. Fahey, Paul E. Kinahan, Robert K. Doot, Mehmet Kocak, Harold Thurston, and Tina Young Poussaint. Variability in pet quantitation within a multicenter consortium. *Medical Physics*, 37, 2010.

[209] Michael C. Adams, Timothy G. Turkington, Joshua M. Wilson, and Terence Z. Wong. A systematic review of the factors affecting accuracy of suv measurements, 2010.

[210] Benjamin Houdu, Charline Lasnon, Idlir Licaj, Guy Thomas, Pascal Do, Anne Valerie Guizard, Cédric Desmonts, and Nicolas Aide. Why harmonization is needed when using fdg pet/ct as a prognosticator: demonstration with earl-compliant suv as an independent prognostic factor in lung cancer. *European Journal of Nuclear Medicine and Molecular Imaging*, 46, 2019.

[211] Elske Quak, Pierre Yves Le Roux, Charline Lasnon, Philippe Robin, Michael S. Hofman, David Bourhis, Jason Callahan, David S. Binns, Cédric Desmonts, Pierre Yves Salaun, Rodney J. Hicks, and Nicolas Aide. Does pet suv harmonization affect percist response classification? *Journal of Nuclear Medicine*, 57, 2016.

[212] Jianhua Yan, Jason Lim Chu-Shern, Hoi Yin Loi, Lih Kin Khor, Arvind K. Sinha, Swee Tian Quek, Ivan W.K. Tham, and David Townsend. Impact of image

reconstruction settings on texture features in 18f-fdg pet. *Journal of Nuclear Medicine*, 56, 2015.

[213] Sylvain Reuzé, Fanny Orlhac, Cyrus Chargari, Christophe Nioche, Elaine Limkin, François Riet, Alexandre Escande, Christine Haie-Meder, Laurent Dercle, Sébastien Gouy, Irène Buvat, Eric Deutsch, and Charlotte Robert. Prediction of cervical cancer recurrence using textural features extracted from 18f-fdg pet images acquired with different scanners. *Oncotarget*, 8, 2017.

[214] Isaac Shiri, Arman Rahmim, Pardis Ghaffarian, Parham Geramifar, Hamid Abdollahi, and Ahmad Bitarafan-Rajabi. The impact of image reconstruction settings on 18f-fdg pet radiomic features: multi-scanner phantom and patient studies. *European Radiology*, 27, 2017.

[215] Elisabeth Pfaehler, Joyce Van Sluis, Bram B.J. Merema, Peter Van Ooijen, Ralph C.M. Berendsen, Floris H.P. Van Velden, and Ronald Boellaard. Experimental multicenter and multivendor evaluation of the performance of pet radiomic features using 3-dimensionally printed phantom inserts. *Journal of Nuclear Medicine*, 61, 2020.

[216] Matthew J. Nyflot, Fei Yang, Darrin Byrd, Stephen R. Bowen, George A. Sandison, and Paul E. Kinahan. Quantitative radiomics: impact of stochastic effects on textural feature analysis implies the need for standards. *Journal of Medical Imaging*, 2, 2015.

[217] W. Evan Johnson, Cheng Li, and Ariel Rabinovic. Adjusting batch effects in microarray expression data using empirical bayes methods. *Biostatistics*, 8, 2007.

[218] Isaac Shiri, Mehdi Amini, Mostafa Nazari, Ghasem Hajianfar, Atlas Haddadi Avval, Hamid Abdollahi, Mehrdad Oveisi, Hossein Arabi, Arman Rahmim, and Habib Zaidi. Impact of feature harmonization on radiogenomics analysis: Prediction of egfr and kras mutations from non-small cell lung cancer pet/ct images. *Computers in Biology and Medicine*, 142, 2022.

[219] Doris Leithner, Heiko Schöder, Alexander Haug, H. Alberto Vargas, Peter Gibbs, Ida Häggström, Ivo Rausch, Michael Weber, Anton S. Becker, Jazmin Schwartz, and Marius E. Mayerhoefer. Impact of combat harmonization on pet radiomics-based tissue classification: A dual-center pet/mri and pet/ct study. *Journal of Nuclear Medicine*, 63, 2022.

[220] R. N. Mahon, M. Ghita, G. D. Hugo, and E. Weiss. Combat harmonization for radiomic features in independent phantom and lung cancer patient computed tomography datasets. *Physics in Medicine and Biology*, 65, 2020.

[221] Hannah Horng, Apurva Singh, Bardia Yousefi, Eric A. Cohen, Babak Haghighi, Sharyn Katz, Peter B. Noël, Russell T. Shinohara, and Despina Kontos. Generalized combat harmonization methods for radiomic features with multi-modal distributions and multiple batch effects. *Scientific Reports*, 12, 2022.

[222] Norihide Maikusa, Yinghan Zhu, Akiko Uematsu, Ayumu Yamashita, Kousaku Saotome, Naohiro Okada, Kiyoto Kasai, Kazuo Okanoya, Okito Yamashita, Saori C. Tanaka, and Shinsuke Koike. Comparison of traveling-subject and combat harmonization methods for assessing structural brain characteristics. *Human Brain Mapping*, 42, 2021.

[223] Fanny Orlhac, Jakoba J. Eertink, Anne Ségolène Cottereau, Josée M. Zijlstra, Catherine Thieblemont, Michel Meignan, Ronald Boellaard, and Irène Buvat. A guide to combat harmonization of imaging biomarkers in multicenter studies. *Journal of Nuclear Medicine*, 63, 2022.

[224] Jean-Philippe Fortin. *neuroCombat: Harmonization of multi-site imaging data with ComBat*, 2023. R package version 1.0.13.

[225] William E. Klunk, Robert A. Koeppe, Julie C. Price, Tammie L. Benzinger, Michael D. Devous, William J. Jagust, Keith A. Johnson, Chester A. Mathis, Davneet Minhas, Michael J. Pontecorvo, Christopher C. Rowe, Daniel M. Skovronsky, and Mark A. Mintun. The centiloid project: Standardizing quantitative amyloid plaque estimation by pet. *Alzheimer's and Dementia*, 11, 2015.

[226] Aurora Monter-Pozos and Elizabeth González-Estrada. On testing the skew normal distribution by using shapiro–wilk test. *Journal of Computational and Applied Mathematics*, 440, 4 2024.

[227] S. S. Shapiro and M. B. Wilk. An analysis of variance test for normality (complete samples). *Biometrika*, 52, 1965.

[228] Siddhant Thukral, Stefan Kovac, and Mounica Paturu. *t-test*. 2023.

[229] Justine Rochon, Matthias Gondan, and Meinhard Kieser. To test or not to test: Preliminary assessment of normality when comparing two independent samples. *BMC Medical Research Methodology*, 12, 2012.

[230] Tae Kyun Kim. T test as a parametric statistic. *Korean Journal of Anesthesiology*, 68, 2015.

[231] Sarah Boslaugh and Paul Andrew Watters. *Statistics in a nutshell: a desktop quick reference*, volume 130. 1984.

[232] Younis Skaik. The bread and butter of statistical analysis "t-test": Uses and misuses, 2015.

[233] N. A.C. Cressie, L. J. Sheffield, and H. J. Whitford. Use of the one sample t-test in the real world. *Journal of Chronic Diseases*, 37, 1984.

[234] Manfei Xu, Drew Fralick, Julia Z. Zheng, Bokai Wang, Xin M. Tu, and Changyong Feng. The differences and similarities between two-sample t-test and paired t-test. *Shanghai Archives of Psychiatry*, 29, 2017.

[235] James E. De Muth. Overview of biostatistics used in clinical research, 2009.

[236] Stephen W. Scheff. *Fundamental Statistical Principles for the Neurobiologist: A Survival Guide*. 2016.

[237] Michael P. Fay and Michael A. Proschan. Wilcoxon-mann-whitney or t-test? on assumptions for hypothesis tests and multiple interpretations of decision rules. *Statistics Surveys*, 4, 2010.

[238] George W. Divine, H. James Norton, Anna E. Barón, and Elizabeth Juarez-Colunga. The wilcoxon–mann–whitney procedure fails as a test of medians. *American Statistician*, 72, 2018.

[239] Myles Hollander, Douglas A. Wolfe, and Eric Chicken. *Nonparametric statistical methods*. 2015.

[240] Jan Hauke and Tomasz Kossowski. Comparison of values of pearson's and spearman's correlation coefficients on the same sets of data. *Quaestiones Geographicae*, 30, 2011.

[241] KADAKATLA PAVAN KUMAR and VISWESWARAO REDDI. Significance of spearman's rank correlation coefficient. *International Journal For Multidisciplinary Research*, 5, 2023.

[242] Jerome L. Myers, Arnold D. Well, and Robert F. Lorch. *Research design and statistical analysis, third edition*, volume 9780203726631. 2013.

[243] Hossin M and Sulaiman M.N. A review on evaluation metrics for data classification evaluations. *International Journal of Data Mining and Knowledge Management Process*, 5, 2015.

[244] W. J. Youden. Index for rating diagnostic tests. *Cancer*, 3, 1950.

[245] Ronen Fluss, David Faraggi, and Benjamin Reiser. Estimation of the youden index and its associated cutoff point. *Biometrical Journal*, 47, 2005.

[246] Julius Sim and Chris C. Wright. The kappa statistic in reliability studies: Use, interpretation, and sample size requirements, 2005.

[247] Mary L. McHugh. Interrater reliability: The kappa statistic. *Biochemia Medica*, 22, 2012.

[248] Lidija Bilić-Zulle. Comparison of methods: Passing and bablok regression, 2011.

[249] Davide Giavarina. Understanding bland altman analysis. *Biochemia Medica*, 25, 2015.

[250] Nurettin Özgür Doğan. Bland-altman analysis: A paradigm to understand correlation and agreement, 2018.

[251] Mohammad Ali Mansournia, Rachel Waters, Maryam Nazemipour, Martin Bland, and Douglas G. Altman. Bland-altman methods for comparing methods of measurement and response to criticisms. *Global Epidemiology*, 3, 2021.

[252] P. S. Myles and J. Cui. I. using the bland-altman method to measure agreement with repeated measures, 2007.

[253] Junkang An and Inwhee Joe. Attention map-guided visual explanations for deep neural networks. *Applied Sciences (Switzerland)*, 12, 2022.

[254] Jie Hu, Li Shen, Samuel Albanie, Gang Sun, and Enhua Wu. Squeeze-and-excitation networks. *IEEE Transactions on Pattern Analysis and Machine Intelligence*, 42, 2020.

[255] Karen Simonyan, Andrea Vedaldi, and Andrew Zisserman. Deep inside convolutional networks: Visualising image classification models and saliency maps. In *2nd International Conference on Learning Representations, ICLR 2014 - Workshop Track Proceedings*, 2014.

[256] Daniel Smilkov, Nikhil Thorat, Been Kim, Fernanda Viégas, and Martin Wattenberg. Smoothgrad: removing noise by adding noise, 2017.

[257] Ramprasaath R. Selvaraju, Michael Cogswell, Abhishek Das, Ramakrishna Vedantam, Devi Parikh, and Dhruv Batra. Grad-cam: Visual explanations from deep networks via gradient-based localization. *International Journal of Computer Vision*, 128(2):336–359, October 2019.

[258] Keith A. Johnson, Nick C. Fox, Reisa A. Sperling, and William E. Klunk. Brain imaging in alzheimer disease. *Cold Spring Harbor Perspectives in Medicine*, 2, 2012.

[259] Maria Teresa Gandia-Ferrero, Irene Torres-Espallardo, Begoña Martínez-Sanchis, Enrique Muñoz, Constantino Morera-Ballester, Pablo Sopena-Novales, Lourdes Álvarez Sánchez, Miquel Baquero-Toledo, and Luis Martí-Bonmatí. Amyloid brain-dedicated pet images can diagnose alzheimer's pathology with centiloid scale. *Physica Medica*, 121:103345, 2024.

[260] Ellen H Singleton, Jay L P Fieldhouse, Jochum J van 't Hooft, Marta Scarioni, Marie-Paule E van Engelen, Sietske A M Sikkes, Casper de Boer, Diana I Bocancea, Esther van den Berg, Philip Scheltens, Wiesje M van der Flier, Janne M Papma, Yolande A L Pijnenburg, and Rik Ossenkoppele. Social cognition deficits and biometric signatures in the behavioural variant of alzheimer's disease. *Brain*, 2022.

[261] Emre Bora and Görsev G. Yener. Meta-analysis of social cognition in mild cognitive impairment. *Journal of Geriatric Psychiatry and Neurology*, 30, 2017.

[262] Namita Multani, Foad Taghdiri, Cassandra J. Anor, Brenda Varriano, Karen Misquitta, David F. Tang-Wai, Ron Keren, Susan Fox, Anthony E. Lang, Anne Catherine Vijverman, Connie Marras, and Maria Carmela Tartaglia. Association between social cognition changes and resting state functional connectivity in frontotemporal dementia, alzheimer's disease, parkinson's disease, and healthy controls. *Frontiers in Neuroscience*, 13:477970, 11 2019.

[263] Morris Freedman, Malcolm A. Binns, Sandra E. Black, Cara Murphy, and Donald T. Stuss. Theory of mind and recognition of facial emotion in dementia: Challenge to current concepts. *Alzheimer Disease and Associated Disorders*, 27, 2013.

[264] Martin Comon, Isabelle Rouch, Arlette Edjolo, Catherine Padovan, Pierre Krolak-Salmon, and Jean Michel Dorey. Impaired facial emotion recognition and gaze direction detection in mild alzheimer's disease: Results from the paco study. *Journal of Alzheimer's Disease*, 89, 2022.

[265] Mandy Roheger, Jana Brenning, Steffen Riemann, Andrew K. Martin, Agnes Flöel, and Marcus Meinzer. Progression of socio-cognitive impairment from healthy aging to alzheimer's dementia: A systematic review and meta-analysis, 2022.

[266] Yanica Klein-Koerkamp, Marine Beaudoin, Monica Baciu, and Pascal Hot. Emotional decoding abilities in alzheimer's disease: A meta-analysis. *Journal of Alzheimer's Disease*, 32, 2012.

[267] Simon Baron-Cohen, Sally Wheelwright, Jacqueline Hill, Yogini Raste, and Ian Plumb. The "reading the mind in the eyes" test revised version: A study with normal adults, and adults with asperger syndrome or high-functioning autism. *Journal of Child Psychology and Psychiatry*, 42, 2001.

[268] Beth F.M. Oakley, Rebecca Brewer, Geoffrey Bird, and Caroline Catmur. Theory of mind is not theory of emotion: A cautionary note on the reading the mind in the eyes test. *Journal of Abnormal Psychology*, 125, 2016.

[269] Enrique G. Fernández-Abascal, Rosario Cabello, Pablo Fernández-Berrocal, and Simon Baron-Cohen. Test-retest reliability of the 'reading the mind in the eyes' test: A one-year follow-up study. *Molecular Autism*, 4, 2013.

[270] Kate L. Harkness, Mark A. Sabbagh, Jill A. Jacobson, Neeta K. Chowdrey, and Tina Chen. Enhanced accuracy of mental state decoding in dysphoric college students. *Cognition and Emotion*, 19, 2005.

[271] Matthias L. Schroeter, Timo Stein, Nina Maslowski, and Jane Neumann. Neural correlates of alzheimer's disease and mild cognitive impairment: A systematic and quantitative meta-analysis involving 1351 patients. *NeuroImage*, 47, 2009.

[272] Camille Heitz, Vincent Noblet, Clélie Phillipps, Benjamin Cretin, Natacha Vogt, Nathalie Philippi, Jennifer Kemp, Xavier de Petigny, Mathias Bilger, Catherine Demuynck, Catherine Martin-Hunyadi, Jean-Paul Armspach, and Frédéric Blanc. Cognitive and affective theory of mind in dementia with lewy bodies and alzheimer's disease. *Alzheimer's Research and Therapy*, 8, 12 2016.

[273] L. Bäckman, S. Jones, A. K. Berger, E. J. Laukka, and B. J. Small. Multiple cognitive deficits during the transition to alzheimer's disease. In *Journal of Internal Medicine*, volume 256, 2004.

[274] Mercedes Fernández-Ríos, Rosa Redolat, Emilia Serra, and Gregorio González-Alcaide. A systematic review of facial emotion recognition in alzheimer's disease: A developmental and gender perspective, 2021.

[275] Giulia Francesca Barbieri, Elena Real, Jessica Lopez, José Manuel García-Justicia, Encarnación Satorres, and Juan C. Meléndez. Comparison of emotion recognition in young people, healthy older adults, and patients with mild cognitive impairment. *International Journal of Environmental Research and Public Health*, 19, 2022.

[276] Fijanne Strijkert, Rients Bauke Huitema, and Jacoba Margje Spikman. Measuring emotion recognition: Added value in diagnosing dementia of the alzheimer's disease type. *Journal of Neuropsychology*, 16, 2022.

[277] Beatrice Orso, Luigi Lorenzini, Dario Arnaldi, Nicola Girtler, Andrea Brugnolo, Elisa Doglione, Pietro Mattioli, Erica Biassoni, Federico Massa, Enrico Peira, Matteo Bauckneht, Maria I. Donegani, Silvia Morbelli, Flavio Nobili, and Matteo Pardini. The role of hub and spoke regions in theory of mind in early alzheimer's disease and frontotemporal dementia. *Biomedicines*, 10, 2022.

[278] Agostino Chiaravalloti, Gaetano Barbagallo, Maria Ricci, Alessandro Martorana, Francesco Ursini, Pasqualina Sannino, Georgios Karalis, and Orazio Schillaci. Brain metabolic correlates of csf tau protein in a large cohort of alzheimer's disease patients: A csf and fdg pet study. *Brain Research*, 1678, 2018.

[279] Amirata Ghorbani, Abubakar Abid, and James Zou. Interpretation of neural networks is fragile. In *33rd AAAI Conference on Artificial Intelligence, AAAI 2019, 31st Innovative Applications of Artificial Intelligence Conference, IAAI 2019 and the 9th AAAI Symposium on Educational Advances in Artificial Intelligence, EAAI 2019*, 2019.

[280] Yiming Ding, Jae Ho Sohn, Michael G. Kawczynski, Hari Trivedi, Roy Harnish, Nathaniel W. Jenkins, Dmytro Lituiev, Timothy P. Copeland, Mariam S. Aboian, Carina Mari Aparici, Spencer C. Behr, Robert R. Flavell, Shih Ying Huang, Kelly A. Zalocusky, Lorenzo Nardo, Youngho Seo, Randall A. Hawkins, Miguel Hernandez Pampaloni, Dexter Hadley, and Benjamin L. Franc. A deep learning model to predict a diagnosis of alzheimer disease by using 18 f-fdg pet of the brain. *Radiology*, 290, 2019.

[281] Kobra Etminani, Amira Soliman, Anette Davidsson, Jose R. Chang, Begoña Martínez-Sanchis, Stefan Byttner, Valle Camacho, Matteo Bauckneht, Roxana Stegeran, Marcus Ressner, Marc Agudelo-Cifuentes, Andrea Chincarini, Matthias Brendel, Axel Rominger, Rose Bruffaerts, Rik Vandenberghe, Milica G. Kramberger, Maja Trost, Nicolas Nicastro, Giovanni B. Frisoni, Afina W. Lemstra, Bart N. M. van Berckel, Andrea Pilotto, Alessandro Padovani, Silvia Morbelli, Dag Aarsland, Flavio Nobili, Valentina Garibotto, and Miguel Ochoa-Figueroa. A 3d deep learning model to predict the diagnosis of dementia with lewy bodies, alzheimer's disease, and mild cognitive impairment using brain 18f-fdg pet. *European Journal of Nuclear Medicine and Molecular Imaging*, 2021.

[282] Nguyen Thanh Duc, Seungjun Ryu, Muhammad Naveed Iqbal Qureshi, Min Choi, Kun Ho Lee, and Boreom Lee. 3d-deep learning based automatic diagnosis of alzheimer's disease with joint mmse prediction using resting-state fmri. *Neuroinformatics*, 18, 2020.

[283] Chiyu Feng, Ahmed Elazab, Peng Yang, Tianfu Wang, Feng Zhou, Huoyou Hu, Xiaohua Xiao, and Baiying Lei. Deep learning framework for alzheimer's disease diagnosis via 3d-cnn and fsbi-lstm. *IEEE Access*, 7, 2019.

[284] Manhua Liu, Danni Cheng, and Weiwu Yan. Classification of alzheimer's disease by combination of convolutional and recurrent neural networks using fdg-pet images. *Frontiers in Neuroinformatics*, 12, 2018.

[285] Georg Schramm, Jens Langner, Frank Hofheinz, Jan Petr, Bettina Beuthien-Baumann, Ivan Platzek, Jörg Steinbach, Jörg Kotzerke, and Jörg Van Den Hoff. Quantitative accuracy of attenuation correction in the philips ingenuity tf whole-body pet/mr system: A direct comparison with transmission-based attenuation correction. *Magnetic Resonance Materials in Physics, Biology and Medicine*, 26, 2013.

[286] Pierrick Bourgeat, Victor L. Villemagne, Vincent Dore, Belinda Brown, S. Lance Macaulay, Ralph Martins, Colin L. Masters, David Ames, Kathryn Ellis, Christopher C. Rowe, Olivier Salvado, and Jurgen Fripp. Comparison of mr-less pib suvr quantification methods. *Neurobiology of Aging*, 36, 2015.

[287] Paul Blanc-Durand, Maya Khalife, Brian Sgard, Sandeep Kaushik, Marine Soret, Amal Tiss, Georges El Fakhri, Marie Odile Habert, Florian Wiesinger, and Aurélie Kas. Attenuation correction using 3d deep convolutional neural network for brain 18ffdg pet/mr: Comparison with atlas, zte and ct based attenuation correction. *PLoS ONE*, 14, 2019.

[288] Joshua S. Scheuermann, Janet R. Saffer, Joel S. Karp, Anthony M. Levering, and Barry A. Siegel. Qualification of pet scanners for use in multicenter cancer clinical trials: The american college of radiology imaging network experience. *Journal of Nuclear Medicine*, 50, 2009.

[289] María Nieves Cabrera-Martín, Gabriel González-Pavón, Miguel Sanchís Hernández, Constantino Morera-Ballester, Jordi A. Matías-Guiu, and José Luis Carreras Delgado. Validation technique and improvements introduced in a new dedicated brain positron emission tomograph (caremibrain). *Revista Española de Medicina Nuclear e Imagen Molecular (English Edition)*, 40, 2021.

[290] Bruno Dubois, Harald Hampel, Howard H. Feldman, Philip Scheltens, Paul Aisen, Sandrine Andrieu, Hovagim Bakardjian, Habib Benali, Lars Bertram, Kaj Blennow, Karl Broich, Enrica Cavedo, Sebastian Crutch, Jean François Dartigues, Charles Duyckaerts, Stéphane Epelbaum, Giovanni B. Frisoni, Serge Gauthier, Remy Genthon, Alida A. Gouw, Marie Odile Habert, David M. Holtzman, Miia Kivipelto, Simone Lista, José Luis Molinuevo, Sid E. O'Bryant, Gil D. Rabinovici, Christopher Rowe, Stephen Salloway, Lon S. Schneider, Reisa Sperling, Marc Teichmann, Maria C. Carrillo, Jeffrey Cummings, and Cliff R. Jack. Preclinical alzheimer's disease: Definition, natural history, and diagnostic criteria, 2016.

[291] Gemma Salvadó, José Luis Molinuevo, Anna Brugulat-Serrat, Carles Falcon, Oriol Grau-Rivera, Marc Suárez-Calvet, Javier Pavia, Aida Niñerola-Baizán, Andrés Perissinotti, Francisco Lomeña, Carolina Minguillon, Karine Fauria, Henrik Zetterberg, Kaj Blennow, and Juan Domingo Gispert. Centiloid cut-off values for optimal agreement between pet and csf core ad biomarkers. *Alzheimer's Research and Therapy*, 11, 2019.

[292] Santiago Bullich, Núria Roé-Vellvé, Marta Marquié, Susan M. Landau, Henryk Barthel, Victor L. Villemagne, Ángela Sanabria, Juan Pablo Tartari, Oscar Sotolongo-Grau, Vincent Doré, Norman Koglin, Andre Müller, Audrey Perrotin, Aleksandar Jovalekic, Susan De Santi, Lluís Tárraga, Andrew W. Stephens, Christopher C. Rowe, Osama Sabri, John P. Seibyl, and Mercè Boada. Early detection of amyloid load using 18f-florbetaben pet. *Alzheimer's Research and Therapy*, 13, 2021.

[293] Sanka Amadoru, Vincent Doré, Catriona A. McLean, Fairlie Hinton, Claire E. Shepherd, Glenda M. Halliday, Cristian E. Leyton, Paul A. Yates, John R. Hodges, Colin L. Masters, Victor L. Villemagne, and Christopher C. Rowe. Comparison of amyloid pet measured in centiloid units with neuropathological findings in alzheimer's disease. *Alzheimer's Research and Therapy*, 12, 2020.

[294] Anne M. Smith, Nancy A. Obuchowski, Norman L. Foster, Gregory Klein, P. David Mozley, Adriaan A. Lammertsma, Richard L. Wahl, John J. Sunderland, Jean Luc Vanderheyden, Tammie L.S. Benzinger, Paul E. Kinahan, Dean F. Wong, Eric S. Perlman, Satoshi Minoshima, and Dawn Matthews. The rsna qiba profile for amyloid pet as an imaging biomarker for cerebral amyloid quantification. *Journal of Nuclear Medicine*, 64:294–303, 2 2023.

List of Figures

List of Tables

Resum extens en valencià

INTRODUCCIÓ:

Fins fa poc, en medicina nuclear i particularment en els estudis PET, la interpretació d'imatges es basava principalment en la inspecció i avaluació visual o qualitativa, encara que també s'extreien algunes avaluacions quantitatives (com ara ràtios i altres mètriques simples), la qual cosa introduïa una alta variabilitat entre observadors i limitava la precisió en el seguiment i comparació d'estudis. Aquesta falta d'estandarditzación impedia obtenir dades fiables per a avaluar la progressió de malalties o la resposta als tractaments.

Davant aquesta limitació, la quantificació d'imatges PET es presenta com una necessitat essencial. Amb l'arribada d'instrumentació avançada i la capacitat de la imatge PET per reproduir amb precisió la concentració d'activitat, la quantificació d'imatges ha evolucionat significativament. Convertir les imatges en dades numèriques permet realitzar anàlisis objectius, comparables i reproduïbles, proporcionant una base sòlida per a les decisions clíniques.

Avui en dia, l'anàlisi informatitzada d'imatges mèdiques juga un paper fonamental en la medicina moderna, oferint als metges informació addicional per a guiar els processos de presa de decisions. A més, la quantificació millora la precisió diagnòstica, impulsa la medicina personalitzada i facilita la realització d'estudis multicèntrics amb menor variabilitat, contribuint així a una pràctica mèdica més rigorosa i efectiva.

La hipòtesi d'aquesta tesi és que l'extracció i l'anàlisi de dades quantitatives a partir de diferents imatges PET proporciona informació significativa que té un impacte en les decisions clíniques. Per tant, els objectius consisteixen a millorar aquesta presa de decisions gràcies a la quantificació de les imatges PET en dos casos d'ús: en demència i en tumors neuroendocrins.

En la part de demència, explorarem dues aplicacions principals. La primera té com a objectiu millorar la detecció precoç de malalties neurodegeneratives. La segona se centra en l'avaluació d'un escànner PET dedicat al cervell, assegurant al mateix temps

que oferisca una qualitat d'imatge i una precisió diagnòstica comparables a les d'un PET/TC convencional. En la part de tumors neuroendocrins, l'aplicació consisteix en l'harmonització de variables per a recomanacions de tractaments consistents.

La demència és una epidèmia global impulsada per l'envelliment de la població, amb més de 50 milions de casos actuals i projeccions que superen els 130 milions per a l'any 2050. Les malalties més comunes inclouen l'Alzheimer, la demència frontotemporal i la demència amb cossos de Lewy. L'Alzheimer representa el 70% dels casos i presenta una llarga fase preclínica. Davant aquesta realitat, els escànners PET dedicats al cervell ofereixen millores en el diagnòstic precoç.

A més, el deteriorament cognitiu lleu (DCL) és una alteració cognitiva que supera el declivi normal associat a l'envelliment, però que no és prou greu per a limitar de manera significativa el funcionament diari. Es considera un estat transitori entre l'envelliment i la demència.

El diagnòstic precoç de les malalties neurodegeneratives és una prioritat clínica, especialment en persones amb deteriorament cognitiu lleu, ja que els símptomes inicials poden confondre's amb els propis de l'envelliment fisiològic. En aquest context, la combinació d'una avaluació neuropsicològica, mitjançant eines com el "Clinical Dementia Rating" (CDR), el "Mini-Mental State Examination" (MMSE) i la bateria "Repeatable Battery for the Assessment of Neuropsychological Status" (RBANS), juntament amb la quantificació de biomarcadors en líquid cefaloraquidi (com ara Aβ_{42}, T-Tau i P-Tau) i les tècniques de neuroimatge, constitueix l'enfocament més sòlid.

La quantificació de biomarcadors en líquid cefaloraquidi permet identificar alteracions bioquímiques associades a la malaltia d'Alzheimer, amb una sensibilitat i especificitat elevades. Tanmateix, per la seva naturalesa invasiva, aquests mètodes es complementen cada vegada més amb tècniques d'imatge molecular.

En aquest sentit, la imatge PET ha adquirit un paper fonamental. El [^{18}F]FDG PET avalua el metabolisme cerebral de la glucosa, revelant hipometabolisme regional fins i tot abans que l'atròfia sigui detectable per ressonància magnètica. El PET amb traçadors amiloides permet la visualització directa i quantitativa de plaques de β-amiloide *in vivo*, la qual cosa suposa una revolució diagnòstica respecte al diagnòstic *post mortem* tradicional.

Aquestes eines no sols milloren la precisió diagnòstica, sinó que també permeten l'estratificació de pacients, la monitorització de tractaments modificadors de la malaltia i la implementació d'estratègies terapèutiques personalitzades. Amb l'aprovació recent de tractaments antiamiloide, s'espera un augment exponencial en la demanda d'estudis PET, que es consoliden com un pilar clau en la gestió clínica de les demències.

Els escànners dedicats al cervell són necessaris davant la urgència de reduir la gran càrrega que representen les malalties neurològiques i psiquiàtriques al PET/CT

convencional. Aquests dispositius naixen amb l'objectiu de superar les limitacions dels sistemes de cos sencer, oferint una major resolució i sensibilitat, especialment útils per a l'estudi de regions cerebrals de xicotet tamany. A més, són més portàtils i assequibles en comparació amb els escànners PET/TC convencionals, encara que presenten certes limitacions, com la cobertura geomètrica i les dificultats associades a la correcció de l'atenuació.

Per altra banda, els tumors neuroendocrins (TNE) són un grup heterogeni de neoplàsies que s'originen en cèl · lules endocrines del tub digestiu, pàncrees i arbre bronquial. Es classifiquen segons el seu grau i nivell de diferenciació, amb els tumors ben diferenciats subdividits en G1, G2 i G3 (alt grau). Dins dels TNE, destaquen els PGGL —és a dir, els paragangliomes i feocromocitomes—, que són tumors poc freqüents amb una elevada càrrega genètica: fins a un 40% dels casos estan associats a mutacions germinals.

A més, el deteriorament cognitiu lleu (DCL) és una alteració cognitiva que supera el declivi normal associat a l'envelliment, però que no és prou greu per a limitar de manera significativa el funcionament diari. Es considera un estat transitori entre l'envelliment i la demència.

El diagnòstic precoç de les malalties neurodegeneratives és una prioritat clínica, especialment en persones amb deteriorament cognitiu lleu, ja que els símptomes inicials poden confondre's amb els propis de l'envelliment fisiològic. En aquest context, la combinació d'una avaluació neuropsicològica, mitjançant eines com el "Clinical Dementia Rating" (CDR), el "Mini-Mental State Examination" (MMSE) i la bateria "Repeatable Battery for the Assessment of Neuropsychological Status" (RBANS), juntament amb la quantificació de biomarcadors en líquid cefaloraquidi (com ara Aβ_{42}, T-Tau i P-Tau) i les tècniques de neuroimatge, constitueix l'enfocament més sòlid.

La quantificació de biomarcadors en líquid cefaloraquidi permet identificar alteracions bioquímiques associades a la malaltia d'Alzheimer, amb una sensibilitat i especificitat elevades. Tanmateix, per la seva naturalesa invasiva, aquests mètodes es complementen cada vegada més amb tècniques d'imatge molecular.

En aquest sentit, la imatge PET ha adquirit un paper fonamental. El [^{18}F]FDG PET avalua el metabolisme cerebral de la glucosa, revelant hipometabolisme regional fins i tot abans que l'atròfia sigui detectable per ressonància magnètica. El PET amb traçadors amiloides permet la visualització directa i quantitativa de plaques de β-amiloide *in vivo*, la qual cosa suposa una revolució diagnòstica respecte al diagnòstic *post mortem* tradicional.

Aquestes eines no sols milloren la precisió diagnòstica, sinó que també permeten l'estratificació de pacients, la monitorització de tractaments modificadors de la malaltia i la implementació d'estratègies terapèutiques personalitzades. Amb l'aprovació recent de tractaments antiamiloide, s'espera un augment exponencial en la demanda d'estudis

PET, que es consoliden com un pilar clau en la gestió clínica de les demències.

Els escànners dedicats al cervell són necessaris davant la urgència de reduir la gran càrrega que representen les malalties neurològiques i psiquiàtriques al PET/CT convencional. Aquests dispositius naixen amb l'objectiu de superar les limitacions dels sistemes de cos sencer, oferint una major resolució i sensibilitat, especialment útils per a l'estudi de regions cerebrals de xicotet tamany. A més, són més portàtils i assequibles en comparació amb els escànners PET/TC convencionals, encara que presenten certes limitacions, com la cobertura geomètrica i les dificultats associades a la correcció de l'atenuació.

Per altra banda, els tumors neuroendocrins (TNE) són un grup heterogeni de neoplàsies que s'originen en cèl · lules endocrines del tub digestiu, pàncrees i arbre bronquial. Es classifiquen segons el seu grau i nivell de diferenciació, amb els tumors ben diferenciats subdividits en G1, G2 i G3 (alt grau). Dins dels TNE, destaquen els PGGL —és a dir, els paragangliomes i feocromocitomes—, que són tumors poc freqüents amb una elevada càrrega genètica: fins a un 40% dels casos estan associats a mutacions germinals.

MATERIALS I MÈTODES:

Amb l'objectiu de millorar la detecció precoç de malalties neurodegeneratives, s'han dut a terme dos estudis. El primer consisteix en l'anàlisi de la relació entre la imatge cerebral amb [^{18}F]FDG PET i l'estat cognitiu en casos de deteriorament cognitiu lleu, amb la finalitat d'avaluar el potencial de la cognició social en la detecció precoç de la malaltia d'Alzheimer.

Aquest estudi inclou 124 pacients seleccionats retrospectivament a l'Hospital Universitari i Politècnic La Fe, amb cognició normal, deteriorament cognitiu molt lleu i lleu, que es van sotmetre a una prova d'imatge [^{18}F]FDG PET en un equip PET/TC, així com a un test de reconeixement d'emocions.

El diagnòstic final es va establir tenint en compte avaluacions físiques i neuropsicològiques, proves de neuroimatge realitzades dins dels 12 mesos següents a l'avaluació neuropsicològica, i anàlisis moleculars del líquid cefaloraquidi obtingut mitjançant punció lumbar. En el moment de la realització de les proves de biomarcadors en LCR i de les imatges PET/TC, tots els pacients presentaven un deteriorament cognitiu lleu, segons els criteris del CDR, amb un declivi cognitiu de com a mínim sis mesos de duració i confirmat de manera objectiva.

El reconeixement emocional es va avaluar mitjançant el test *Reading the Mind*

in the Eyes (RMET). Aquest test inclou 36 imatges de la zona ocular que expressen emocions complexes. Les 36 imatges es divideixen en tres categories emocionals: 8 de caràcter positiu (per exemple, amistós), 12 negatives (per exemple, molest), i 16 neutres (per exemple, reflexiu). Els participants havien de seleccionar l'adjectiu més adequat entre quatre opcions (tres incorrectes i una correcta) per a cada imatge. En cas necessari, se'ls oferien definicions dels adjectius per facilitar la comprensió.

El segon estudi orientat a millorar la detecció precoç de malalties neurodegeneratives es va centrar en la validació d'un algoritme d'aprenentatge profund capaç de classificar si els pacients amb deteriorament cognitiu lleu presentaven o no una malaltia neurodegenerativa.

Per a aquesta intervenció, es van reclutar retrospectivament pacients diagnosticats de DCL mitjançant el mateix procediment emprat en l'estudi anterior. Inicialment, es van incloure pacients amb deteriorament cognitiu, principalment de tipus amnèsic, però sense afectació significativa de la funcionalitat en les activitats quotidianes. Es van excloure del grup d'estudi aquells participants que no presentaven una puntuació de 0,5 en l'escala CDR, que no tenien un diagnòstic definitiu, o que no comptaven amb una imatge de [^{18}F]FDG PET.

En total, es van incloure 90 pacients que complien amb els criteris d'elegibilitat. Aquests es van dividir en dos grups: 71 casos de DCL associat a una malaltia neurodegenerativa, dels quals 64 corresponien a malaltia d'Alzheimer, 4 a degeneració frontotemporal i 3 a demència amb cossos de Lewy. L'altre grup estava compost per 19 casos de DCL no associat a cap malaltia neurodegenerativa.

Aquest estudi representa un pas important cap a l'aplicació d'eines d'intel · ligència artificial en el diagnòstic precoç de trastorns neurodegeneratius, amb potencial per complementar l'avaluació clínica i millorar l'estratificació dels pacients. Per a aquesta primera aplicació, totes les imatges [^{18}F]FDG PET es van adquirir amb l'equip PET/TC Philips Gemini TF 64.

La segona aplicació en l'àmbit de la demència tenia com a objectiu avaluar la qualitat d'imatge i la fiabilitat diagnòstica d'un escànner PET dedicat exclusivament al cervell, amb la finalitat de reduir la càrrega neurològica associada a l'ùs del PET/TC convencional. Els equips PET utilitzats en aquest estudi van ser el PET/TC Philips Gemini TF 64 i el PET cerebral dedicat CareMiBrain (CMB).

El Philips Gemini TF 64 ofereix una resolució de 4,8 mm pròxima al centre i compta amb un camp de visió transversal de 576 mm i un d'axial de 180 mm. A més, està dissenyat per oferir una bona resolució temporal gràcies a la informació de temps de vol (TOF), essencial per a l'exactitud diagnòstica.

Per altra banda, el CareMiBrain incorpora 48 mòduls amb fotomultiplicadors de silici combinats amb cristalls LYSO, que permeten una millor resolució espacial i

una major precisió en la determinació de la profunditat d'interacció dels raigs gamma. Aquest sistema aconsegueix una resolució de fins a 1,87 mm en les direccions radials i tangencials a només 10 mm del centre, oferint una imatge cerebral d'alta definició.

En l'escànner CMB, el mapa d'atenuació es genera a partir de la pròpia imatge d'emissió. Primer, es realitza una iteració OSEM sense correcció d'atenuació ni de dispersió i es retalla la imatge per reduir el soroll. A continuació, s'aplica un algoritme k-means amb quatre nivells per segmentar la imatge: els voxels del nivell més baix s'identifiquen com a soroll i s'estableixen a zero, mentre que la resta s'assignen a un valor uniforme. Finalment, al mapa d'atenuació resultant s'assigna el coeficient de la substància grisa a tots els voxels no nuls, millorant així la precisió de l'escaneig.

Pel que fa a l'avaluació de la qualitat d'imatge del PET cerebral dedicat, l'estudi es va dur a terme tant en imatges [^{18}F]FDG PET d'un maniquí Hoffmann com en pacients. En el cas del maniquí, es van fer tres adquisicions de 20 minuts en dies diferents, tant amb el PET/TC com amb el CMB. A partir de cada adquisició es van generar quatre reconstruccions: una utilitzant els 20 minuts complets i tres amb fragments de 10 minuts.

Respecte als pacients, aquells que acudiren a l'hospital per a una exploració diagnòstica amb el PET/TC van ser convidats a participar voluntàriament en la validació del PET cerebral dedicat. Tots els participants van ser reclutats de manera prospectiva. Les imatges es poden dividir en dos grups.

El primer grup està format per 80 pacients amb imatges [^{18}F]FDG PET cerebrals no oncològiques. Aquestes dades s'utilitzaren tant per a l'avaluació objectiva de la qualitat d'imatge com per a l'anàlisi del rendiment diagnòstic mitjançant una xarxa neuronal d'aprenentatge profund. Les adquisicions es van fer amb 20 minuts al PET/TC i 12 minuts al CMB. Les imatges del CMB es reconstruïren tant amb el mapa d'atenuació basat en emissió com amb el basat en TC. Cal esmentar que es van excloure 31 pacients en els quals el cerebel no apareixia completament en la imatge, a causa de les limitacions del camp de visió axial del CMB (15 cm) i a l'ús de referències anatòmiques externes per al posicionament.

El segon grup està integrat per 26 pacients amb imatges PET amiloide, adquirides amb tres radiofàrmacs diferents (^{18}F-Flutemetamol, ^{18}F-Florbetaben i ^{18}F-Florbetapir), també reclutats prospectivament. D'aquests, 14 van ser diagnosticats amb malaltia d'Alzheimer i 12 sense. En aquest cas, la intervenció se centrà en avaluar la capacitat diagnòstica del PET dedicat mitjançant quatre reconstruccions diferents i l'ús de l'escala Centiloide.

Per altra banda, amb l'objectiu d'harmonitzar variables per a recomanacions de tractaments consistents de pacients amb tumors neuroendocrins, l'estudi prospectiu va incloure pacients diagnosticats amb paragangliomes o feocromocitomes localment avançats o metastàtics, confirmats histològicament. Els pacients van ser derivats al

nostre centre de referència acreditat en tumors neuroendocrins entre setembre de 2020 i juny de 2022 per a estadificació, seguiment o presa de decisions terapèutiques.

Els criteris d'exclusió foren: embaràs, edat inferior a 18 anys, contraindicacions per a la ressonància magnètica i la incapacitat per comprendre el protocol de l'estudi o per proporcionar consentiment informat. Les exploracions PET/TC i PET/RM es van realitzar consecutivament després d'una única injecció intravenosa de [^{68}Ga]Ga-DOTATOC, sense ús de contrast radiològic. Primer es va efectuar l'exploració PET/TC, seguida immediatament per una exploració PET/RM. Els escàners utilitzats van ser el Philips Gemini TF 64 PET/TC i el General Electric SIGNA™ PET/RM.

L'escàner General Electric SIGNA™ PET/RM utilitza fotomultiplicadors de silici combinats amb cristalls de luteci per aconseguir una alta resolució espacial, amb una resolució PET propera al centre de 4,2 mm. El seu camp de visió axial és de 25 cm i el transversal de 60 cm. A més, la seva capacitat TOF millora la relació senyal soroll i la qualitat de la imatge. Aquest sistema està dissenyat per assegurar una integració òptima entre PET i RM, optimitzant el rendiment de les imatges sense interferències.

L'objectiu principal de les mesures quantitatives o semiquantitatives en la interpretació d'imatges PET és eliminar la variabilitat entre diferents lectors. La quantificació de la imatge PET permet realitzar comparacions entre estudis de diferents pacients, que s'utilitzen sovint per al diagnòstic o per monitoritzar i avaluar la resposta al tractament.

Les imatges de diferents pacients, o fins i tot d'un mateix pacient obtingudes amb escàners diferents, no sempre estaran en el mateix espai de referència, ja que els pacients no es col · loquen exactament a la mateixa posició. Per tant, per a la quantificació d'imatges PET en demència és necessari utilitzar transformacions matemàtiques que reescriguin cada imatge dins d'un mateix espai de referència, creant una correspondència punt a punt (voxel a voxel) entre pacients per tal de poder comparar-les. Existeixen diverses transformacions matemàtiques aplicables a les imatges mèdiques. Les més utilitzades són: rotació, translació, remostrage, cisallament i deformació.

La rotació és una transformació afí que gira una imatge un cert angle al voltant del seu origen o centre. Aquesta transformació modifica l'orientació de la imatge segons l'angle establert, però manté la mateixa forma i grandària. La translació és una transformació afí que desplaça una imatge una quantitat determinada de píxels al llarg dels eixos x i y. Aquest procés reubica cada píxel en una nova posició sense alterar la forma ni la mida de la imatge. El remostrage és una transformació que modifica la resolució espacial d'una imatge interpolant els valors dels píxels per crear una nova graella. Això pot implicar augmentar la resolució o disminuir-la. El cisallament és una transformació afí que desplaça els punts en una direcció fixa segons un factor proporcional a la seva distància signada respecte a una línia que es mou paral · lela a aquesta direcció. Finalment, la deformació és una transformació geomètrica que altera la configuració espacial d'una imatge, permetent la seva distorsió o deformació per ajustar-la a una forma o

mapeig desitjat.

Aquestes transformacions matemàtiques es poden agrupar en diferents tipus de tècniques segons les característiques de les imatges a processar: realineament, corregistre i normalització espacial.

Les tècniques de realineament són transformacions matemàtiques que reescriuen diverses imatges del mateix pacient i modalitat dins d'un únic espai de referència. Els procediments de realineament s'utilitzen, per exemple, quan es comparen dues imatges PET del mateix pacient obtingudes abans i després d'un tractament. En aquest cas, realinear ambdues imatges PET permetria una comparació píxel a píxel per identificar canvis. Un procediment de realineament implica transformacions afins de "cos rígid" que inclouen rotacions i translacions tridimensionals.

Les tècniques de corregistre s'utilitzen per reescriure imatges del mateix pacient provinents de diferents modalitats. La integració de diferents modalitats d'imatge pot proporcionar informació addicional que no és evident quan s'analitzen les imatges de manera individual. L'emparellament d'imatges funcionals amb imatges estructurals permet localitzar amb més precisió la regió anatòmica on es detecta captació en la imatge PET. Aquesta tècnica és similar al realineament, però la diferència principal entre ambdues és que una imatge per RM té píxels més petits que una imatge PET, fet que requereix afegir transformacions de remostrage. Un altre ús possible d'aquest registre és calcular una normalització espacial més precisa a partir d'una imatge estructural més detallada.

La normalització espacial és una tècnica que reescriu imatges de diferents subjectes dins d'un mateix espai de referència, ja siga de la mateixa modalitat o de modalitats diferents. La normalització espacial és fonamental per comparar la imatge PET d'un pacient amb una imatge PET de referència. Durant la normalització espacial es disposa d'una imatge canònica o plantilla que es modifica per crear una imatge específica del subjecte. La normalització espacial inverteix aquest procés desfent la deformació mitjançant una tècnica d'emparellament amb la plantilla. Aquest procés inclou rotacions, translacions tridimensionals i deformacions com la cisalladura i la distorsió.

A més de les transformacions matemàtiques, es requereix la normalització de la intensitat per eliminar variables biològiques i tecnològiques no relacionades amb la malaltia que podrien influir en les concentracions de [^{18}F]FDG. El valor estàndard de captació (SUV, per les seves sigles en anglès) és un indicador semiquantitatiu del metabolisme de la glucosa que pot utilitzar-se per caracteritzar lesions. El SUV representa la captació de [^{18}F]FDG dins d'un volum, normalitzada respecte a l'activitat administrada i a un factor (com el pes corporal) que tingui en compte la distribució en tot el cos.

No obstant això, aquesta mesura està afectada per diverses variables, com ara el pes del pacient, la durada de l'adquisició i el nivell de glucosa plasmàtica en el moment

de la injecció del radiofàrmac. Això genera un grau important de variabilitat, fins i tot dins d'un mateix subjecte. En aquesta situació, avaluar el SUV relatiu (SUVr) esdevé especialment interessant. En demència, per exemple, la normalització de la intensitat es pot dur a terme normalitzant respecte al cervell sencer o a regions de referència establertes, que es sap que no estan afectades per la malaltia ni pel mètode (com el cerebel). Això fa que els valors obtinguts estiguin relacionats amb la regió de referència i permet comparacions fiables entre pacients o dins del mateix pacient.

Un cop obtingudes les dades preprocessades, en neuroimatge existeixen diverses maneres d'extraure informació rellevant del pacient per a la seua comparativa. La quantificació basada en vòxels compara estadísticament, voxel a voxel, la imatge PET d'un pacient amb un conjunt d'imatges PET de subjectes control. La quantificació basada en volums d'Interès (VOIs) estima la concentració mitjana del radiofàrmac en diferents volums cerebrals d'interès. Sovint s'utilitzen valors relatius, com el SUVr. En les aplicacions de demència d'aquesta tesi, s'ha emprat la quantificació basada en VOIs per extreure informació rellevant de les imatges PET.

Actualment, existeixen nombrosos atles diferents. En les aplicacions de demència d'aquesta tesi, s'ha utilitzat una versió modificada de l'atles de VOIs de Hammers en l'espai de l'Institut Neurològic de Montreal (MNI). La modificació va consistir a combinar algunes de les 95 àrees cerebrals incloses en l'atles de Hammers, creant un nou atles (La Fe atles) amb 28 regions. Aquesta modificació és coherent amb els volums cerebrals d'interès utilitzats en CortexID Suite, un programa comercial d'ús clínic. Un metge especialista en medicina nuclear amb més de deu anys d'experiència va ser qui va identificar aquests volums d'interès. Per altra banda, a més dels atles cerebrals, segmentar el cervell en substància grisa i substància blanca és útil per avaluar la qualitat de la imatge.

Pel que fa a la quantificació d'imatges PET per a l'aplicació en tumors neuroendocrins, metges especialistes en medicina nuclear amb experiència van avaluar els resultats de les imatges. Van analitzar el valor SUV_{max} i la relació lesió-fetge per a totes les lesions detectades. A més, es van mesurar els valors SUV_{max} i SUV_{mean} tant en el fetge com en la melsa. El SUV_{max} es va determinar generant volums d'interès amb isocontorns que incloïen tots els vòxels que superaven el 40% de la captació màxima, tant en les lesions com en el teixit hepàtic normal. Totes aquestes mesures es van realitzar utilitzant el programa *Philips IntelliSpace Portal* i l'estació de treball *GE Advantage Workstation* amb el programa *PET VCAR* (Computer-Assisted Reading). Les lesions es van classificar segons els resultats obtinguts en les exploracions PET/CT i PET/RM.

Pel que fa a l'anàlisi de dades, en una de les aplicacions en demència d'aquest treball, per a distingir entre casos de deteriorament cognitiu lleu amb i sense malaltia neurodegenerativa associada, es va utilitzar una xarxa neuronal convolucional. Aquesta xarxa va ser dissenyada per un grup de la Universitat Politècnica de València i entrenada amb imatges cerebrals [^{18}F]FDG PET de 822 pacients provinents d'un repositori públic d'imatges.

Cal destacar que, en aquest estudi, la xarxa no es va entrenar de nou, sinó que es va validar per avaluar la seva reproductibilitat utilitzant imatges externes del nostre hospital. En resum, l'arquitectura de la xarxa inclou tres blocs de capes convolucionals, de pooling i de dropout. Les capes convolucionals s'encarreguen d'extreure característiques rellevants de la imatge; les capes de pooling redueixen la dimensionalitat de les imatges; i les capes de dropout ajuden a prevenir el sobreajustament desactivant aleatòriament algunes neurones durant l'entrenament. A continuació, s'afegeix una capa completament connectada que uneix totes les neurones de la capa anterior i aplica una funció d'activació ReLU per introduir no linealitat al model.

Les mètriques de qualitat d'imatge calculades inclouen el contrast entre la substància grisa i la substància blanca, així com el coeficient de recuperació de la substància grisa en el maniquí Hoffman, definit com la ràtio entre l'activitat mesurada i l'activitat teòrica. També s'ha avaluat la relació senyal-soroll (SNR) tant de la substància grisa com de la substància blanca, i la relació contrast-soroll (CNR) de la substància grisa en relació amb la blanca. A més, s'ha calculat el coeficient de variació de les mesures de 10 minuts del maniquí Hoffman, una mètrica que descriu el soroll de la imatge. Finalment, s'ha determinat el SUVr per a cadascuna de les 27 VOIs seleccionades, prenent el cerebel com a regió de referència per a la normalització.

Per a l'harmonització de variables, hem emprat el mètode *ComBat*, una tècnica estadística dissenyada per harmonitzar dades procedents de diferents fonts o centres, eliminant l'efecte de lot o *batch* (variabilitat no biològica) en conjunts de dades multidimensionals. *ComBat* originalment va ser desenvolupat per a dades genòmiques, i ajusta les variables mitjançant un model bayesià que separa els efectes biològics reals de les diferències introduïdes per la variabilitat tècnica o metodològica, permetent així comparar dades de forma fiable entre estudis o equips diferents. És àmpliament utilitzat en neuroimatge i altres camps per garantir la coherència i robustesa dels anàlisis quan es treballa amb dades heterogènies.

Per a l'anàlisi de la imatge PET d'amiloide s'ha emprat el mètode Centiloide. Es sap que diversos factors generen certa heterogeneïtat en els resultats, com ara el radiofàrmac utilitzat, la durada de l'adquisició, els diferents paràmetres de reconstrucció o el tipus d'anàlisi realitzat. Per això, és imprescindible disposar d'un mètode estandarditzat per al diagnòstic de la malaltia d'Alzheimer basat en la imatge PET d'amiloide, vàlid per a tots els centres.

Per a uniformitzar les mesures entre diferents centres, Klunk et al. van proposar el mètode Centiloide, que escala linealment la informació obtinguda de les imatges PET d'amiloide a unitats centiloides estàndard que oscil · len entre 0 i 100, on "0" correspon a la captació mitjana dels pacients controls i "100" a la dels pacients amb malaltia d'Alzheimer.

En el seu article, Klunk descriu el procediment per aplicar l'escala Centiloide i els usuaris han de desenvolupar el seu propi codi seguint els passos indicats, a més de

validar-lo amb les dades originals. Aquest primer pas de validació del codi implementat s'anomena replicació de l'anàlisi de nivell 1. Utilitzant el mètode proposat, totes les imatges de ressonància magnètica es van coregistrar i normalitzar espacialment a l'espai MNI. Mitjançant l'aplicació dels paràmetres de transformació calculats a partir de les imatges de RM, les imatges PET es van coregistrar a les imatges RM de cada pacient i es van normalitzar espacialment a l'espai MNI. Posteriorment, es van calcular els valors Centiloide a partir dels valors SUVr de la imatge PET i es van correlacionar linealment amb els valors originals de Centiloide.

No obstant això, aquest procés requereix l'ús d'imatges de RM, i no tots els pacients que realitzen un PET d'amiloide disposen de ressonància magnètica. Per tant, per oferir un mètode més generalista, es va modificar la pipeline per prescindir de les imatges de RM (Pipeline Only PET). Un cop validada aquesta pipeline només PET mitjançant la replicació de l'anàlisi de nivell 1, vam poder aplicar les equacions calibrades prèviament per convertir les nostres imatges obtingudes amb PET/CT i CMB a l'escala Centiloide.

En quant a l'anàlisi estadístic, en aquesta tesi s'han utilitzat diversos mètodes per al tractament de les dades. Per a la comparació entre grups s'han aplicat el test de normalitat de Shapiro-Wilk, el test paramètric de Student i el test no paramètric de Mann-Whitney-Wilcoxon. La correlació entre variables s'ha avaluat mitjançant el coeficient de correlació de rang de Spearman. Per a la classificació i l'avaluació del rendiment dels models, s'han calculat indicadors com l'exactitud, la taxa d'error i la sensibilitat, així com l'índex de Youden. La concordança i el biaix es van analitzar amb l'índex kappa de Cohen, la regressió Passing-Bablok i l'anàlisi de Bland-Altman. També s'han emprat xarxes neuronals per a la classificació, complementades amb tècniques d'interpretabilitat com els mapes d'atenció (Saliency, Grad-CAM i SmoothGrad) per comprendre millor el funcionament dels models.

RESULTATS I CONCLUSIONS:

En el primer estudi es va explorar la relació entre la cognició social i la neuroimatge en pacients amb deteriorament cognitiu lleu. Es va utilitzar el test RMET per avaluar el reconeixement emocional. Els resultats van mostrar que les alteracions emocionals s'associen amb un hipometabolisme en àrees cerebrals clau. El més rellevant és que aquests dèficits no es van relacionar amb biomarcadors de l'Alzheimer, la qual cosa suggereix que no són exclusius d'aquesta malaltia. Per tant, la incorporació d'aquest test pot permetre la detecció precoç de dèficits en pacients amb DCL, però no específics de l'Alzheimer.

En el segon estudi es va validar externament una xarxa neuronal entrenada

per classificar la presència de malalties neurodegeneratives a partir d'imatges PET de pacients amb DCL. El model va assolir una precisió equilibrada del 80% amb dades reals, un resultat rellevant, sobretot tenint en compte que es va centrar en pacients amb DCL, una població difícil de classificar. A diferència d'altres estudis, ací no es van incloure pacients sans ni amb demència avançada. Tot i algunes limitacions, com la mida del conjunt de dades, aquests resultats donen suport a l'ús futur de la intel · ligència artificial com a eina d'ajuda en el diagnòstic clínic.

Pel que fa a l'estudi comparatiu de la qualitat d'imatge entre el PET dedicat CMB i el PET/TC convencional, s'ha observat que, tot i presentar una menor relació senyal-soroll, les imatges CMB mostren un major contrast i resolució espacial. Quan es va aplicar la correcció per atenuació basada en TC, les diferències en els valors SUVr respecte al PET/TC van ser mínimes, al voltant del 4%. No obstant això, amb la correcció per emissió, aquestes diferències van augmentar, especialment en algunes regions cerebrals. També es va demostrar que la tècnica d'harmonització ComBat és molt efectiva per armonitzar les dades entre dispositius, fet essencial per a anàlisis clíniques comparatives. Tot i que el sistema CMB presenta certes limitacions, com un camp de visió reduït que va impedir incloure el 28% dels pacients, en general es conclou que les imatges CMB són comparables a les del PET/TC.

Per avaluar la capacitat diagnòstica del sistema PET dedicat al cervell, es van dur a terme dos estudis. En el primer, s'aplicà una xarxa neuronal a imatges [^{18}F]FDG PET de 55 pacients amb deteriorament cognitiu, i es va observar que el diagnòstic amb CMB té una alta concordança amb el PET/TC quan s'utilitza la correcció per atenuació basada en TC. En canvi, amb la correcció per emissió, la concordança és un poc menor. En el segon estudi, amb imatges PET amiloide, es va demostrar que el CMB, fins i tot sense imatges de RM, pot classificar adequadament els pacients. Els valors de tall obtinguts van ser coherents amb els reportats en la literatura, i la reconstrucció amb 2mmPSF va mostrar els resultats més similars al PET/TC. Tot i les diferències entre escàners, l'estandardització mitjançant l'escala Centiloide permet comparacions fiables. Aquest enfocament es considera prometedor, especialment davant l'augment esperat en la demanda d'estudis PET degut a la introducció de nous fàrmacs per a l'Alzheimer.

En l'àmbit dels tumors neuroendocrins, en pacients amb paragangliomes i feocromocitomes, la imatge PET amb [^{68}Ga]Ga-DOTA-TOC és fonamental per a la presa de decisions sobre el tractament amb teràpia dirigida, com ara [^{177}Lu]Lu-DOTA-TATE. Aquesta decisió es basa en l'escala Krenning, que avalua la captació tumoral en relació amb el fetge. No obstant això, les diferències entre escàners PET/TC i PET/RM generen discrepàncies que poden influir en la decisió terapèutica.

En aquest estudi, abans de l'harmonització, un 23% de les lesions es classificaven de manera diferent entre ambdós sistemes, amb una concordança moderada. Després de l'harmonització, la concordança va millorar de manera significativa, especialment quan es va utilitzar el PET/TC com a referència, assolint un valor kappa de 0,74. Tot i la mostra reduïda, els resultats són prometedors i suggereixen que l'harmonització

de dades permet prendre decisions terapèutiques més coherents, independentment de l'escàner utilitzat.

Finalment, es conclou que l'anàlisi quantitatiu d'imatges PET millora significativament la presa de decisions clíniques, ja que permet diagnòstics més precisos i tractaments personalitzats, especialment en casos de demència i tumors neuroendocrins, ressaltant així la importància de continuar optimitzant aquesta tecnologia. En el diagnòstic de la demència, s'ha observat que la combinació de [^{18}F]FDG PET amb proves de cognició social no augmenta la precisió per al diagnòstic de la malaltia d'Alzheimer. D'altra banda, l'ús de xarxes neuronals permet identificar malalties neurodegeneratives amb un 80% de precisió, i pel que fa als escàners PET dedicats al cervell, aquests podrien alleugerir la càrrega dels sistemes generals sense perdre qualitat. En tumors neuroendocrins, les diferències entre escàners afecten directament els valors de SUV, fet que pot modificar l'elegibilitat per a certs tractaments; per això, harmonitzar aquestes dades és clau per alinear els resultats entre diferents tipus d'escàner i millorar la coherència en les decisions clíniques. De cara al futur, el repte serà validar aquests mètodes amb més dades i en diversos centres, a més d'estandarditzar les tècniques per assegurar la fiabilitat en la presa de decisions i reforçar el paper de les imatges PET com a eina clau en la medicina de precisió.